PLANET: a new approach for quantitative MRI

Yulia Shcherbakova

geboren op 21 augustus 1985
te Bogoroditsk, Rusland

PLANET: a new approach for quantitative MRI
PhD Thesis, Utrecht University, The Netherlands

PLANET: a new approach for quantitative MRI

PLANET: een nieuwe methode voor kwantitatieve MRI

(met een samenvatting in het Nederlands)

Proefschrift

ter verkrijging van de graad van doctor
aan de Universiteit Utrecht op gezag van de
rector magnificus, prof. dr. H.R.B.M. Kummeling,
ingevolge het besluit van het college voor promoties
in het openbaar te verdedigen op

donderdag 5 december 2019 des middags te 12:45 uur

door

Yulia Shcherbakova

geboren op 21 augustus 1985
te Bogoroditsk, Rusland

Promotor:
Prof. dr. C.T.W. Moonen

Copromotoren:
Dr. ir. L.W. Bartels
Dr. ir. C.A.T. van den Berg

Contents

List of Abbreviations

2D Two-dimensional

3D Three-dimensional

AFI Actual Flip-Angle Imaging

ADC Apparent Diffusion Coefficient

AP Anterior-Posterior

bSSFP balanced Steady-State Free Precession

CSF Cerebrospinal Fluid

CT Computed Tomography

EBRT External Beam Radiotherapy

EPT Electric Properties Tomography

FA Flip Angle

FID Free Induction Decay

FLAIR Fluid-Attenuated Inversion Recovery

FM Fiducial Marker

FOV Field-of-View

GE Gradient-Echo

GM Gray Matter

GS Geometric Solution

HIFU High Intensity Focused Ultrasound

IR Inversion Recovery

IR-SE Inversion Recovery Spin-Echo

LinAc Linear Accelerator

LR Left-Right

ME Multi-Echo

ME-SE Multi-Echo Spin-Echo

MR Magnetic Resonance

MRF Magnetic Resonance Fingerprinting

MRgHIFU MRI guided High Intensity Focused Ultrasound

MRgRT MRI guided Radiation Therapy

MRI Magnetic Resonance Imaging

MT Magnetization Transfer

MTR Magnetization Transfer Ratio

NMR Nuclear Magnetic Resonance

NSA Number of Signal Averages

PD Proton Density

QIB Quantitative Imaging Biomarker

QMRI Quantitative Magnetic Resonance Imaging

QSM Quantitative Susceptibility Mapping

RF Radiofrequency

ROI Region Of Interest

RT Radiotherapy

SE Spin-Echo

SENSE Sensitivity Encoding

SNR Signal-to-Noise Ratio

SPAIR Spectral Attenuated Inversion Recovery

SPGR Spoiled Gradient-Echo

STIR Short-Tau Inversion Recovery

TE Echo Time

TSE Turbo Spin-Echo

TR Repetition Time

VFA Variable Flip Angle

WM White Matter

Chapter *1*

Introduction

1.1 Magnetic Resonance Imaging

Magnetic Resonance Imaging (MRI) is a medical imaging modality, the story of which started in the 1930s when nuclear magnetic resonance (NMR) was discovered (1). In 1977 the first image of the human body was produced on the first MR Scanning Machine. Since then tremendous progress has been made, and MRI nowadays is widely used in clinics and hospitals for medical diagnosis, for planning, guidance, and evaluation of image-guided therapies, and as an instrument in many fields of scientific research, e.g. neuroscience.

To perform an MR examination, a patient is positioned on a bed, called the table, and then moved into a scanner, where a strong static magnetic field is present. The hydrogen nuclei (protons) in tissues possess a magnetic moment as well as angular momentum. This combination leads to precession of the magnetic moment of the proton spins around the direction of the applied magnetic field at a certain frequency, called the Larmor frequency. When a radiofrequency (RF) pulse at the Larmor frequency (i.e. an on-resonance pulse) is temporarily applied to the patient by a transmit coil, the hydrogen nuclei absorb energy. This is the excitation process. After excitation, an induction signal caused by coherent precession of nuclear spins can be picked up using an RF coil. In general, in MR imaging the RF signals are spatially encoded prior to signal read-out by using gradient coils. After collection of a sufficient number of spatially encoded signals, an image of the patient's body is reconstructed. Such images typically show predetermined contrasts created by the mechanism of signal weighting, where scanner parameters are set to highlight specific image contrasts in tissues that are related to certain differences in tissue magnetic relaxation parameters (T_1 and T_2). This is what conventional MRI is based on, as will be described in more detail below in §1.2. Clinical diagnosis is typically based on visual evaluation of multiple sets of weighted MR images, i.e. images acquired with different specific contrast settings. Differentiation between tissues (e.g. of different organs) and between pathological tissue and healthy tissue is based on contrasts in the images.

Besides its use for clinical diagnostic imaging, MRI has attracted considerable attention for non-invasive image-guided therapies, such MRI guided High Intensity Focused Ultrasound (MRgHIFU) therapy, and MRI guided Radiation Therapy (MRgRT).

The most commonly used therapeutic principle of HIFU treatment is thermal ablation of cancer cells. High-intensity ultrasound waves are focused on a particular area of tissue and deliver a certain thermal dose which causes tissue coagulation and further necrosis (2,3). The use of MRI for the guidance of HIFU therapy provides excellent anatomical details and soft-tissue contrasts for treatment planning and evaluation and allows to perform MR thermometry (4).

Radiation therapy or radiotherapy (RT) is a commonly used cancer therapy, which relies on delivering ionizing radiation to the tumor tissue. In external beam radiotherapy, high energy x-rays generated by a Linear Accelerator (LinAc) are shaped and directed into the patient's tumor to destroy it by damaging its DNA (5) leading finally to cell death. MRI is increasingly used for the better delineation of tumor volumes and organs at risk due to its superior soft tissue contrast. Furthermore, the recent development of hybrid MRI-Linacs that allow MRI imaging during radiation delivery, has created the possibility to guide radiation delivery based on MR imaging.

1.2 Conventional MRI

Conventional MRI is based on acquiring a series of scans with different contrasts and geometries leading to sets of 2D contrast weighted MR images. The magnetic relaxation times (T_1, T_2) are intrinsic tissue parameters, on which the contrasts in conventional MRI is often based. Different tissues have different values for the relaxation times, and in case of disease, the values typically change. The relaxation times reflect how quickly the net magnetization caused by all "excited" hydrogen protons inside an imaging voxel together returns to its "normal" equilibrium state (6,7). The type of "weighting" is determined by the pulse sequence used, the sequence parameter setting for the repetition time TR, the echo time TE, the flip angle FA, and the signal preparations (such as an inversion pulse) used to acquire the images (7). Examples of T1-weighted, T2-weighted, FLAIR (fluid-attenuated inversion recovery), STIR (short-tau inversion recovery), PD (proton density) images of the human brain are shown in Figure 1.1. For example, performing a spin-echo pulse sequence with a relatively short repetition time (TR) and a fairly short echo time (TE) will result in what is called a T1-weighted scan, as the contrasts in the resulting images will mainly reflect differences in the T_1 values of the tissues.
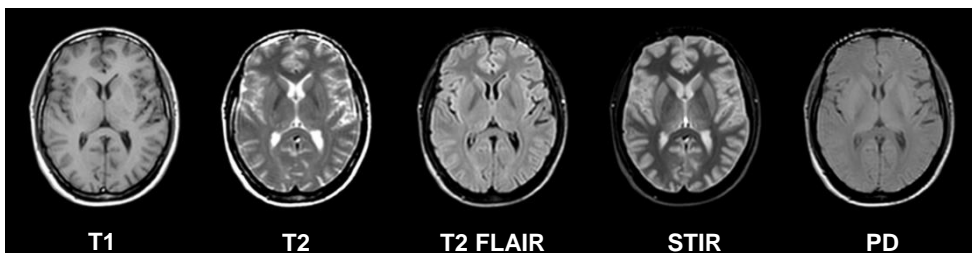

FIGURE 1.1. Examples of T1-weighted, T2-weighted, T2FLAIR, STIR, and PD-weighted axial images of the brain of a healthy volunteer.

 In conventional MRI, a multi-slice approach is typically used, allowing to cover the whole organ of interest by scanning multiple 2D slices in sequential or interleaved order.

The typical radiological assessment in conventional MRI relies on a visual evaluation of the signal intensities in the images and finding the regions of anomalous contrast. Tissues are usually referred to as "hypointense" or "hyperintense" compared to reference tissues.

Conventional MRI does not provide any quantitative characteristics of tissue with respect to being healthy or pathological. The MR signal is usually arbitrarily scaled and does not have a direct relationship with tissue properties. Furthermore, the MR signal is highly dependent on electromagnetic imperfections (B_0- and B_1-field inhomogeneities, RF receive coil sensitivities, gradient distortions) that are related to a physical interplay of the hardware characteristics of the scanner and the physical properties of the patient (e.g. RF interferences). Furthermore, in addition to these physical imperfections, MR vendors apply additional processing to the images such as image scaling, vendor-determined corrections for gradient nonlinearities, reconstruction algorithms that affect image magnitude and phase.

1.3 Quantitative MRI: mapping of Quantitative Imaging Biomarkers (QIBs)

In recent years, there has been a lot of attention for the quantification of imaging findings by using quantitative imaging biomarkers (QIBs), by creating quantitative maps of parameters, which are related to biological and physiological characteristics of tissues. The concept of QIB implies a direct or modeled relationship between a measurable quantity and some targeted biological or physiological tissue property (8,9). Based on these quantities, tissues can be depicted, differentiated, or associated with specific diseases (10–12). Furthermore, the ability to monitor changes in QIBs due to therapy is important for longitudinal evaluation of treatment effects (13–16).

A common approach to estimate QIBs with MRI is to employ a pulse sequence with a known signal model to acquire data to which the model is then fitted with the unknown QIB as a fitting parameter. This approach was successfully used to measure many parameters, such as the proton density ρ, the relaxation times (T_1, T_2, T_2^*), the apparent diffusion coefficient (ADC), and others. This concept is commonly referred to as quantitative MRI (QMRI).

Ideally, QMRI should provide reproducible QIB measurements independently of the institution, the MR scanner used, MR protocol parameter settings, and image scaling. Thus, it would enable comparison across different patients and would allow the diagnosis to be based on quantitative tissue information, not just on subjective visual evaluation of contrasts resulting from differences in such parameters. QMRI has the potential to improve clinical

diagnosis, detection and monitoring of diseases, therapy planning and response assessment, as well as the development of new therapies.

1.4 Quantitative relaxometry

Longitudinal (T_1) and transverse (T_2) relaxation times are intrinsic tissue parameters, which are relevant QIBs. Examples of T_1 and T_2 maps of the brain of a healthy volunteer are shown in Figure 1.2. Different tissues have different values for the relaxation times, and measuring these values (referred to as quantitative relaxometry) has been a research focus for a long time (17). Protocols for routine clinical diagnostic MRI are developed with the knowledge of T_1 and T_2 values for contrast optimization. Furthermore, quantitative relaxometry has been widely used in research studies and clinical applications in oncology and regenerative medicine, in the brain as well as in the body (18–20). Relaxometry analysis has been applied in the brain in the context of the assessment of multiple sclerosis, demyelination, stroke, epilepsy, edema, tumors, etc (21–32). Furthermore, volumetric T_1 and T_2 data can be used for automatic brain tissue segmentation and volume measurements in many neuroradiological applications (33–35). In the body, T_2 and T_2^* relaxometry has been applied for assessment of disorders of the prostate, kidneys, pancreas, liver (36–39).
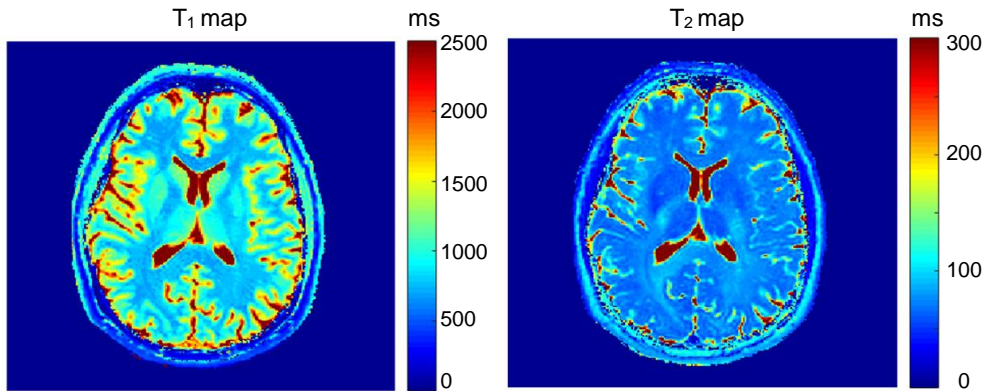
FIGURE 1.2. Examples of T_1 and T_2 maps of the brain of a healthy volunteer, reconstructed using the interleaved SE+IR 2D MIXED method at 3T (40).

1.5. Quantitative relaxometry techniques

With rapid technological developments, many different techniques have been proposed for quantitative relaxometry. In most cases, T_1 and T_2 values are determined using two separate acquisitions. For T_1 mapping, the 2D inversion-recovery (IR) spin-echo sequence with

multiple inversion times is considered to be the gold-standard technique (7). For T_2 mapping, the gold-standard method is based on 2D multiple TE spin-echo acquisitions (7,41). Unfortunately, scans based on these 2D techniques have long acquisition times, particularly when coverage of larger volumes, like the brain, is needed. To reduce scan time, simultaneous 2D T_1-T_2 mapping can be done using a combined approach, consisting of a multi-echo SE sequence interleaved with a multi-echo IR sequence and called 2D MIXED (40), but it is still a time-consuming approach. It takes about 15 min to acquire a typical 2D brain slice with 1.5x1.5x4 mm^3 voxel size and 220x220x4 mm^3 FOV.

Another approach for T_1 mapping is called the Look-Locker method. It is closely related to the gold-standard IR-SE, but instead of acquiring a single image for each inversion time, the Look-Locker method uses an inversion pulse followed by a train of low flip angle (FA) pulses, each followed by a read-out, within each repetition time (TR). Each low FA pulse perturbs the longitudinal magnetization recovery slightly depending on the T_1 of the tissue, leading to the measurement of the effective T_1 (T_1^*), and then converting it back to T_1. Although this method considerably reduces the scan time compared with the conventional IR approach, it still is a time-consuming 2D method, which in practice results in several hours scanning time when coverage of a 3D volume is required.

Very popular rapid methods for T_1-T_2 quantification use the steady-state signal from multiple spoiled and balanced steady-state free precession gradient-echo sequences with variable flip angles (42), which are known as DESPOT1&2 (43,44). These methods are usually implemented in 3D. At least two acquisitions of spoiled gradient-echo (SPGR) with different FAs are required for T_1 mapping with DESPOT1, and consequently, at least two acquisitions of balanced steady-state free precession (bSSFP) with different FAs are required for T_2 mapping with DESPOT2. DESPOT2 requires prior knowledge of T_1 values, often obtained from a DESPOT1 acquisition. To increase the precision of DESPOT relaxometry, a joint system relaxometry (JSR) approach was introduced (45) where both SPGR and bSSFP signals are simultaneously evaluated, allowing for full coverage 3D relaxation mapping of the human brain within around 10 min. However, B_1- and B_0 field inhomogeneities, imperfect spoiling of SPGR sequences demand the optimization of the protocol parameter settings for improved accuracy and precision (46–51).

Another interesting approach for simultaneous T_1-T_2 quantification is the IR balanced SSFP sequence (52), which is based on T_1-prepared steady-state imaging. The sequence includes an inversion pulse followed by the acquisition of several steady-state bSSFP images. However, it is still a 2D approach with a relatively long acquisition time. To speed up the IR bSSFP-based T_1 and T_2 mapping, a new approach was introduced where a method was combined with a radial trajectory with a golden-ratio-based profile (53). With this

acceleration, the scanning time for the method became very similar to the combined DESPOT1&2 method.

There are many other approaches for rapid quantification of T_1 and T_2, such as the QRAPMASTER method, which is based on multi-echo acquisition of a saturation-recovery using a turbo spin-echo readout, or TESS method (Triple-Echo-Steady-State), which allows for a simultaneous rapid 3D estimation of T_1 and T_2 within one single scan using two specific signal ratios between three echoes (SSFP-FID and two SSFP-echo modes) and an iterative golden section search algorithm. This method was used as a base for another approach called MIRACLE (54), where the unbalanced gradient scheme of TESS was replaced by a balanced one leading to "motion-insensitive rapid configuration relaxometry".

MR Fingerprinting (MRF) is another recently introduced approach for quantitative MRI (55) no longer relying on steady states and on algebraic inverse models. MRF includes two components: a specific pseudo-randomized, transient MR acquisition with a varying flip angle train from which a set of highly undersampled images are reconstructed. The resulting signal evolutions on a voxel level (fingerprint) are unique for a particular tissue property combination, but are highly corrupted by aliasing noise arising from the undersampling. However, robust parameter quantification is still achieved by a pattern recognition algorithm to match the acquired fingerprints to a predefined dictionary of predicted signal evolutions, which can then be used to generate QMRI maps. MRF is characterized by very short acquisition times and is a topic of intense recent research (56).

Another recent method, called MR-STAT (Magnetic Resonance Spin TomogrAphy in Time-domain), was introduced tor multi-parametric MRI (57), where the quantitative parameters are estimated by inverting a "coupled space-time model" from time domain data. This is obtained by combining time signal models (e.g. Bloch simulator) with numerical large-scale nonlinear inversion techniques. MR-STAT can achieve comparable acquisition times as MRF and since it performs reconstruction directly from the time domain signal it is not affected by aliasing noise.

Despite the fact that many different QMRI methods for relaxometry have been proposed, considerable variations can be observed in the results obtained on different scanners, e.g. equipment from different manufacturers, and with different protocol parameter settings or different implementations of the methods (58–62). A comprehensive review of the reported relaxation times in the literature *in vivo* at 3T for different tissues is presented in the paper by Bojorquez et al (61). For example, in white matter of the human brain at 3T, the reported T_1 values vary from 532 ± 56 ms measured with MIRACLE method (54) to 1085 ± 64 ms measured with VFA technique by (48), the reported T_2 values vary from 44 ± 5 ms (54) to 80 ± 1 ms (63).

A method for QMRI that simultaneously provides accurate, reproducible quantitative tissue parameter estimates, independently on the MR scanner, and MR protocol parameter settings, still has to be established.
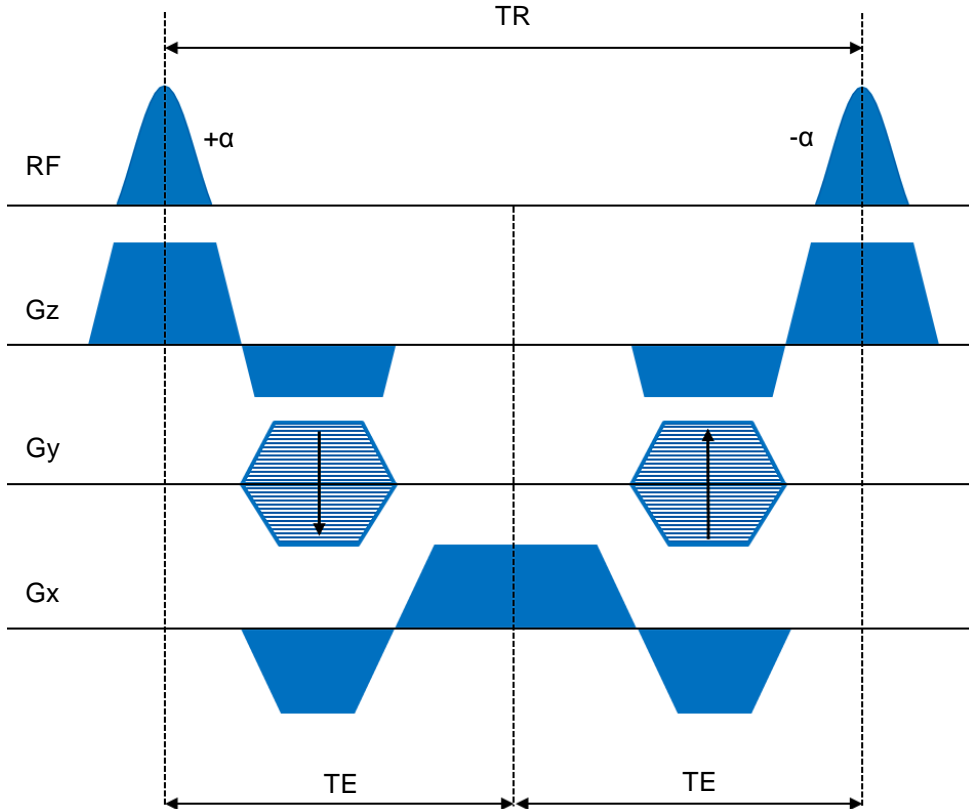
FIGURE 1.3. Sequence diagram of a standard bSSFP sequence. The gradients on all axis (Gx, Gy, Gz) are balanced within each TR interval. The echo is acquired in the middle of the TR interval (TE = TR/2). An RF phase cycling of 0 and 180° is employed.

1.6 Balanced Steady-State Free Precession

Balanced Steady-State Free Precession (bSSFP, also known as TrueFISP, bFFE, or FIESTA) sequences deserve special attention due to their rapid acquisition time and the highest signal-to-noise (SNR) efficiency among all known sequences (64).

bSSFP produces a unique "unconventional" T_2/T_1–weighted image contrast, which is typically used for imaging fluids (e.g. blood, ascites, etc.). The mixed T_2/T_1 contrast in

combination with high speed and the highest SNR efficiency makes bSSFP a perfect candidate for QMRI acquisition for quantitative relaxometry (49,52–54,65,66).

The simple pulse sequence diagram of a standard bSSFP sequence is shown in Figure 1.3. bSSFP requires the gradients in all three orthogonal directions (Gx, Gy, Gz) to be balanced, which means that all gradient moments are zero within each TR interval. The sign of the RF pulse usually alternates between the RF pulses, so-called (0,180°) RF phase cycling. The echo is acquired in the middle of the TR interval (TE = TR/2).

FIGURE 1.4. bSSFP signal behavior for several tissues with different T_1 and T_2 combinations, computed for FA = 30°, TR = 10 ms, TE = TR/2. The shape of bSSFP off-resonance profiles is a strong function of T_1/T_2. The phase is almost independent on T_1/T_2.

bSSFP sequences are sensitive to local off-resonance caused by magnetic field inhomogeneities. Some examples of steady-state bSSFP signal behavior depending on the off-resonance (deviations of 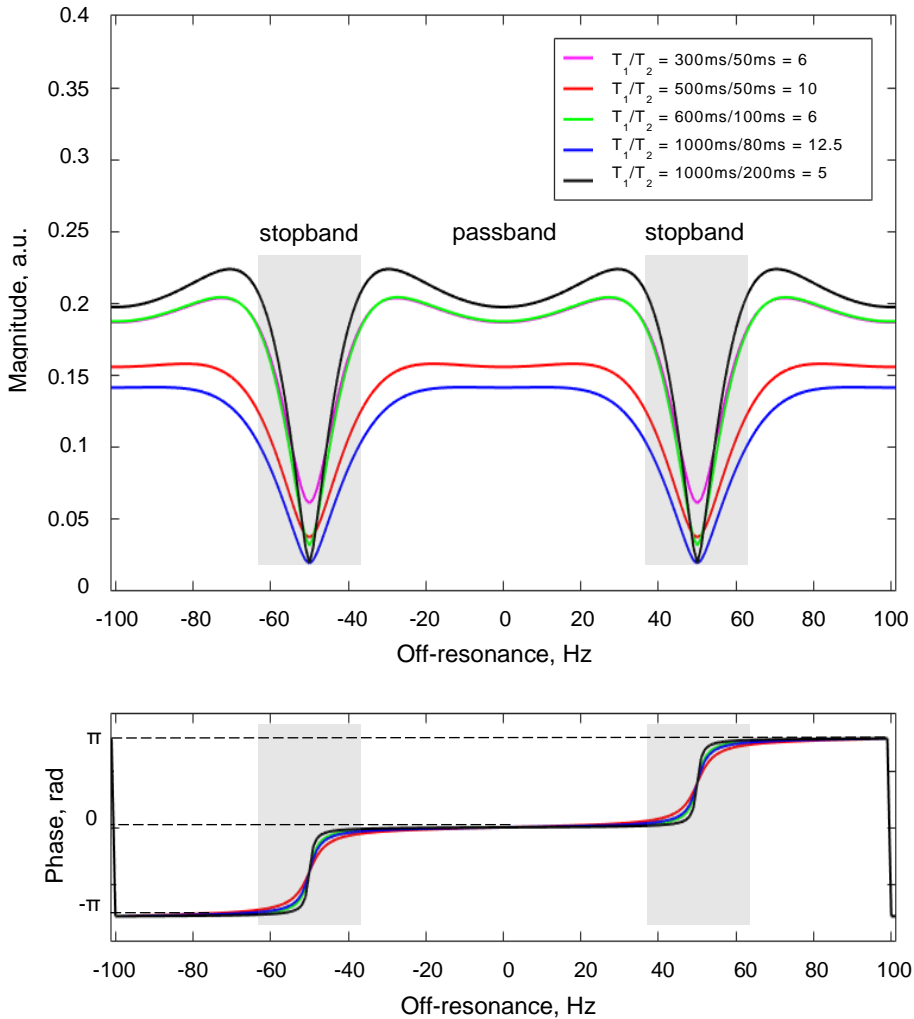the frequency of the applied RF pulse from the "on-resonant" Larmor frequency) are shown in Figure 1.4 for different values of tissue relaxation parameters. The high signal regions in the profile are commonly referred to as "passbands", whereas the signal regions close to zero are referred to as "stopbands". Signals at stopband frequencies are represented as spatial bands of signal loss in the reconstructed magnitude images, which are called "banding artifacts", see Figure 1.6. These banding artifacts can be very prominent in regions with considerable field inhomogeneities, like the abdomen, which hampers routine clinical use of bSSFP sequences in such anatomical regions, particularly when a large field-of-view (FOV) is required. However, this problem can be solved by using phase-cycled acquisition, which is explained in § 1.7.

bSSFP off-resonance profiles show a strong dependence on the protocol parameter settings, such as repetition time (TR) and the flip angle (FA). Decreasing TR increases the bandwidth of the bSSFP off-resonance profile, extending the "passband" regions. That is why bSSFP with shortest TR values are recommended for robust imaging without banding artifacts. The shape of the bSSFP profile varies with the FA as well: the "passband" regions can become narrower for higher flip angles, or even a dip in the middle of the "passband" can be observed for very low flip angles.

1.7 Phase-cycled bSSFP

Radiofrequency (RF) phase-cycled bSSFP is an acquisition technique, which is used to eliminate the banding artifacts and to avoid signal loss in the acquired bSSFP images. The phase increment of each subsequent RF excitation pulse is increased stepwise with a unique value for each acquisition. The off-resonance profiles of the bSSFP signal depend on the value of the RF phase increment, as shown in Figure 1.5. Given a certain spatial B_0 inhomogeneity, the banding artifacts will appear at different spatial locations in the resulting images acquired with different RF phase increments. Several algorithms were proposed to reduce banding artifacts by different combination strategies of the different RF phase cycled images, such as Complex-Sum bSSFP (67), Maximum-Intensity SSFP (67), Sum-of-Squares SSFP (67), nonlinear averaging (NLA) algorithm (68), Geometrical Solution (69), LORE-GN algorithm (70). Examples of images acquired with different RF phase increments and the reconstructed banding-free magnitude image using the Geometrical solution algorithm are shown in Figure 1.6.

An interesting feature is that the complex transverse magnetization M_{xy} acquired over different RF phase increments, produces an ellipse in the transverse plane, as shown

in Figure 1.7. This can be verified by mapping out the signal of a given voxel in the complex plane for various RF phase cycled images. The shape and the geometrical characteristics of the ellipse depend on the relaxation times T_1 and T_2, whereas the rotation of the ellipse around the origin is determined by the local off-resonance Δf_0.

An elliptical signal model was used in the work by Xiang and Hoff (69) to solve the bSSFP banding problem. Inspired by this, a new approach for quantitative relaxometry based on the elliptical signal model of the phase-cycled bSSFP signal was developed, which is described in this thesis.
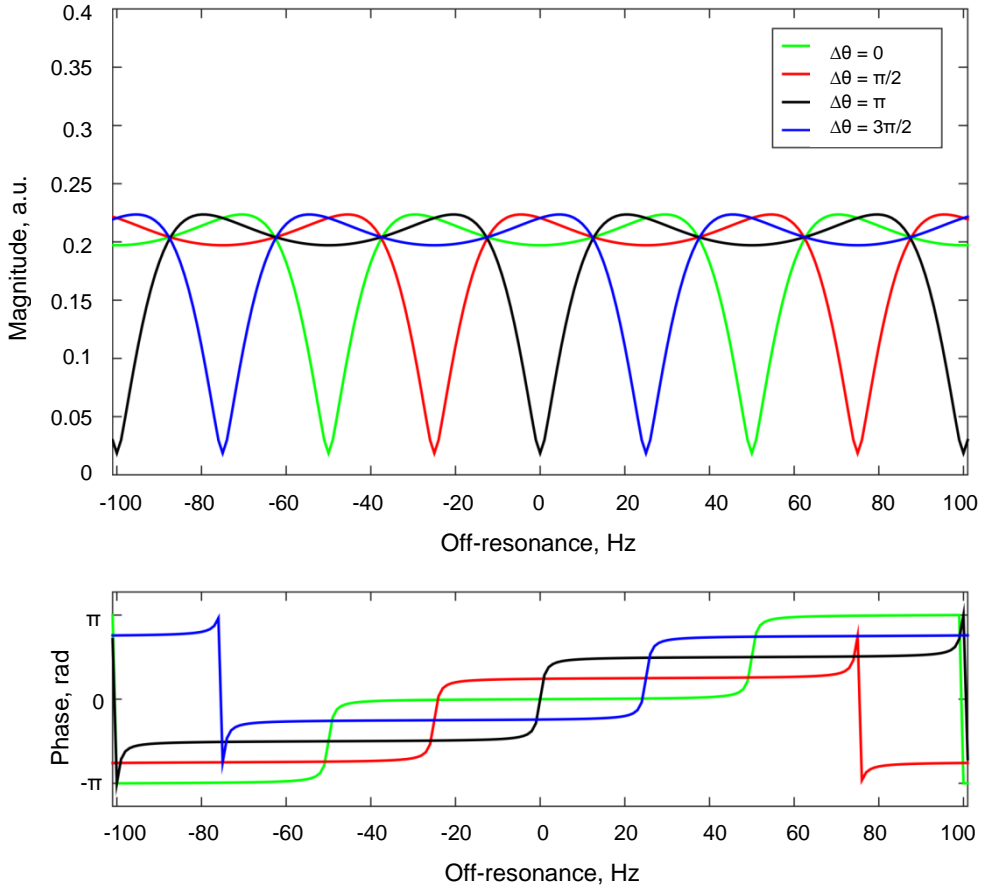
FIGURE 1.5. Balanced SSFP signal behavior for several RF phase increment settings $\Delta\theta$, computed for TR = 10 ms, FA = 30˚, TE = TR/2, T_1 = 1000 ms, T_2 = 200 ms. The bSSFP magnitude and phase off-resonance profile shift depending on the RF phase increment. RF phase cycling (0,180˚) is assumed.
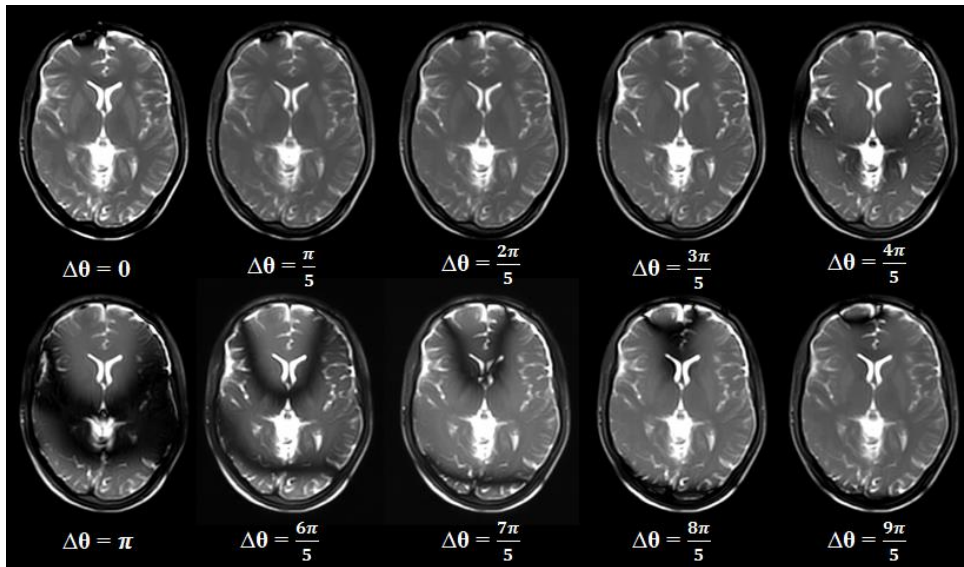
Banding-free magnitude
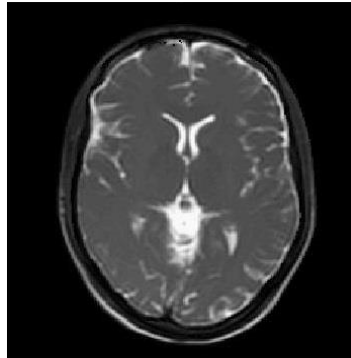
FIGURE 1.6. Examples of magnitude bSSFP images of the brain of a healthy volunteer, acquired with different RF phase increment settings, and the reconstructed banding-free magnitude image using the Geometrical Solution (GS) algorithm (69).
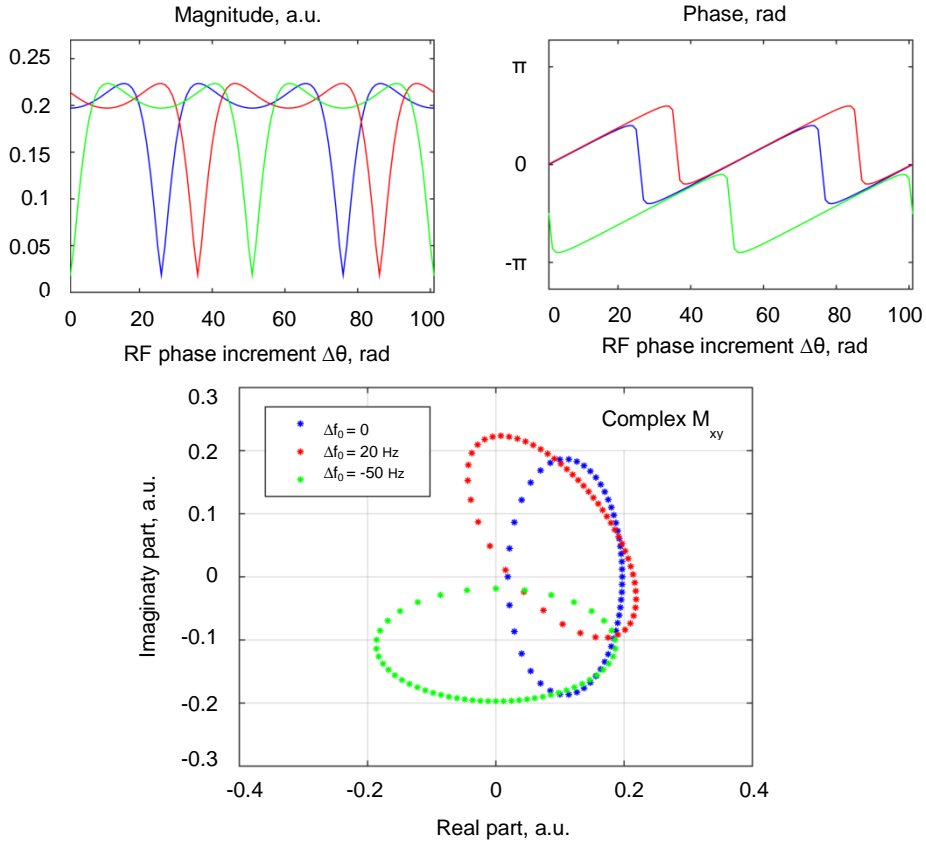
FIGURE 1.7. Phase-cycled bSSFP signal behavior, computed for TR = 10 ms, TE = TR/2, T_1 = 1000 ms, T_2 = 200 ms for different local off-resonance values Δf_0: blue lines correspond to Δf_0 = 0, red lines correspond to Δf_0 = 20 Hz, green lines correspond to Δf_0 = - 50 Hz.

1.8 Thesis outline

The main goal of the research described in this thesis was to develop a novel approach for multi-parametric MRI, to investigate its performance in terms of accuracy and precision for realistic SNR levels, and to optimize it for different applications.

The method that has been developed is called PLANET: an elli**P**se fitting approach for simu**L**taneous T_1 and T_2 m**A**pping using phase-cycled bala**N**ced st**E**ady-s**T**ate free precession. This method allows to simultaneously reconstruct maps of the magnetic relaxation times T_1 and T_2, the local off-resonance, the RF phase (related to the combination of RF transmit and receive phases), and the banding free bSSFP signal magnitude image.

Chapter 2 is an introduction of the method. The methodology of the PLANET reconstruction algorithm is described in this chapter, and the results of the performance of the method in a dedicated phantom and in the brain of healthy volunteers are presented.

In addition, the possible sources of errors in the estimated quantitative parameters were investigated, and the protocol parameter settings of the PLANET method were optimized.

Chapter 3 addresses the influence of relevant MR sequence parameter settings (namely the repetition time TR, the flip angle FA, and the number of RF phase increments N) on the accuracy and precision in PLANET-estimated quantitative parameters. By performing numerical simulations and experiments, the errors in quantitative parameter estimates were assessed using a single-component PLANET reconstruction for a single-component signal (coming from tissue with mono-exponential T_1 and T_2). Furthermore, the minimum SNR required for accurate and precise parameter estimation was calculated. In many biological tissues, like white matter in the human brain, fat tissue, or bone marrow, multiple components with different relaxation times and different resonance frequencies are present in a voxel. In that case, a single-component PLANET reconstruction might fail. The performance of the PLANET method for a two-component signal model of WM tissue (with a second myelin-related short relaxation component) was investigated in this chapter. Finally, the effects of Gibbs ringing were investigated, motivated by the realization that the RF phase-cycling spatially shifts the banding artifacts, causing the Gibbs ringing around stopbands to be in principle different for each phase-cycled image.

The main prerequisite for the PLANET model is a temporally stable main magnetic field (B_0) throughout the phase-cycled bSSFP acquisition, which can take up to 10-15 min depending on the resolution and the required field-of-view (FOV). Due to intensive gradient activity, which causes the heating of metallic components of the scanner, spatio-temporal B_0 drift can occur, which might result in errors in the estimated parameters. **Chapter 4** focuses on the investigation of the influence of B_0 drift on the performance of the PLANET method

for single-component and two-component signal models. The influence of B_0 drift on the quantitative parameter estimates was assessed experimentally in a phantom and in the brain of healthy volunteers. The results were subsequently verified by numerical simulations. This chapter also contains the description of a simple drift correction algorithm that was developed and tested on a phantom and *in vivo*.

By performing the PLANET scans in the patients undergoing prostate radiotherapy, it was observed by chance that the phase-cycled bSSFP sequence can be rather useful for qualitative assessment of fiducial markers in the prostate, which are used as landmarks for localization of the prostate during radiotherapy. **Chapter 5** is a case of "serendipity" and it demonstrates a clinical application of the phase-cycled bSSFP imaging in the prostate. A new method for visualization of fiducial markers (FMs) in the prostate with positive contrast for MRI-only radiotherapy is presented. The phase-cycled bSSFP signal was simulated in the presence of a gold FM, and then the geometrical manifestation of the artifacts around FMs was assessed and validated by performing the experiments in phantoms and *in vivo*. The accuracy of the localization of FMs was also assessed.

The results of the research presented in this thesis are discussed in **Chapter 6**. **Chapter 7** contains a summary of this thesis.

1.9 References

1. Rabi II, Zacharias JR, Millman S, Kusch P. A new method of measuring nuclear magnetic moment. Phys. Rev. 1938;53:318. doi: 10.1103/PhysRev.53.318.

2. Bailey MR, Khokhlova VA, Sapozhnikov OA, Kargl SG, Crum LA. Physical mechanisms of the therapeutic effect of ultrasound (a review). Acoust. Phys. 2003;49:369–388. doi: 10.1134/1.1591291.

3. Ter Haar G. Ultrasound focal beam surgery. Ultrasound Med. Biol. 1995;21:1089–1100. doi: 10.1016/0301-5629(95)02010-1.

4. Rieke V, Pauly KB. MR thermometry. J. Magn. Reson. Imaging 2008;27:376–390. doi: 10.1002/jmri.21265.

5. Baskar R, Dai J, Wenlong N, Yeo R, Yeoh K-W. Biological response of cancer cells to radiation treatment. Front. Mol. Biosci. 2014;1:1–9. doi: 10.3389/fmolb.2014.00024.

6. Bloembergen N, Purcell EM, Pound R V. Relaxation effects in nuclear magnetic resonance absorption. Phys. Rev. 1948;73:679–712. doi: 10.1103/PhysRev.73.679.

7. Brown RW, Cheng YCN, Haacke EM, Thompson MR, Venkatesan R. Magnetic Resonance Imaging: Physical Principles and Sequence Design: Second Edition. 2014. doi: 10.1002/9781118633953.

8. Kessler LG, Barnhart HX, Buckler AJ, Choudhury KR, Kondratovich M V., Toledano A, Guimaraes AR, Filice R, Zhang Z, Sullivan DC. The emerging science of quantitative imaging biomarkers terminology and definitions for scientific studies and regulatory submissions. Stat. Methods Med. Res. 2015;24:9–26. doi: 10.1177/0962280214537333.

9. Sullivan DC, Obuchowski NA, Kessler LG, et al. Metrology Standards for Quantitative Imaging Biomarkers. Radiology 2015;277:813–825. doi: 10.1148/radiol.2015142202.

10. Abramson RG, Yankeelov TE. Imaging biomarkers and surrogate endpoints in oncology clinical trials. In: Functional Imaging in Oncology: Biophysical Basis and Technical Approaches - Volume 1. ; 2014. pp. 29–42. doi: 10.1007/978-3-642-40412-2_2.

11. Rosenkrantz AB, Mendiratta-Lala M, Bartholmai BJ, et al. Clinical Utility of Quantitative Imaging. Acad. Radiol. 2015;22:33–49. doi: 10.1016/j.acra.2014.08.011.

12. Abramson RG, Burton KR, Yu JPJ, et al. Methods and Challenges in Quantitative Imaging Biomarker Development. Acad. Radiol. 2015;22:25–32. doi: 10.1016/j.acra.2014.09.001.

13. O'Connor JP, Jackson A, Asselin MC, Buckley DL, Parker GJ, Jayson GC. Quantitative imaging biomarkers in the clinical development of targeted therapeutics: current and future perspectives. Lancet Oncol. 2008;9:766–776. doi: 10.1016/S1470-2045(08)70196-7.

14. Garcia-Donas J, Rodriguez-Antona C, Jonasch E. Molecular markers to predict

response to therapy. Semin. Oncol. 2013;40:444–458. doi: 10.1053/j.seminoncol.2013.05.005.

15. Kurland BF, Gerstner ER, Mountz JM, et al. Promise and pitfalls of quantitative imaging in oncology clinical trials. Magn. Reson. Imaging 2012;30:1301–1312. doi: 10.1016/j.mri.2012.06.009.

16. Chenevert TL, Meyer CR, Moffat BA, et al. Diffusion MRI: A new strategy for assessment of cancer therapeutic efficacy. Mol. Imaging 2002;1:336–343. doi: 10.1162/153535002321093945.

17. Deoni SCL. Magnetic resonance relaxation and quantitative measurement in the brain. Methods Mol. Biol. 2010;711:65–108. doi: 10.1007/978-1-61737-992-5_4.

18. Cheng HL, Stikov N, Ghugre NR, Wright GA. Practical medical applications of quantitative MR relaxometry. J. Magn. Reson. Imaging 2012;36:805–824. doi: 10.1002/jmri.23718.

19. Larsson HBW, Frederiksen J, Petersen J, Nordenbo A, Zeeberg I, Henriksen O, Olesen J. Assessment of demyelination, edema, and gliosis by in vivo determination of T1 and T2 in the brain of patients with acute attack of multiple sclerosis. Magn. Reson. Med. 1989;11:337–348. doi: 10.1002/mrm.1910110308.

20. Jackson A. Quantitative MRI of the brain: measuring changes caused by disease. Br. J. Radiol. 2014;78:87–87. doi: 10.1259/bjr.78.925.780087a.

21. Vrenken H, Geurts JJG, Knol DL, et al. Whole-Brain T1 Mapping in Multiple Sclerosis: Global Changes of Normal-appearing Gray and White Matter. Radiology 2006;240:811–820. doi: 10.1148/radiol.2403050569.

22. Manfredonia F, Ciccarelli O, Khaleeli Z, Tozer DJ, Sastre-Garriga J, Miller DH, Thompson AJ. Normal-appearing brain T1 relaxation time predicts disability in early primary progressive multiple sclerosis. Arch. Neurol. 2007;64:411–415. doi: 10.1001/archneur.64.3.411.

23. Mackay A, Whittall K, Adler J, Li D, Paty D, Graeb D. In vivo visualization of myelin water in brain by magnetic resonance. Magn. Reson. Med. 1994;31:673–677. doi: 10.1002/mrm.1910310614.

24. Englund E, Brun A, Györffy-Wagner Z, Larsson EM, Persson B. Relaxation times in relation to grade of malignancy and tissue necrosis in astrocytic gliomas. Magn. Reson. Imaging 1986;4:425–429. doi: 10.1016/0730-725X(86)90051-2.

25. Just M, Thelen M. Tissue characterization with T1, T2, and proton density values: results in 160 patients with brain tumors. Radiology 2014;169:779–785. doi: 10.1148/radiology.169.3.3187000.

26. Rugg-Gunn FJ, Boulby PA, Symms MR, Barker GJ, Duncan JS. Whole-brain T2 mapping demonstrates occult abnormalities in focal epilepsy. Neurology 2005;64:318–325.

doi: 10.1212/01.WNL.0000149642.93493.F4.

27. Townsend TN, Bernasconi N, Pike GB, Bernasconi A. Quantitative analysis of temporal lobe white matter T2 relaxation time in temporal lobe epilepsy. Neuroimage 2004;23:318–324. doi: 10.1016/j.neuroimage.2004.06.009.

28. Dewitt LD, Kistler JP, Miller DC, Richardson EP, Buonanno FS. Nmr-neuropathologic correlation in stroke. Stroke 1987;18:342–351. doi: 10.1161/01.STR.18.2.342.

29. Li Y, Srinivasan R, Ratiney H, Lu Y, Chang SM, Nelson SJ. Comparison of T 1 and T 2 metabolite relaxation times in glioma and normal brain at 3T. J. Magn. Reson. Imaging 2008;28:342–350. doi: 10.1002/jmri.21453.

30. Hoque R, Ledbetter C, Gonzalez-Toledo E, Misra V, Menon U, Kenner M, Rabinstein AA, Kelley RE, Zivadinov R, Minagar A. The Role of Quantitative Neuroimaging Indices in the Differentiation of Ischemia From Demyelination: An Analytical Study With Case Presentation. Int. Rev. Neurobiol. 2007;79:491–519. doi: 10.1016/S0074-7742(07)79022-0.

31. Kaur J, Tuor UI, Zhao Z, Petersen J, Jin AY, Barber PA. Quantified T1 as an adjunct to apparent diffusion coefficient for early infarct detection: A high-field magnetic resonance study in a rat stroke model. Int. J. Stroke 2009;4:159–168. doi: 10.1111/j.1747-4949.2009.00288.x.

32. Lescher S, Jurcoane A, Veit A, Bähr O, Deichmann R, Hattingen E. Quantitative T1 and T2 mapping in recurrent glioblastomas under bevacizumab: earlier detection of tumor progression compared to conventional MRI. Neuroradiology 2014;57:11–20. doi: 10.1007/s00234-014-1445-9.

33. Schmidt-Wilcke T. Variations in brain volume and regional morphology associated with chronic pain. Curr. Rheumatol. Rep. 2008;10:467–474. doi: 10.1007/s11926-008-0077-7.

34. Bozzali M, Cercignani M, Caltagirone C. Brain volumetrics to investigate aging and the principal forms of degenerative cognitive decline: a brief review. Magn. Reson. Imaging 2008;26:1065–1070. doi: 10.1016/j.mri.2008.01.044.

35. West J, I. B, M. E, J.B.M. W, P. L. Application of Quantitative MRI for Brain Tissue Segmentation at 1.5 T and 3.0 T Field Strengths. PLoS One 2013;8.

36. Bazelaire CMJ de, Duhamel GD, Rofsky NM, Alsop DC. Radiology of Abdominal and Pelvic Tissues Measured in Vivo at 3.0 T : Preliminary Results. Radiology 2004;230:652–659.

37. Yamauchi FI, Penzkofer T, Fedorov A, Fennessy FM, Chu R, Maier SE, Tempany CMC, Mulkern R V., Panych LP. Prostate cancer discrimination in the peripheral zone with a reduced field-of-view T2-mapping MRI sequence. Magn. Reson. Imaging 2015;33:525–530. doi: 10.1016/j.mri.2015.02.006.

38. Papakonstantinou O, Alexopoulou E, Economopoulos N, Benekos O, Kattamis A, Kostaridou S, Ladis V, Efstathopoulos E, Gouliamos A, Kelekis NL. Assessment of iron

distribution between liver, spleen, pancreas, bone marrow, and myocardium by means of r2 relaxometry with mri in patients with β-thalassemia major. J. Magn. Reson. Imaging 2009;29:853–859. doi: 10.1002/jmri.21707.

39. Schein A, Enriquez C, Coates TD, Wood JC. Magnetic resonance detection of kidney iron deposition in sickle cell disease: A marker of chronic hemolysis. J. Magn. Reson. Imaging 2008;28:698–704. doi: 10.1002/jmri.21490.

40. In den Kleef JJ, Cuppen JJ. RLSQ: T1, T2, and rho calculations, combining ratios and least squares. Magn. Reson. Med. 1987;5:513–24.

41. Bernstein MA, King KF, Zhou XJ. Handbook of MRI Pulse Sequences. 2004. doi: 10.1016/B978-0-12-092861-3.X5000-6.

42. Christensen KA, Grant DM, Schulman EM, Walling C. Optimal determination of relaxation times of fourier transform nuclear magnetic resonance. Determination of spin-lattice relaxation times in chemically polarized species. J. Phys. Chem. 1974;78:1971–1977. doi: 10.1021/j100612a022.

43. Homer J, Beevers MS. Driven-equilibrium single-pulse observation of T1 relaxation. A reevaluation of a rapid "new" method for determining NMR spin-lattice relaxation times. J. Magn. Reson. 1985;63:287–297. doi: 10.1016/0022-2364(85)90318-X.

44. Deoni SCL, Rutt BK, Peters TM. Rapid combined T1 and T2 mapping using gradient recalled acquisition in the steady state. Magn. Reson. Med. 2003;49:515–526. doi: 10.1002/mrm.10407.

45. Teixeira RPAG, Malik SJ, Hajnal J V. Joint system relaxometry (JSR) and Crámer-Rao lower bound optimization of sequence parameters: A framework for enhanced precision of DESPOT T1 and T2 estimation. Magn. Reson. Med. 2018;79:234–245. doi: 10.1002/mrm.26670.

46. Wang HZ, Riederer SJ, Lee JN. Optimizing the precision in T1 relaxation estimation using limited flip angles. Magn. Reson. Med. 1987;5:399–416. doi: 10.1002/mrm.1910050502.

47. Deoni SCL, Peters TM, Rutt BK. Determination of Optimal Angles for Variable Nutation Proton Magnetic Spin-Lattice, T1, and Spin-Spin, T2, Relaxation Times Measurement. Magn. Reson. Med. 2004;51:194–199. doi: 10.1002/mrm.10661.

48. Cheng HLM, Wright GA. Rapid high-rsolution T1 mapping by variable flip angles: Accurate and precise measurements in the presence of radiofrequency field inhomogeneity. Magn. Reson. Med. 2006;55:566–574. doi: 10.1002/mrm.20791.

49. Deoni SCL. Transverse relaxation time (T2) mapping in the brain with off-resonance correction using phase-cycled steady-state free precession imaging. J. Magn. Reson. Imaging 2009;30:411–417. doi: 10.1002/jmri.21849.

50. Preibisch C, Deichmann R. Influence of RF spoiling on the stability and accuracy of T1

mapping based on spoiled FLASH with varying flip angles. Magn. Reson. Med. 2009;61:125–135. doi: 10.1002/mrm.21776.

51. Yarnykh VL. Optimal radiofrequency and gradient spoiling for improved accuracy of T1 and B1 measurements using fast steady-state techniques. Magn. Reson. Med. 2010;63:1610–1626. doi: 10.1002/mrm.22394.

52. Schmitt P, Griswold MA, Jakob PM, Kotas M, Gulani V, Flentje M, Haase A. Inversion recovery TrueFISP: quantification of T(1), T(2), and spin density. Magn. Reson. Med. 2004;51:661–7. doi: 10.1002/mrm.20058.

53. Ehses P, Seiberlich N, Ma D, Breuer FA, Jakob PM, Griswold MA, Gulani V. IR TrueFISP with a golden-ratio-based radial readout: Fast quantification of T1, T2, and proton density. Magn. Reson. Med. 2013;69:71–81. doi: 10.1002/mrm.24225.

54. Nguyen D, Bieri O. Motion-insensitive rapid configuration relaxometry. Magn. Reson. Med. 2016. doi: 10.1002/mrm.26384.

55. Ma D, Gulani V, Seiberlich N, Liu K, Sunshine JL, Duerk JL, Griswold MA. Magnetic resonance fingerprinting. Nature 2013;495:187–192. doi: 10.1038/nature11971.

56. Panda A, Mehta BB, Coppo S, Jiang Y, Ma D, Seiberlich N, Griswold MA, Gulani V. Magnetic resonance fingerprinting – An overview. Curr. Opin. Biomed. Eng. 2017;3:56–66. doi: 10.1016/j.cobme.2017.11.001.

57. Sbrizzi A, Heide O van der, Cloos M, Toorn A van der, Hoogduin H, Luijten PR, van den Berg CAT. Fast quantitative MRI as a nonlinear tomography problem. Magn. Reson. Imaging 2018;46:56–63. doi: 10.1016/j.mri.2017.10.015.

58. Bauer CM, Jara H, Killiany R. Whole brain quantitative T2 MRI across multiple scanners with dual echo FSE: Applications to AD, MCI, and normal aging. Neuroimage 2010;52:508–514. doi: 10.1016/j.neuroimage.2010.04.255.

59. Keenan KE, Stupic KF, Boss MA, et al. Multi-site, multi-vendor comparison of T1 measurement using ISMRM/NIST system phantom. In: Proceedings of the 24th Annual Meeting of ISMRM, Singapore, Singapore, 2016. Abstract 3290.

60. Panda A, Jokerst CE, Cummings KW, Panse PM. Inter-Scanner T1 and T2 Measurement Variability Evaluation on Two 3T Scanners with Identical Hardware and Software Configuration. In: Proceedings of the 24th Annual Meeting of ISMRM, Honolulu, HI, USA, 2017. Abstract 2766.

61. Bojorquez JZ, Bricq S, Acquitter C, Brunotte F, Walker PM, Lalande A. What are normal relaxation times of tissues at 3 T? Magn. Reson. Imaging 2017;35:69–80. doi: 10.1016/j.mri.2016.08.021.

62. Lee Y, Callaghan MF, Acosta-Cabronero J, Lutti A, Nagy Z. Establishing intra- and inter-vendor reproducibility of T 1 relaxation time measurements with 3T MRI. Magn. Reson. Med. 2019;81:454–465. doi: 10.1002/mrm.27421.

63. Wansapura JP, Holland SK, Dunn RS, Ball WS. NMR relaxation times in the human brain at 3.0 Tesla. J. Magn. Reson. Imaging 1999;9:531–538. doi: 10.1002/(SICI)1522-2586(199904).

64. Bieri O, Scheffler K. Fundamentals of balanced steady state free precession MRI. J. Magn. Reson. Imaging 2013;38:2–11. doi: 10.1002/jmri.24163.

65. Scheffler K, Hennig J. T1 quantification with inversion recovery TrueFISP. Magn. Reson. Med. 2001;45:720–723. doi: 10.1002/mrm.1097.

66. Deoni SCL, Ward HA, Peters TM, Rutt BK. Rapid T2 estimation with phase-cycled variable nutation steady-state free precession. Magn. Reson. Med. 2004;52:435–439. doi: 10.1002/mrm.20159.

67. Bangerter NK, Hargreaves BA, Vasanawala SS, Pauly JM, Gold GE, Nishimura DG. Analysis of Multiple-Acquisition SSFP. Magn. Reson. Med. 2004;51:1038–1047. doi: 10.1002/mrm.20052.

68. Elliott AM, Bernstein MA, Ward HA, Lane J, Witte RJ. Nonlinear averaging reconstruction method for phase-cycle SSFP. Magn. Reson. Imaging 2007;25:359–364. doi: 10.1016/j.mri.2006.09.013.

69. Xiang QS, Hoff MN. Banding artifact removal for bSSFP imaging with an elliptical signal model. Magn. Reson. Med. 2014;71:927–933. doi: 10.1002/mrm.25098.

70. Björk M, Ingle RR, Gudmundson E, Stoica P, Nishimura DG, Barral JK. Parameter estimation approach to banding artifact reduction in balanced steady-state free precession. Magn. Reson. Med. 2014;72:880–892. doi: 10.1002/mrm.24986.

PLANET*: an elliPse fitting approach for simuLtaneous T1 and T2 mApping using phase-cycled balaNced stEady-sTate free precession*

ABSTRACT

Purpose:

To demonstrate the feasibility of a novel, ellipse fitting approach, named PLANET, for simultaneous estimation of relaxation times T_1 and T_2 from a single 3D phase-cycled balanced steady-state free precession sequence.

Methods:

A method is presented in which the elliptical signal model is used to describe the phase-cycled bSSFP steady-state signal. The fitting of the model to the acquired data is reformulated into a linear convex problem, which is solved directly by a linear least squares method, specific to ellipses. Subsequently, the relaxation times T_1 and T_2, the banding free magnitude, and the off-resonance are calculated from the fitting results.

Results:

Maps of T_1 and T_2, as well as an off-resonance and a banding free magnitude, can be simultaneously, quickly and robustly estimated from a single 3D phase-cycled bSSFP sequence. The feasibility of the method was demonstrated in a phantom and the brain of healthy volunteers on a clinical MR scanner. The results were in good agreement for the phantom, but a systematic underestimation of T_1 was observed in the brain.

Conclusion:

The presented method allows for accurate mapping of relaxation times and off-resonance, and for the reconstruction of banding free magnitude images at realistic SNRs.

Key words: ellipse fitting; T_1; T_2; off-resonance; phase-cycled bSSFP

2.1 Introduction

Quantitative MR imaging plays an important role in accurate tissue characterization for improving clinical diagnostic imaging and for planning, guidance and evaluation of image-guided therapy. The mapping of longitudinal (T_1) and transverse (T_2) relaxation times is a particularly important tool for many clinical applications in oncology and regenerative medicine (1). Knowledge of T_1 and T_2 values allows for optimizing the contrast-to-noise-ratio between tissues by finding the optimal sequence parameter settings.

Various techniques are widely used for T1 and T2 relaxation time mapping. Two-dimensional (2D) Inversion Recovery Spin Echo (IR-SE) and Multi-Echo Spin Echo (ME-SE) (2) are considered gold standard techniques, allowing accurate measurements of relaxation times. Unfortunately, scans based on these methods typically have a long acquisition time, which makes it challenging to use them in clinical practice. To speed up IR-based T_1 mapping, the Look-Locker method was introduced (3). This approach is closely related to the IR-SE, but instead of acquiring a single image for each inversion time, the Look-Locker method uses an inversion pulse followed by a train of low flip angle (FA) pulses, each followed by a read-out, within each repetition time (TR). Although that considerably reduces the required scan time, it still is a time-consuming 2D method, which results in a very long acquisition time to cover a complete three-dimensional (3D) volume.

Another widely used method, which uses the variable flip angle (VFA) approach (4,5), is DESPOT1 (6). The method allows for rapid three-dimensional (3D) high-resolution T_1 mapping and is easily implemented on clinical scanners. For this method at least two acquisitions of spoiled gradient-echo (SPGR) scans with different flip angles are required. A signal model for the steady-state is subsequently fitted to variable flip angle data. A similar approach was developed by Deoni et al for T_2 mapping under the name DESPOT2 and extended to the combined T_1 and T_2 mapping (7). DESPOT2 also requires at least two acquisitions of 3D balanced steady-state free precession (bSSFP) with different flip angles using prior knowledge of T_1, often estimated using DESPOT1. Both methods have been shown error-prone, which demands the optimization of the parameter settings. The combination of used flip angles needs to be optimized for improved accuracy and precision (8–10). Furthermore, the influence of radiofrequency field inhomogeneity (11), off-resonance effects (12,13), and radiofrequency and gradient spoiling efficiency (14,15) on the accuracy and precision of T_1 and T_2 measurements was investigated.

With the advent of stronger and faster gradient systems, bSSFP sequences have become widely employed for rapid imaging with high signal-to-noise (SNR) efficiency. Although the signal is a complex function of relaxation parameters T_1 and T_2, several bSSFP-based approaches for relaxometry have been proposed, such as 2D Inversion

Recovery TrueFISP (16), 3D Triple Echo Steady-State (TESS) (17). For instance, the TESS method allows for simultaneous rapid 3D estimation of T_1 and T_2 within one single scan using two specific signal ratios between three echoes (SSFP-FID and two SSFP-Echo modes) and an iterative golden section search algorithm.

Generally, bSSFP imaging has a high sensitivity to local magnetic field inhomogeneities, which results in banding artifacts. Radiofrequency (RF) phase-cycled bSSFP imaging was introduced as a solution, and several algorithms were proposed to reduce banding artifacts (18).

M.Björk et al (19) introduced a parameter estimation algorithm to remove banding artifacts and to simultaneously estimate relaxation times T_1 and T_2 from phase-cycled bSSFP. In their work, a combination of linear least squares fitting followed by a subsequent non-linear iterative fitting was used, called the two-step LORE-GN algorithm. They successfully reconstructed banding free magnitude images of a phantom and in-vivo. Based only on simulations and numerical assessment of the Cramer-Rao Bound (CRB), they concluded that the simultaneous estimation of T_1 and T_2 from phase-cycled bSSFP would be difficult at common SNR because the CRB is high.

In this work, we introduce a novel approach, named PLANET, for simultaneous T_1 and T_2 estimation from phase-cycled bSSFP (20). The elliptical signal model is used to describe the phase-cycled bSSFP steady-state signal (21). The fitting of the model to the acquired data is reformulated into a linear convex problem, which is solved directly by a linear least squares method, specific to ellipses (22). Subsequently, the relaxation times T_1 and T_2 are analytically calculated from the fitting results.

Our work shows that accurate mapping of the relaxation times T_1, T_2, the off-resonance caused by local field deviations, and banding-free magnitude is feasible for realistic SNRs and can be performed with a regular coil setup and scan protocol parameter settings.

2.2 Methods

2.2.1 The elliptical signal model

The elliptical signal model for bSSFP was first used by Xiang and Hoff (23) to remove banding artifacts. The complex bSSFP signal right after the RF pulse (at echo time $t = 0+$) can be described as:

$$I = M\frac{1 - ae^{i\theta}}{1 - b\cos\theta},$$

[2.1]

where

$$M = \frac{M_0(1 - E_1)\sin\alpha}{1 - E_1\cos\alpha - E_2^2(E_1 - \cos\alpha)}, \quad a = E_2, \quad b = \frac{E_2(1 - E_1)(1 + \cos\alpha)}{1 - E_1\cos\alpha - E_2^2(E_1 - \cos\alpha)}, \quad [2.2]$$

$E_1 = \exp(-\frac{TR}{T_1})$, $E_2 = \exp(-\frac{TR}{T_2})$, M_0 – the thermal equilibrium magnetization, α – the flip angle, TR – the repetition time, θ – the resonance offset angle (in radians), $\theta = \theta_0 - \Delta\theta$, where $\theta_0 = 2\pi(\delta_{CS} + \Delta f_0)TR$, Δf_0 – the off-resonance caused by local field deviations, δ_{CS} – the chemical shift of the species (in Hz) with respect to the water peak, $\Delta\theta$ – the user-controlled RF phase increment (in radians). Parameters M, a, b are all θ-independent.

The parametric Equation [2.1] describes an ellipse in the complex signal plane. Each point on the ellipse represents real and imaginary components of the transverse magnetization, which are acquired with a certain RF phase increment, as illustrated in Figure 2.1. The total number of acquisitions N and the RF phase increment $\Delta\theta$ are user-defined parameters.

Directly after the RF pulse (i.e. at t = 0+), the long axis of the ellipse is oriented vertically in the complex plane and the values for the parameters a and b are within the interval (0,1) (21). The cross-point M is the Geometric Solution, which is independent of θ and can be used to calculate a banding-free magnitude image.

$$I = M\frac{1 - ae^{i\theta}}{1 - b\cos\theta}, \quad \theta = \theta_0 - \Delta\theta_n$$

$$\Delta\theta_n = \frac{2\pi n}{N}, \quad n = \{0, 1, ..., N - 1\}$$

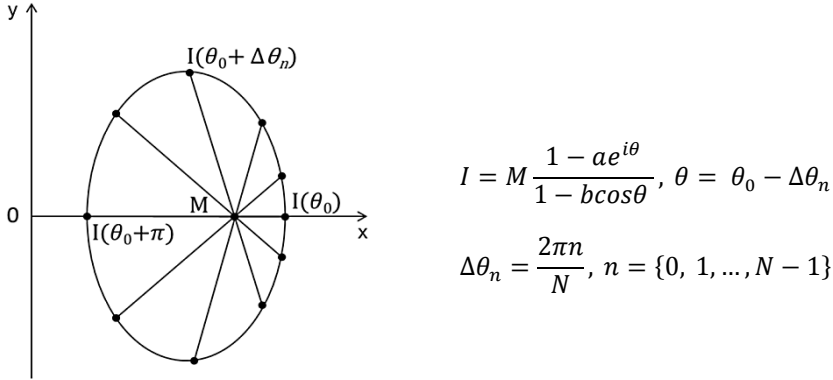FIGURE 2.1. The elliptical signal model of the bSSFP in the complex plane as a function of the resonance offset angle θ. In this particular case, $\theta_0 = 2\pi n$ and N = 10 acquisitions with different RF phase increments are shown.

At echo time t = TE > 0 after the RF pulse, the signal is still a function of the resonance offset angle (21), but then the real and imaginary components of the signal are

modulated by a factor $\exp\left(-\frac{TE}{T_2}\right)$ and rotated around the origin by:

$$\varphi = \Omega TE = 2\pi(\delta_{CS} + \Delta f_0)TE \qquad [2.3]$$

Taking into account the RF contribution, eddy current effects and B_0 drift, the complex signal can be then described as:

$$I = M_{\text{eff}} \cdot \frac{1 - ae^{i\theta}}{1 - b\cos\theta} \cdot e^{i\varphi}, \qquad [2.4]$$

$$\varphi = 2\pi(\delta_{CS} + \Delta f_0)TE + \varphi_{RF} + \varphi_{\text{edd}} + \varphi_{\text{drift}}, \qquad [2.5]$$

where $M_{\text{eff}} = KM\exp\left(-\frac{TE}{T_2}\right)$ – the effective magnetization, K – the magnitude of the combined receive field, φ_{RF} – the RF phase offset, related to the combination of RF transmit and receive phases, φ_{edd} – the extra phase errors due to eddy current effects, and φ_{drift} – the extra phase errors due to B_0 drift.

2.2.2 Reconstruction method for parametric mapping

Essential to the PLANET method is a 3-step reconstruction algorithm to simultaneously estimate relaxation parameters T_1 and T_2, and an effective banding free magnitude M_{eff} from phase-cycled bSSFP data. However, an additional step is required when the reconstruction of the off-resonance map Δf_0 is also desired.

Step 1. Direct linear least squares ellipse fitting to phase-cycled bSSFP data

The first step consists of performing voxel-wise direct linear least squares fitting of a general quadratic polynomial function to the data points in the complex plane (22):

$$F(\boldsymbol{C}, \boldsymbol{x}) = C_1 x^2 + C_2 xy + C_3 y^2 + C_4 x + C_5 y + C_6 = 0, \qquad [2.6]$$

where x and y are real and imaginary components of transverse magnetization.

By minimizing the sum of squared algebraic distances of the ellipse to the data points under a proper scaling and an appropriate constraint specific to ellipses (discriminant $C_2^2 - 4C_1C_3 = -1$), we avoid the trivial solution $\boldsymbol{C} = \boldsymbol{0}$ and exclude all non-elliptical fits, such as hyperbola and parabola. As a result, we find a unique set of coefficients $\boldsymbol{C} = [C_1, C_2, C_3, C_4, C_5, C_6]$ representing the ellipse. The fitting is based on a numerically stable version of the ellipse fit (24). This is a fast, direct, linear, non-iterative ellipse fit. Since there are 6 unknowns, we need at least 6 data points $\boldsymbol{x}$, which can be acquired by scanning with at least

6 different RF phase increment settings.

Step 2. Rotation of the ellipse to initial vertical conic form

The rotation of data points of the ellipse to the initial vertical form, i.e. the orientation directly after RF excitation pulse, was performed by applying basic algebraic transformations to the polynomial representation of the ellipse found in the previous step (Equation [6]). We found the rotation angle φ_{rot} to be:

$$\varphi_{rot} = \frac{1}{2} \tan^{-1} \frac{C_2}{C_1 - C_3} \tag{2.7}$$

Since φ_{rot} is defined within $\left(-\frac{\pi}{4}, \frac{\pi}{4}\right)$, we unwrapped it to cover the $(-\pi, \pi)$ range by verifying that the ellipse of every voxel is vertical and that its center lies on the positive real axis.

$$\cos \theta_n = \frac{\vec{a} \cdot \vec{b}}{|\vec{a}||\vec{b}|} = \frac{M - X_n}{\sqrt{(X_n - M)^2 + Y_n^2}}$$
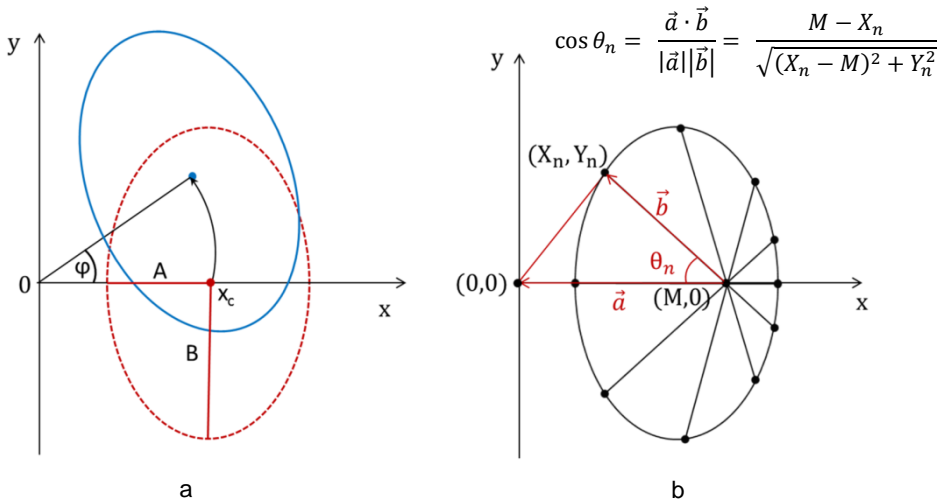
FIGURE 2.2. a) Schematic representation of the ellipse at t = 0+ (red dashed line) and t = TE > 0 (blue solid line), which is rotated around the origin by φ. (X_c, 0) – geometrical center of the ellipse, A, B – semi-axes of the ellipse; b) Geometrical determination of the angle θ_n using the locations of the data points (X_n, Y_n) on the vertical ellipse.

After rotation, illustrated in Figure 2.2 (a), the conic equation for the vertical orientation can be used to describe the ellipse:

$$\frac{(X - X_c)^2}{A^2} + \frac{Y^2}{B^2} = 1, \tag{2.8}$$

where $(X_c, 0)$ – is the geometrical center of the ellipse, A and B – are the semi-axes of the ellipse.

Step 3. Analytical solution for parameters M_{eff}, T_1, T_2

Parameters a, b, M_{eff} of the parametric form of the ellipse in Equation [2.4] are related to the geometric characteristics X_c, A, B from the cartesian form of ellipse in Equation [2.8] through a system of nonlinear equations (23):

$$\begin{cases} X_c = M_{\text{eff}} \dfrac{1 - ab}{1 - b^2} \\ A = M_{\text{eff}} \dfrac{|a - b|}{1 - b^2} \\ B = M_{\text{eff}} \dfrac{a}{\sqrt{1 - b^2}} \end{cases} \tag{2.9}$$

We have solved this system for parameters a, b, M_{eff} analytically. The results are presented in the Appendix. The T_1 and T_2 estimates can be found from parameters a and b using the following equations:

$$T_1 = -\frac{TR}{\ln \dfrac{a(1 + \cos\alpha - ab\cos\alpha) - b}{a(1 + \cos\alpha - ab) - b\cos\alpha}}, \quad T_2 = -\frac{TR}{\ln a} \tag{2.10}$$

Additional step 4. Estimation of the local off-resonance Δf_0

The rotation angle in Equation [2.7] includes the local off-resonance $\Delta f_0 = \gamma \Delta B_0$ and RF phase offset φ_{RF}, which cannot be separated from Equation [2.5]. For simplicity, the chemical shift is ignored and the additional phase errors due to eddy current effects and B_0 drift are assumed to be negligible:

$$\varphi_{rot} = 2\pi \Delta f_0 TE + \varphi_{RF} \tag{2.11}$$

The off-resonance Δf_0, however, can be estimated from the locations of the data points with different RF phase increment settings $\Delta\theta_n$ on the vertical ellipse: the precession angle θ_n during each TR depends only on the RF phase increment $\Delta\theta_n$ and the local off-resonance Δf_0, and not on the RF phase offset φ_{RF}:

$$\theta_n = \theta_0 - \Delta\theta_n = 2\pi TR \Delta f_0 - \Delta\theta_n \qquad [2.12]$$

Using a cartesian parametric equation of the ellipse:

$$\begin{cases} x = x_c + A\cos t \\ y = B\sin t \end{cases}, \quad \text{where } t = \tan^{-1}\left(\frac{A}{B}\tan\beta\right) \qquad [2.13]$$

and after substitution of x and y from Equation [2.13] by the real and imaginary components of the signal in Equation [2.4], the relationship between parameters t and θ can be found as:

$$\cos\theta = \frac{\cos t - b}{b\cos t - 1} \qquad [2.14]$$

For each individual n^{th} data point with n = {0, 1,..,N-1} Equation [2.14] is equivalent to

$$\cos\theta_n = \frac{\cos t_n - b}{b\cos t_n - 1} \qquad [2.15]$$

The set of t_n can be found from the set of β_n using Equation [2.13]. The set of β_n can be found geometrically from the data points on the vertical ellipse as illustrated in Figure 2(b) and consequently, the set of $\cos\theta_n$ can be found from Equation [2.15] and can be represented by the sum of a sine function and a cosine function: $\cos(\theta_n) = \cos(\theta_0 - \Delta\theta_n) = \cos\theta_0\cos\Delta\theta_n + \sin\theta_0\sin\Delta\theta_n = K_1\cos\Delta\theta_n + K_2\sin\Delta\theta_n$

Next, the coefficients K_1 and K_2 can be found by taking a linear least squares fitting approach and θ_0 can be estimated from:

$$\theta_0 = \tan^{-1}\frac{K_2}{K_1} \qquad [2.16]$$

The off-resonance Δf_0 can be found from Equations [2.12, 2.16]. Since θ_0 is defined within $\left(-\frac{\pi}{2}, \frac{\pi}{2}\right)$, we unwrapped it to cover the range $(-\pi, \pi)$, which results in bandwidth $\left(-\frac{1}{2TR}, \frac{1}{2TR}\right)$.

2.2.3 Sensitivity to the actual Flip Angle errors

To investigate how sensitive the method is to errors in the actual flip angle, simulations were performed for a range of nominal flip angles between 1° and 90° and a range of deviation in actual flip angles of -10% and +10%. The initial parameter settings were: KM_0 = 1, T_1 = 675 ms, T_2 = 75 ms, Δf_0 = 10 Hz, TR = 10 ms, TE = 5 ms, φ_{RF} = 0, δ_{CS} = 0, N = 10 phase cycles

with phase increments $\Delta\theta_n = \frac{2\pi n}{N} - \pi$, $n = \{0,1,\ldots,9\}$. The chosen T_1 and T_2 represent white matter at 1.5T. No Gaussian noise was added.

2.2.4 Experimental validation

To investigate the performance of our method, both phantom and human volunteer experiments were performed on a clinical 1.5T MR scanner (Philips Ingenia, Best, The Netherlands). For all scans, a 16-channel head coil (dS HeadSpine, Philips Ingenia, Best, The Netherlands) was used as a receive coil.

The phantom experiments were performed on a calibrated phantom consisting of gel tubes with known T_1 and T_2 values (TO5, Eurospin II test system, Scotland). Twelve tubes were chosen with T_1, T_2 combinations in the following ranges: T_1 (220-1600 ms), T_2 (50-360 ms).

First, the known temperature dependence of the relaxation times of the calibrated gels was used to assess the T_1 and T_2 values of the test tubes for the actual scanner room temperature. The temperature inside the phantom water was measured before and right after the experiment using a T-type thermocouple. The difference between measured temperature values was below 0.5° and the average value was chosen for the correction.

The 3D phase-cycled bSSFP sequence was performed with the protocol parameter settings, shown in Table 2.1. Complex-valued data were acquired. Reference T_1 and T_2 maps of the phantom were acquired using standard T_1 and T_2 mapping techniques. For the reference T_1 mapping, a 2D Inversion Recovery Turbo Spin Echo approach was used. For the reference T_2 map, a 2D Multi Echo Spin Echo approach was used. The corresponding protocol parameter settings are shown in Table 2.1. A reference off-resonance map was calculated using a dual echo SPGR method with the protocol parameter settings shown in Table 2.1.

Before voxel-wise parameter estimation, all images were masked to exclude the borders of the tubes and the background from the analysis. The reference T_1 values were calculated voxel-wise by performing the non-linear fit of $S(TI) = \rho \left| 1 - 2e^{-TI/T_1} \right|$ to multi TI IR-SE data, with ρ and T_1 as the fitting parameters. The reference T_2 values were calculated voxel-wise by performing the non-linear fit of $S(TE) = \rho e^{-TE/T_2}$ to multi Echo SE data, with ρ and T_2 as the fitting parameters.

Table 2.1. Protocol parameter settings

Phantom experiments

3D phase-cycled bSSFP

FOV (mm^3)	Voxel Size (mm^3)	Acq. Matrix	TR (ms)	TE (ms)	Flip Angle (°)	Number of RF increment steps	Number of Signal Averages (NSA)	Readout direction	Total scan time (min:s)
200x200x80	1.5x1.5x2.5	132x132x32	10	5	30	10	1	AP	06:51

Reference T$_1$ map (2D IR-TSE)

FOV (mm^3)	Voxel Size (mm^3)	Acq. Matrix	TR (ms)	TE (ms)	Turbo Factor	Inversion Times (ms)	NSA	Readout direction	Total scan time (min:s)
200x200x5	2.5x2.5x5	80x80x1	7000	10	5	[25; 50; 100; 200; 500; 1000; 2000; 5000]	1	AP	16:00

Reference T$_2$ map (2D ME-SE)

FOV (mm^3)	Voxel Size (mm^3)	Acq. Matrix	TR (ms)	TE (ms)		NSA	Readout direction	Total scan time (min:s)
200x200x5	2.5x2.5x5	80x80x1	5000	[20; 40; 60; 80; 100; 120; 140; 160]		1	AP	06:45

Reference off-resonance map (3D dual echo SPGR)

FOV (mm^3)	Voxel Size (mm^3)	Acq. Matrix	TR (ms)	TE (ms)	Flip Angle (°)	NSA	Readout direction	Total scan time (min:s)
200x200x80	2x2x2.5	100x100x32	30	[4.6; 9.2]	60	1	AP	03:08

In vivo experiments

3D phase-cycled bSSFP

FOV (mm^3)	Voxel Size (mm^3)	Acq. Matrix	TR (ms)	TE (ms)	Flip Angle (°)	Number of RF increment steps	NSA	Readout direction	Total scan time (min:s)
220x220x100	1.5x1.5x4	148x148x25	10	5	30	10	1	AP	06:04

Reference T$_1$ and T$_2$ map (2D MIXED)

FOV (mm^3)	Voxel Size (mm^3)	Acq. Matrix	TR SE (ms)	TR IR (ms)	IR delay (ms)	TE (ms)	NSA	Readout direction	Total scan time (min:s)
220x220x4	1.5x1.5x4	148x148x1	3000	6000	500	[30; 60; 90; 120; 150; 80; 210; 240]	1	AP	16:00

B$_1$ map (3D dual TR SPGR)

FOV (mm^3)	Voxel Size (mm^3)	Acq. Matrix	TR (ms)	TE (ms)	Flip Angle (°)	Overcontiguous slice	NSA	Readout direction	Total scan time (min:s)
220x220x100	2.5x2.5x4	88x88x25	[30; 150]	2.1	60	yes	1	AP	03:17

To demonstrate the method *in vivo*, experiments were performed on the brain of three healthy volunteers on the same scanner. The protocol parameter settings for 3D phase-cycled bSSFP are presented in Table 2.1. As shown in the Appendix, the flip angle should fulfill the condition $FA > \cos^{-1}\left(\exp(-\frac{TR}{T_{1\,shortest}})\right)$. Thus, FA 30° was used, which should allow an accurate estimation from $T_1 > 100$ ms onwards for TR = 10 ms.

The reference T_1 and T_2 values of the brain were measured using a simultaneous (interleaved) Spin Echo and Inversion Recovery method (2D MIXED) (25) with the protocol parameter settings, shown in Table 2.1.

B_1 map was calculated using a dual TR actual flip-angle imaging (AFI) (26) method with the protocol parameter settings, presented in Table 2.1. B_1 correction was performed voxel-wise for the calculated T_1 maps.

To investigate the influence of Magnetization Transfer (MT) effects on the quantitative T_1 and T_2 mapping *in vivo*, experiments were performed on one volunteer using 3D phase-cycled bSSFP with different RF excitation pulse durations, as suggested in work by Bieri et al (27). The protocol parameter settings were the same as shown in Table 2.1 (3D phase-cycled bSSFP *in vivo*). The default pulse had a duration of 0.84 ms. The long pulse optimized to minimize the MT effects had a duration of 2.86 ms.

The Signal Ratio ΔS and Magnetization Transfer Ratio MTR were calculated as:
$\Delta S = \frac{M_{def}}{M_0}$, $MTR = 100\frac{M_0 - M_{def}}{M_0}$, where M_{def} – the banding free magnitude measured with the default RF pulse, M_0 – the banding free magnitude measured with the long RF pulse (minimized MT effects).

A linear phase-encoding profile order was used to minimize the eddy currents induced by changing phase-encoding gradients (28).

The standard (Fast Channel Combination) method, available on the scanner, was used for the combined phase reconstruction. Note that the RF phase offset φ_{RF} remains the same for all dynamics with different RF phase increments settings.

To check the amount of B_0 field drift, one additional dataset with RF phase increment $\Delta\theta_{RF} = \pi$ was usually acquired at the end of the acquisition. In case of absence of B_0 drift during the acquisition, the complex signals should be the same for data with $\Delta\theta_{RF} = -\pi$ and $\Delta\theta_{RF} = \pi$, otherwise, the phase difference between these datasets is proportional to the amount of the drift.

The SNR for both phantom and in-vivo data was calculated as defined in the work by Björk et al (19):

$$SNR = \frac{\sum_{n=1}^{N}|I_n(\theta)|}{N\sigma},$$ [2.17]

where $|I_n(\theta)|$ – the magnitude of an nth phase-cycled image, σ – the standard deviation of the noise, N – number of scans with different RF phase increment settings. The standard deviation of the noise was calculated over the ROI on noise images (real and imaginary components), acquired dynamically using the same bSSFP sequence, without RF excitation and with no gradients applied.

All simulations and calculations were performed in MATLAB R2015a (The MathWorks Inc, Natick, USA).

2.3 Results

2.3.1 Sensitivity to the actual Flip Angle errors

As can be observed from Figure 2.3, T_1 estimates are highly sensitive to errors of the actual flip angle. The dependence is almost linear and the errors in T_1 estimates increase with increasing FA. For example, a 5% error (0.95) in actual FA results in 10% underestimation in T_1 for the nominal FA of 30˚ and 12% underestimation in T_1 for the nominal FA of 60˚. T_2 estimates are not affected by the errors in the actual flip angle.

2.3.2 Phantom results

T_1, T_2 and Δf_0 maps were first validated in a phantom. Magnitude images corresponding to different RF phase increment settings are presented in Figure 2.4 (a). The banding artifacts, the locations of which depend on the resonance offset angle, are shifted depending on the RF phase increment setting. The Geometric Solution (GS), representing the banding-free effective magnitude image, was calculated for a set of acquired data and presented in Figure 2.4 (b). The off-resonance maps of the phantom were calculated using the PLANET method and using the reference method. The results are presented in Figure 2.4 (c,d). The two off-resonance maps look almost similar. A minor deviation between the two calculated maps of [-2; +1] Hz was observed.
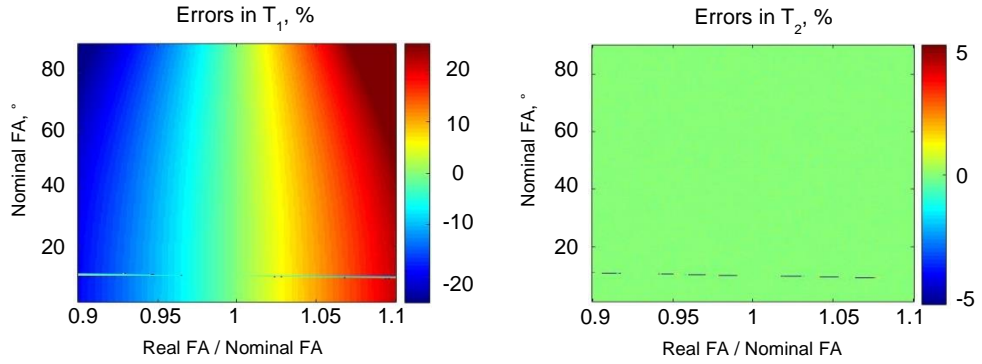
FIGURE 2.3. Simulation results of sensitivity to the actual flip angle errors. The initial $T_1 = 675$ ms, $T_2 = 75$ ms, TR = 10 ms, TE = 5 ms. The horizontal line corresponds to the nominal FA = 10°, which leads to collapsing of the ellipse to a line, as discussed in the Appendix.
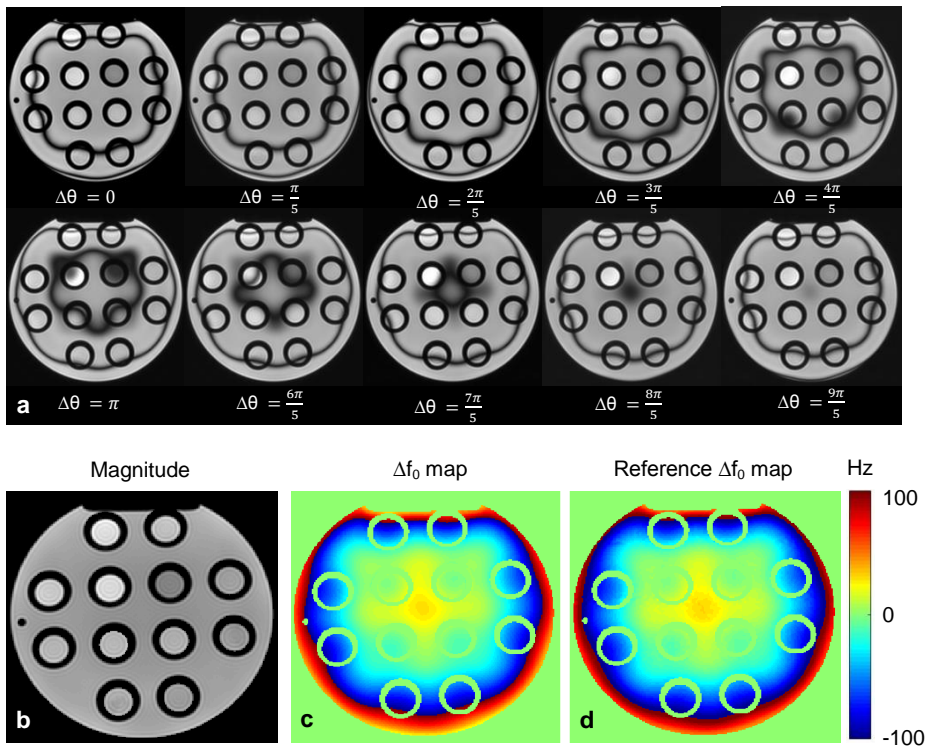
FIGURE 2.4. a) Magnitude images corresponding to different RF phase increments setting $\Delta\theta$; b) The banding-free effective magnitude; c)-d) The off-resonance maps calculated using the PLANET method and using the reference method.

T$_1$ and T$_2$ maps of the phantom were calculated using the PLANET method and using the reference methods. The results are presented in Figure 2.5. The processing time for the reconstruction of T$_1$, T$_2$, Δf$_0$ and banding-free effective magnitude M_{eff} for one slice was 6 s. We generally see a good quantitative agreement between reference and calculated from the PLANET method maps. However, there are some inhomogeneous regions inside some of the phantom tubes. The comparisons between the average T$_1$ and T$_2$ values for each of the phantom tubes are shown in Figure 2.6. Standard deviations in T$_1$ and T$_2$ were calculated for each tube. The estimated accuracy of tabulated T$_1$ and T$_2$ values of the test object provided by the manufacturer is ± 3%.
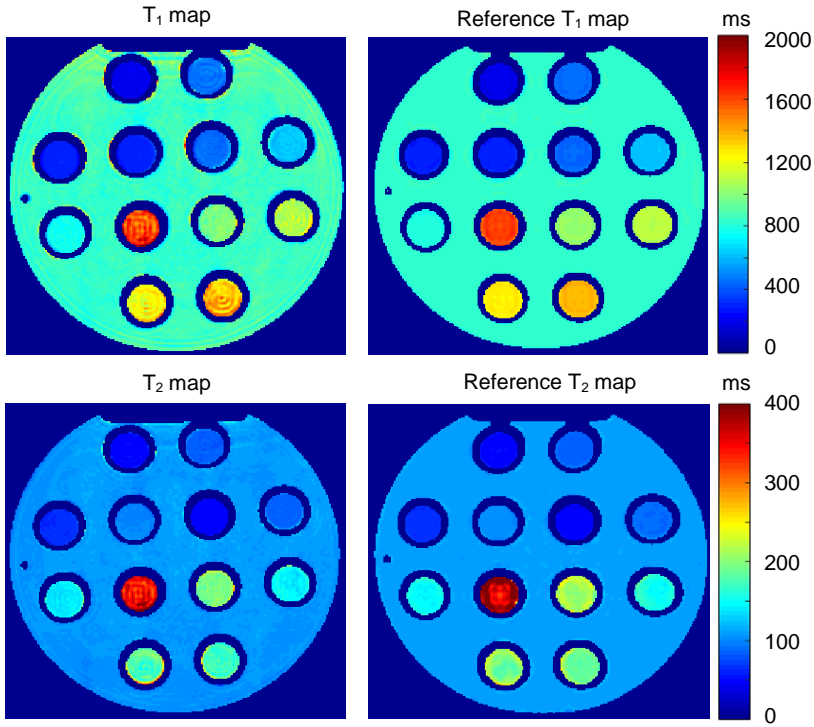
FIGURE 2.5. Experimental results from the phantom study: T$_1$ and T$_2$ maps calculated using the PLANET method and using the reference method.
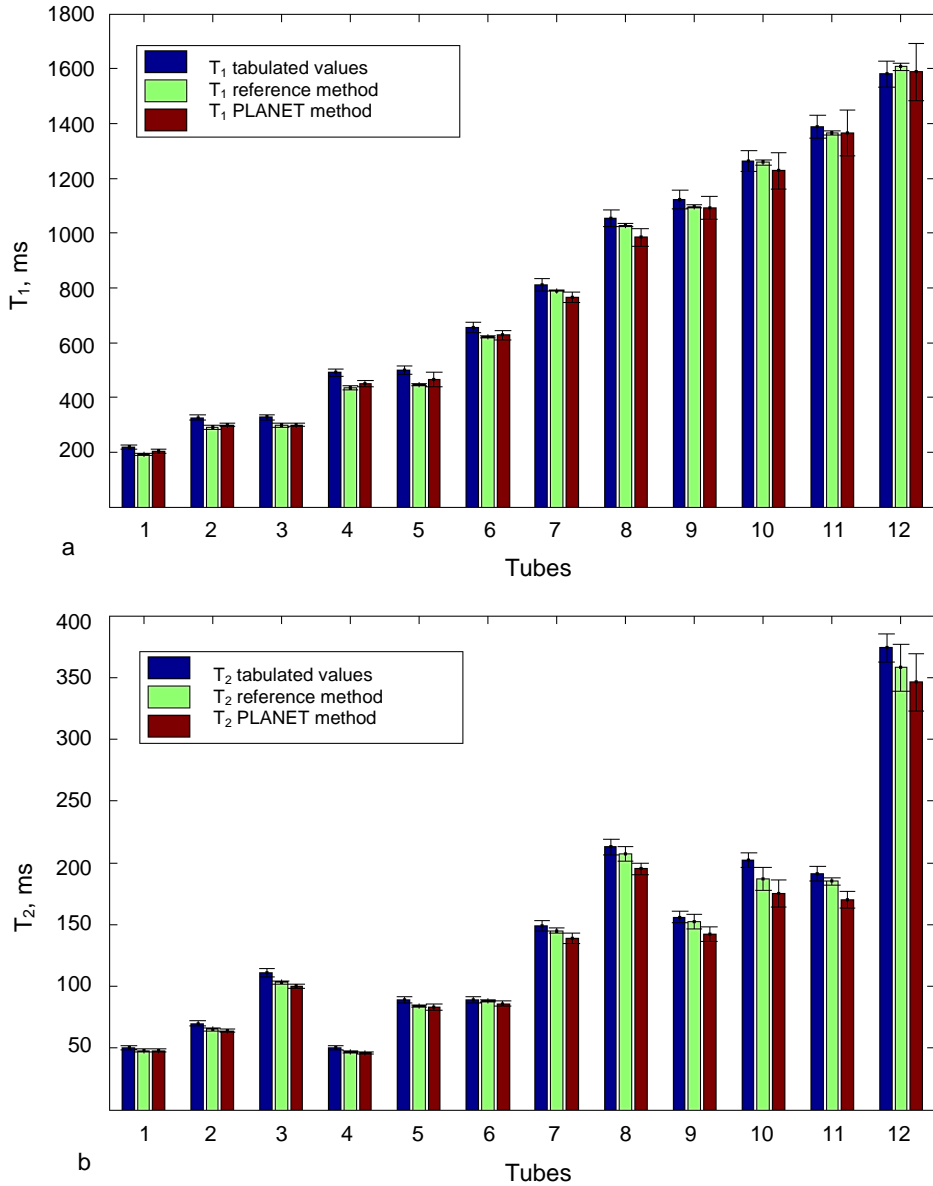
FIGURE 2.6. Experimental results from the phantom study: comparison between average T_1 (a) and T_2 (b) values for the phantom tubes: blue – the tabulated values, green – calculated from the reference methods, red – calculated from the PLANET method. The mean T_1 and T_2 values of the gels were calculated for one slice in the center of the phantom by averaging over a region of interest (ROI) (around 250 voxels) inside each tube on estimated T_1 and T_2 maps. Precision of T_1 and T_2 measurement was evaluated by calculating standard deviations on estimated T_1 and T_2 maps over the same ROIs.

2.3.3 Results *in vivo*

Figure 2.7 (a,b) shows the reference T_1 and T_2 maps of one axial slice of the brain of a healthy volunteer. The results of measurements in three different axial slices through the brain are shown in Figure 2.7 (c-f). The banding-free effective magnitude is presented, as well as the T_1 and T_2 maps, calculated using the PLANET method. The off-resonance maps were calculated using the PLANET method and using the reference method. The minor observed deviation between the off-resonance maps was [-3; +3] Hz. The processing time for the reconstruction of T_1, T_2, Δf_0 and M_{eff} for one slice was 7 s.
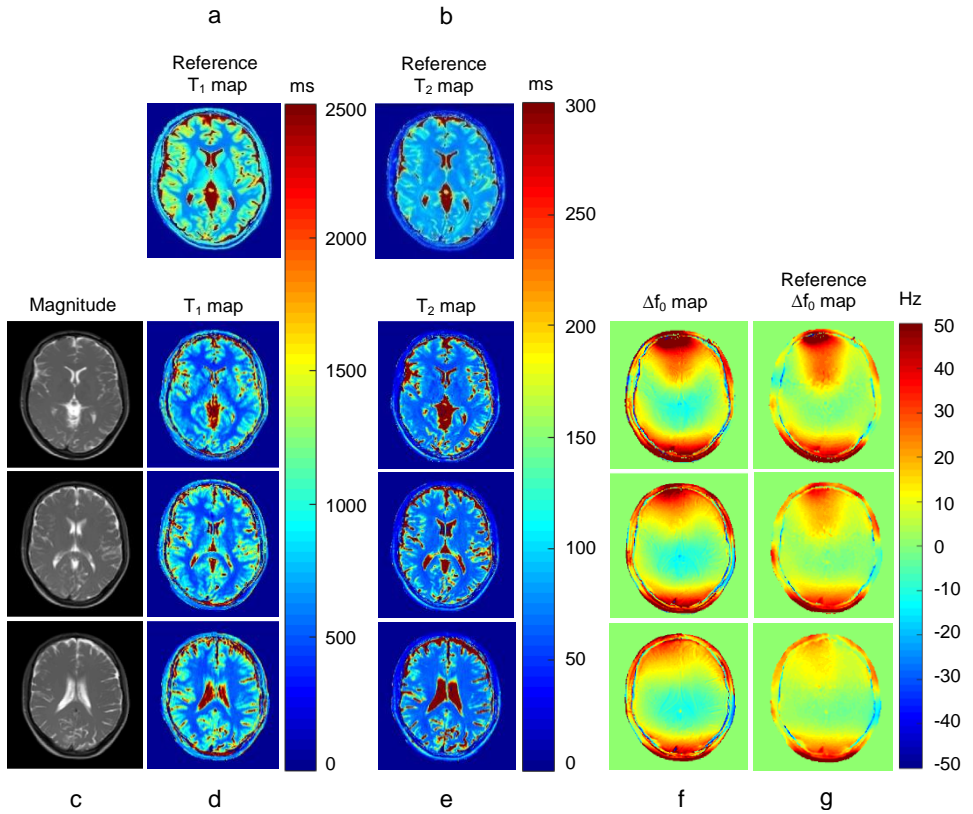
FIGURE 2.7. Experimental results from the volunteer study: a) T_1 map for one axial slice of the brain calculated using the reference method; b) T_2 map for one axial slice of the brain calculated using the reference method; c) The banding free effective magnitude images; d) T_1 maps calculated using the PLANET method; e) T_2 maps calculated using the PLANET method; f) The off-resonance maps calculated using the PLANET method; g) The off-resonance maps calculated using the reference method. The position of the axial slice a)-b) is different from the positions of slices c)-g).

On the T_1 and T_2 maps a good contrast between gray matter (GM), white matter (WM) and cerebrospinal fluid (CSF) can be seen. The calculated mean T_1 and T_2 for WM and GM after B_1 correction are presented in Table 2.2 in comparison with the reference values and those published in the literature (7,29). An underestimation in T_1 by about 15-20% in WM and GM compared to the reference values was observed. T_2 values in WM were underestimated by about 10% compared to the reference values, T_2 values in GM were determined very precisely compared to the reference values.

Examples of the acquired complex signals for WM, GM, and CSF with the corresponding elliptical fits are shown in Figure 2.8. The orientation of three ellipses is different, which is explained by the difference in off-resonance for those voxels.

T_1 and T_2 maps, calculated from datasets, acquired using the default and long RF excitation pulses, as well as Signal Ratio and MTR are presented in Supporting Figure S2.1. The quantitative results from three ROIs placed in WM are shown in Supporting Table S2.1. The average relative signal loss due to MT effects in WM was found to be 13% and the average T_1 shortening was 8%. The estimated SNR maps of the phantom and the brain are presented in Supporting Figure S2.2. The estimated SNR maps of the phantom and the brain are presented in Supporting Figure S2.2.

Table 2.2. The results from *in vivo* experiment: T_1 and T_2 values determined using the PLANET method and using the reference method compared with the published values[a]

	PLANET					Reference 2D MIXED method			
	White matter		Grey matter			White matter		Grey matter	
ROI #	T_1 (ms)	T_2 (ms)	T_1 (ms)	T_2 (ms)	ROI #	T_1 (ms)	T_2 (ms)	T_1 (ms)	T_2 (ms)
1	461 ± 19	62 ± 2	754 ± 47	80 ± 2	1	636 ± 15	75 ± 2	1016 ± 53	84 ± 3
2	466 ± 25	61 ± 2	749 ± 75	84 ± 8	2	602 ± 14	75 ± 2	1014 ± 30	82 ± 4
3	453 ± 15	62 ± 2	836 ± 70	83 ± 5	3	597 ± 13	73 ± 2	999 ± 52	84 ± 2
4	524 ± 19	64 ± 2	876 ± 71	82 ± 4	Mean	612 ± 14	74 ± 2	1010 ± 46	83 ± 3
5	512 ± 30	64 ± 2	837 ± 67	80 ± 4	Literature published values [a]				
6	525 ± 18	63 ± 2	787 ± 24	98 ± 9					
7	528 ± 22	64 ± 3	906 ± 48	90 ± 14	Ref [a]	T_1 (ms)	T_2 (ms)	T_1 (ms)	T_2 (ms)
8			789 ± 24	84 ± 4	Ref IR;SE (7)	615 ± 12	69 ± 2	1002 ± 56	92 ± 3
9			787 ± 24	84 ± 4	Ref (7)	621 ± 61	58 ± 4	1060 ±133	98 ± 7
Mean	496 ± 22	63 ± 2	813 ± 54	85 ± 5	Ref (29)	561 ± 12	73 ± 2	1048 ± 61	94 ± 6

[a] Numbers in parentheses are reference citations.
[b] The mean T_1 and T_2 values of WM were calculated for five slices of the brain by averaging over seven ROIs (each approximately 100 voxels) in WM on estimated T_1 and T_2 maps. The reference mean T_1 and T_2 values of WM were calculated for one slice of the brain by averaging over three ROIs (each approximately 100 voxels) in WM on the reference T_1 and T_2 maps. The mean T_1 and T_2 values of GM were calculated for five slices of the brain by averaging over nine ROIs (each approximately 30 voxels) in GM on estimated T_1 and T_2 maps. The reference mean T_1 and T_2 values of GM were calculated for one slice of the brain by averaging over three ROIs (each approximately 30 voxels) in GM on the reference T_1 and T_2 maps. The precision of T_1 and T_2 measurement was evaluated by calculating standard deviations on estimated T_1 and T_2 maps over the same ROIs.

We did not observe any significant B_0 drift between acquisitions with increments $\Delta\theta_{RF} = -\pi$ and $\Delta\theta_{RF} = \pi$, which were performed at the start and the end of the sequence. The maximum phase difference between these datasets was 0.04 rad for the phantom and 0.06 rad for the brain experiment.
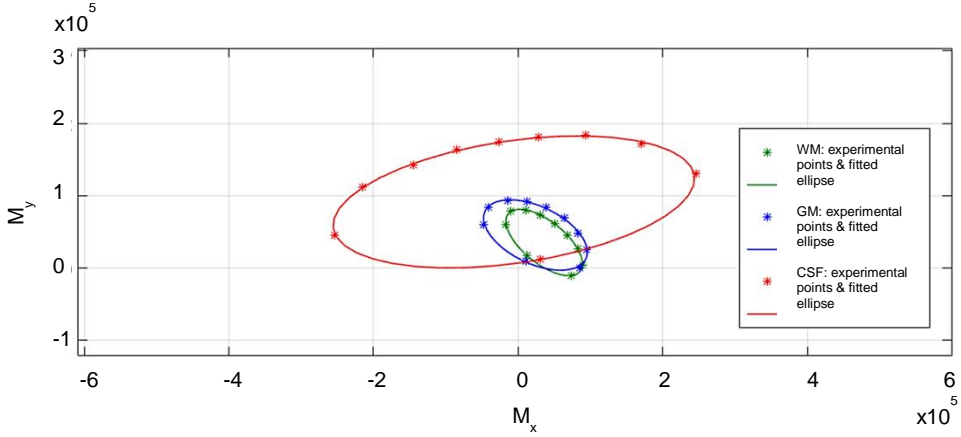
FIGURE 2.8. Examples of the acquired complex signals for white matter, gray matter and CSF with the corresponding elliptical fits from three voxels of the brain of a healthy volunteer.
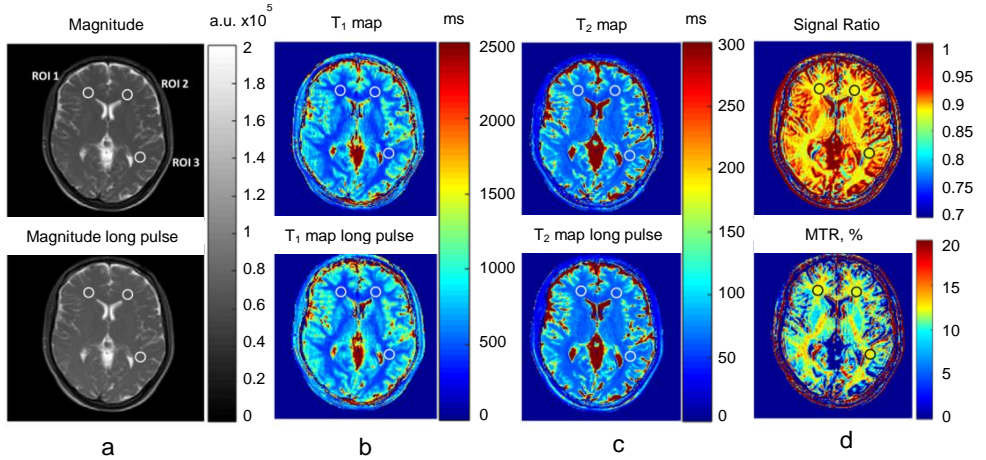
SUPPORTING FIGURE S2.1. Experimental results from the MT study: a) The banding free effective magnitude images, calculated for the default and long RF pulses; b) T_1 maps calculated for the default and long RF pulses; c) T_2 maps calculated for the default and long RF pulses; d) The Signal Ratio and MTR calculated for the default RF pulse compared to the long RF pulse. The duration of the default RF pulse was 0.84 ms. The duration of long RF pulse was 2.86 ms.

SUPPORTING TABLE S2.1. The quantitative results from three ROI placed in white matter for the default and long RF excitation pulses.

ROI #	Pulse type	T_1, ms	T_2, ms	Signal Ratio	MTR, %
ROI 1 (103 voxels)	Default pulse	401 ± 14	59 ± 2	0.875 ± 0.005	12.5 ±0.5
	Long pulse	425 ± 13	59 ± 2		
ROI 2 (108 voxels)	Default pulse	430 ± 16	59 ± 2	0.878 ± 0.005	12.2 ± 0.5
	Long pulse	468 ± 26	62 ± 2		
ROI 3 (102 voxels)	Default pulse	432 ± 16	62 ± 3	0.871 ± 0.008	12.9 ± 0.8
	Long pulse	466 ± 25	63 ± 4		
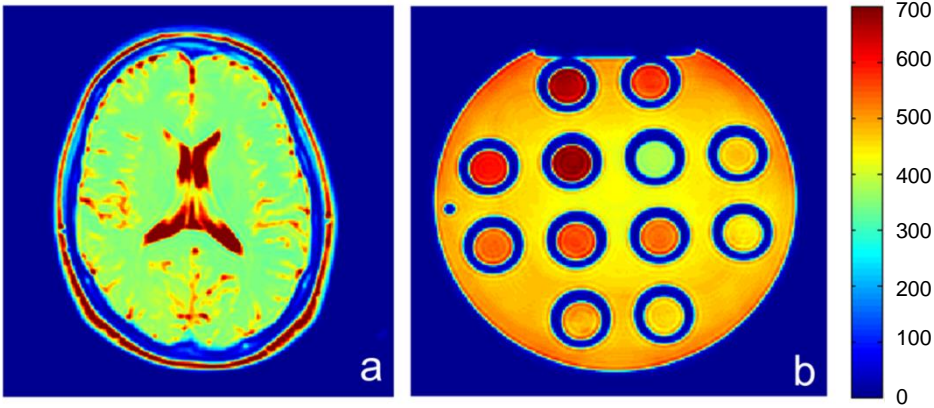
SUPPORTING FIGURE S2.2. SNR maps calculated for one axial slice of the brain (a) and the phantom (b).

2.4 Discussion

The fitting of the elliptical signal model is a very important aspect of the proposed PLANET method. We reformulated the fitting procedure into a linear convex problem, which can be solved directly by using a linear least-squares method. Prior knowledge of the elliptical trajectory in the complex plane allows to reduce the solution space to one unique solution by applying a proper scaling and an ellipse-specific constraint. In combination with analytical solutions for parameters T_1, T_2, and M_{eff}, which take the fitting results as input, our approach becomes simple, robust and fast. This is a clear advantage of our method compared to all iterative algorithms, which usually have longer reconstruction time and fitting problems related to local minima. The whole reconstruction time is very fast, which facilitates the adoption of the proposed method into clinical practice.

Compared to the work by Björk et al (19), who used a combination of linear fitting followed by subsequent non-linear fitting and only four phase-cycled acquisitions, the PLANET method requires at least six phase-cycled acquisitions to directly fit the model to the experimental data. The inclusion of prior knowledge of the elliptical trajectory is essential and differs clearly from the methodology followed by Bjork et al. Contrary to their conclusions, which were based only on simulations, that the simultaneous T_1 and T_2 estimation using their algorithm is not feasible for realistic SNRs, we experimentally demonstrated that it is feasible to employ the PLANET method at realistic SNRs, both in a phantom and *in vivo*, with a regular coil setup and protocol parameters settings.

The reported values of T_1 and T_2 in the phantom are in good agreement with the calibrated values and those calculated with reference methods. However, in some of the tubes some inhomogeneous regions in the form of "ghosts" near the tube borders are observed in the resultant T_1 and T_2 maps of the phantom, which leads to an underestimation of the calculated T_1 and T_2 values for those tubes. This effect may have been caused by Gibbs ringing artifacts. The influence of these artifacts on estimated T_1 maps needs to be further investigated and minimized.

T_1 and T_2 maps obtained in the brain of volunteers were generally in agreement with the reference maps and values in literature (7,29), however, the T_1 values were underestimated. B_1 field inhomogeneities, resulting in errors in the actual flip angle, have shown a significant influence on the estimated T_1 values. The errors caused by this effect depend on the used FA and were corrected using additionally acquired B_1 maps. Unlike T_1 estimates, T_2 estimates were not affected by the errors in the actual flip angle. MT effects were shown influence T_1 quantification, particularly in WM. A partial mitigation strategy to minimize the impact of MT effects, as proposed by Bieri et al, was to use long RF excitation

pulses in a combination with relatively low FA and long TR. Note that effects related to the presence of deoxyhemoglobin (30) and diffusion effects (31) were not included.

We believe that the observed underestimation of T_1 and T_2 in the human brain (particularly in WM) even after B_1 correction might be caused by an inhomogeneous intra voxel frequency distribution and multi-component relaxation (32–37). The presence of different frequencies within a voxel results in asymmetries in the bSSFP signal profile, which have been found and comprehensively studied by Miller (38,39). We also observed such asymmetries when we plotted the frequency responses for WM and GM. In the phantom, we did not observe asymmetries since there are no structures with different frequency components, which can explain a good agreement of the found T_1 and T_2 values with the reference values. Similar results were found in the work by Nguyen et al (40). Their methodology, named MIRACLE, for T_1 and T_2 mapping, is based on frequency-shifted bSSFP scans with subsequent TESS processing for relaxometry. They used a similar experimental setup at 3T and showed a systematic underestimation of T_1 values even after B_1 correction in the brain, while the phantom results were in agreement with the reference. Particularly, they found a 40% underestimation in T_1 for WM and a 20% underestimation of T_1 for GM. They also believe that this is likely due to the asymmetric shape of the bSSFP frequency response in WM and GM due to the presence of myelin (35–37). They investigated the effect by characterizing brain tissues with a two-component relaxation parameter model, as proposed by Miller et al (39) and Deoni et al (41), in which the smaller myelin component had a lower combination of T_1 and T_2 compared with the dominant component. In their simulation, they observed a shift towards lower apparent T_1 values which was in agreement with their experimental results and with the results which we presented in this paper.

We believe that the performance and the results of the presented method in the brain deserve further examinations. In addition, further investigation of the *in vivo* protocol optimization will be the subject of our further research.

The relaxation times T_1 and T_2, the off-resonance, and the banding free magnitude can be simultaneously and robustly estimated from one dynamic 3D phase-cycled bSSFP sequence. This is an important difference and advantage compared to all existing bSSFP-based techniques for relaxometry purposes.

Such quantitative mapping may be a useful addition to the common techniques for banding artifacts removal that rely on phase-cycling (18). In order to accomplish this, just a few more additional bSSFP data sets with other RF phase increment settings are required. PLANET may be applied for investigating the local susceptibility and the electrical tissue properties: the off-resonance maps can be used for quantitative susceptibility mapping

(QSM) (42). RF phase offset maps, which can be in principle retrieved from Equation [2.11], could potentially be used for electric properties tomography (EPT) (43).

Although bSSFP, in general, is a fast imaging technique with a high SNR efficiency, the disadvantage of using multiple phase-cycled acquisitions is the increased scan duration. In this work, we used ten steps, but theoretically, considering the number of fitting parameters, the minimum number of required steps is six. Even though the scan duration is much shorter compared to the duration of the combined 2D gold standard IR-SE and ME-SE and 2D IR-TrueFISP techniques when 3D coverage is desired, and comparable to that of the combined 3D DESPOT1&2 or 3D TESS technique, we intend to further investigate ways to shorten the scan duration. Shorter acquisition times may be realized by minimizing the number of phase increment steps or by using acceleration techniques, such as compressed sensing (44) or dynamically phase-cycled radial bSSFP (45).

We limited the model to the 3D acquisition mode, assuming a constant flip angle profile in the slice direction for each voxel. When volumetric coverage is not required, switching to the 2D acquisition mode would considerably decrease the acquisition time, but would lead to a non-ideal flip angle profile over the slice which would compromise the required elliptical behavior of the integrated complex magnetization. An investigation of the feasibility of a 2D approach is subject of our further research.

In this study, we assumed that the chemical shift for all resonances was negligible (i.e. only water resonances present), which indeed was the case for the phantom and the brain experiments. For species with other chemical shifts, like fat, the model should be adjusted to account for different initial conditions, corresponding to $\delta_{CS} \neq 0$.

The method is sensitive to B_0 drift when it appears while acquiring acquisitions with different phase increment settings. This results in deviations from the single elliptical distribution in the complex plane and errors in the estimated parameters. In our experiments, we did not observe any significant B_0 drift and did not compensate for it. In case if severe B_0 drift appears, there is a need for correction.

The extension of this work will include a more detailed study of the precision and accuracy of the method in relation to the SNR.

2.5 Conclusion

We have presented a novel approach, named PLANET, for simultaneous estimation of relaxation times T_1 and T_2 from phase-cycled bSSFP. Prior knowledge about the elliptical signal model was used to reformulate the fitting problem into a convex one, which can be

solved directly using a linear least-squares method. The unique ellipse-specific solution of the fitting problem in combination with analytical solutions for T_1 and T_2 makes our approach simple, robust and fast, additionally allowing for the calculation of the off-resonance and the banding-free magnitude image from the same set of the acquired data.

We have demonstrated that accurate T_1 and T_2 mapping in a phantom as well as in the brain of healthy volunteers is feasible for realistic SNRs and can be performed with a regular coil setup and protocol parameter settings on a clinical MR scanner.

We believe that the presented method may be applied in a wide range of applications.

Appendix. The analytical solution for parameters a, b, M_{eff}

The system of nonlinear Equations [2.9] can be solved for parameters a, b, M_{eff} by considering two cases, as illustrated in Supporting Figure S2.3: a > b and a < b, and taking into account the physical constraints for parameters a and b: $0 < a < 1$, $0 < b < 1$, and the condition of the vertical ellipse: $A < B$ or $b < \frac{2a}{1+a^2}$.

The case a = b, which from Equation [2.2] equivalent to $E_2 = \frac{E_2(1-E_1)(1+\cos\alpha)}{1-E_1\cos\alpha-E_2^2(E_1-\cos\alpha)}$, and after expanding equivalent to $\alpha = \cos^{-1}(E_1) = \cos^{-1}\left(\exp(-\frac{TR}{T_1})\right)$, would lead to a collapse of the ellipse to a line $x = M_{eff}$ and should be excluded from consideration by choosing the FA = $\alpha \neq \cos^{-1}(E_1)$.

After solving the Equation [2.8] using trivial algebraic transformations, the solutions for parameters a, b, M_{eff} within interval (0,1) are:

1. In case a > b , which is equivalent to $\alpha > \cos^{-1}(E_1) = \cos^{-1}\left(\exp(-\frac{TR}{T_1})\right)$

$$b_1 = \frac{-X_c A + \sqrt{(X_c A)^2 - (x_c^2 + B^2)(A^2 - B^2)}}{(X_c^2 + B^2)}$$

$$a_1 = \frac{B}{X_c\sqrt{1-b_1^2}+b_1 B}, \qquad M_{eff1} = \frac{X_c(1-b_1^2)}{1-a_1 b_1}$$

2. In case a < b , which is equivalent to $\alpha < \cos^{-1}(E_1) = \cos^{-1}\left(\exp(-\frac{TR}{T_1})\right)$

$$b_2 = \frac{X_c A + \sqrt{(X_c A)^2 - (X_c^2 + B^2)(A^2 - B^2)}}{(X_c^2 + B^2)}$$

$$a_2 = \frac{B}{X_c\sqrt{1 - b_2^2} + b_2 B}, \qquad M_{\text{eff2}} = \frac{X_c\,(1 - b_2^2)}{1 - a_2 b_2}$$

To cover the range of T_1 of 200-2000 ms for the fixed TR = 10 ms, the FA corresponding to $a > b$ for all T_1 should be more than 18°, while $a < b$ area for all T_1 corresponds to FA less than 5°. Therefore the correct choice of FA should be done by choosing the flip angle:

$$FA > \cos^{-1}\left(\exp(-\frac{TR}{T_{1\,\text{shortest}}})\right)$$

.
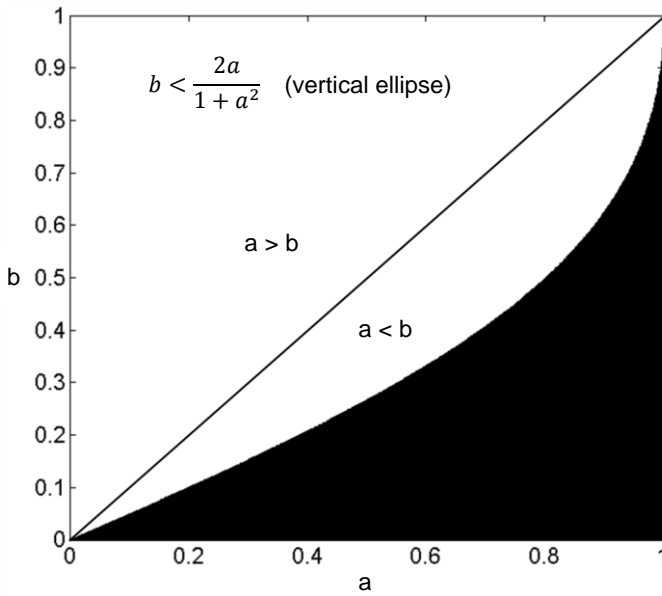
SUPPORTING FIGURE S2.3. Geometrical representation of the parameter space for a and b. The white area corresponds to the vertical ellipse for cases a > b and a < b, and the black area corresponds to the horizontal ellipse.

2.6 References

1. Cheng HL, Stikov N, Ghugre NR, Wright GA. Practical medical applications of quantitative MR relaxometry. J. Magn. Reson. Imaging 2012;36:805–824. doi: 10.1002/jmri.23718.

2. Bernstein M a, King KE, Zhou XJ, Fong W. Handbook of MRI Pulse Sequences. 2005. doi: 10.1118/1.1904597.

3. Look DC, Locker DR. Time saving in measurement of NMR and EPR relaxation times. Rev. Sci. Instrum. 1970;41:250–251. doi: 10.1063/1.1684482.

4. Christensen KA, Grant DM, Schulman EM, Walling C. Optimal determination of relaxation times of fourier transform nuclear magnetic resonance. Determination of spin-lattice relaxation times in chemically polarized species. J. Phys. Chem. 1974;78:1971–1977. doi: 10.1021/j100612a022.

5. Fram EK, Herfkens RJ, Johnson GA, Glover GH, Karis JP, Shimakawa A, Perkins TG, Pelc NJ. Rapid calculation of T1 using variable flip angle gradient refocused imaging. Magn. Reson. Imaging 1987;5:201–208. doi: 10.1016/0730-725X(87)90021-X.

6. Homer J, Beevers MS. Driven-equilibrium single-pulse observation of T1 relaxation. A reevaluation of a rapid "new" method for determining NMR spin-lattice relaxation times. J. Magn. Reson. 1985;63:287–297. doi: 10.1016/0022-2364(85)90318-X.

7. Deoni SCL, Rutt BK, Peters TM. Rapid combined T1 and T2 mapping using gradient recalled acquisition in the steady state. Magn. Reson. Med. 2003;49:515–526. doi: 10.1002/mrm.10407.

8. Wang HZ, Riederer SJ, Lee JN. Optimizing the precision in T1 relaxation estimation using limited flip angles. Magn. Reson. Med. 1987;5:399–416. doi: 10.1002/mrm.1910050502.

9. Deoni SCL, Peters TM, Rutt BK. Determination of Optimal Angles for Variable Nutation Proton Magnetic Spin-Lattice, T1, and Spin-Spin, T2, Relaxation Times Measurement. Magn. Reson. Med. 2004;51:194–199. doi: 10.1002/mrm.10661.

10. Wood TC. Improved formulas for the two optimum VFA flip-angles. Magn. Reson. Med. 2015;74:1–3. doi: 10.1002/mrm.25592.

11. Cheng HLM, Wright GA. Rapid high-rsolution T1 mapping by variable flip angles: Accurate and precise measurements in the presence of radiofrequency field inhomogeneity. Magn. Reson. Med. 2006;55:566–574. doi: 10.1002/mrm.20791.

12. Deoni SCL, Ward HA, Peters TM, Rutt BK. Rapid T2 estimation with phase-cycled variable nutation steady-state free precession. Magn. Reson. Med. 2004;52:435–439. doi: 10.1002/mrm.20159.

13. Deoni SCL. Transverse relaxation time (T2) mapping in the brain with off-resonance correction using phase-cycled steady-state free precession imaging. J. Magn. Reson.

Imaging 2009;30:411–417. doi: 10.1002/jmri.21849.

14. Preibisch C, Deichmann R. Influence of RF spoiling on the stability and accuracy of T1 mapping based on spoiled FLASH with varying flip angles. Magn. Reson. Med. 2009;61:125–135. doi: 10.1002/mrm.21776.

15. Yarnykh VL. Optimal radiofrequency and gradient spoiling for improved accuracy of T1 and B1 measurements using fast steady-state techniques. Magn. Reson. Med. 2010;63:1610–1626. doi: 10.1002/mrm.22394.

16. Schmitt P, Griswold MA, Jakob PM, Kotas M, Gulani V, Flentje M, Haase A. Inversion recovery TrueFISP: quantification of T(1), T(2), and spin density. Magn. Reson. Med. 2004;51:661–7. doi: 10.1002/mrm.20058.

17. Heule R, Ganter C, Bieri O. Triple echo steady-state (TESS) relaxometry. Magn. Reson. Med. 2014;71:230–237. doi: 10.1002/mrm.24659.

18. Bangerter NK, Hargreaves BA, Vasanawala SS, Pauly JM, Gold GE, Nishimura DG. Analysis of Multiple-Acquisition SSFP. Magn. Reson. Med. 2004;51:1038–1047. doi: 10.1002/mrm.20052.

19. Björk M, Ingle RR, Gudmundson E, Stoica P, Nishimura DG, Barral JK. Parameter estimation approach to banding artifact reduction in balanced steady-state free precession. Magn. Reson. Med. 2014;72:880–892. doi: 10.1002/mrm.24986.

20. Shcherbakova Y, van den Berg CAT, Lagendijk JJW, Moonen CTW, Bartels LW. Accurate T1 and T2 mapping by direct least-squares ellipse fitting to phase-cycled bSSFP data. In: Proceedings of the 24th Annual Meeting of ISMRM, Singapore, 2016. Abstract. 0695. ; 2016. p. 695.

21. Lauzon M. Louis, Frayne R. Analytical Characterization of RF Phase-Cycled Balanced Steady-State Free Precession. Concepts Magn. Reson. Part A 2009;34A:133–143. doi: 10.1002/cmr.a.20138.

22. Fitzgibbon AW, Fisher RB, Hill F, Eh E. Direct Least Squres Fitting of Ellipses. IEEE Trans. Pattern Anal. Mach. Intell. 1996;21:1–15.

23. Xiang QS, Hoff MN. Banding artifact removal for bSSFP imaging with an elliptical signal model. Magn. Reson. Med. 2014;71:927–933. doi: 10.1002/mrm.25098.

24. Hal R, Flusser J. Numerically stable direct least squares fitting of ellipses. Proc. 6th Int. Conf. Cent. Eur. Comput. Graph. Vis. 1998;98:125–132. doi: 10.1109/34.765658.

25. In den Kleef JJ, Cuppen JJ. RLSQ: T1, T2, and rho calculations, combining ratios and least squares. Magn. Reson. Med. 1987;5:513–24.

26. Yarnykh VL. Actual flip-angle imaging in the pulsed steady state: A method for rapid three-dimensional mapping of the transmitted radiofrequency fleld. Magn. Reson. Med. 2007;57:192–200. doi: 10.1002/mrm.21120.

27. Bieri O, Scheffler K. Optimized balanced steady-state free precession magnetization transfer imaging. Magn Reson Med 2007;58:511–518. doi: 10.1002/mrm.21326.

28. Bieri O, Markl M, Scheffler K. Analysis and compensation of eddy currents in balanced SSFP. Magn. Reson. Med. 2005;54:129–137. doi: 10.1002/mrm.20527.

29. Warntjes JBM, Dahlqvist Leinhard O, West J, Lundberg P. Rapid magnetic resonance quantification on the brain: Optimization for clinical usage. Magn. Reson. Med. 2008;60:320–329. doi: 10.1002/mrm.21635.

30. Dharmakumar R, Hong J, Brittain JH, Plewes DB, Wright GA. Oxygen-sensitive contrast in blood for steady-state free precession imaging. Magn. Reson. Med. 2005;53:574–583. doi: 10.1002/mrm.20393.

31. Bieri O, Scheffler K. Effect of diffusion in inhomogeneous magnetic fields on balanced steady-state free precession. NMR Biomed. 2007;20:1–10. doi: 10.1002/nbm.1079.

32. Lancaster JL, Andrews T, Hardies LJ, Dodd S, Fox PT. Three-pool model of white matter. J. Magn. Reson. Imaging 2003;17:1–10. doi: 10.1002/jmri.10230.

33. Laule C, Vavasour IM, Moore GRW, Oger J, Li DKB, Paty DW, MacKay AL. Water content and myelin water fraction in multiple sclerosis. A T2 relaxation study. J. Neurol. 2004;251:284–93. doi: 10.1007/s00415-004-0306-6.

34. Lee J, Shmueli K, Fukunaga M, van Gelderen P, Merkle H, Silva AC, Duyn JH. Sensitivity of MRI resonance frequency to the orientation of brain tissue microstructure. Proc. Natl. Acad. Sci. USA 2010;107:5130–5135. doi: 10.1073/pnas.0910222107.

35. van Gelderen P, de Zwart JA, Lee J, Sati P, Reich DS, Duyn JH. Nonexponential $T_2{}^*$ decay in white matter. Magn. Reson. Med. 2012;67:110–117. doi: 10.1002/mrm.22990.

36. Lee J, Shmueli K, Kang BT, Yao B, Fukunaga M, Van Gelderen P, Palumbo S, Bosetti F, Silva AC, Duyn JH. The contribution of myelin to magnetic susceptibility-weighted contrasts in high-field MRI of the brain. Neuroimage 2012;59:3967–3975. doi: 10.1016/j.neuroimage.2011.10.076.

37. van Gelderen P, Jiang X, Duyn JH. Effects of magnetization transfer on T1 contrast in human brain white matter. Neuroimage 2016;128:85–95. doi: 10.1016/j.neuroimage.2015.12.032.

38. Miller KL. Asymmetries of the balanced SSFP profile. Part I: Theory and Observation. Magn. Reson. Med. 2010;63:385–395. doi: 10.1002/mrm.22212.

39. Miller KL, Smith SM, Jezzard P. Asymmetries of the balanced SSFP profile. Part II: White matter. Magn. Reson. Med. 2010;63:396–406. doi: 10.1002/mrm.22249.

40. Nguyen D, Bieri O. Motion-insensitive rapid configuration relaxometry. Magn. Reson. Med. 2016. doi: 10.1002/mrm.26384.

41. Deoni SCL, Rutt BK, Arun T, Pierpaoli C, Jones DK. Gleaning multicomponent T1 and T2 information from steady-state imaging data. Magn. Reson. Med. 2008;60:1372–1387. doi: 10.1002/mrm.21704.

42. Wang Y, Liu T. Quantitative susceptibility mapping (QSM): Decoding MRI data for a tissue magnetic biomarker. Magn. Reson. Med. 2015;73:82–101. doi: 10.1002/mrm.25358.

43. Katscher U, Voigt T, Findeklee C, Vernickel P, Nehrke K, Dössel O. Determination of electric conductivity and local SAR via B1 mapping. IEEE Trans. Med. Imaging 2009;28:1365–1374. doi: 10.1109/TMI.2009.2015757.

44. Cukur T. Accelerated phase-cycled SSFP imaging with compressed sensing. IEEE Trans. Med. Imaging 2015;34:107–115. doi: 10.1109/TMI.2014.2346814.

45. Benkert T, Ehses P, Blaimer M, Jakob PM, Breuer FA. Dynamically phase-cycled radial balanced SSFP imaging for efficient banding removal. Magn. Reson. Med. 2015;73:182–194. doi: 10.1002/mrm.25113.

Chapter 3

On the accuracy and precision of PLANET for multi-parametric MRI using phase-cycled bSSFP imaging

ABSTRACT

Purpose:

In this work, we demonstrate how the sequence parameter settings influence the accuracy and precision in T_1, T_2, and off-resonance maps obtained with the PLANET method for a single-component signal model. In addition, the performance of the method for the particular case of a two-component relaxation model for white matter tissue was assessed.

Methods:

Numerical simulations were performed to investigate the influence of sequence parameter settings on the accuracy and precision in the estimated parameters for a single-component model, as well as for a two-component WM model. Phantom and *in vivo* experiments were performed for validation. In addition, the effects of Gibbs ringing were investigated.

Results:

By making a proper choice for sequence parameter settings, accurate and precise parameter estimation can be achieved for a single-component signal model over a wide range of relaxation times at realistic SNR levels. Due to the presence of a second myelin-related signal component in WM, an underestimation of around 30% in T_1 and T_2 was observed, predicted by simulations and confirmed by measurements. Gibbs ringing artifacts correction improved the precision and accuracy of the parameter estimates.

Conclusion:

For a single-component signal model, there is a broad "sweet spot" of sequence parameter combinations for which high accuracy and precision in the parameter estimates are achieved over a wide range of relaxation times. For a multi-component signal model, the single-component PLANET reconstruction results in systematic errors in the parameter estimates as expected.

Key words: SNR, accuracy, precision, relaxometry, phase-cycled bSSFP

3.1 Introduction

Measurements of longitudinal (T_1) and transverse (T_2) relaxation times are widely used in many different applications to assess physical and physiological characteristics of tissues (1) associated with a specific disease, and changes therein with disease progression or regression as a response to therapy. Another emerging application is synthetic MRI (2,3), where images with various contrasts based on signal weighting are synthetically generated from T_1, T_2 and proton density maps.

    Many quantitative MRI techniques exist, including many approaches for relaxometry and the recently introduced MR fingerprinting approach (4). Besides the standard time-consuming methods for T_1 and T_2 mapping, which are based on 2D inversion recovery spin-echo (IR-SE) and multi-echo spin-echo (ME-SE) sequences, there are many fast steady-state free precession (SSFP)-based imaging techniques (5). Some of them rely on the IR method with multiple low flip angle (FA) excitation pulses, such as the Look-Locker method (6). Some are based on the variable FA approach, such as DESPOT (7–9), or multiple echo approaches, such as DESS and TESS (10,11).

    Balanced SSFP (bSSFP) sequences deserve special attention due to their rapid acquisition time and high signal-to-noise ratio (SNR) efficiency. Despite sensitivity to local off-resonance, bSSFP has been successfully employed for quantitative relaxometry (12–14), especially for simultaneous T_1 and T_2 quantification (15,16).

    We recently proposed a method named PLANET (17) to simultaneously map the relaxation parameters T_1 and T_2, the local off-resonance Δf_0, the RF phase, and the banding free magnitude image using a phase-cycled bSSFP sequence. Linear least squares fitting of an ellipse to the complex-valued bSSFP data acquired with an RF phase incrementing scheme is first applied. This is followed by quantitative parameter estimation through analytical expressions that were derived from the geometrical characteristics of the ellipse (17). The method uses standard pulse sequences and can be easily performed on clinical MR scanners within an acceptable time. Additionally, the reconstruction time is very short due to the use of a linear least squares fitting ($\sim$ 6-7 sec per slice of matrix size 224x224).

    In this work, we investigated how the sequence parameter settings, such as flip angle (FA), repetition time (TR), and number of RF phase increment steps influence the accuracy and precision of quantitative T_1, T_2, and Δf_0 estimation using the PLANET method.

    The PLANET model is based on a Lorentzian single-component relaxation model, which results in a symmetric bSSFP magnitude profile. However, in the case of the presence of a second component with different frequency distribution and different relaxation parameter values, the bSSFP profile becomes asymmetric, as was pointed out by Miller et al (18).

To investigate this issue, we paid special attention to the particular case of WM tissue in the human brain, where the bSSFP profile is known to be asymmetric (19) due to the presence of a second signal component related to myelin with relatively short relaxation times. Many studies have demonstrated the presence of multi-component T_1 and T_2 in the brain (20–32), many of them were reviewed by Alonso-Ortiz et al (33). We performed numerical simulations for WM using a two-component model to assess the accuracy and precision in parameter estimates. In addition, we validated the results experimentally.

The impact and mitigation of Gibbs ringing on PLANET were studied more in-depth motivated by the realization that the RF phase-cycling spatially shifts the banding artifacts, causing the Gibbs ringing to be in principle different for each phase-cycled image. This may result in systematic errors in calculated T_1 and T_2 maps, especially when low spatial resolution data are acquired.

In our previous study (17), we demonstrated the feasibility of quantitative parameter mapping at realistic SNRs using the PLANET method. The results we present here demonstrate that improvement of the accuracy and precision in all quantitative parameter estimates can be obtained by making an optimal choice for the sequence parameter settings.

3.2 Methods

First, for a single-component signal model, we investigated how the precision and accuracy of the estimated relaxation times T_1 and T_2, the local off-resonance Δf_0, as well as the SNR depend on the sequence parameter settings. For this purpose, we performed numerical simulations to investigate how the choice of parameter settings for FA, TR, and number of cycles N influences the absolute and relative errors in the parameter estimates. To provide guidance in practical use of the PLANET method, we determined the minimum SNR required to achieve a certain precision in all estimated parameters, which we chose equal to 5% of the mean parameter values. The simulation framework we developed can easily be used to repeat such investigations using other criteria. To demonstrate the performance of the method at high and low SNR levels, experiments were performed using a calibrated phantom on 1.5T MR scanner.

Second, we investigated the case of a two-component relaxation model, particularly WM tissue. Again, we performed Monte Carlo simulations to assess the accuracy and precision of the quantitative parameter estimates. To validate the simulation results of a two-component model, *in vivo* brain experiments were performed in healthy volunteers on 3T.

Third, we investigated the effects of Gibbs ringing on the performance of the PLANET

method. Using numerical simulations, we assessed the accuracy and precision in parameter estimates dependent on the chosen acquisition voxel size, and the effects of using Gibbs ringing filtering. To demonstrate the extent of Gibbs ringing effects, experiments in a phantom and *in vivo* in the brain of a healthy volunteer were performed on 1.5T.

3.2.1 Single-component phase-cycled bSSFP signal model

The complex phase-cycled bSSFP signal can be described as (34,35):

$$I = M_{\text{eff}} \cdot \frac{1 - ae^{i\theta}}{1 - b\cos\theta} \cdot e^{i\varphi}, \qquad [3.1]$$

where

$$M_{\text{eff}} = e^{-\frac{TE}{T_2}} \frac{KM_0(1 - E_1)\sin\alpha}{1 - E_1\cos\alpha - E_2^2(E_1 - \cos\alpha)}, \quad a = E_2, \quad b = \frac{E_2(1 - E_1)(1 + \cos\alpha)}{1 - E_1\cos\alpha - E_2^2(E_1 - \cos\alpha)} \quad [3.2]$$

$$\varphi = 2\pi(\delta_{CS} + \Delta f_0)TE + \varphi_{RF}, \qquad [3.3]$$

φ - is the rotation angle of an ellipse around the origin regarding to its initial vertical form (34) at TE = 0, $E_1 = \exp(-\frac{TR}{T_1})$, $E_2 = \exp(-\frac{TR}{T_2})$, KM_0 - is product of the thermal equilibrium magnetization M_0 and the magnitude of the combined receive field K , α - is the flip angle, TR - is the repetition time, θ - is the resonance offset angle (in radians), $\theta = \theta_0 - \Delta\theta$, where $\theta_0 = 2\pi(\delta_{CS} + \Delta f_0)TR$, Δf_0 - is the off-resonance (in Hz), δ_{CS} - is the chemical shift of the species (in Hz) with respect to the water peak, $\Delta\theta$ - is the user controlled RF phase increment (in radians), φ_{RF} - is the RF phase offset, related to the combination of RF transmit and receive phases (in radians).

3.2.1.1 Accuracy and precision

The accuracy of the method for a single-component model was assessed by calculating the relative error (ε) in T_1, T_2, and Δf_0 estimates:

$$\varepsilon_{T_1} = \frac{\overline{T_1} - T_{1\,true}}{T_{1\,true}} \cdot 100\%, \quad \varepsilon_{T_2} = \frac{\overline{T_2} - T_{2\,true}}{T_{2\,true}} \cdot 100\%, \quad \varepsilon_{\Delta f_0} = \frac{\overline{\Delta f_0} - \Delta f_{0\,true}}{\Delta f_{0\,true}} \cdot 100\% \qquad [3.4]$$

The precision of the method was assessed by calculating the relative standard deviation

(SD) of T_1, T_2, and Δf_0 estimates:

$$SD_{T_1} = \frac{\sqrt{\frac{1}{Z}\sum_{i=1}^{Z}\left(T_1^i - \overline{T_1}\right)^2}}{\overline{T_1}} \cdot 100\%, \quad SD_{T_2} = \frac{\sqrt{\frac{1}{Z}\sum_{i=1}^{Z}\left(T_2^i - \overline{T_2}\right)^2}}{\overline{T_2}} \cdot 100\%,$$

$$SD_{\Delta f_0} = \frac{\sqrt{\frac{1}{Z}\sum_{i=1}^{Z}\left(\Delta f_0^i - \overline{\Delta f_0}\right)^2}}{\overline{\Delta f_0}} \cdot 100\%, \qquad\qquad [3.5]$$

where $\overline{X} = \frac{1}{Z}\sum_{i=1}^{Z}X^i$ refers to the average of the simulated values X^i, assuming a true value of X_{true} (for parameters T_1, T_2, Δf_0), and Z – is the total number of simulations.

3.2.1.2 Numerical simulations

To investigate how the precision and accuracy in all parameter estimates depend on choices for FA, TR, N, Monte Carlo simulations were performed for FA in the range of 0 - 90˚, TR in the range of 0 - 50 ms, and number N of RF phase increment steps from 6 to 16 with increments $\Delta\theta_n = \frac{2\pi n}{N} - \pi$, n = {0, 1,.., N-1} and the initial parameter settings: $KM_0 = 10000$, $\Delta f_0 = 10$ Hz, single-peak with $\delta_{CS} = 0$, $\varphi_{RF} = 0$. The chosen Δf_0 corresponds to the average off-resonance observed experimentally in the brain at 3T in the center of the FOV, and the chosen combination of $T_1 = 830$ ms and $T_2 = 80$ ms represents WM at 3T (36). Gaussian noise was added independently to the real and imaginary data, resulting in an SNR ranging from 30 to 150 for WM, which corresponds to the range of experimentally measured SNR in this tissue. The number of performed Monte Carlo simulations was 10,000. Similar simulations were performed for WM at low SNR in the range from 5 to 40.

3.2.1.3 SNR

In this work, we adopted the definition of the SNR, as described in the work by Björk et al (37), taking into account each phase-cycled bSSFP acquisition:

$$SNR = \frac{\sum_{n=1}^{N}|I_n(\theta)|}{N\sigma}, \qquad\qquad [3.6]$$

where $|I_n(\theta)|$ – is the magnitude of nth phase-cycled image, σ – is the standard deviation of Gaussian noise, N – is the number of phase-cycled bSSFP acquisitions.

The minimum SNR required to achieve a standard deviation in T_1, T_2, and Δf_0, equal to 5% of the corresponding true values, was calculated for T_1 values in the range of 100 - 3000 ms, and for T_2 values in the range of 10 - 500 ms. The same initial settings for KM_0, Δf_0, δ_{CS}, φ_{RF} and the combination of TR, FA, and N, chosen from the previously described simulations for a single-component model, were used.

3.2.1.4 Experimental validation

All experiments were performed on a clinical 1.5T or 3T MR scanner (Ingenia, Philips Healthcare, Best, The Netherlands) on a calibrated phantom consisting of gel tubes with known T_1 and T_2 values (TO5, Eurospin II test system, Diagnostic Sonar Ltd, Livingston, Scotland). Twelve tubes were chosen with T_1, T_2 combinations in the following ranges: T_1 (220 - 1600 ms), T_2 (50 - 360 ms).

To investigate the performance of the method at high and low SNR levels, 3D phase-cycled bSSFP data were acquired using a 16-channel head coil (dS HeadSpine, Philips Ingenia, Best, The Netherlands) and using the integrated body coil as a receiver for high and low SNR scans, respectively. The body coil was used as a transmitter in both cases. The following sequence parameter settings were used: FOV 220x220x60 mm^3, voxel size 1.5x1.5x3 mm^3, TR = 10 ms, TE = 5 ms, FA = 30°, number of signal averages (NSA) 1, 10 RF phase increment steps with $\Delta\theta = \frac{\pi}{5}$. The total scan time was 05:55 min. Complex-valued data were acquired. To minimize transient magnetization state effects, six seconds of dummy cycles were added before each dynamic acquisition. B_1 correction was performed voxel-wise using additionally acquired B_1 map (38). The SNR was calculated using Equation [6]. The noise level was measured using a double acquisition method (39,40). ROI analysis was performed on three selected reference tubes.

3.2.2 Two-component phase-cycled bSSFP signal model

The complex phase-cycled bSSFP signal in case of two-component relaxation model can be described as a weighted complex sum of two signals, each of them described by Equations [3.1-3.3]:

$$I = w_1 I_1 + w_2 I_2 = w_1 M_{\text{eff},1} \cdot \frac{1 - a_1 e^{i\theta_1}}{1 - b_1 cos\theta_1} \cdot e^{i\varphi_1} + w_2 M_{\text{eff},2} \cdot \frac{1 - a_2 e^{i\theta_2}}{1 - b_2 cos\theta_2} \cdot e^{i\varphi_2}, \qquad [3.7]$$

where $M_{\text{eff},1}$, a_1, b_1 - are parameters describing a first component with a volume fraction of

w_1, and $M_{\text{eff},2}$, a_2, b_2 - are parameters describing a second component with a volume fraction of $w_2 = 1 - w_1$.

Human brain tissue, particularly WM, is often modeled to be a two-component non-exchanging system consisting of a dominant long T_{1L} and T_{2L} component and a smaller short T_{1S} and T_{2S} component related to the presence of myelin (20,25,41–44). The frequency distributions for both components is often taken to be Lorentzian. At 3T the dominant component is assumed to be on-resonance with a FWHM Γ_1 = 0.1 Hz, while the smaller component has average frequency shift of Δf = 20 Hz and a FWHM Γ_2 = 20 Hz (19). A volume fraction of a small component is often referred as myelin water fraction (MWF).

After substituting relaxation times and volume fractions into Equation [3.7], the signal from WM can be described as:

$$I = (1 - MWF) \cdot M_{\text{eff},L} \cdot \frac{1 - a_L e^{i(2\pi\Delta f_0 TR - \Delta\theta)}}{1 - b_L \cos(2\pi\Delta f_0 TR - \Delta\theta)} \cdot e^{i(2\pi\Delta f_0 TE + \varphi_{RF})} +$$

$$+ MWF \cdot M_{\text{eff},S} \cdot \frac{1 - a_S e^{i(2\pi(\Delta f + \Delta f_0)TR - \Delta\theta)}}{1 - b_S \cos(2\pi(\Delta f + \Delta f_0)TR - \Delta\theta)}, \qquad [3.8]$$

where $M_{\text{eff},L}$, a_L, b_L - parameters describing the dominant long component, and $M_{\text{eff},S}$, a_S, b_S − parameters describing the small component.

3.2.2.1 Accuracy and precision

The accuracy and precision were assessed using Equations [3.4, 3.5], with X_{true} − the true parameter values for the dominant component.

3.2.2.2 Numerical simulations

To assess the accuracy and precision of the parameter estimates, Monte Carlo simulations were performed for the same range of FA, TR and number N of RF phase increment steps as used in case of a single-component model. The initial parameter settings: KM_0 = 10000, Δf_0 = 10 Hz, φ_{RF} = 0. We used the average values for T_1, T_2 and a volume fraction from literature to describe the components (19,27,28,31–33): the dominant component is on-resonance and has T_{1L} = 1000 ms and T_{2L} = 80 ms, with a volume fraction of 0.88; the smaller component has shift Δf = 20 Hz, T_{1S} = 400 ms and T_{2S} = 10 ms, with a MWF of 0.12.

Gaussian noise was added independently to the real and imaginary data of the complex sum, resulting in an SNR ranging from 30 to 150. The number of performed Monte Carlo simulations was 1,000. The PLANET single-component model reconstruction was not changed and was applied to data from a two-component tissue.

Additional noise free simulations were performed to access the influence of the volume fraction, the frequency shift, and relaxation parameters of the two components on the accuracy of the method. Five different cases were simulated:

1) T_{1L} = 1000 ms and T_{2L} = 80 ms, volume fraction of 0.88;
T_{1S} = 400 ms and T_{2S} = 20 ms, volume fraction of 0.12, shift Δf = 20 Hz

2) T_{1L} = 1000 ms and T_{2L} = 80 ms, volume fraction of 0.88;
T_{1S} = 1000 ms and T_{2S} = 80 ms, volume fraction of 0.12, shift Δf = 20 Hz

3) T_{1L} = 1000 ms and T_{2L} = 80 ms, volume fraction of 0.88;
T_{1S} = 400 ms and T_{2S} = 20 ms, volume fraction of 0.12, shift Δf = 0 Hz

4) T_{1L} = 1000 ms and T_{2L} = 80 ms, volume fraction of 0.5;
T_{1S} = 400 ms and T_{2S} = 20 ms, volume fraction of 0.5, shift Δf = 0 Hz

5) T_{1L} = 1000 ms and T_{2L} = 80 ms, volume fraction of 0.5;
T_{1S} = 400 ms and T_{2S} = 20 ms, volume fraction of 0.5, shift Δf = 20 Hz

3.2.2.3 Experimental validation

To validate the simulation results for the brain tissue, experiments on 5 healthy volunteers on 3T MR scanner were performed with the following sequence parameter settings: FOV 220x220x100 mm^3, TR = 10 ms, TE = 5 ms, FA = 20°, NSA 1, parallel imaging was used with SENSE factor 2 in RL direction, N = 10 RF phase increment steps with $\Delta\theta = \frac{\pi}{5}$, voxel size 0.98x0.98x4 mm^3 with the total scan time of 6:14 min. Complex-valued data were acquired. To minimize transient effects, ten seconds of dummy cycles (1000 RF pulses) were added before each dynamic acquisition. A 2.5 ms long RF excitation pulse was used to minimize MT effects (45). B$_1$ correction was performed voxel-wise using additionally acquired B$_1$ map (38).

Reference T$_1$ and T$_2$ maps of the brain were calculated on one volunteer on 3T MR scanner. For the reference T$_1$ mapping, a 2D turbo IR-SE approach was used with TR = 7000 ms, TI = [50, 100, 200, 400, 800, 1600, 3200] ms with the following nonlinear fit of $S(TI) = \rho \left| 1 - \alpha e^{-TI/T_1} \right|$ to multi TI IR-SE data (with α related to imperfect inversion pulses). For the reference T$_2$ map, a 2D ME-SE approach was used with TR = 5000 ms, TE = [20,

40, 60, 80, 100, 120, 140, 160] ms with the following nonlinear fit of $S(TE) = \rho e^{-TE/T_2}$ to multi echo SE data using all acquired echoes.

ROI analyses were performed on the quantitative T_1 and T_2 maps calculated over five healthy volunteers on 3T. ROIs in WM (each around 70 voxels) were placed manually in frontal and occipital parts in each hemisphere. ROIs in GM (each approximately 20 voxels) were placed manually in peripheral parts in each hemisphere.

3.2.3 Gibbs ringing analysis

3.2.3.1 Numerical simulations

To investigate the influence of Gibbs ringing artifacts on parameter maps estimated using PLANET, we performed simulations using a numerical brain phantom (46). T_1, T_2, PD, and Δf_0 maps of one axial slice of the brain were generated. Using the combination of FA, TR, number N of RF phase increment steps chosen from the previously described simulations, and generated maps, the complex single-component phase-cycled bSSFP signal was calculated using the model in Equation [3.1]. Gaussian noise was added to achieve realistic SNR values, similar to those in our experimental setups (of approximately 150-200). Pseudo-infinite Cartesian k-space was generated using 2D fast Fourier transform (matrix size 1000x1000). Subsequently, different reconstructions of k-space data were performed to create Gibbs ringing artifacts of varying severity:

1. 2D inverse fast Fourier transform was performed on the fully simulated k-space. The quantitative maps were estimated using the PLANET method (no Gibbs ringing).
2. Before computing 2D inverse fast Fourier transform k-space truncation was performed, corresponding to a low-resolution acquisition matrix 132x132.
3. Before computing 2D inverse fast Fourier transform k-space truncation was performed, corresponding to a high-resolution acquisition matrix 512x512.

In case 1 there is no Gibbs ringing produced, while for cases 2 and 3 some degree of Gibbs ringing was expected and the Gibbs ringing artifact removal method based on local sub-voxel shifts, proposed by Kellner et. al (47) was applied before applying the PLANET parameter estimation method. No apodization on k-space was applied.

3.2.3.2 Experimental validation

To validate the Gibbs ringing effects, experimental 3D phase-cycled bSSFP data were acquired on the phantom and *in vivo* on the brain of a healthy volunteer on 1.5T MR scanner. Different acquisition voxel sizes were used under the same sequence parameter settings (TR, TE, FA, FOV were equal). To remove the Gibbs-ringing artifacts, a method based on resampling of the image based on local subvoxel-shifts (47) was additionally applied before performing the PLANET reconstruction for all setups. For the phantom the following sequence parameter settings were used: FOV 220x220x81 mm^3, TR = 10 ms, TE = 5 ms, FA = 30°, NSA 1, N = 10 RF phase increment steps with $\Delta\theta = \frac{\pi}{5}$, voxel size 1.96x1.96x3 mm^3 and 0.98x0.98x3 mm^3 for the low and high spatial resolution with a total scan duration of 06:03 min and 10:54 min, respectively. Six seconds of dummy cycles were added before each dynamic acquisition. For the brain the following sequence parameter settings were used: FOV 220x220x100 mm^3, TR = 10 ms, TE = 5 ms, FA = 20°, NSA 1, N = 10 RF phase increment steps with $\Delta\theta = \frac{\pi}{5}$, voxel size 1.53x1.53x4 mm^3 and 0.98x0.98x4 mm^3 for the low and high spatial resolution with the total scan time of 07:39 min and 10:59 min, respectively. To minimize transient effects, ten seconds of dummy cycles were added before each dynamic acquisition. Complex-valued data were acquired, no B_1 correction was performed for both cases.

All simulations and calculations were performed in MATLAB R2015a (The MathWorks Inc, Natick, USA).

To minimize eddy-currents effects, a linear phase-encoding profile order was used, as suggested by Bieri et al (48), for all experimental setups.

3.3 Results

3.3.1 Single-component phase-cycled bSSFP signal model

3.3.1.1 Simulation results

The ellipse fitting step is an important part of the PLANET method (17). The performance of this fitting procedure depends on the shape of the ellipse, which depends on the relaxation times but also on the chosen FA and TR combination. Figure 3.1 shows a schematic example of geometrical shape of an ellipse and its location in the complex signal plane for different FA and TR combinations for T_1 = 830 ms and T_2 = 80 ms, representing white matter at 3T. To make a comparison easier, the case of $\Delta f_0 = 0$, $\delta_{cs} = 0$, and $\varphi_{RF} = 0$ is shown,

which corresponds to the vertical form of an ellipse. For low FA the ellipse is elongated and approaches the limit case when FA = $\cos^{-1}(E_1)$, which corresponds to a collapse of an ellipse to a line (case FA = 9° and TR = 10 ms), where the ellipse fitting would fail and parameters cannot be properly estimated. This FA is the Ernst angle $FA_E = \cos^{-1}\left(\exp\left(-TR/T_1\right)\right)$. As we suggested in (17), the correct choice of FA should be done by choosing $FA > \cos^{-1}\left(\exp\left(-TR/T_{1\,shortest}\right)\right)$. For high FA the ellipse approaches a circle (where semi-axis A is equal to semi-axis B), which can be only achieved if $E_2 = 1$, or $T_2 \rightarrow \infty$, as was shown by Xiang et al in the Appendix of (34).
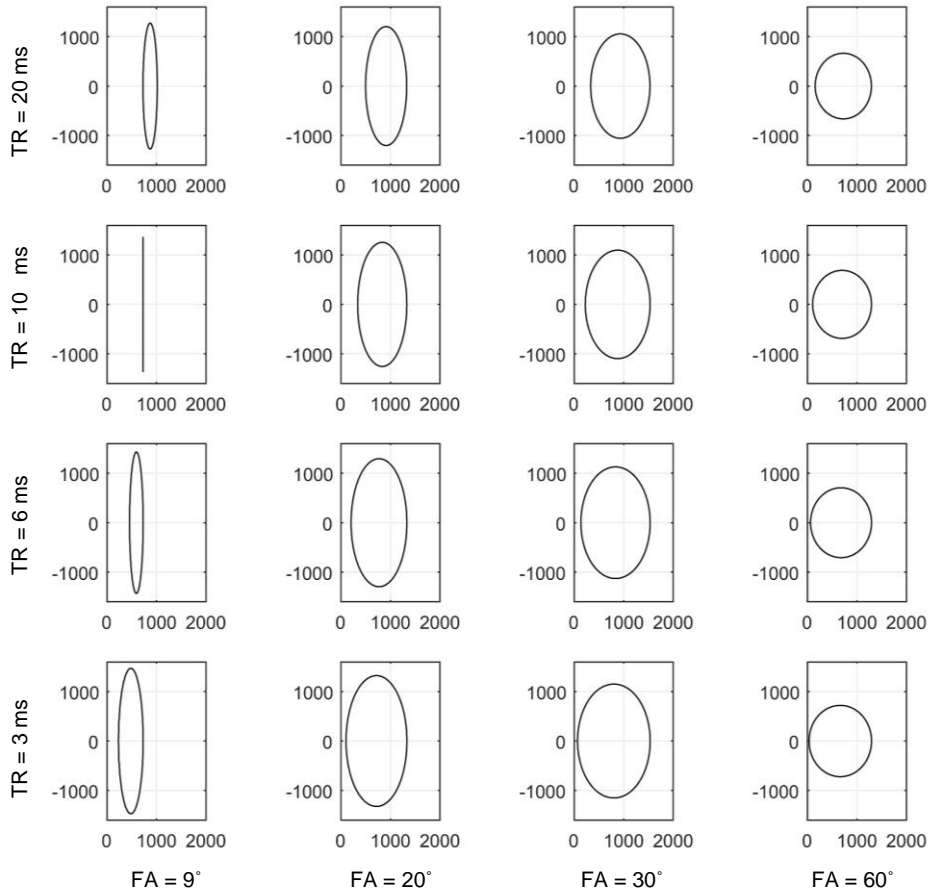
FIGURE 3.1. Illustration of the dependence of the geometrical shape and the location of an ellipse on FA and TR in the complex signal plane. Example for T_1 = 830 ms, T_2 = 80 ms. Δf_0 = 0, φ_{RF} = 0

For short TR the ellipse is located very close to the origin, in cases with considerable noise the fitting can be such that the origin is inside of the ellipse, which results in obviously erroneous negative T_1 and T_2 estimates. The use of longer TR shifts the ellipse along the real axis, avoiding the described situation, however, it also results in a longer acquisition duration. Based on these observations, we suggest the optimal elliptical shape for fitting is obtained using TR > 6 ms and FA ~ 20˚- 30˚.

An analysis of the SNR, relative errors and standard deviations in T_1, T_2, and Δf_0 estimates for a single-component WM is presented in Figure 3.2. The SNR is calculated using Equation [3.6] for different combinations of FA and TR and is shown in Figure 3.2 (a). The high SNR values can be achieved for FA in a range of 20˚- 30˚. As can be seen from Figure 3.2 (b,c), there is a broad "sweet spot" of TR and FA combinations, with high accuracy and precision in T_1, T_2, and Δf_0 estimates. A small bias in T_1, T_2 parameter estimates can be observed (see Figure 3.2 (b)). For FA > FA_E, T_1 and T_2 values are overestimated.

The distributions of the parameter estimates as a function of the number of RF phase increment steps N are compared in the boxplots in Figure 3.2 (d). Increasing the number N from 6 to 8 improves the precision in all parameter estimates, however increasing N further almost does not influence the precision in the estimates. The results of the analysis for WM at low SNR levels are presented in Supporting Figure S3.1.

The minimum SNR required to achieve a standard deviation of T_1, T_2, Δf_0 parameter estimates, equal to 5% of their mean values, is shown in Figure 3.3. It can be seen that the minimum required SNR depends on T_1 and T_2 values themselves. For example, to estimate T_1 values of around 800 ms, T_2 values of around 80 ms, and Δf_0 of around 20 Hz with 5% relative standard deviation in the corresponding parameter estimates compared to their mean values, an SNR of 80, 60, and 30 is required correspondingly.

3.3.1.2 Experimental results

Figure 3.4 (a,b) shows the phantom results at different SNR levels: SNR maps, a banding free magnitude image, T_1 and T_2 maps are presented for different coils used. The scatterplots of the parameter estimated within ROIs are shown in Figure 3.4 (c). The average calculated relaxation times for high and low SNR levels are shown as well, and they match the predictions of the performed simulations (the standard deviation in estimated parameters should be less than 5% of their mean values at high SNR and around 10-15% of their mean values at low SNR). The artifacts in T_1 maps in the background fluid are caused by the artifacts in B_1 map, which is shown in Supporting Figure S3.3.
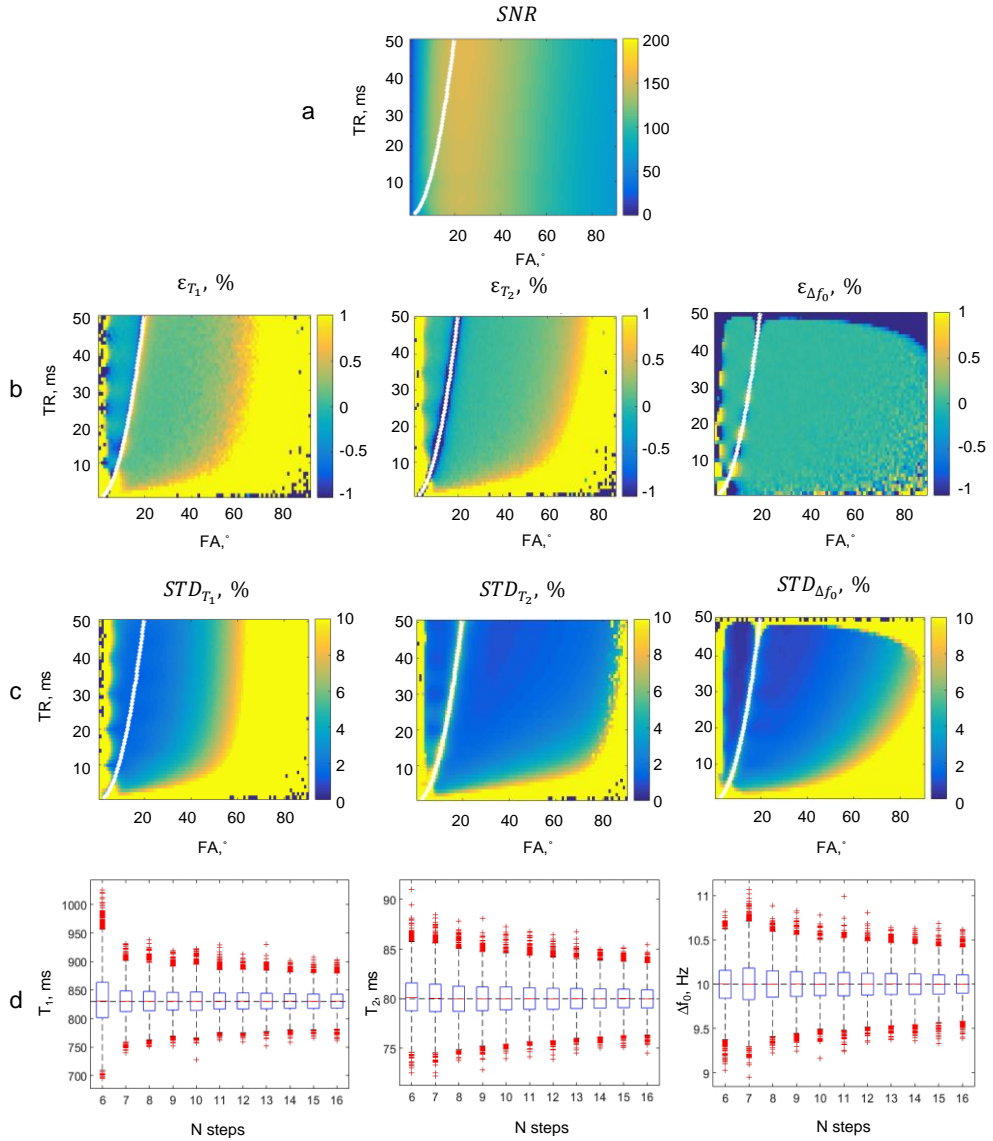
FIGURE 3.2. Simulation results for a single-component WM model at 3T (T_1 = 830 ms, T_2 = 80 ms), Δf_0 = 10 Hz. 10 RF phase increment steps: a) SNR as a function of FA and TR; b) relative errors ε (in percent) in all parameter estimates compared to their true values; c) standard deviation STD (in percent) in all parameter estimates compared to their mean values. The white line corresponds to FA = FA_E, only the region to the right is allowed; d) the distribution of all parameter estimates in the boxplots as a function of number of RF phase increment steps N. Black dashed lines correspond to the true parameter values.
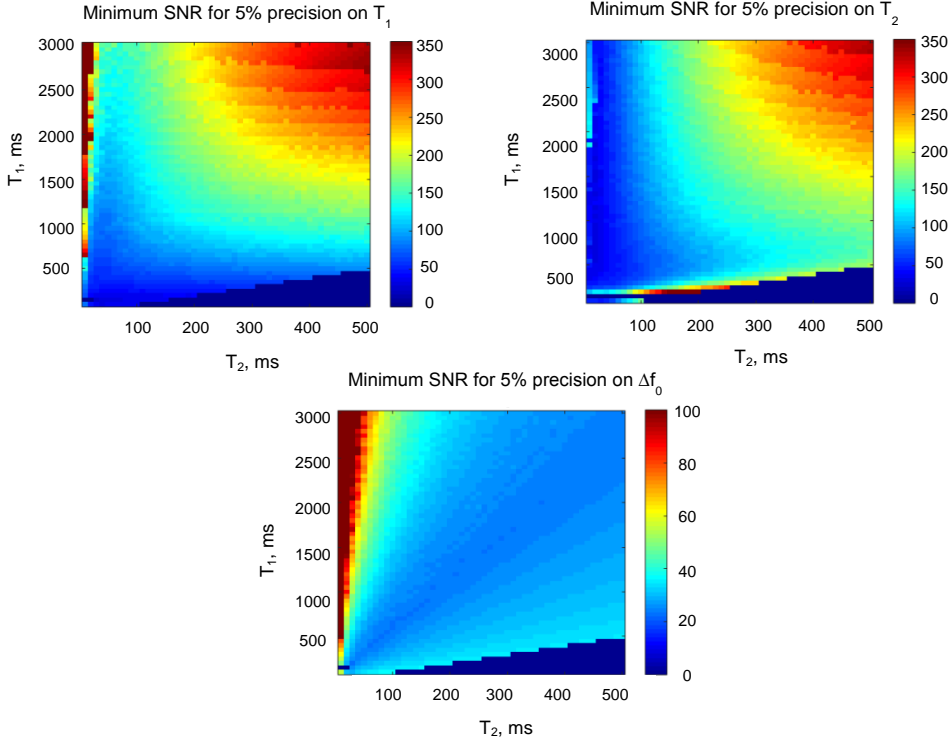
FIGURE 3.3. Minimum SNR required to achieve a precision to 5% of the mean values of the parameters T_1, T_2, Δf_0. The initial sequence parameter settings: TR = 10 ms, FA = 20°, Δf_0 = 20 Hz, N = 10 RF phase increment steps. The values $T_1 < T_2$ are excluded (blue). Note that SNR range for precision in T_1 and T_2 is saturated at 350, and in Δf_0 at 100.

3.3.2 Two-component phase-cycled bSSFP signal model

3.3.2.1 Simulation results

Figure 3.5 (a,b) shows a schematic example of an ellipse observed in case of a two-component model and corresponding frequency distributions used in the simulations. The SNR values, the relative errors, and the standard deviations in T_1, T_2, and Δf_0 estimates are presented in Figure 3.5 for a two-component model (c-e). The errors in the parameters are related to the presence of the second component and are defined as the deviation from the true values of the corresponding parameters of the dominant component. The ellipse of the smaller component interferes with the ellipse of the dominant WM component. The fitting of a single component ellipse to the complex sum of the two ellipses results in systematic underestimation of T_1 and T_2 parameters, which depends on the choice of TR and FA, as

can be seen from Figure 3.4. For example, a combination of TR = 10 ms, FA = 20° leads to underestimation in T_1 by around 30%, underestimation in T_2 by around 35%, and overestimation in Δf_0 by around 10%. However, precision of the parameter estimates stays within 3% for this range of FA-TR.
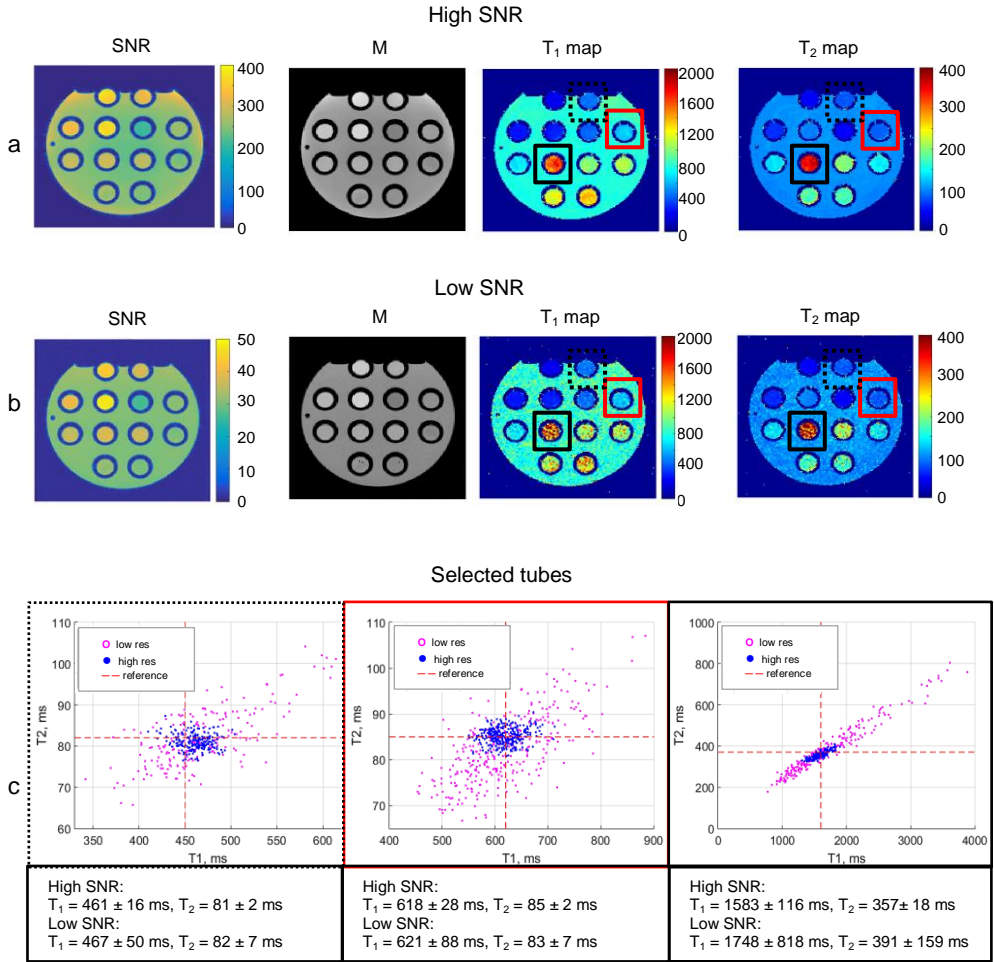
FIGURE 3.4 Experimental results from the phantom study: a) SNR map, banding free magnitude image, T_1 and T_2 maps, calculated using the PLANET method at high SNR level (using a head coil); b) SNR map, banding free magnitude image, T_1 and T_2 maps, calculated using the PLANET method at low SNR level (using the integrated body coil); c) The scatterplot of T_1-T_2 estimates over an ROI inside three selected tubes (black dashed, red solid, and black solid squares) for high and low SNR levels and the average calculated relaxation times for the selected tubes.
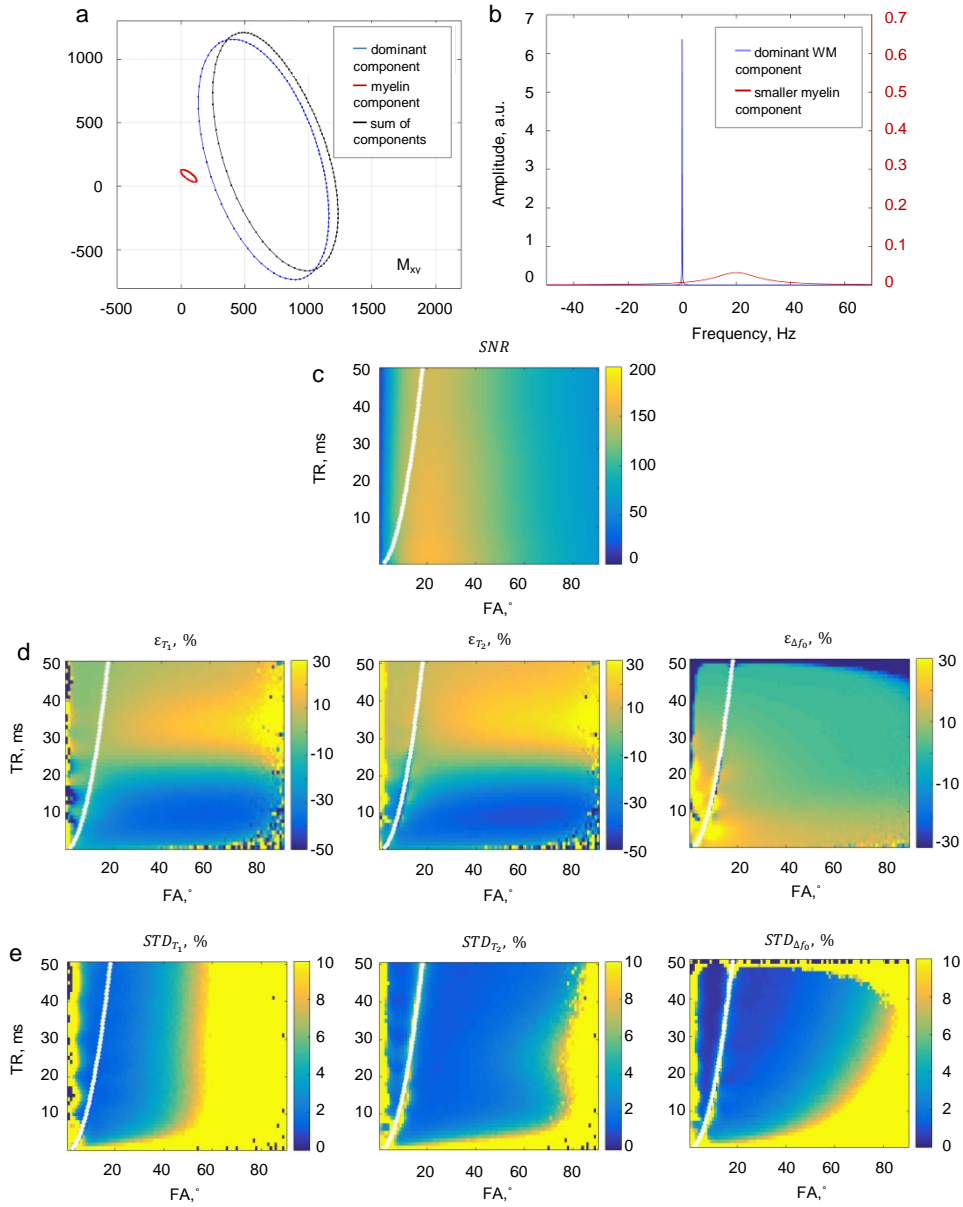
FIGURE 3.5. Simulation results for a two-component WM model at 3T (T_{1L} = 1000 ms, T_{2L} = 80 ms, T_{1S} = 400 ms, T_{2S} = 20 ms, MWF = 0.12): a) Schematic representation of the observed ellipses for TR = 10ms, FA = 20, Δf_0 = 10 Hz, φ_{RF} = 0; b) The frequency distributions for both components used in the simulations; c) SNR as a function of FA and TR; d) relative errors ε (in percent) in T_1, T_2, Δf_0 estimates compared to the true values (of the dominant component); e) standard deviation STD (in percent) in T_1, T_2, Δf_0 estimates compared to their mean values (of the dominant component). The results are presented for N = 10 RF phase increment steps used.

The relative errors in parameter estimates, simulated for different combinations of the volume fraction, frequency shift, and relaxation times of the components are shown in Supporting Figure S3.2.

The errors depend on the relaxation times of the smaller component. The case when the smaller component has shorter relaxation times is presented in Supporting Figure S3.2 (a), the results for equal relaxation times are shown in Supporting Figure S3.2 (b). The errors increase with increasing relaxation times of the smaller component.

In case if there is no frequency shift between the components, the ellipses of both components have the same orientation, and their complex sum will remain an ellipse with the same orientation and with the T_1 and T_2 in between the respective T_1 and T_2 values of both components. It is a "clear" partial volume effect in this case. Small errors in T_1 and T_2 can be observed (Supporting Figure S3.2 (c)), which increase with increasing volume fraction of the second component (Supporting Figure S3.2 (d)). Δf_0 estimates are quite accurate, which is expected due to the same orientation of both ellipses.

The biggest relative errors in estimated T_1, T_2, Δf_0 can be observed for the case of equal volume fractions of the component (which is an exaggeration of the realistic case) in combination with a frequency shift (Supporting Figure S3.2 (e)).

3.3.2.2 Experimental results

The quantitative maps calculated for human brain at 3T are shown in Figure 3.6. The reference T_1 and T_2 maps are presented for one middle axial slice. The banding free magnitude images, the maps of T_1, T_2 are shown for three axial slices. Image registration (rigid) and Gibbs ringing filtering was applied to all data before performing the PLANET reconstruction.

The estimated and reference Δf_0 maps, the estimated RF phase maps, as well as B_1 maps used for FA correction are shown in Figure 3.7 for the same three axial slices of the brain.

The results of ROI analysis are shown in Table 3.1. The reference values, calculated by placing ROIs on the reference T_1 and T_2 maps acquired on a volunteer 4, are provided for comparison, as well as the values published in literature and reviewed by Bojorquez et al (55).
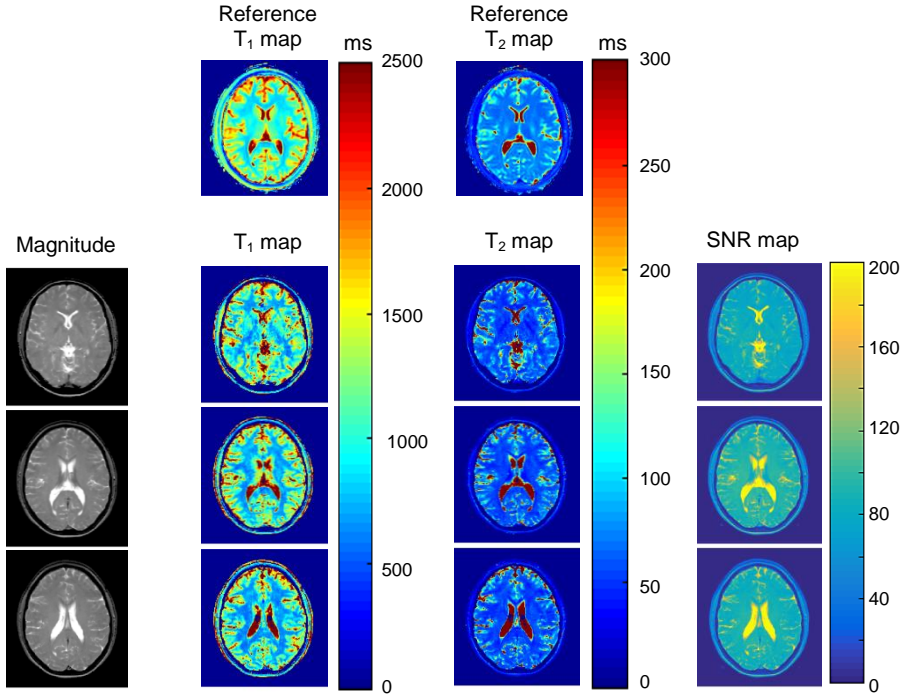
FIGURE 3.6. Experimental results from the volunteer study: Reference T_1 and T_2 maps of one axial slice of the brain, the banding free magnitude images, the estimated T_1 and T_2 maps, and calculated SNR maps for three axial slices of the brain.

3.3.3 Gibbs ringing analysis

3.3.3.1 Simulation results

Figure 3.8 shows the results of Gibbs ringing simulations on a numerical brain phantom. Banding free magnitude, T_1 and T_2 maps of one slice are presented for different reconstructions of *k*-space data. For the low acquisition matrix 132x132 the Gibbs ringing artifacts on the reconstructed quantitative maps were the most pronounced and were minimized after the correction. For high acquisition matrix 512x512 the Gibbs ringing artifacts were less visible and disappeared after the correction. The distributions of T_1 and T_2 estimates in histograms and in boxplots are shown in Supporting Figure S3.4. The results are presented for three cases: fully simulated *k*-space, truncated *k*-space to low and high acquisition matrix sizes (132^2 and 512^2 respectively). Additionally, for both truncated *k*-space cases, the Gibbs ringing correction (47) was performed after reconstruction before applying

PLANET. Visually no influence of Gibbs ringing was seen in the reconstructed off-resonance maps. For this reason, we did not include the off-resonance maps in the analysis.
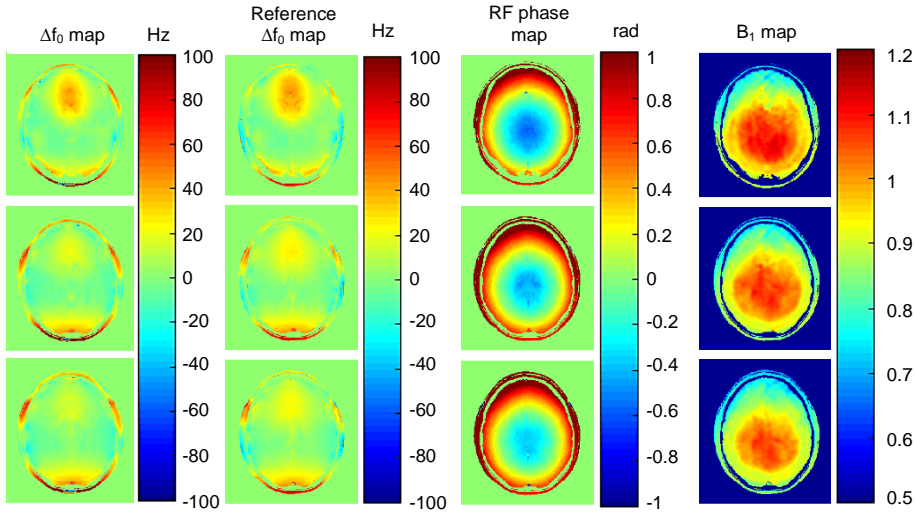
FIGURE 3.7. Experimental results from the volunteer study: the estimated and the reference off-resonance maps, the estimated RF phase maps, and the additionally acquired B_1 maps for three axial slices of the brain.

3.3.3.2 Experimental results

The quantitative maps of the phantom and the brain calculated using the PLANET method with different reconstructions of *k*-space (low and high resolution) are presented in Figure 3.9. The phantom has many sharp signal transitions and all quantitative maps, calculated from the low-resolution data suffer from severe Gibbs ringing artifacts, which are minimized after correction, see Figure 3.9 (a). Still there are inhomogeneous regions inside almost all tubes in quantitative maps. The quantitative maps, calculated from the high-resolution data do not suffer from Gibbs ringing artifacts and a minor smoothing effect can be observed after correction. As can be seen from Figure 3.9 (b), there are less sharp signal transitions in the brain compared to the phantom and Gibbs ringing almost does not affect the quantitative parameter maps.

Table 3.1. Results from *in vivo* experiments: T_1 and T_2 values determined using the PLANET method and using the reference method compared with literature published values.

Volunteer №	ROI	PLANET White matter T_1, ms	PLANET White matter T_2, ms	PLANET Grey matter T_1, ms	PLANET Grey matter T_2, ms	Literature White matter T_1, ms	Literature White matter T_2, ms	Literature Grey matter T_1, ms	Literature Grey matter T_2, ms
Volunteer 1	1	657 ± 71	54 ± 5	1128 ± 71	65 ± 5	832 ± 1 (36)	80 ± 1 (36)	1331 ± 31 (36)	110 ± 2 (36)
	2	686 ± 61	55 ± 5	1125 ± 73	68 ± 8	1084 ± 45 (22)	69 ± 3 (22)	1820 ± 114 (22)	99 ± 7 (22)
	3	640 ± 40	52 ± 4	1095 ± 99	69 ± 8	840 ± 50 (49)	75 ± 3 (50)	1600 ± 110 (49)	83 ± 4 (50)
	4	664 ± 40	51 ± 5	1056 ± 53	64 ± 5	1110 ± 40 (51)	65 ± 6 (52)	1470 ± 50 (51)	109 ± 11 (52)
	5	691 ± 45	53 ± 4			532 ± 56 (16)	44 ± 5 (16)	1061 ± 169 (16)	63 ± 12 (16)
	6	647 ± 47	51 ± 4			1085 ± 64 (53)		1717 ± 61 (53)	
Volunteer 2	7	664 ± 51	50 ± 5	1070 ± 71	64 ± 7	954 ± 39 (42)		968 ± 85 (54)	
	8	668 ± 67	54 ± 4	1172 ± 82	70 ± 6	781 ± 61 (52)			
	9	695 ± 32	53 ± 6	1102 ± 95	71 ± 10				
	10	696 ± 58	52 ± 3	1080 ± 84	60 ± 7				
	11	700 ± 38	53 ± 6						
Volunteer 3	12	664 ± 61	51 ± 6	1185 ± 84	68 ± 9	Reference values** from 2D IR-SE and 2D ME-SE			
	13	623 ± 47	51 ± 6	1082 ± 99	66 ± 12	White matter T_1, ms	White matter T_2, ms	Grey matter T_1, ms	Grey matter T_2, ms
	14	603 ± 49	50 ± 5	1129 ± 94	59 ± 12				
	15	686 ± 58	51 ± 5	1049 ± 51	63 ± 10				
	16	635 ± 58	50 ± 4	1036 ± 63	60 ± 9				
	17	678 ± 64	51 ± 5						
	18	669 ± 49	50 ± 3						
Volunteer 4	19	670 ± 37	50 ± 4	1128 ± 91	58 ± 6	824 ± 14	69 ± 3	1135 ± 34	70 ± 3
	20	661 ± 51	51 ± 4	1051 ± 90	57 ± 7	810 ± 14	70 ± 2	1132 ± 42	69 ± 3
	21	644 ± 37	53 ± 4	1076 ± 63	57 ± 5	836 ± 17	74 ± 4	1180 ± 53	74 ± 3
	22	636 ± 45	50 ± 4	1052 ± 61	58 ± 3	811 ± 24	77 ± 5	1118 ± 29	67 ± 6
	23	652 ± 36	54 ± 4			817 ± 24	74 ± 4	1170 ± 58	75 ± 5
						809 ± 29	74 ± 3	1148 ± 39	65 ± 5
Volunteer 5	24	654 ± 52	53 ± 4	1113 ± 99	70 ± 10				
	25	660 ± 45	52 ± 5	1043 ± 68	68 ± 6				
	26	687 ± 41	51 ± 5	1139 ± 99	70 ± 14				
	27	693 ± 48	51 ± 5	1110 ± 97	72 ± 15				
	28	684 ± 45	55 ± 4						
	29	659 ± 46	53 ± 4						
	30	664 ± 64	50 ± 5						
	Mean	664 ± 58	52 ± 5	1096 ± 91	65 ± 10	818 ± 21	73 ± 4	1147 ± 43	70 ± 4

*Numbers in parentheses are reference citations.
**Reference values calculated by placing ROIs on the reference T_1 and T_2 maps acquired on a Volunteer 4.
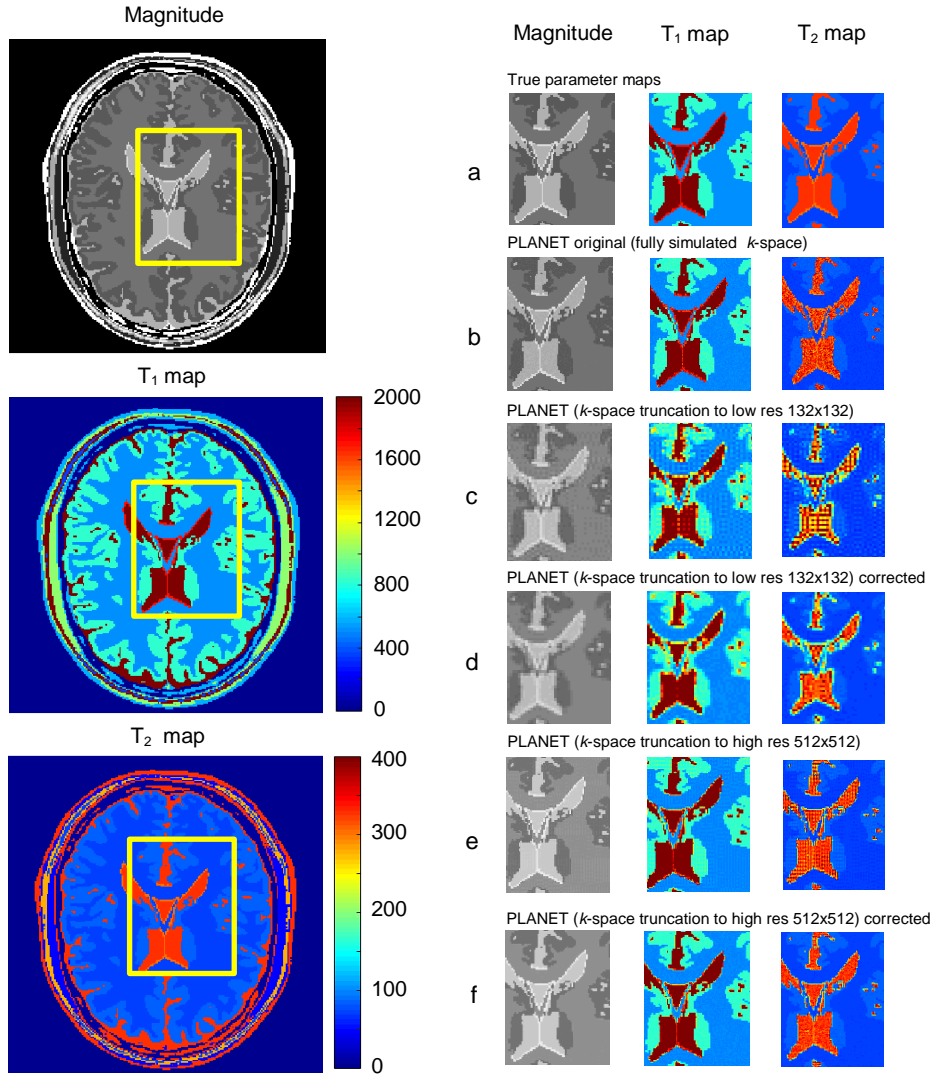
FIGURE 3.8. The results of simulations on a numerical brain phantom: banding free magnitude M, relaxation parameters T_1 and T_2 for cases: a) true parameter maps; b)-f) parameter maps calculated using PLANET: on fully simulated *k*-space (b), on truncated *k*-space to low resolution matrix 132x132 (c,d) with additionally applied Gibbs ringing correction (d), on truncated *k*-space to high resolution matrix 512x512 (e,f) with additionally applied Gibbs ringing correction (f).

FIGURE 3.9. The quantitative maps of the phantom (a) and of the brain (b), calculated using the PLANET method for low- and high-resolution scans with and without Gibbs ringing filtering.

3.4 Discussion

The proper choice of the sequence parameters such as FA, TR, and number of RF phase increment steps results in more accurate and precise estimation of the relaxation times T_1 and T_2, and the off-resonance Δf_0 using the PLANET method.

For a single-component signal model the settings of FA and TR along with the relaxation times T_1 and T_2 determine the shape of the ellipse. As can be seen from Figure 1, the ellipse should be elongated (FA of 20°- 30°) and shifted further from the origin (TR > 6 ms) to achieve robust fitting in the presence of noise. The simulation results in Figure 3.2 show, that there is a broad "sweet spot" of TR, FA, and number of RF phase increment steps with a high accuracy and precision in all parameter estimates. However, a small bias observed in T_1 and T_2 estimates (see Figure 3.2 (b)) for FA > FA_E, may be caused by the ellipse fitting method, which was shown to be biased towards smaller ellipses due to the use of algebraic distances of points (56).

The properly chosen combination of these sequence parameters should work for a wide range of relaxation times, as can be seen in Supporting Table S3.1. This can be of importance when trying to detect changes in relaxation times due to pathology in the tissues.

The combination of FA of 20°, TR of 10 ms seems to be a proper choice for a single-component signal model to estimate T_1 in the range 200 - 3000 ms, and T_2 in the range 50 - 500 ms with a high accuracy and precision at realistic SNRs. The optimal choice for TR is different compared to that for conventional bSSFP imaging, where TR is usually set to be shortest to minimize banding artifacts. Using a longer TR results in improved precision and accuracy when using PLANET, but also in more banding artifacts on the magnitude source images. However, these are successfully removed in the reconstruction of the banding free magnitude image. For these reasons, for speeding up PLANET the use of a longer TR in combination with an acceleration technique that sacrifices SNR for speed, like parallel imaging, is a better choice than to make use of a short TR.

Based upon the number of degrees of freedom in the ellipse fitting procedure, the minimally required number of RF phase increment steps is six. This would be enough for accurate parameter estimation using data without noise, but for realistic SNRs (100-250 in the performed experiments) the precision in the estimated parameters increases when the number of RF phase increment steps is increased. Interestingly, the precision does not further increase much above ten RF phase increment steps. The accuracy almost does not depend on the number of RF phase increment steps. Therefore, using eight to ten RF phase increment steps is sufficient, since using more RF phase increment steps results in a longer acquisition time and does not influence the precision.

The minimum SNR, required to achieve a precision of 5% of the mean values in T_1, T_2, and Δf_0 estimation using the optimized TR-FA-N cycles combination, is lower than that we typically obtained in the phantom (average SNR 250) for a voxel size of 1.4x1.4x3 mm^3 and *in vivo* (average SNR 150) for a voxel size of 1.5x1.5x4 mm^3. Interestingly, similar results were found in the work by Björk et al (37) for the minimum required SNR, however, they concluded that the application of their method was not feasible at common SNRs, which were rather low in their work. However, they calculated the minimum SNR to achieve the precision of 5% of the true parameter values, not the mean.

For a two-component system like WM, however, the use of the optimal parameter combination defined above, would result in underestimation of T_1 and T_2 values. Unlike a single-component relaxation model, a two-component model describes the signal as a complex sum of weighted signals from the two components with different frequency distributions and different relaxation parameters. The frequency shift between the components in combination with the difference of their volume fractions causes asymmetries in the bSSFP profile, which has an impact on the performance of the method. The ellipse of the dominant component is disturbed by the presence of the second component. Their weighted complex sum generally does not have an elliptical shape and cannot be fitted as an ellipse. However, the myelin component has shorter relaxation times and a smaller volume fraction than the main component has, and their weighted complex sum can still be fitted reasonably well as an ellipse, but with different "observed" T_1 and T_2 values.

In simulations we used the frequency shift between the dominant and myelin components Δf = 20 Hz, which is the average value between those corresponding to different tract orientation in WM at 3T: Δf = 23 ± 3 Hz ($\perp B_0$) and Δf = 17 ± 7 Hz ($\parallel B_0$) (19). We did not take into account the other sources which could contribute to the frequency shifts between the components in WM, like nonheme iron, proteins, lipids, and deoxyhemoglobin (19).

The experimentally observed in WM mean T_1 value is 664 ± 58 ms and mean T_2 value is 52 ± 5 ms. The values are underestimated by around 30% compared to the reference and literature published values (see Table 3.1). Similar underestimation of T_1 and T_2 is also observed from the simulation results (see Figure 3.5), and it depends on the choice of FA and TR. The presented results suggest that the PLANET method can be sensitive for detecting demyelination in human brain, which should be further investigated.

It might be interesting to investigate a different two-component model fitting approach for WM, which can be described with a set of 13-14 parameters (two elliptical models, each described with 6 polynomial coefficients, a certain frequency shift and the volume fraction of the smaller component). In order to solve for all of these parameters, the measurements

have to be performed at least with two or three different settings for TE and TR, maybe trying to suppress the smaller component. This different fitting approach is much more complex and goes beyond the scope of the current paper.

For a single-component model, the off-resonance maps can be calculated with a high accuracy and a high precision even at short TR (3-5 ms) for different tissue types at SNR levels $\sim$ 30. However, for a two-component model, the off-resonance maps are overestimated by around 10% (for TR ~10 ms) with a precision within 2% for a wide TR-FA range.

The truncation of *k*-space during the acquisition leads to Gibbs-ringing artifacts, the severity of which depends on the acquisition voxel size. Additionally, the use of RF phase-cycling shifts banding artifacts between acquired bSSFP phase-cycled data and leads to different Gibbs ringing appearance. As can be seen from Figure 3.8 and Supporting Figure S3.4, this effect can result in additional systematic errors in the quantitative parameters even for a properly chosen sequence parameter combination. We therefore suggest to use a high acquisition matrix in combination with a suitable method for removal of Gibbs ringing artifacts to improve the precision and accuracy of the parameter estimates, when PLANET is applied to a phantom. For *in vivo* use, a relatively high acquisition matrix should be enough to minimize Gibbs ringing artifacts.

We mostly focused on the application of PLANET in the brain, where the high SNR can be easily achieved on 1.5T or 3T clinical MR scanner with a regular coil setup, which is important for clinical use. Given the optimal settings, 1 mm^3 isotropic whole-brain T_1, T_2, M, Δf_0 mapping (with the FOV of 220x220x100 mm^3) can be performed within a 10-15-minute scan time (with SENSE factor of 2). This duration is comparable with that of DESPOT1&2 based T_1 and T_2 mapping (8,9). The clear benefit of PLANET is that in addition to quantitative T_1 and T_2 maps we can estimate the off-resonance map, the RF phase map and reconstruct the banding free magnitude image.

For applications in the abdomen, where considerable motion is present, the current implementation of the method is not fast enough. The use of a different read-out trajectory or an acceleration technique, as well as the use of a 2D approach should be investigated for the specific purpose of abdominal imaging.

RF phase maps which can be retrieved from Equation [3.3] can potentially be used for electric properties tomography (57). We did not focus on it in this study, but provided with the examples of RF phase maps in human brain (Figure 3.7).

3.5 Conclusion

In this work we show the importance of the proper choice of sequence parameter settings, such as TR, FA and number of RF phase increment steps to achieve a high accuracy and precision in quantitative parameter estimation using the PLANET method at realistic SNR levels. Interestingly, this combination holds over a wide range of relaxation times and does not require an exact prior knowledge of T_1 and T_2 of the tissue. However, the PLANET model assumes a single-peak frequency distribution, which is not the case for some biological tissues, like human brain WM tissue, fat tissues, or bone marrow. The presence of second or more components influences the performance of the method and leads to systematic errors in the parameter estimates, which depend on the choice of FA and TR.

Using a high acquisition matrix in combination with a suitable method for removal of Gibbs ringing artifacts improves the precision and accuracy of the parameter estimates, when PLANET is applied to a phantom with sharp signal intensity edges. For *in vivo* use, a relatively high acquisition matrix should be enough to minimize Gibbs ringing artifacts.

This evaluation of the accuracy and precision of PLANET should guide researchers who want to apply the method for different applications.
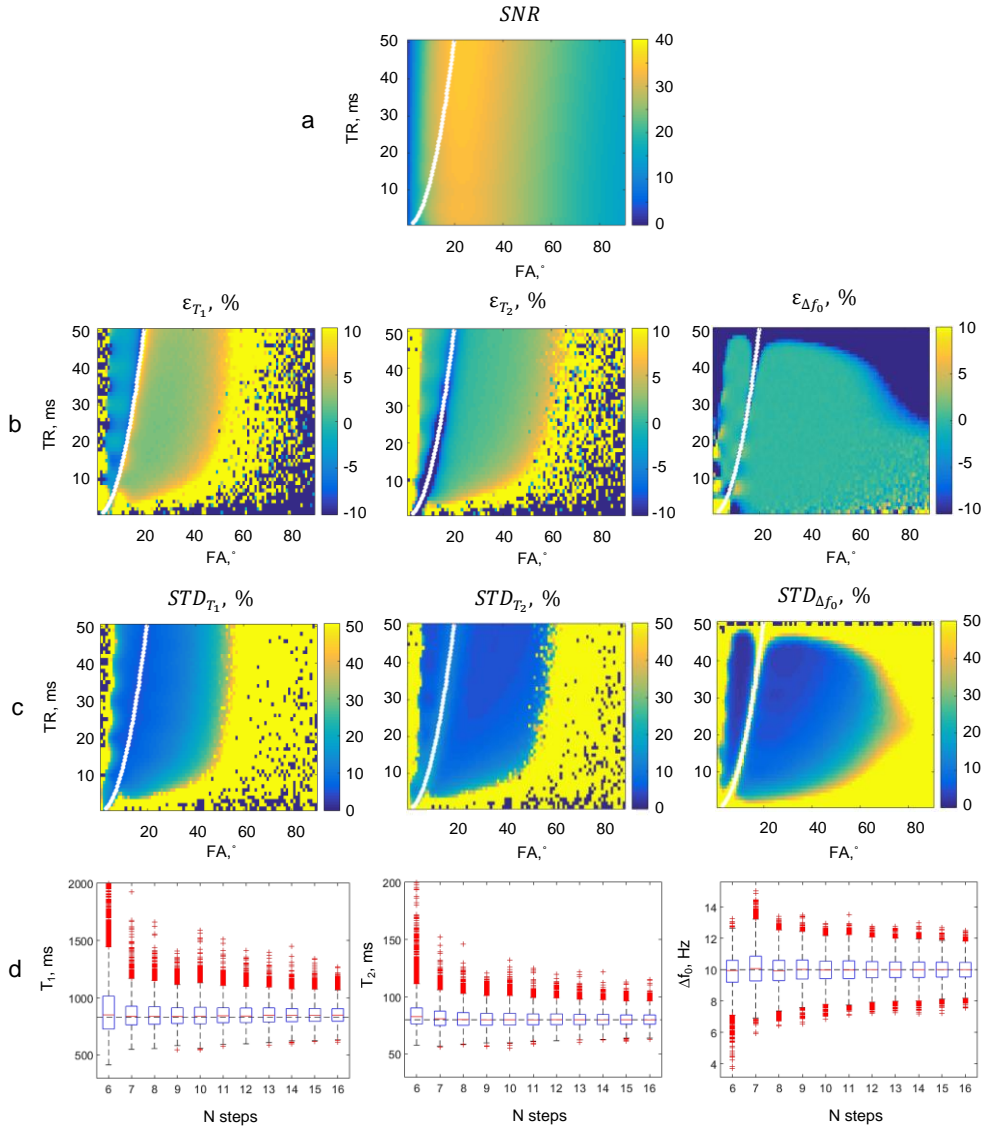
SUPPORTING FIGURE S3.1. Simulation results at low SNR levels for a single-component WM model at 3T (T_1 = 830 ms, T_2 = 80 ms), Δf_0 = 10 Hz: a) SNR as a function of FA and TR; b) relative errors ε (in percent) in the parameter estimates compared to their true values; c) standard deviation STD (in percent) in the parameter estimates compared to their mean values. The white line corresponds to FA = FA_E, only the region to the right is allowed; d) the distribution of the parameter estimates in the boxplots as a function of number of RF phase increment steps N. Black dashed lines correspond to the true parameter values.
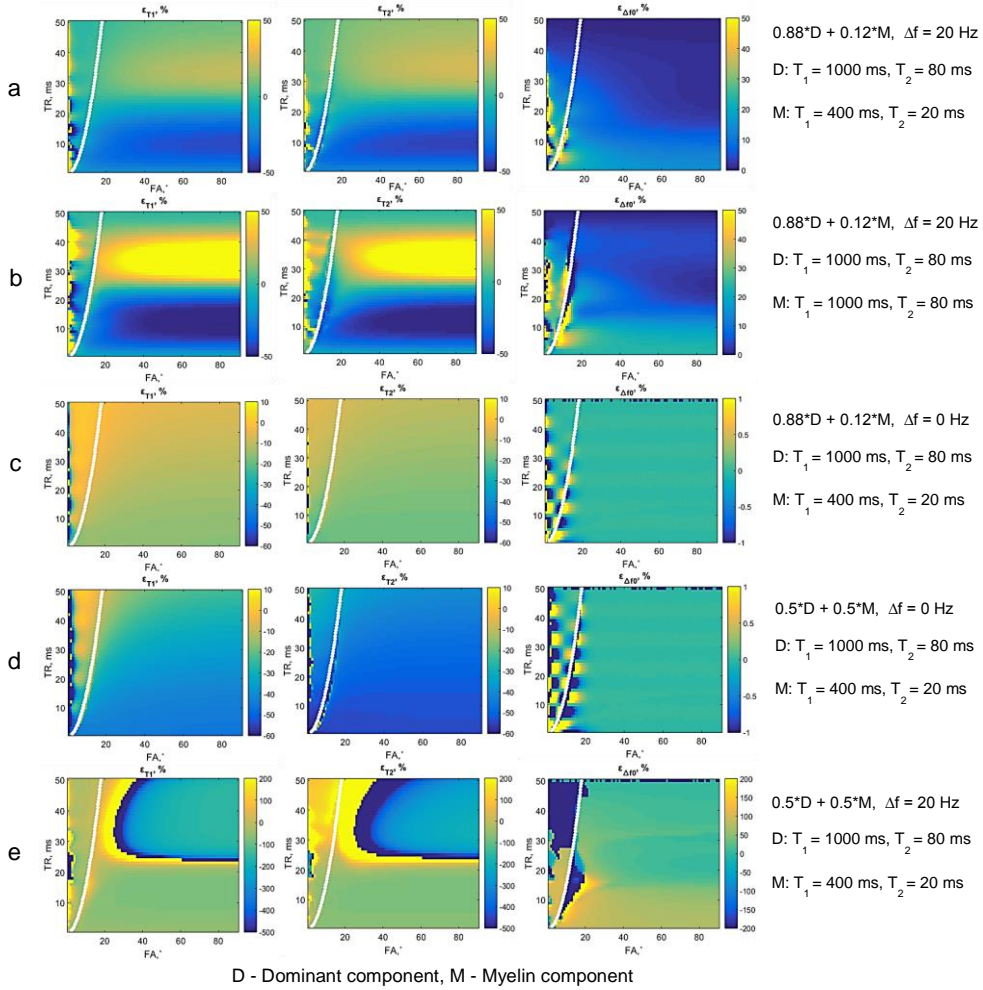
SUPPORTING FIGURE S3.2. Noise free simulation results for a two-component WM model. The relative errors ε (in percent) in the parameter estimates compared to their true values (of the dominant component) for the cases: a) Dominant component (D) has $T_{1L} = 1000$ ms and $T_{2L} = 80$ ms, volume fraction of 0.88; myelin component (M) has $T_{1s} = 400$ ms and $T_{2s} = 20$ ms, volume fraction of 0.12, shift $\Delta f = 20$ Hz; b) Dominant component (D) has $T_{1L} = 1000$ ms and $T_{2L} = 80$ ms, volume fraction of 0.88; myelin component (M) has $T_{1s} = 1000$ ms and $T_{2s} = 80$ ms, volume fraction of 0.12, shift $\Delta f = 20$ Hz; c) Dominant component (D) has $T_{1L} = 1000$ ms and $T_{2L} = 80$ ms, volume fraction of 0.88; myelin component (M) has $T_{1s} = 400$ ms and $T_{2s} = 20$ ms, volume fraction of 0.12, shift $\Delta f = 0$ Hz; d) Dominant component (D) has $T_{1L} = 1000$ ms and $T_{2L} = 80$ ms, volume fraction of 0.5; myelin component (M) has $T_{1s} = 400$ ms and $T_{2s} = 20$ ms, volume fraction of 0.5, shift $\Delta f = 0$ Hz; e) Dominant component (D) has $T_{1L} = 1000$ ms and $T_{2L} = 80$ ms, volume fraction of 0.5; myelin component (M) has $T_{1s} = 400$ ms and $T_{2s} = 20$ ms, volume fraction of 0.5, shift $\Delta f = 20$ Hz. Note that the colorbars are scaled differently.

SUPPORTING TABLE S3.1. The optimal parameter settings and minimum required SNR for different relaxation times combinations for a single-component signal model.

T_1 (msec)	T_2 (msec)	Optimal parameter settings		Minimum required SNR for 5% precision
		TR (msec)	FA (°)	
200	50	6-10	25-35	55
500	50	6-10	20-30	60
800	75	8-10	15-30	80
1000	120	8-10	15-30	105
1500	80	8-10	15-30	110
2000	300	10-15	15-25	230
3000	500	10-15	15-25	330
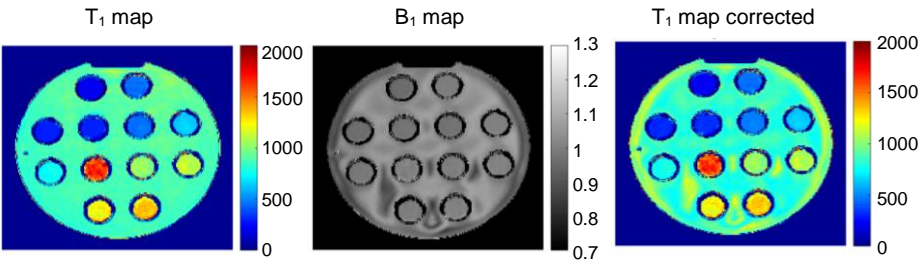
SUPPORTING FIGURE S3.3 Experimental results from the phantom study: T_1 map calculated using the PLANET method at high SNR level, additionally acquired B_1 map for correction, and T_1 map corrected using the B_1 map.
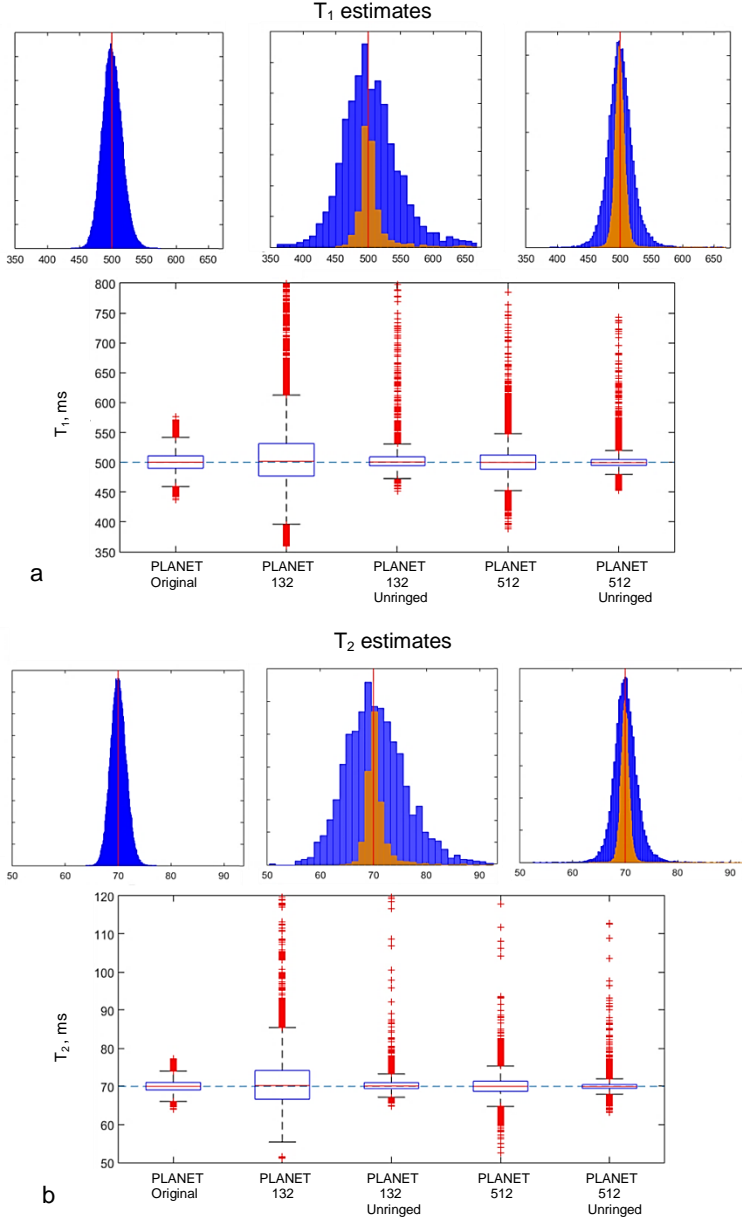
SUPPORTING FIGURE S3.4. Additional results of simulations on a numerical brain phantom: a) the distribution of T_1 estimates in histograms and boxplots for WM for different reconstruction of simulated *k*-space. The blue bars correspond to the results without Gibbs ringing correction, the orange bars – after Gibbs ringing correction applied. The red line is the true parameter value; b) the distribution of T_2 estimates in histograms and boxplots for WM for different reconstruction of simulated *k*-space. The blue bars correspond to the results without Gibbs ringing correction, the orange bars – after Gibbs ringing correction applied. The red line is the true parameter value.

3.6 References

1. Cheng HL, Stikov N, Ghugre NR, Wright GA. Practical medical applications of quantitative MR relaxometry. J. Magn. Reson. Imaging 2012;36:805–824. doi: 10.1002/jmri.23718.

2. Riederer SJ, Lee JN, Farzaneh F, Wang HZ, Wright RC. Magnetic resonance image synthesis. Clinical implementation. Acta Radiol. 1986;369:466–468.

3. Blystad I, Warntjes J, Smedby O, Landtblom A-M, Lundberg P, Larsson E-M. Synthetic MRI of the brain in a clinical setting. Acta radiol. 2012;53:1158–1163. doi: 10.1258/ar.2012.120195.

4. Ma D, Gulani V, Seiberlich N, Liu K, Sunshine JL, Duerk JL, Griswold MA. Magnetic resonance fingerprinting. Nature 2013;495:187–192. doi: 10.1038/nature11971.

5. Bernstein MA, King KF, Zhou XJ. Handbook of MRI Pulse Sequences. 2004. doi: 10.1016/B978-0-12-092861-3.X5000-6.

6. Look DC, Locker DR. Time saving in measurement of NMR and EPR relaxation times. Rev. Sci. Instrum. 1970;41:250–251. doi: 10.1063/1.1684482.

7. Homer J, Beevers MS. Driven-equilibrium single-pulse observation of T1 relaxation. A reevaluation of a rapid "new" method for determining NMR spin-lattice relaxation times. J. Magn. Reson. 1985;63:287–297. doi: 10.1016/0022-2364(85)90318-X.

8. Deoni SCL, Rutt BK, Peters TM. Rapid combined T1 and T2 mapping using gradient recalled acquisition in the steady state. Magn. Reson. Med. 2003;49:515–526. doi: 10.1002/mrm.10407.

9. Deoni SCL. High-resolution T1 mapping of the brain at 3T with driven equilibrium single pulse observation of T1 with high-speed incorporation of RF field inhomogeneities (DESPOT1-HIFI). J. Magn. Reson. Imaging 2007;26:1106–1111. doi: 10.1002/jmri.21130.

10. Welsch GH, Scheffler K, Mamisch TC, Hughes T, Millington S, Deimling M, Trattnig S. Rapid estimation of cartilage T2 based on double echo at steady state (DESS) with 3 Tesla. Magn. Reson. Med. 2009;62:544–549. doi: 10.1002/mrm.22036.

11. Heule R, Ganter C, Bieri O. Triple echo steady-state (TESS) relaxometry. Magn. Reson. Med. 2014;71:230–237. doi: 10.1002/mrm.24659.

12. Scheffler K, Hennig J. T1 quantification with inversion recovery TrueFISP. Magn. Reson. Med. 2001;45:720–723. doi: 10.1002/mrm.1097.

13. Deoni SCL, Ward HA, Peters TM, Rutt BK. Rapid T2 estimation with phase-cycled variable nutation steady-state free precession. Magn. Reson. Med. 2004;52:435–439. doi: 10.1002/mrm.20159.

14. Deoni SCL. Transverse relaxation time (T2) mapping in the brain with off-resonance correction using phase-cycled steady-state free precession imaging. J. Magn. Reson.

Imaging 2009;30:411–417. doi: 10.1002/jmri.21849.

15. Schmitt P, Griswold MA, Jakob PM, Kotas M, Gulani V, Flentje M, Haase A. Inversion recovery TrueFISP: quantification of T(1), T(2), and spin density. Magn. Reson. Med. 2004;51:661–7. doi: 10.1002/mrm.20058.

16. Nguyen D, Bieri O. Motion-insensitive rapid configuration relaxometry. Magn. Reson. Med. 2016. doi: 10.1002/mrm.26384.

17. Shcherbakova Y, van den Berg CAT, Moonen CTW, Bartels LW. PLANET: An ellipse fitting approach for simultaneous T1 and T2 mapping using phase-cycled balanced steady-state free precession. Magn. Reson. Med. 2018;79:711–722. doi: 10.1002/mrm.26717.

18. Miller KL. Asymmetries of the balanced SSFP profile. Part I: Theory and Observation. Magn. Reson. Med. 2010;63:385–395. doi: 10.1002/mrm.22212.

19. Miller KL, Smith SM, Jezzard P. Asymmetries of the balanced SSFP profile. Part II: White matter. Magn. Reson. Med. 2010;63:396–406. doi: 10.1002/mrm.22249.

20. Does MD, Beaulieu C, Allen PS, Snyder RE. Multi-component T1 relaxation and magnetisation transfer in peripheral nerve. Magn. Reson. Imaging 1998;16:1033–1041. doi: 10.1016/S0730-725X(98)00139-8.

21. Laule C, Vavasour IM, Moore GRW, Oger J, Li DKB, Paty DW, MacKay AL. Water content and myelin water fraction in multiple sclerosis. A T2 relaxation study. J. Neurol. 2004;251:284–93. doi: 10.1007/s00415-004-0306-6.

22. Stanisz GJ, Odrobina EE, Pun J, Escaravage M, Graham SJ, Bronskill MJ, Henkelman RM. T1, T2 relaxation and magnetization transfer in tissue at 3T. Magn. Reson. Med. 2005;54:507–512. doi: 10.1002/mrm.20605.

23. Oh J, Han ET, Pelletier D, Nelson SJ. Measurement of in vivo multi-component T2 relaxation times for brain tissue using multi-slice T2 prep at 1.5 and 3 T. Magn. Reson. Imaging 2006;24:33–43. doi: 10.1016/j.mri.2005.10.016.

24. Laule C, Vavasour IM, Kolind SH, Li DKB, Traboulsee TL, Moore GRW, MacKay AL. Magnetic Resonance Imaging of Myelin. Neurotherapeutics 2007;4:460–484. doi: 10.1016/j.nurt.2007.05.004.

25. Deoni SCL, Rutt BK, Arun T, Pierpaoli C, Jones DK. Gleaning multicomponent T1 and T2 information from steady-state imaging data. Magn. Reson. Med. 2008;60:1372–1387. doi: 10.1002/mrm.21704.

26. Kolind SH, Mädler B, Fischer S, Li DKB, MacKay AL. Myelin water imaging: Implementation and development at 3.0T and comparison to 1.5T measurements. Magn. Reson. Med. 2009;62:106–115. doi: 10.1002/mrm.21966.

27. Prasloski T, Rauscher A, MacKay AL, Hodgson M, Vavasour IM, Laule C, Mädler B. Rapid whole cerebrum myelin water imaging using a 3D GRASE sequence. Neuroimage

2012;63:533–539. doi: 10.1016/j.neuroimage.2012.06.064.

28. Labadie C, Lee JH, Rooney WD, Jarchow S, Aubert-Frécon M, Springer CS, Möller HE. Myelin water mapping by spatially regularized longitudinal relaxographic imaging at high magnetic fields. Magn. Reson. Med. 2014;71:375–387. doi: 10.1002/mrm.24670.

29. Zhang J, Kolind SH, Laule C, Mackay AL. Comparison of myelin water fraction from multiecho T2 decay curve and steady-state methods. Magn. Reson. Med. 2015;73:223–232. doi: 10.1002/mrm.25125.

30. Bouhrara M, Spencer RG. Improved determination of the myelin water fraction in human brain using magnetic resonance imaging through Bayesian analysis of mcDESPOT. Neuroimage 2016;127:456–471. doi: 10.1016/j.neuroimage.2015.10.034.

31. Rioux JA, Levesque IR, Rutt BK. Biexponential longitudinal relaxation in white matter: Characterization and impact on T1 mapping with IR-FSE and MP2RAGE. Magn. Reson. Med. 2016;75:2265–2277. doi: 10.1002/mrm.25729.

32. Bouhrara M, Spencer RG. Rapid simultaneous high-resolution mapping of myelin water fraction and relaxation times in human brain using BMC-mcDESPOT. Neuroimage 2017;147:800–811. doi: 10.1016/j.neuroimage.2016.09.064.

33. Alonso-Ortiz E, Levesque IR, Pike GB. MRI-based myelin water imaging: A technical review. Magn. Reson. Med. 2015;73:70–81. doi: 10.1002/mrm.25198.

34. Xiang QS, Hoff MN. Banding artifact removal for bSSFP imaging with an elliptical signal model. Magn. Reson. Med. 2014;71:927–933. doi: 10.1002/mrm.25098.

35. Lauzon M. Louis, Frayne R. Analytical Characterization of RF Phase-Cycled Balanced Steady-State Free Precession. Concepts Magn. Reson. Part A 2009;34A:133–143. doi: 10.1002/cmr.a.20138.

36. Wansapura JP, Holland SK, Dunn RS, Ball WS. NMR relaxation times in the human brain at 3.0 Tesla. J. Magn. Reson. Imaging 1999;9:531–538. doi: 10.1002/(SICI)1522-2586(199904).

37. Björk M, Ingle RR, Gudmundson E, Stoica P, Nishimura DG, Barral JK. Parameter estimation approach to banding artifact reduction in balanced steady-state free precession. Magn. Reson. Med. 2014;72:880–892. doi: 10.1002/mrm.24986.

38. Yarnykh VL. Actual flip-angle imaging in the pulsed steady state: A method for rapid three-dimensional mapping of the transmitted radiofrequency field. Magn. Reson. Med. 2007;57:192–200. doi: 10.1002/mrm.21120.

39. Sijbers J, Den Dekker AJ, Van Audekerke J, Verhoye M, Van Dyck D. Estimation of the noise in magnitude MR images. Magn. Reson. Imaging 1998;16:87–90. doi: 10.1016/S0730-725X(97)00199-9.

40. Firbank MJ, Coulthard A, Harrison RM, Williams ED. A comparison of two methods for

measuring the signal to noise ratio on MR images. Phys. Med. Biol. 1999;44:N261–N264. doi: 10.1088/0031-9155/44/12/403.

41. Kroeker RM, Mark Henkelman R. Analysis of biological NMR relaxation data with continuous distributions of relaxation times. J. Magn. Reson. 1986;69:218–235. doi: 10.1016/0022-2364(86)90074-0.

42. Preibisch C, Deichmann R. Influence of RF spoiling on the stability and accuracy of T1 mapping based on spoiled FLASH with varying flip angles. Magn. Reson. Med. 2009;61:125–135. doi: 10.1002/mrm.21776.

43. Whittall KP, Mackay AL, Graeb DA, Nugent RA, Li DKB, Paty DW. In vivo measurement of T2 distributions and water contents in normal human brain. Magn. Reson. Med. 1997;37:34–43. doi: 10.1002/mrm.1910370107.

44. Stanisz GJ, Kecojevic A, Bronskill MJ, Henkelman RM. Characterizing white matter with magnetization transfer and T2. Magn. Reson. Med. 1999;42:1128–1136. doi: 10.1002/(SICI)1522-2594(199912)42:6<1128::AID-MRM18>3.0.CO;2-9.

45. Bieri O, Scheffler K. Optimized balanced steady-state free precession magnetization transfer imaging. Magn Reson Med 2007;58:511–518. doi: 10.1002/mrm.21326.

46. Aubert-Broche B, Evans AC, Collins L. A new improved version of the realistic digital brain phantom. Neuroimage 2006;32:138–145. doi: 10.1016/j.neuroimage.2006.03.052.

47. Kellner E, Dhital B, Kiselev VG, Reisert M. Gibbs-ringing artifact removal based on local subvoxel-shifts. Magn. Reson. Med. 2016;76:1574–1581. doi: 10.1002/mrm.26054.

48. Bieri O, Markl M, Scheffler K. Analysis and compensation of eddy currents in balanced SSFP. Magn. Reson. Med. 2005;54:129–137. doi: 10.1002/mrm.20527.

49. Wright PJ, Mougin OE, Totman JJ, et al. Water proton T1 measurements in brain tissue at 7, 3, and 1.5 T using IR-EPI, IR-TSE, and MPRAGE: results and optimization. MAGMA 2008;21:121–130. doi: 10.1007/s10334-008-0104-8.

50. Lu H, Nagae-Poetscher LM, Golay X, Lin D, Pomper M, Van Zijl PCM. Routine clinical brain MRI sequences for use at 3.0 tesla. J. Magn. Reson. Imaging 2005;22:13–22. doi: 10.1002/jmri.20356.

51. Ethofer T, Mader I, Seeger U, Helms G, Erb M, Grodd W, Ludolph A, Klose U. Comparison of Longitudinal Metabolite Relaxation Times in Different Regions of the Human Brain at 1.5 and 3 Tesla. Magn. Reson. Med. 2003;50:1296–1301. doi: 10.1002/mrm.10640.

52. Jiang Y, Ma D, Seiberlich N, Gulani V, Griswold MA. MR fingerprinting using fast imaging with steady state precession (FISP) with spiral readout. Magn. Reson. Med. 2015;74:1621–1631. doi: 10.1002/mrm.25559.

53. Cheng HLM, Wright GA. Rapid high-resolution T1 mapping by variable flip angles: Accurate and precise measurements in the presence of radiofrequency field inhomogeneity.

Magn. Reson. Med. 2006;55:566–574. doi: 10.1002/mrm.20791.

54. Dieringer MA, Deimling M, Santoro D, Wuerfel J, Madai VI, Sobesky J, Von Knobelsdorff-Brenkenhoff F, Schulz-Menger J, Niendorf T. Rapid parametric mapping of the longitudinal relaxation time T1 using two-dimensional variable flip angle magnetic resonance imaging at 1.5 Tesla, 3 Tesla, and 7 Tesla. PLoS One 2014;9. doi: 10.1371/journal.pone.0091318.

55. Bojorquez JZ, Bricq S, Acquitter C, Brunotte F, Walker PM, Lalande A. What are normal relaxation times of tissues at 3 T? Magn. Reson. Imaging 2017;35:69–80. doi: 10.1016/j.mri.2016.08.021.

56. Hal R, Flusser J. Numerically stable direct least squares fitting of ellipses. Proc. 6th Int. Conf. Cent. Eur. Comput. Graph. Vis. 1998;98:125–132. doi: 10.1109/34.765658.

57. Katscher U, van den Berg CAT. Electric properties tomography: Biochemical, physical and technical background, evaluation and clinical applications. NMR Biomed. 2017;30. doi: 10.1002/nbm.3729.

Chapter 4

Investigation of the influence of B$_0$ drift on the performance of the PLANET method and an algorithm for drift correction

ABSTRACT

Purpose:

The PLANET method was designed to simultaneously reconstruct maps of T_1 and T_2, the off-resonance, the RF phase, and the banding free signal magnitude. The method requires a stationary B_0 field over the course of a phase-cycled bSSFP acquisition. In this work we investigated the influence of B_0 drift on the performance of PLANET method for single-component and two-component signal models, and we propose a strategy for drift correction.

Methods:

The complex phase-cycled bSSFP signal was modeled with and without frequency drift. The behavior of the signal influenced by drift was mathematically interpreted as a sum of drift-dependent displacement of the data points along an ellipse and drift-dependent rotation around the origin. The influence of drift on parameter estimates was investigated experimentally on a phantom and on the brain of healthy volunteers, and was verified by numerical simulations. A drift correction algorithm was proposed and tested on a phantom and *in vivo*.

Results:

Drift can be assumed to be linear over the typical duration of a PLANET acquisition. In a phantom (a single-component signal model) drift induced errors of 4% and 8% in the estimated T_1 and T_2 values. In the brain, where multiple components are present, drift only had a minor effect. For both single-component and two-component signal models, drift-induced errors were successfully corrected by applying the proposed drift correction algorithm.

Conclusion:

We have demonstrated theoretically and experimentally the sensitivity of PLANET method to B_0 drift and have proposed a drift correction method.

Key words: B_0 drift, PLANET, quantitative MRI, relaxometry

4.1 Introduction

Quantitative Magnetic Resonance Imaging (QMRI) is widely used to obtain quantitative characteristics of tissues related to their biological and physiological properties, based on which tissues can be differentiated and associated with specific diseases. The measurement of the relaxation times of tissues (or quantitative relaxometry) is particularly important for clinical applications in oncology and regenerative medicine (1). Many different techniques exist for quantitative relaxometry, such as standard inversion-recovery (IR) and multi-echo spin-echo based approaches (2–4), many rapid steady-state free precession approaches, like IR TrueFISP (5,6), the variable flip angle approach, or DESPOT1&2 (7–9), the triple echo steady-state approach, or TESS (10), the MR fingerprinting approach (11), and many others.

We recently introduced a method called PLANET to simultaneously reconstruct maps of the relaxation times T_1 and T_2, the local off-resonance Δf_0, the RF phase, and the banding free signal magnitude, using phase-cycled balanced steady-state free precession (bSSFP) data (12). The method is based on linear least squares fitting of an ellipse to phase-cycled bSSFP data in the complex signal plane and subsequent analytical parameter estimation from the fitting results.

A bSSFP signal is strongly dependent on local resonant frequency, and the use of RF phase cycling shifts the off-resonance profile of the signal dependent on the RF phase increment. The main requirement of the PLANET model is a stationary main magnetic field (B_0) over the course of the acquisition, which usually consists of 8-10 dynamics and takes around 10 min for full brain coverage with FOV 220x220x100 mm^3, and voxel size 1x1x4 mm^3 (without any acceleration technique). In this case, accurate and precise parameter estimation can be achieved for a single-component voxel, as we showed in a previous study (13), whereas systematic errors in parameter estimates are expected when multiple signal components with different relaxation times and frequencies are present within a voxel (13).

Due to intensive gradient activity, the requirement of a stationary B_0 field can be difficult to meet, and as a result, B_0 drift can occur, which might result in errors in the estimated parameters. The severity of drift effect depends on the field strength, history of gradient activity and heating of metallic components of the scanner, the acquisition time, the used gradient mode, shimming, etc., which vary among different systems and over time.

The purpose of this work was to investigate the effects of B_0 drift and to assess the influence of drift on the quantitative parameters estimated using the PLANET method. We first derived a geometrical interpretation of the influence of drift on a single-component phase-cycled bSSFP signal based on a mathematical model. Subsequently, based on this geometrical interpretation, we developed a strategy for drift correction. Next, we

experimentally showed the influence of drift on the parameter estimates for a single-component model in a phantom and for a two-component model of white matter (WM) in the human brain. We assessed the effects of drift for both single-component and two-component signal models, and evaluated the performance of the drift correction algorithm in both cases by looking at drift-induced errors in the quantitative parameter estimates. Finally, we performed numerical simulations for both single-component and two-component signal models to verify the experimental results.

4.2 Methods

4.2.1 How drift influences a single-component phase-cycled bSSFP signal

For a single-component model with mono-exponential transverse and longitudinal relaxation, the complex phase-cycled bSSFP signal can be represented as an ellipse in the complex plane (14,15) as

$$I = M_{\text{eff}} \frac{1 - ae^{i(\theta_0 - \Delta\theta)}}{1 - b\cos(\theta_0 - \Delta\theta)} e^{i\varphi}, \qquad [4.1]$$

where M_{eff}, a, and b are parametric functions of T_1, T_2, TR, and FA. $\Delta\theta$ is the user-controlled RF phase increment (rad), $\varphi = 2\pi(\delta_{CS} + \Delta f_0)TE + \varphi_{RF}$ is the rotation angle of the ellipse around the origin with respect to its vertical form (14), $\theta_0 = 2\pi(\delta_{CS} + \Delta f_0)TR$, Δf_0 is the local off-resonance (Hz), φ_{RF} is the combined RF transmit and receive phase, δ_{CS} is the chemical shift of the species (Hz) with respect to the water peak. After substitution, Equation [4.1] can be rewritten as

$$I = M_{\text{eff}} \frac{1 - ae^{i(2\pi(\delta_{CS} + \Delta f_0)TR - \Delta\theta)}}{1 - b\cos(2\pi(\delta_{CS} + \Delta f_0)TR - \Delta\theta)} e^{i(2\pi(\delta_{CS} + \Delta f_0)TE + \varphi_{RF})} \qquad [4.2]$$

A graphical representation of the ellipse described by this equation in the complex plane is shown in Figure 4.1 (a).

With frequency drift modeled as $\Delta f_0 \rightarrow \Delta f_0 + \Delta f_{\text{drift}}(t)$, where $\Delta f_{\text{drift}}(t)$ is the time-dependent frequency drift during PLANET acquisition, and is equal to $\gamma \Delta B_0(t)$, where γ is the gyromagnetic ratio equal to 42.58 MHz/T. Then Equation [4.2] becomes

$$I = M_{\text{eff}} * \frac{1 - ae^{i(2\pi(\delta_{CS}+\Delta f_0)TR - \Delta\theta + 2\pi TR\Delta f_{\text{drift}}(t))}}{1 - b\cos(2\pi(\delta_{CS} + \Delta f_0)TR - \Delta\theta + 2\pi TR\Delta f_{\text{drift}}(t))} * e^{i(2\pi(\delta_{CS}+\Delta f_0)TE + \varphi_{RF})} *$$

$$* e^{i2\pi TE\Delta f_{\text{drift}}(t)} \tag{4.3}$$

The first part of Equation [4.3] multiplied by the first exponential represents the elliptical equation in Equation [4.2], but with a modified time-dependent RF phase increment scheme: $\Delta\theta_{\text{new}}(t) = \Delta\theta - 2\pi TR\Delta f_{\text{drift}}(t)$.

This corresponds to a drift-dependent displacement of all data points along the ellipse as illustrated in Figure 4.1 (b). Note that if only this effect of drift is taken into account, the data points remain on the "non-drifted" ellipse. By "non-drifted" ellipse we mean the ellipse fitted to the data points not influenced by drift.
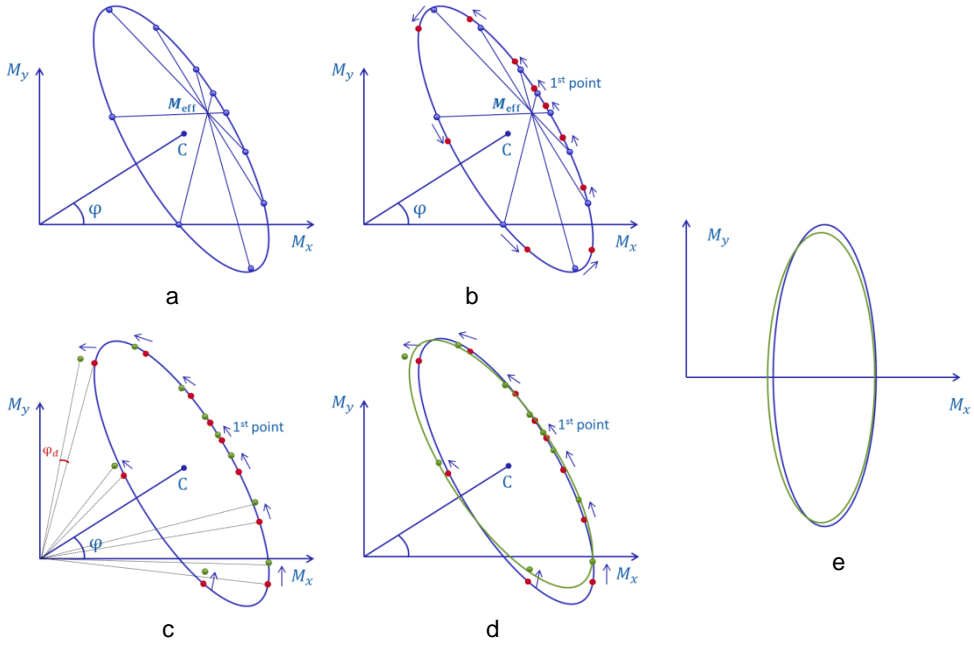
FIGURE 4.1. Schematic representation of the influence of B₀ drift on the data points in the complex signal plane: a) the ellipse without drift; b) time-dependent displacement of the data points along the ellipse due to B₀ drift. The "non-drifted" data points (not influenced by drift) are blue, the displaced data points are red; c) time-dependent rotation of the data points around the origin. The rotated data points are green; d) the ellipse without drift is blue and the ellipse fitted to the "drifted" data points (influenced by drift) is green; e) the vertical conic forms of the ellipse without drift is blue and the ellipse fitted to the "drifted" data points is green.

There is, however, another effect of the drift, caused by the last exponential factor in Equation [4.3]. Using this factor, drift leads to an additional rotation of the data points around the origin, as illustrated in Figure 4.1 (c,d). As drift is time-dependent, the rotation angle differs per data point.

These two effects together relocate the data points in the complex plane away from the "non-drifted" ellipse and result in a non-elliptical distribution of the points. Ignoring the effects of B_0 drift, fitting an ellipse to the "drifted" data points would lead to different fit results compared to the fit for the "non-drifted" case, see Figure 4.1 (e). By "drifted" data points we mean the data points relocated by drift from their "non-drifted" positions. After performing PLANET post-processing (12), this would result in errors in the parameter estimates.

We propose a drift correction method, which aims to relocate each data point back to the position in the complex plane that it would have in the case without drift.

4.2.2 Drift correction method

Based on the analysis presented above, we propose a 3-step drift correction algorithm:

1. Calculation of the spatio-temporal B_0 drift during the phase-cycled PLANET acquisition $\Delta f_{\mathrm{drift},n}(i,j)(t)$, where n is the number of the dynamic acquisition, t is the time, (i, j) are the spatial indices of the voxel. One phase-cycled PLANET acquisition consists of N acquisitions. Assuming temporally linear drift over the duration of the phase-cycled PLANET acquisition, the frequency drift over the nth phase-cycled acquisition is estimated by:

$$\Delta f_{\mathrm{drift},n}(i,j)(t) = n * \frac{\Delta f_{\mathrm{total\ drift}}(i,j)}{N} \ (Hz), \qquad n = \{1, \dots N\}, \qquad [4.4]$$

where the total drift over the phase-cycled PLANET acquisition $\Delta f_{\mathrm{total\ drift}}(i,j)$ is calculated by subtracting two reference B_0 maps acquired right before and right after PLANET acquisition, $t = n\Delta t$ is the time point within the PLANET acquisition scheme, corresponding to n^{th} dynamic acquisition, where the dynamic acquisitions in the phase-cycled acquisition each have a duration Δt.

2. Correction of M_{eff}, T_1, T_2 by multiplying the experimental complex data by $e^{-i2\pi TE \Delta f_{\mathrm{drift},n}(i,j)(t)}$, the geometrical equivalent of which is the rotation of each "drifted" data points around the origin back to the "non-drifted" ellipse.

3. Correction of Δf_0 and φ_{RF} by defining $\Delta\theta_{\mathrm{new}}(i,j)(t) = \Delta\theta_n - 2\pi TR \Delta f_{\mathrm{drift},n}(i,j)(t)$, which geometrically moves the "drifted" data points along the ellipse back to their "non-drifted" positions. $\Delta\theta_n$ is the user controlled RF phase increment: $\Delta\theta_n = (n-1) * \frac{2\pi}{N} - \pi$, $n = \{1, \dots N\}$ covering a full cycle of 2π.

4.2.3 Temporal drift model

As we observed experimentally, B$_0$ drift on a long-time scale can be represented by an exponential function. In the proposed drift correction algorithm, we assumed the temporal evolution of the drift to be linear over the duration of one PLANET acquisition.

Here we compared two temporal drift models:
- a linear model described by Equation [4.4];
- an exponential model described by:

$$\Delta f_{\text{drift},n}(i,j)(t) = A_{\text{drift}}(i,j)\left(1 - exp\left(-\frac{t}{b_{\text{drift}}(i,j)}\right)\right), \qquad [4.5]$$

where $\Delta f_{\text{drift},n}(i,j)(t)$ is the frequency drift over time t, A_{drift} and b_{drift} are parameters describing the global spatial drift characteristics, (i, j) are the spatial indices of the voxel.

4.2.4 Accuracy and precision in the estimated parameters and drift correction performance

The accuracy of the method was assessed by calculating relative errors (ε) in T$_1$, T$_2$, Δf_0, and φ_{RF} estimates before and after drift correction:

$$\varepsilon_X = \frac{\overline{X} - X_{true}}{X_{true}} \cdot 100\%, \quad \varepsilon_{X_{cor}} = \frac{\overline{X_{cor}} - X_{true}}{X_{true}} \cdot 100\% \qquad [4.6]$$

The precision of the method was assessed by calculating the relative standard deviation (SD) of T$_1$, T$_2$, Δf_0, and φ_{RF} estimates before and after drift correction:

$$SD_X = \frac{\sqrt{\frac{1}{Z}\sum_{i=1}^{Z}\left(X^i - \overline{X}\right)^2}}{\overline{X}} \cdot 100\%, \quad SD_{X_{cor}} = \frac{\sqrt{\frac{1}{Z}\sum_{i=1}^{Z}\left(X_{cor}^i - \overline{X_{cor}}\right)^2}}{\overline{X_{cor}}} \cdot 100\%, \quad [4.7]$$

where $\overline{X} = \frac{1}{Z}\sum_{i=1}^{Z}X^i$ refers to the average of the values X^i, affected by drift, $\overline{X_{cor}} = \frac{1}{Z}\sum_{i=1}^{Z}X_{cor}^i$ refers to the average of the values X_{cor}^i, estimated after drift correction, assuming a true value of X_{true} for parameters T$_1$, T$_2$, Δf_0, and φ_{RF}, i is an index for the voxels in an ROI (in experiments) or the current number of the simulation (in numerical simulations), and Z is the total number of voxels in an ROI (in experiments) or the total number of simulations (in numerical simulations).

To quantify the drift correction on T$_1$, T$_2$, Δf_0, and φ_{RF} estimates, Δ_{cor} were

determined as:

$$\Delta_{cor\,T_1} = T_{1cor} - T_{1uncor}, \qquad \Delta_{cor\,T_2} = T_{2cor} - T_{2uncor},$$

$$\Delta_{cor\,\Delta f_0} = \Delta f_{0cor} - \Delta f_{0uncor}, \qquad \Delta_{cor\,\varphi_{RF}} = \varphi_{RF_{cor}} - \varphi_{RF_{uncor}}, \qquad [4.8]$$

$$\Delta_{cor\,T_1}(\%) \; = \frac{T_{1cor} - T_{1uncor}}{T_{1cor}} \cdot 100\%, \qquad \Delta_{cor\,T_2}(\%) = \frac{T_{2cor} - T_{2uncor}}{T_{2cor}} \cdot 100\%$$

4.2.5 Experiments

4.2.5.1 Phantom experiments

To investigate the effects of drift on a single-component phase-cycled bSSFP signal model, and to test the drift correction algorithm, MRI experiments on a phantom (1.5-L plastic bottle filled with an aqueous solution of $MnCl_2 \cdot 4H_2O$ (concentration of approximately 55-60 mg/l)) were performed on a clinical 1.5T MR scanner (Philips Ingenia, Best, The Netherlands). A 15-channel head coil was used as a receiver. Experimental design is shown in Figure 4.2 (a).

To compare two temporal drift models, after the first reference B_0 mapping acquisition we repeated five times the PLANET acquisition over the course of a 65-min experiment. Each PLANET acquisition was followed by the reference B_0 mapping acquisition. This allowed us to assess the performance of the linear drift correction method in the presence of more pronounced long-term drift, which is expected to be non-linear. Six reference B_0 maps were acquired over the course of a 65-min experiment alternated with phase-cycled PLANET acquisitions. The reference B_0 maps were obtained using a dual echo approach. B_0 drift over the duration of each PLANET acquisition was calculated by subtracting the two reference B_0 maps acquired just before and after the PLANET acquisition concerned. For the PLANET acquisition with more severe drift, T_1, T_2, Δf_0, and φ_{RF} maps were reconstructed.

Both linear and exponential temporal drift models were used to correct the drift over this PLANET acquisition: T_1, T_2, Δf_0, and φ_{RF} maps were recalculated by applying the drift correction. Since T_1 estimates depend on FA, see Equation [10] in (12), B_1 mapping sequence was acquired, and voxel-wise B_1 correction was performed while calculating T_1 maps. B_1 maps were calculated using a dual TR AFI technique (16). The reference T_1 and T_2 values of the phantom were measured using a simultaneous spin echo and inversion recovery method (2D MIXED) (3). Relevant protocol parameter settings are presented in Table 4.1.
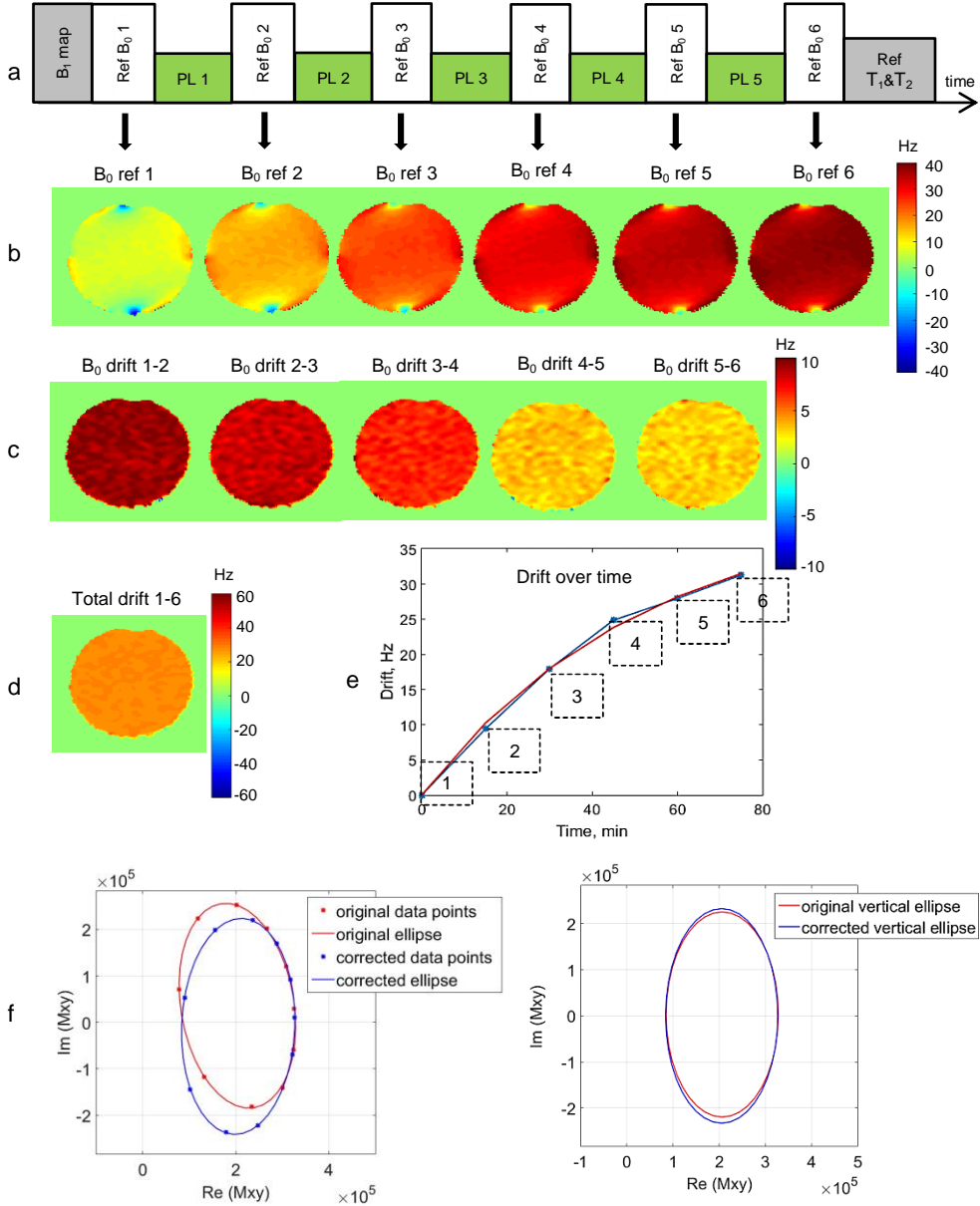
FIGURE 4.2. Experimental drift measurements in the phantom: a) Experimental design; b) The reference B_0 maps (obtained in 3D and shown only for one axial slice of the phantom); c) Calculated B_0 drift maps; d) Total drift map; e) Drift over 65-min time for one voxel in the center of the slice: exponential temporal drift curve (red) fitted to the experimental data points (blue dots); lines connecting the experimental data points (blue); f) The example of original (measured) data points and drift corrected data points with corresponding elliptical fits for one voxel in the middle of the slice; g) The example of original vertical ellipse and drift corrected vertical ellipse for one voxel in the center of the slice.

The accuracy and precision in the parameter estimates before and after linear drift correction were assessed using Equations [4.6, 4.7]. Deviations quantifying the drift correction performed on T_1, T_2, Δf_0, and φ_{RF} estimates were calculated using Equation [4.8]. The ROI analysis was performed on the quantitative T_1 and T_2 maps calculated for the phantom: The ROI (approximately 2000 voxels) was placed in the center of the phantom on the selected slice.

4.2.5.2 *In vivo* experiments

To investigate the effects of drift for a tissue where multiple components are present, and to test the drift correction algorithm, experiments on the brain of healthy volunteers were performed on clinical 1.5T and 3T MR scanners. Both protocols included B_1 mapping acquisition, one PLANET acquisition in between two reference B_0 mapping acquisitions, and the reference T_1 and T_2 mapping acquisition with the protocol parameter settings shown in Table 4.1.

A 2.5-ms-long RF excitation pulse was used in each PLANET acquisition to minimize magnetization transfer effects (17). Image registration (rigid) and Gibbs ringing filtering (18) was applied to the brain data before performing the PLANET reconstruction. B_0 drift maps were filtered (using a circular averaging filter with radius of 15) before applying the drift correction algorithm.

The T_1, T_2, Δf_0, and φ_{RF} maps were calculated before and after drift correction. B_1 correction was performed voxel-wise while calculating the T_1 maps. Deviations quantifying the drift correction performed on T_1, T_2, Δf_0, and φ_{RF} estimates were calculated using Equation [4.8]. The ROI analyses were performed on the quantitative T_1 and T_2 maps for both 1.5T and 3T data. The ROIs were manually delineated in WM on the selected slice in the area where the drift was the most pronounced (each ROI was approximately 100-150 voxels). The precision of the T_1 and T_2 measurements was evaluated by calculating standard deviations on T_1 and T_2 maps over the ROIs.

4.2.6 Numerical simulations

4.2.6.1 Drift-induced errors and drift correction for a single-component signal model

To investigate the errors caused by B_0 drift for a single-component tissue model, numerical simulations were performed with relaxation times equal to those of the phantom material: T_1 = 430 ms and T_2 = 50 ms. The following parameter settings were used in simulations: FA in

the range of 0º-45º, TR in the range of 0-20 ms, 10 RF phase increment values $\Delta\theta_n = \frac{2\pi n}{10} - \pi$, n = {0, 1,.., 9}, M$_{\text{eff}}$ = 10000, single peak with δ_{CS} = 0, Δf_0 = 5 Hz, and φ_{RF} = -0.2 rad (these values were obtained experimentally in the phantom). B$_0$ drift was assumed to be linear over time and spatially independent (Δf_{drift} = [1 2 3 4 5 6 7 8 9 10] Hz), as we found in the experimental results in the phantom. Gaussian noise was added independently to the real and imaginary data, resulting in an SNR about 230, which corresponds to the experimentally measured SNR in the phantom. The number of performed Monte Carlo simulations was 10,000. The accuracy and precision in the T$_1$, T$_2$, Δf_0, and φ_{RF} estimates were assessed using Equations [4.6, 4.7]. All simulations and calculations were performed in MATLAB R2015a (The MathWorks Inc, Natick, USA).

4.2.6.2 Drift-induced errors and drift correction for a two-component signal model

To investigate the errors in the parameter estimates caused by B$_0$ drift in the case where two components are present in the signal, numerical simulations were performed for WM tissue at 3T, which is known to be a two-component tissue (19,20). Two single peaks were used in simulations: the on-resonant dominant component and the smaller component with an average frequency shift Δf = 20 Hz (20). The dominant component has T$_{1D}$ = 1000 ms and T$_{2D}$ = 80 ms, with a volume fraction of 0.88; the smaller component has T$_{1S}$ = 400 ms and T$_{2S}$ = 10 ms, with a MWF of 0.12. The off-resonance Δf_0 = 10 Hz was used and the RF phase offset φ_{RF} = -0.15 rad was used. Gaussian noise was added independently to the real and imaginary data, resulting in an SNR ranging from 30 to 150. The number of performed Monte Carlo simulations was 10,000. The simulations were performed using the complex phase-cycled bSSFP signal described by Equations [7, 8] in our previous study (13) for three cases:

-   No B$_0$ drift;
-   Linearly increasing over time and spatially independent frequency drift Δf_{drift} = [1 2 3 4 5 6 7 8 9 10] Hz;
-   Linearly increasing over time and spatially independent frequency drift Δf_{drift} = [1 2 3 4 5 6 7 8 9 10] Hz with subsequently applied proposed drift correction algorithm.

The accuracy and precision in the T$_1$, T$_2$, Δf_0, and φ_{RF} estimates were assessed using Equations [4.6,4.7], where the true parameter values were taken for the dominant WM component.

Table 4.1. Protocol parameter settings

Phantom experiment at 1.5T

PLANET: 3D phase-cycled bSSFP

FOV (m³)	Voxel Size (mm³)	Acq. Matrix	Rec. Matrix	TR (ms)	TE (ms)	Flip Angle (°)	Number of RF increment steps	NSA	Readout direction	Dummy pulses	Total scan time (min:s)
160x160x159	1.1x1.1x3	144x145x53	160x160x53	10	5	30	10	1	AP	6 s for each dynamic	13:46

Reference B₁ map (3D dual-TR SPGR)

FOV (m³)	Voxel Size (mm³)	Acq. Matrix	Rec. Matrix	TR (ms)	TE (ms)	Flip Angle (°)	NSA	Readout direction	Parallel Imaging	Total scan time (min:s)
160x160x159	2.5x4x3	64x40x53	160x160x53	[30;150]	1.82	60	1	AP	SENSE 2 in RL	03:12

Reference off-resonance map (3D dual-echo SPGR)

FOV (m³)	Voxel Size (mm³)	Acq. Matrix	Rec. Matrix	TR (ms)	TE (ms)	Flip Angle (°)	NSA	Readout direction	Parallel Imaging	Total scan time (min:s)
160x160x159	2.5x4x3	64x40x53	160x160x53	30	[4.6; 9.2]	60	1	AP	SENSE 2 in RL	01:04

Reference T₁ and T₂ map (2D MIXED)

FOV (m³)	Voxel Size (mm³)	Acq. Matrix	Rec. Matrix	TR SE (ms)	TR IR (ms)	IR delay (ms)	TE (ms)	NSA	Readout direction	Total scan time (min:s)
160x160x3	2x2x3	80x80x1	160x160x1	1500	2000	500	[30; 60; 90; 120; 150; 180]	1	AP	04:47

In vivo experiments at 1.5T and 3T

PLANET: 3D phase-cycled bSSFP

FOV (m³)	Voxel Size (mm³)	Acq. Matrix	Rec. Matrix	TR (ms)	TE (ms)	Flip Angle (°)	Number of RF increment steps	NSA	Readout direction	Dummy pulses	Total scan time (min:s)
220x220x100	0.98x0.98x4	220x220x25	224x224x25	10	5	20	10	1	AP	10 s for each dynamic	11:00

Reference B₁ map (3D dual-TR SPGR)

FOV (m³)	Voxel Size (mm³)	Acq. Matrix	Rec. Matrix	TR (ms)	TE (ms)	Flip Angle (°)	NSA	Readout direction	Parallel Imaging	Total scan time (min:s)
220x220x100	3.44x4x4	64x55x25	224x224x25	[30; 150]	1.82	60	1	AP	SENSE 1.5 in RL	02:43

Reference off-resonance map (3D dual-echo SPGR)

FOV (m³)	Voxel Size (mm³)	Acq. Matrix	Rec. Matrix	TR (ms)	TE (ms)	Flip Angle (°)	NSA	Readout direction	Parallel Imaging	Total scan time (min:s)
220x220x100	3.44x4x4	64x40x53	224x224x25	30	[4.6; 9.2]	60	1	AP	No	01:21

Reference T₁ and T₂ map (2D MIXED)

FOV (m³)	Voxel Size (mm³)	Acq. Matrix	Rec. Matrix	TR SE (ms)	TR IR (ms)	IR delay (ms)	TE (ms)	NSA	Readout direction	Total scan time (min:s)
220x220x4	2x2x4	80x80x1	112x110x1	2500	5000	500	[30; 60; 90; 120; 150; 180; 210; 240]	1	AP	14:00

4.3 Results

4.3.1 Experimental results in the phantom

Experimental results in the phantom are shown in Figure 4.2. Six reference B$_0$ maps acquired before and after each of five PLANET acquisitions and corresponding calculated B$_0$ drift maps are presented in Figure 4.2 (b, c). A total drift of 28 Hz over a 65-min scanning session was observed (Figure 4.2 (d)). The temporal drift was analyzed voxel-wise, and the example of the experimental data for one voxel (in the center of the phantom) is shown in Figure 4.2 (e). Over a 65-min scanning time the temporal drift can be considered as an exponential function. Over the 11-min duration of the PLANET acquisition the drift with an average value of 10 Hz can be very well approximated with a linear function.

As an example, the initial data points and the data points after drift correction for one voxel are shown in Figure 4.2 (f) with corresponding elliptical fits. The conic vertical forms of these ellipses are shown in Figure 4.2 (g). The ellipses are different, as expected due to the drift. Estimated T$_1$, T$_2$, Δf_0, and φ_{RF} maps of the phantom before and after linear drift correction, as well as the reference T$_1$, T$_2$, and Δf_0 maps are shown in Figure 4.3 (a-c). The drift correction was performed for the first PLANET acquisition, where the drift was more severe. The performance of linear and exponential drift correction was very similar, therefore we did not include the maps of T$_1$, T$_2$, Δf_0, and φ_{RF} after exponential drift correction in Figure 4.3. Reference RF phase map was not acquired and therefore is not shown. Deviations quantifying the amount of linear drift correction performed on all quantitative parameters are shown in Figure 4.3 (d,e). The drift correction decreased the T$_1$ values by about 4%, it increased the T$_2$ values by about 8%, decreased Δf_0 values by about 120%, and increased φ_{RF} values by about 3%. The magnitude image with white vertical and horizontal lines used for T$_1$ and T$_2$ profiles, and T$_1$ and T$_2$ profiles on estimated, corrected and reference maps are shown in Figure 4.3 (f,g). T$_2$ estimates are more sensitive to the drift than T$_1$ estimates.

The quantitative ROI analysis for parameters T$_1$, T$_2$, Δf_0, and the relative errors in these parameters before and after drift correction is presented in Supporting Information Table S4.1. The T$_1$ values were overestimated due to drift by about 5% compared to the reference values, and the corrected T$_1$ values were in agreement with the reference values with an accuracy of 1%. The T$_2$ values were underestimated due to drift by about 10% compared to the reference values and after drift correction they were in agreement with the reference values with an accuracy of 2%. The Δf_0 values estimated by means of PLANET were about 80% overestimated due to drift and after drift correction they became similar to the reference Δf_0 acquired right before PLANET acquisition.
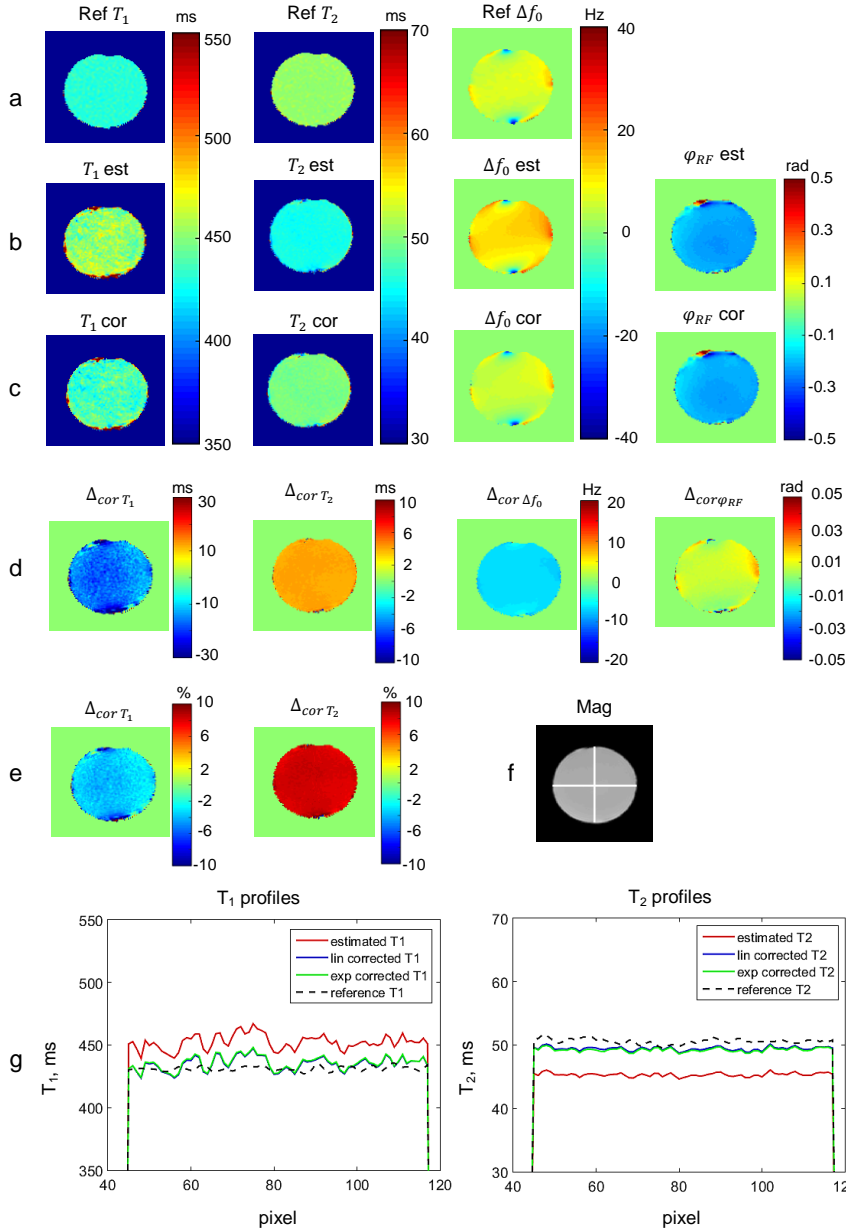
FIGURE 4.3. Experimental results in the phantom: a) The reference T_1, T_2, and Δf_0 maps; b) T_1, T_2, Δf_0, and φ_{RF} maps before drift correction; c) T_1, T_2, Δf_0, and φ_{RF} maps after linear drift correction; d) Maps of absolute Δ_{cor} quantifying the drift correction performed on T_1, T_2, Δf_0, and φ_{RF}; e) Maps of relative Δ_{cor} quantifying the drift correction performed on T_1 and T_2; f) The magnitude image with white vertical and horizontal lines in the center of the slice, used for T_1 and T_2 profiles; g) T_1 and T_2 profiles: T_1 and T_2 values representing single voxels along the selected lines on estimated, corrected and reference maps. The values were averaged voxel-wise between the horizontal and vertical selected lines.

A remaining underestimation of about 20% in T$_1$ values and of about 30% in T$_2$ values compared to the reference values can be seen in Figures 4.4, 4.5 and Table 4.2. Despite the fact that there are no directly visible B$_0$ drift related artifacts in quantitative parameter maps, there are B$_0$ drift related errors in quantitative T$_1$, T$_2$, and Δf_0 maps.

4.3.2 Experimental results in the brain

4.3.2.1   1.5T

The results of the experiment in the brain of a healthy volunteer at 1.5T are shown in Figure 4.4. The results are presented for one central slice. Spatially homogeneous drift was observed over 11-min PLANET acquisition, see Figure 4.4 (a) with an average value of 9 Hz. T$_1$, T$_2$, Δf_0, and φ_{RF} maps before and after linear drift correction are shown in Figure 4.4 (c-d). The banding free magnitude and the reference T$_1$ and T$_2$ maps are shown in Figure 4.4 (b). Deviations quantifying the amount of linear drift correction performed on all parameters are shown in Figure 4.4 (e). The mean T$_1$ and T$_2$ values were calculated for WM. The results of the ROI analysis are given in Table 4.2 for the estimated, drift corrected, reference, and literature published T$_1$ and T$_2$ values.

After drift correction, T$_1$ values decreased by about 1% compared to the uncorrected values, T$_2$ values increased by about 5% compared to the uncorrected values, see Figure 4.4 (e,f) and Table 4.2. The B$_0$ values after decreased by about 50% and the corrected B$_0$ map resembles the reference B$_0$ map acquired right before the PLANET acquisition. The RF phase maps almost did not change after drift correction.

4.3.2.1   3T

A spatially inhomogeneous drift was observed over the same 11-min PLANET acquisition in the brain of another healthy volunteer at 3T with a maximum value of 10 Hz for the selected slice, see Figure 4.5 (a). T$_1$, T$_2$, Δf_0, and φ_{RF} maps before and after linear drift correction, the banding free magnitude and the reference T$_1$ and T$_2$ maps, and deviations quantifying the amount of linear drift correction performed on all parameters are shown. The results of the ROI analysis are given in Table 4.2. Similar to the results at 1.5T, T$_1$ values after drift correction almost did not change, they locally decreased by about 2% compared with the uncorrected values in the area with more pronounced drift. T$_2$ values were more sensitive to drift, and after drift correction they increased by about 5-6% compared with the uncorrected values in the area with more pronounced drift, see Figure 4.5 (e,f) and Table 4.2. The B$_0$ values decreased by about 50% and the corrected B$_0$ map resembles the reference B$_0$ map

acquired just prior to the PLANET acquisition. The RF phase maps almost did not change after drift correction.

Table 4.2. Quantitative results from the experiments in the brain at 1.5T and 3T: estimated, drift corrected, and reference T_1 and T_2 values in WM

1.5T	Estimated values		Drift corrected values		Reference values		Literature published values*	
ROI	T_1, ms	T_2, ms	T_1, ms	T_2, ms	T_1, ms	T_2, ms	T_1, ms	T_2, ms
1	508 ± 34	55 ± 3	501 ± 26	61 ± 2	596 ± 21	76 ± 2	621 ± 61 (9)	58 ± 4 (9)
2	460 ± 33	55 ± 3	458 ± 20	57 ± 3	596 ± 19	77 ± 3	561 ± 12 (21)	73 ± 2 (21)
3	475 ± 30	56 ± 4	475 ± 32	58 ± 4	595 ± 27	84 ± 4		
4	495 ± 33	57 ± 5	487 ± 38	58 ± 5	629 ± 24	85 ± 5		
Mean	485 ± 33	56 ± 4	480 ± 30	59 ± 4	604 ± 23	81± 4		

3T	Estimated values		Drift corrected values		Reference values		Literature published values*	
ROI	T_1, ms	T_2, ms	T_1, ms	T_2, ms	T_1, ms	T_2, ms	T_1, ms	T_2, ms
1	678 ± 33	51 ± 2	664 ± 35	53 ± 2	771 ± 19	68 ± 2	832 ± 1 (22)	80 ± 1 (22)
2	660 ± 42	50 ± 3	642 ± 39	53 ± 3	781 ± 18	70 ± 3	1084 ± 45 (23)	69 ± 3 (23)
3	636 ± 30	50 ± 2	624 ± 29	53 ± 2	771 ± 16	69 ± 2	781 ± 61 (24)	65 ± 6 (24)
Mean	658 ± 36	50 ± 2	643 ± 35	53 ± 2	774 ± 18	69 ± 2		

The mean T_1 and T_2 values at 1.5T were calculated for one slice of the brain by averaging over four ROIs (each approximately 150 voxels) in white matter on corresponding T_1 and T_2 maps. The mean T_1 and T_2 values at 3T were calculated for one slice of the brain by averaging over three ROIs (each approximately 100 voxels) in white matter on corresponding T_1 and T_2 maps.
*Numbers in parentheses are reference citations.

4.3.3 Simulation results

4.3.3.1 Single-component phase-cycled bSSFP signal model of the phantom

Relative errors and standard deviations in T_1, T_2, Δf_0, and φ_{RF} estimates for a single-component signal model of the phantom are presented in Figure 4.6: affected by linear drift (a-b) and after applying drift correction (c-d). As can be seen, drift induced errors depend on the choice of FA and TR. For combination of FA = 30° and TR = 10 ms, which was used in the experimental setup, the quantitative analysis of the errors is presented in Table 4.3. T_1 values are overestimated due to drift by about 4% compared with the true values, T_2 values

are underestimated due to drift by about 8% compared with the true values, Δf_0 values are overestimated due to drift by about 100%, φ_{RF} values are underestimated due to drift by about 5%. After applying the proposed drift correction algorithm, relative errors in all estimated parameters are almost zero, which demonstrates an accurate performance of drift correction. The standard deviations in all estimated parameters are almost not affected by drift correction and are below 5%.

These results are in agreement with the experimental results for the phantom shown above: the simulated expected errors due to drift match the calculated errors in the estimated parameters.

4.3.3.2 Two-component phase-cycled bSSFP signal model

The simulation results for a two-component signal model of WM are shown in Figure 4.7. Relative errors in T_1, T_2, Δf_0, and φ_{RF} are shown for three cases: no drift, linear drift, and after applying the drift correction algorithm. The errors in the estimated parameters depend on the choice of FA and TR. As we showed in a previous study (13), in WM brain tissue the PLANET post-processing results in systematic errors in estimated T_1, T_2, and Δf_0 values due to the presence of a second myelin related component in WM. Here we can observe similar behavior for the case without drift.

For combination of FA = 20° and TR = 10 ms, which was used in the experimental setup, the quantitative analysis of the errors is presented in Table 4.3. T_1 values are underestimated by 30% without drift, underestimated by 29.5% in the presence of drift, and underestimated by 30.5% after drift correction. T_2 values are underestimated by 35% without drift, underestimated by 39% in the presence of drift, and underestimated by 34.5% after drift correction. Δf_0 values are overestimated by 14% without drift, overestimated by 58% in the presence of drift, and overestimated by 10% after drift correction. The φ_{RF} values are overestimated by 20% without drift, overestimated by 25% in the presence of drift, and overestimated by 23% after drift correction.

The drift correction performed on all estimated parameters predicted by the simulations for combination of TR = 10 ms and FA = 20° is similar to the drift correction performed experimentally in the brain: after drift correction, T_1 values decreased by about 1% compared with the uncorrected values, T_2 values increased by about 5% compared with the uncorrected values, Δf_0 values decreased by about 48%, φ_{RF} values slightly decreased by about 1.5%. In all cases drift-induced errors were corrected.

FIGURE 4.4. Experimental results obtained in the brain at 1.5T: a) The reference B_0 maps before (1) and after (2) PLANET acquisition, the corresponding drift map (1-2), and the drift map filtered using a circular averaging filter; b) Banding free magnitude image, the reference T_1 and T_2 maps; c) T_1, T_2, Δf_0, and φ_{RF} maps before drift correction; d) T_1, T_2, Δf_0, and φ_{RF} maps after linear drift correction; e) Maps of absolute Δ_{cor} quantifying the drift correction performed on Δf_0, T_1 and T_2 and φ_{RF}; f) Maps of relative Δ_{cor} quantifying the drift correction performed on T_1 and T_2.
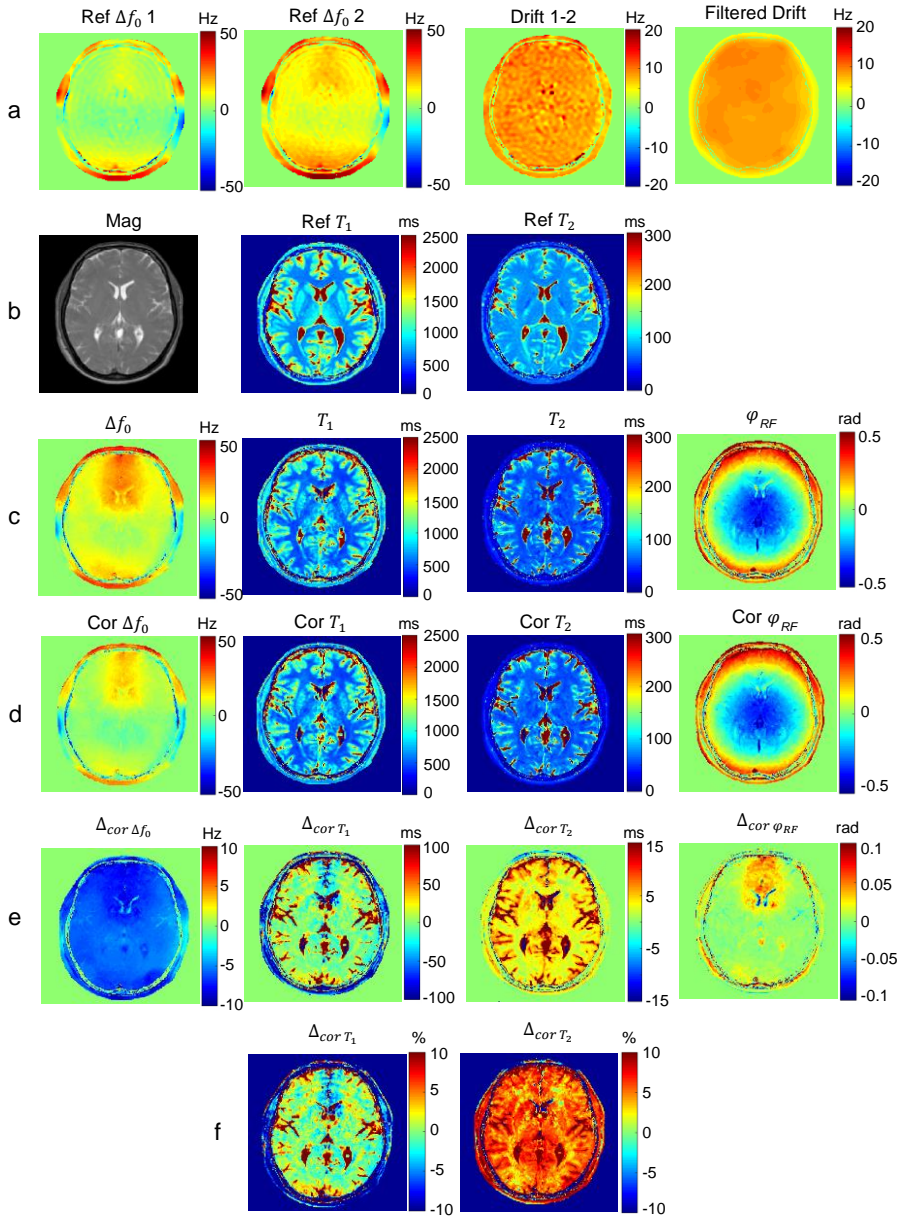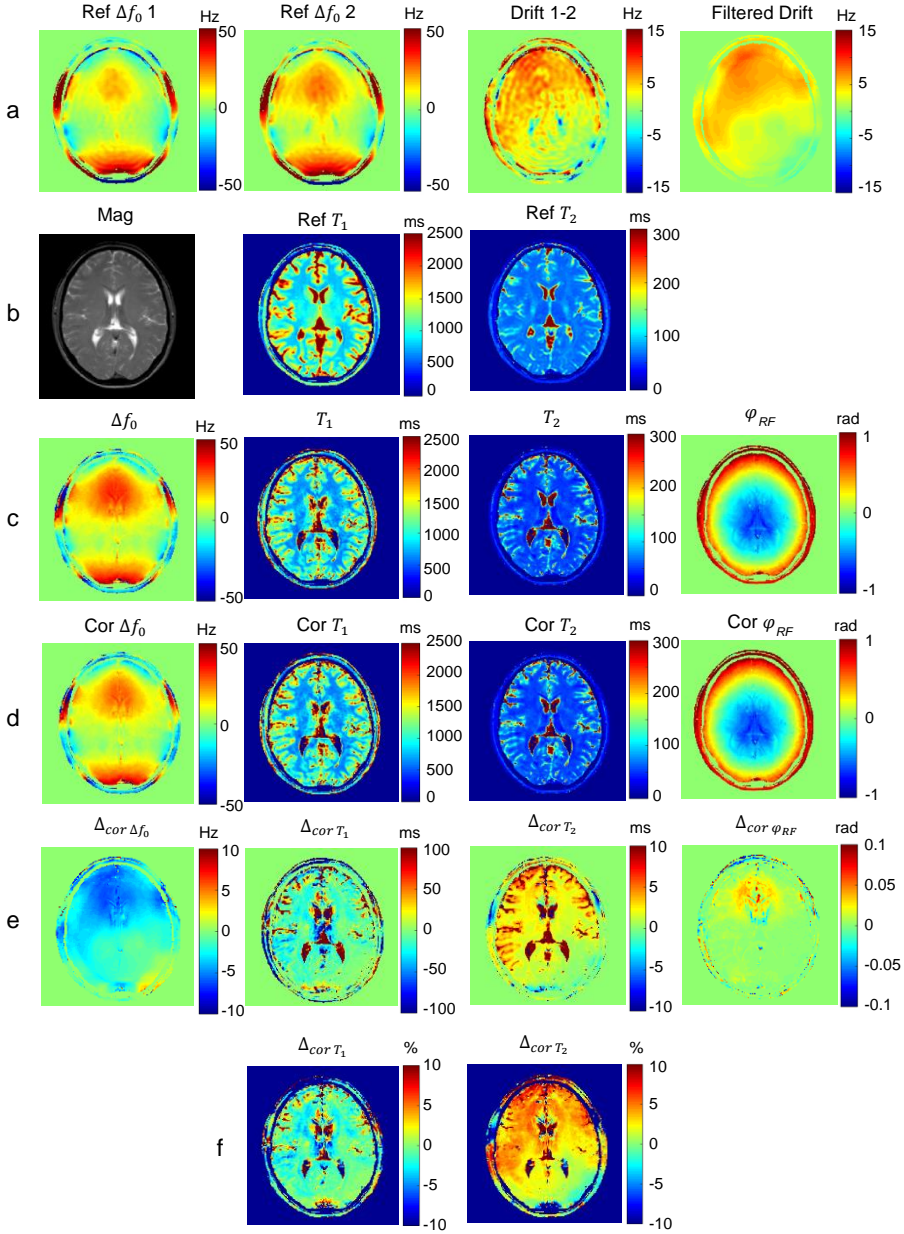
FIGURE 4.5. Experimental results obtained in the brain at 3T: a) The reference B$_0$ maps before (1) and after (2) PLANET acquisition, the corresponding drift map (1-2), and the drift map filtered using a circular averaging filter; b) Banding free magnitude image, the reference T$_1$ and T$_2$ maps; c) T$_1$, T$_2$, Δf_0, and φ_{RF} maps before drift correction; d) T$_1$, T$_2$, Δf_0, and φ_{RF} maps after linear drift correction; e) Maps of absolute Δ_{cor} quantifying the drift correction performed on Δf_0, T$_1$ and T$_2$ and φ_{RF}; f) Maps of relative Δ_{cor} quantifying the drift correction performed on T$_1$ and T$_2$.

4.3 Discussion

The PLANET method requires a stationary main magnetic field over the course of the acquisition. This requirement, however, can be difficult to meet, and as a consequence, B_0 drift can occur. In this work we investigated the sensitivity of the PLANET method to B_0 drift and assessed the errors which drift can cause in the estimated T_1, T_2, Δf_0, and φ_{RF} parameters.

We presented a mathematical interpretation of the influence of drift on the elliptical phase-cycled bSSFP single-component signal behavior and proposed a general strategy for drift correction. We demonstrated how drift influences the performance of the PLANET method experimentally in a phantom and in the brain of healthy volunteers. Consequently, we verified the effects of the drift by performing numerical simulations for the same phantom and in-vivo setups.

The experimental results in the phantom showed that the drift of about 10 Hz, which occurred over the 11-min duration of the PLANET acquisition, induced the errors in estimated quantitative parameters: the T1 values were overestimated due to drift by about 5%, the T2 values were underestimated due to drift by about 10%, and the Δf_0 values were by about 80% overestimated due to drift compared to the corresponding reference values. The variance in the estimated parameters only slightly changed after drift correction. We demonstrated that both linear and exponential correction algorithms performed identically. The linear model for temporal evolution of the drift on a short time scale (0-15 min) may be a fair approximation of the exponential drift in the experiments reported in this paper. Drift-induced errors in T_1, T_2, Δf_0, and φ_{RF} estimates in a phantom were successfully corrected by applying the drift correction algorithm. These results obtained experimentally were verified by numerical simulations for a similar setup: the bias and variance in all parameter estimates predicted by simulations matched the ones calculated using the experimental data of phantom.

The investigation of the drift effects in the human brain showed that similar drift of about 10 Hz over the 11-min duration of the PLANET acquisition had a significant effect only on the estimated Δf_0 values: an overestimation of about 50% in Δf_0 values was caused by drift. The other quantitative parameters were only affected slightly: the drift induced an overestimation of about 1% in T_1 estimates, an underestimation of about 5% in T_2 estimates, and an overestimation of about 5% in φ_{RF} estimates. The errors in the quantitative parameters calculated in the brain were in agreement with errors predicted by simulations for a similar experimental setup. The proposed drift correction algorithm performed well and corrected the errors caused by drift. However, the remaining underestimation by about 20-30% in T_1 and T_2 values compared to the reference and literature published values, which

can be seen in Figures 4.4, 4.5 and Table 4.2, is not caused by B_0 drift. It is caused by the effect that in WM tissue where multiple components are present, a single-component PLANET model is not valid, as we already pointed out in a previous study (13). Obviously, such underlying errors were not and cannot be corrected by the drift correction algorithm. Keep in mind, that any other techniques that assume a single-component relaxation model will fail in this case as well.
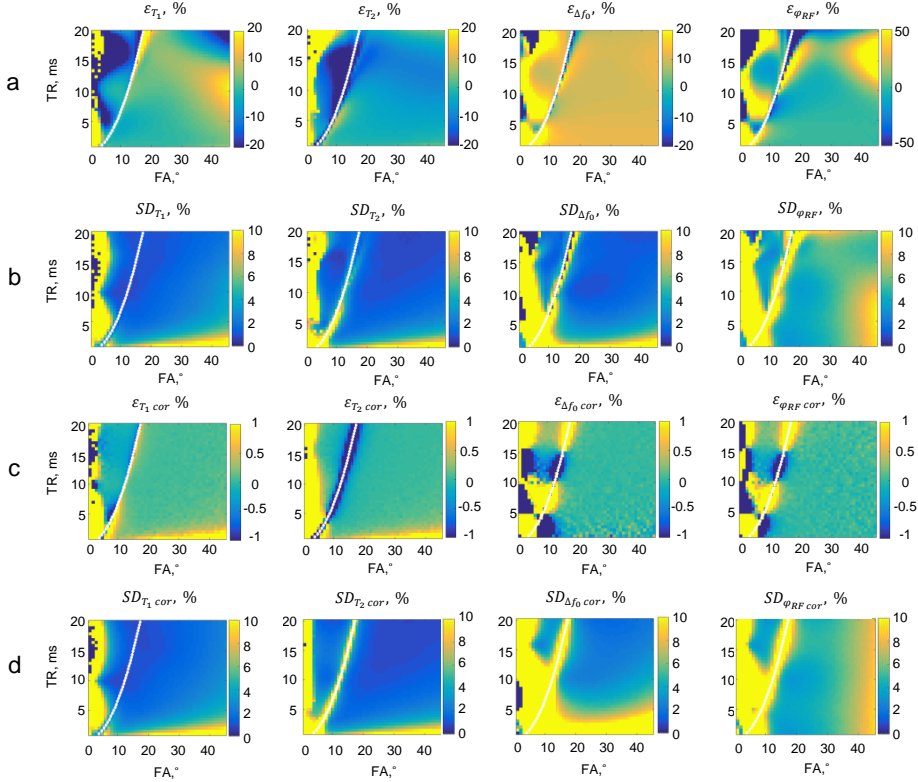
FIGURE 4.6 Simulation results for a single-component signal model. a-b) Relative errors (ε) and relative standard deviations (SD) in T_1, T_2, Δf_0, and φ_{RF} estimates (in percent) compared to their true values in the presence of linear over time and spatially independent drift: Δf_{drift} = [1 2 3 4 5 6 7 8 9 10] Hz; c-d) Relative errors (ε) and relative standard deviations (SD) in T_1, T_2, Δf_0, and φ_{RF} estimates (in percent) compared to their true values after applying linear drift correction algorithm. The initial settings: T_1 = 430 ms, T_2 = 50 ms, Δf_0 = 5 Hz, and φ_{RF} = - 0.2 rad, and 10 RF phase increments.

The severity of drift effect depends on the field strength, history of gradient activity and heating of metallic components of the scanner, PLANET acquisition time, the used gradient mode, shimming, etc., which vary among different systems and over time. Even though the errors in estimated quantitative parameters caused by drift in human brain are small (1-5%) compared to the errors caused by the presence of multiple components (about 30% underestimation), as we have shown in this study, they cannot be predicted and can potentially affect reproducibility of the results as drift effects are generally not reproducible. We have now shown that the drift-induced errors can be successfully corrected by applying the proposed drift correction algorithm. Acquiring two quick low-resolution reference B_0 maps before and after the PLANET acquisition is generally a simple direct way to correct for drift and improve the quantitative parameter estimation using the PLANET method.

Table 4.3. Quantitative results of simulations for a single-component signal model of the phantom and a two-component signal model of WM at 3T: the accuracy and precision in T_1, T_2, Δf_0, and φ_{RF} estimates without drift, with drift and after drift correction

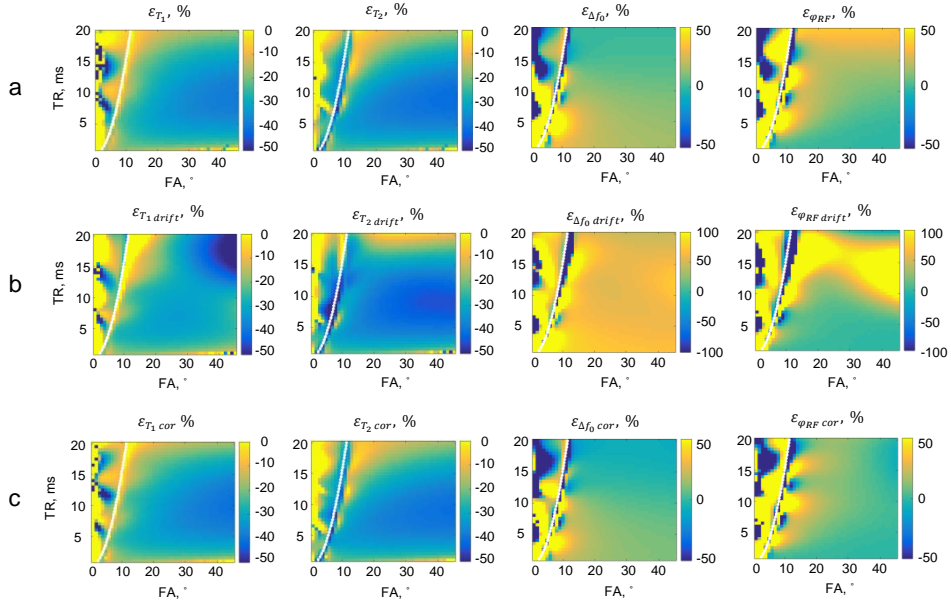| Parameter	Single-component model of the phantom, TR = 10ms, FA = 30˚		Two-component signal model of WM at 3T, TR = 10ms, FA = 20˚	
	Relative error ε, %	Standard deviation SD, %	Relative error ε, %	Standard deviation SD, %
No drift				
T_1	0.07	1.7	-30.2	2.1
T_2	0.04	1.0	-34.8	1.4
Δf_0	-0.01	2.8	13.7	1.5
φ_{RF}	-0.01	4.7	20.0	5.6
Drift				
T_1	4.2	1.9	-29.5	2.0
T_2	-7.5	1.1	-38.8	1.5
Δf_0	97.8	1.2	58.3	1.4
φ_{RF}	-4.7	4.8	24.7	6.9
Drift-corrected				
T_1	0.06	1.8	-30.6	1.9
T_2	0.03	1.1	-34.3	1.5
Δf_0	0.01	2.7	10.1	1.9
φ_{RF}	0.01	4.5	23.2	6.7

FIGURE 4.7. Simulation results for a two-component signal model of WM at 3T (T_{1D} = 1000 ms, T_{2D} = 80 ms, T_{1S} = 400 ms, T_{2S} = 20 ms, Δf = 20 Hz, and myelin water fraction = 0.12). Δf_0 = 10 Hz, and φ_{RF} = -0.15 rad, 10 RF phase increments. Relative errors (ε) caused by drift in T_1, T_2, Δf_0, and φ_{RF} estimates (in percent) compared to their true values (of the dominant component): a) without drift; b) in the presence of linear over time and spatially independent drift: Δf_{drift} = [1 2 3 4 5 6 7 8 9 10] Hz; c) after linear drift correction algorithm.

4.1 Conclusion

We have demonstrated that PLANET method is sensitive to B_0 drift. Although there may be no directly visible B_0 drift related artifacts on the estimated parameter maps, drift can induce errors in these parameters. In the phantom, which can be described with a single-component signal model, drift induced significant errors in the estimated parameters. However, in the human brain, where multiple components are present, drift only had a minor effect. We have now shown that the drift-induced errors can be successfully corrected by applying the proposed drift correction algorithm for both cases of single- and two-component signal models.

Supporting Table S4.1. Quantitative results from the phantom experiment: the reference, estimated, and drift-corrected T_1, T_2, and Δf_0 values; and the relative errors in estimated and drift-corrected T_1, T_2, and Δf_0 values.

T_1 ref, ms	432 ± 3	T_2 ref, ms	50.6 ± 0.5	Δf_0 ref, Hz	6.6 ± 0.5
T_1 est, ms	453 ± 12	T_2 est, ms	45.4 ± 0.4	Δf_0 est, Hz	12.1 ± 0.6
T_1 cor, ms	436 ± 11	T_2 cor, ms	49.5 ± 0.4	Δf_0 cor, Hz	5.5 ± 0.5
ε_{T_1}, %	5.3 ± 1.9	ε_{T_2}, %	-10.3 ± 1.1	$\varepsilon_{\Delta f_0}$, %	79.4 ± 10.3
$\varepsilon_{T_1\,cor}$, %	1.2 ± 1.8	$\varepsilon_{T_2\,cor}$, %	-2.2 ± 1.2	$\varepsilon_{\Delta f_0\,cor}$, %	-1.2 ± 4.8

The values were calculated over a circular ROI (approximately 1300 voxels) placed on the corresponding parameter maps on the selected slice.

4.6 References

1. Cheng HL, Stikov N, Ghugre NR, Wright GA. Practical medical applications of quantitative MR relaxometry. J. Magn. Reson. Imaging 2012;36:805–824. doi: 10.1002/jmri.23718.

2. Look DC, Locker DR. Time saving in measurement of NMR and EPR relaxation times. Rev. Sci. Instrum. 1970;41:250–251. doi: 10.1063/1.1684482.

3. In den Kleef JJ, Cuppen JJ. RLSQ: T1, T2, and rho calculations, combining ratios and least squares. Magn. Reson. Med. 1987;5:513–24.

4. Bernstein MA, King KF, Zhou XJ. Handbook of MRI Pulse Sequences. 2004. doi: 10.1016/B978-0-12-092861-3.X5000-6.

5. Schmitt P, Griswold MA, Jakob PM, Kotas M, Gulani V, Flentje M, Haase A. Inversion recovery TrueFISP: quantification of T(1), T(2), and spin density. Magn. Reson. Med. 2004;51:661–7. doi: 10.1002/mrm.20058.

6. Ehses P, Seiberlich N, Ma D, Breuer FA, Jakob PM, Griswold MA, Gulani V. IR TrueFISP with a golden-ratio-based radial readout: Fast quantification of T1, T2, and proton density. Magn. Reson. Med. 2013;69:71–81. doi: 10.1002/mrm.24225.

7. Christensen KA, Grant DM, Schulman EM, Walling C. Optimal determination of relaxation times of fourier transform nuclear magnetic resonance. Determination of spin-lattice relaxation times in chemically polarized species. J. Phys. Chem. 1974;78:1971–1977. doi: 10.1021/j100612a022.

8. Homer J, Beevers MS. Driven-equilibrium single-pulse observation of T1 relaxation. A reevaluation of a rapid "new" method for determining NMR spin-lattice relaxation times. J. Magn. Reson. 1985;63:287–297. doi: 10.1016/0022-2364(85)90318-X.

9. Deoni SCL, Rutt BK, Peters TM. Rapid combined T1 and T2 mapping using gradient recalled acquisition in the steady state. Magn. Reson. Med. 2003;49:515–526. doi: 10.1002/mrm.10407.

10. Heule R, Ganter C, Bieri O. Triple echo steady-state (TESS) relaxometry. Magn. Reson. Med. 2014;71:230–237. doi: 10.1002/mrm.24659.

11. Ma D, Gulani V, Seiberlich N, Liu K, Sunshine JL, Duerk JL, Griswold MA. Magnetic resonance fingerprinting. Nature 2013;495:187–192. doi: 10.1038/nature11971.

12. Shcherbakova Y, van den Berg CAT, Moonen CTW, Bartels LW. PLANET: An ellipse fitting approach for simultaneous T1 and T2 mapping using phase-cycled balanced steady-state free precession. Magn. Reson. Med. 2018;79:711–722. doi: 10.1002/mrm.26717.

13. Shcherbakova Y, van den Berg CAT, Moonen CTW, Bartels LW. On the accuracy and

precision of PLANET for multiparametric MRI using phase-cycled bSSFP imaging. Magn. Reson. Med. 2019;81:1534–1552. doi: 10.1002/mrm.27491.

14. Xiang QS, Hoff MN. Banding artifact removal for bSSFP imaging with an elliptical signal model. Magn. Reson. Med. 2014;71:927–933. doi: 10.1002/mrm.25098.

15. Lauzon M. Louis, Frayne R. Analytical Characterization of RF Phase-Cycled Balanced Steady-State Free Precession. Concepts Magn. Reson. Part A 2009;34A:133–143. doi: 10.1002/cmr.a.20138.

16. Yarnykh VL. Actual flip-angle imaging in the pulsed steady state: A method for rapid three-dimensional mapping of the transmitted radiofrequency field. Magn. Reson. Med. 2007;57:192–200. doi: 10.1002/mrm.21120.

17. Bieri O, Scheffler K. Optimized balanced steady-state free precession magnetization transfer imaging. Magn Reson Med 2007;58:511–518. doi: 10.1002/mrm.21326.

18. Kellner E, Dhital B, Kiselev VG, Reisert M. Gibbs-ringing artifact removal based on local subvoxel-shifts. Magn. Reson. Med. 2016;76:1574–1581. doi: 10.1002/mrm.26054.

19. Miller KL. Asymmetries of the balanced SSFP profile. Part I: Theory and Observation. Magn. Reson. Med. 2010;63:385–395. doi: 10.1002/mrm.22212.

20. Miller KL, Smith SM, Jezzard P. Asymmetries of the balanced SSFP profile. Part II: White matter. Magn. Reson. Med. 2010;63:396–406. doi: 10.1002/mrm.22249.

21. Warntjes JBM, Dahlqvist Leinhard O, West J, Lundberg P. Rapid magnetic resonance quantification on the brain: Optimization for clinical usage. Magn. Reson. Med. 2008;60:320–329. doi: 10.1002/mrm.21635.

22. Bouhrara M, Spencer RG. Rapid simultaneous high-resolution mapping of myelin water fraction and relaxation times in human brain using BMC-mcDESPOT. Neuroimage 2017;147:800–811. doi: 10.1016/j.neuroimage.2016.09.064.

23. Stanisz GJ, Odrobina EE, Pun J, Escaravage M, Graham SJ, Bronskill MJ, Henkelman RM. T1, T2 relaxation and magnetization transfer in tissue at 3T. Magn. Reson. Med. 2005;54:507–512. doi: 10.1002/mrm.20605.

24. Jiang Y, Ma D, Seiberlich N, Gulani V, Griswold MA. MR fingerprinting using fast imaging with steady state precession (FISP) with spiral readout. Magn. Reson. Med. 2015;74:1621–1631. doi: 10.1002/mrm.25559.

Chapter 5

Visualization of gold fiducial markers in the prostate using phase-cycled bSSFP imaging for MRI-only radiotherapy

ABSTRACT

Purpose:

In this work, we present a new method for visualization of fiducial markers (FMs) in the prostate for MRI-only radiotherapy with a positive contrast directly at the MR console. The method is based on high bandwidth phase-cycled balanced steady-state free precession (bSSFP) sequence, which is available on many clinical scanners, does not require any additional post-processing or software, and has a higher signal-to-noise (SNR) compared to conventional gradient-echo (GE) imaging. Complex phase-cycled bSSFP data is acquired with different RF phase increment settings such that the manifestation of the artifacts around FMs in the acquired complex images is different for each dynamic acquisition and depends on the RF phase increment used.

Methods:

First, we performed numerical simulations to investigate the complex-valued phase-cycled bSSFP signal in the presence of a gold FM, and to investigate the relation of the true physical location of the FM with the geometrical manifestation of the artifacts. Next, to validate the simulations, we performed phantoms and *in vivo* studies and compared the experimentally obtained artifacts with those predicted in simulations. The accuracy of the method was assessed by comparing the distances between the FM's centers and the center of mass of FMs system measured using phase-cycled bSSFP MR images and using reference CT (or MRI-only) images.

Results and Conclusion:

The results show accurate (within 1 mm) matching of FMs localization between CT and MR images on 5 patients, proving the feasibility of *in vivo* FMs detection on MR images only. The FMs show a positive contrast with respect to the prostate background on real/imaginary phase-cycled bSSFP images, which was confirmed by simulations. The proposed method facilitates robust FMs visualization with positive contrast directly at the MR console, allowing RT technicians to obtain immediate feedback on the anticipated feasibility of accurate FMs localization while the patient is being scanned.

Key words:
MRI-only radiotherapy, bSSFP, MRI, phase-cycled bSSFP, prostate radiotherapy, fiducial marker

5.1 Introduction

External-beam radiotherapy (EBRT) is one of the treatment options for prostate cancer. Fiducial markers (FMs) are used as landmarks for localization of the prostate before the delivery of each radiation fraction (1–3). For this purpose three or four gold cylindrical FMs (1 mm diameter, 3-5 mm length) are usually implanted in the prostate a couple of weeks before treatment under trans-rectal ultrasound guidance (two markers at the prostatic base on the right and left side and one or two towards the apex of the prostate) (4).

Manual localization of FMs during the treatment planning phase (referred to as simulation phase) is currently done on treatment planning computed tomography (CT) images, considered as the gold standard. FMs can be localized based on their distinct, local streaking artifacts in CT images. This procedure has been shown to be very robust (5–7). Currently, also MR images are being acquired for treatment planning as the soft tissue contrast of MRI offers superior localization of the tumor process. However, such a dual-modality workflow requires two separate imaging sessions, complicating workflow and patient comfort. Also from a more fundamental point of view, a dual imaging modality workflow has a drawback: an extra source of uncertainties is introduced due to a potential registration error between CT and MRI required to fuse the information (8,9).

A potential solution would be to switch to an MRI-only workflow for treatment planning where all information needed in the treatment planning process is acquired solely by MRI (10,11). A key step towards the clinical feasibility of MRI-only planning has been recent progress to derive electron density information, so-called "synthetic CT images", from MR images (12–15). Currently, MRI-only planning for radiotherapy treatment of prostate cancer is being performed by several clinics worldwide (16).

A key challenge in the clinical implementation of MRI-only planning of prostate radiotherapy, has been the robust and accurate visualization and localization of FMs on MR images. FMs induce magnetic field distortions around them due to the magnetic susceptibility difference between the metallic marker and the tissue surrounding it. These field inhomogeneities cause local artifacts in MR images (17,18), the appearance of which depends on the pulse sequence used and the imaging parameter settings. These artifacts are usually used to determine the position of FMs (19). As the local magnetic field disturbance caused by the presence of FMs depends on their shape and orientation with respect to the direction of the main magnetic field, so does the visualization of FMs on MR images (20).

Gradient-echo (GE) MR imaging is commonly used as a technique for visualization of FMs in the prostate. FMs typically appear as signal voids in GE MR magnitude images, which allows to identify and localize them. However, it is difficult to distinguish FMs from

other sources of local field inhomogeneities, like hemorrhages and calcifications, which appear as dark spots as well, and thus may resemble FMs (7,19,21,22).

Recently, an MR-based automatic gold FMs detection method was presented (23), which is based on a template matching method applied to the complex MRI data (24). This method utilizes not only the signal voids observed on magnitude images for localization, but also phase variations around the markers. Although this facilitates robust automatic localization, the method requires dedicated image processing software which is not readily available at the MR console.

To facilitate successful FM localization, FMs need to be assessed directly at the MR console while a patient is being scanned. This direct feedback allows RT technicians to immediately attempt a new scan or to refer a patient to a regular planning CT exam in case FMs are not present or cannot be directly visualized on the acquired MR images.

In this work, we present a new method for FMs visualization in the prostate for MRI-only radiotherapy, which facilitates FMs visualization with a positive contrast directly at the MR console, allowing RT technicians to immediately and easily localize FMs. The method is based on high bandwidth phase-cycled balanced steady-state free precession (bSSFP) imaging, which has a higher signal-to-noise (SNR) compared to conventional GE imaging. Phase-cycled bSSFP is a well-known MR acquisition technique, which is commonly used to eliminate the banding artifacts and to avoid signal loss in the magnitude images, which are caused by sensitivity of bSSFP signal to main magnetic field (B_0) inhomogeneities (25–28). Phase-cycled bSSFP is a dynamic sequence with a predetermined number of dynamic acquisitions, in which the RF phase is linearly increased from one dynamic to another, which shifts the off-resonance profile of the signal dependent on the RF phase increment. The contrast of FMs in the phase-cycled bSSFP images varies between each dynamic acquisition because the manifestations of the susceptibility artifacts around FMs on MR images depend on the RF phase increment.

To be able to optimize the method, we performed simulations to investigate the complex-valued phase-cycled bSSFP MR signal in the presence of one gold FM, and to investigate the relation of the true physical location of the FM with the geometrical manifestation of the artifacts. To validate the simulations, we performed phantoms and *in vivo* studies and compared the obtained experimentally artifacts with those predicted in simulations. The accuracy of the method was assessed in a phantom and *in vivo* by comparing the distances between the FM's centers and the center of mass of FMs system measured using MR images acquired with the proposed phase-cycled bSSFP method and using CT (or MRI-only) images acquired with the reference techniques.

5.2 Methods

5.2.1 Phase-cycled bSSFP signal model

RF phase cycled bSSFP is a dynamic scan, where for each dynamic acquisition the phase of the RF excitation pulse is increased stepwise from one dynamic to another according to a certain RF phase incrementing scheme. For each dynamic acquisition the complex transverse magnetization M_{xy} can be described as (27,29,30):

$$M_{xy} = M_{\text{eff}} \cdot \frac{1 - a e^{i\theta}}{1 - b \cos\theta} \cdot e^{i\varphi}, \qquad [5.1]$$

where M_{eff}, a, b are the parameters dependent on the repetition time TR, the echo time TE, the relaxation times T_1 and T_2, the flip angle α, see Equations [1-3] in (31). θ is the resonance offset angle (in radians), $\theta = \theta_0 - \Delta\theta$, where $\theta_0 = 2\pi(\delta_{CS} + \gamma\Delta B_0)TR$, $\gamma\Delta B_0$ is the spatially varying off-resonance (in Hz), which includes the background term $\gamma\Delta B_{0\,background}$ and the term related to the presence of the FM $\gamma\Delta B_{0\,FM}$, $\gamma\Delta B_0 = \gamma\Delta B_{0\,background} + \gamma\Delta B_{0\,FM}$, both terms are spatially dependent although $\gamma\Delta B_{0\,FM}$ is strongly spatially localized around the FM. δ_{CS} is the chemical shift of the species (in Hz) with respect to the water peak, $\Delta\theta$ is the phase increment (in radians) of the RF excitation pulse, $\varphi = 2\pi(\delta_{CS} + \gamma\Delta B_0)TE + \varphi_{RF\,offset}$. $\varphi_{RF\,offset}$ is the RF phase offset, related to the combination of RF transmit and receive phases (in radians). The use of phase-cycling shifts the off-resonance profile of the signal dependent on the RF phase increment, which is usually set to $\Delta\theta = \frac{2\pi n}{N}$ (26), where n is the number of nth dynamic acquisition, N is the total number of dynamic acquisitions.

The RF phase offset $\varphi_{RF\,offset}$ and the chemical shift of the species δ_{CS} are constant offsets. Without loss of generality, we chose them to be zero.

5.2.2 Simulations

Simulations of the phase-cycled bSSFP signal in the presence of one cylindrical gold FM (1 mm diameter, 5 mm length) were performed. Simulations were adopted from the work by Beld et al (32), where the bSSFP steady-state signal in Equation [5.1] was assumed to be proportional to the effective spin density distribution. The complex-valued 3D phase-cycled bSSFP MR signal was simulated for two cases: $\gamma\Delta B_{0\,background}$ = 0 and $\gamma\Delta B_{0\,background}$ = -15 Hz. The RF phase incrementing scheme $\Delta\theta = [0, \frac{\pi}{3}, \frac{2\pi}{3}, \pi, \frac{4\pi}{3}, \frac{5\pi}{3}]$ was used.

The scan parameter settings in the simulations were the same as the protocol parameter settings of the MR sequence used for the experiment on the phantom with one FM: field strength 3T, TE = 3.3 ms, TR = 6.7 ms, FA = 25°, FOV = 50x50x50 mm^3, readout bandwidth = 905.8 Hz, readout direction LR, 6 dynamic acquisitions with increment $\Delta\theta = \pi/3$, voxel size 1x1x1 mm^3, susceptibility of gold χ_{Au} = -34 ppm, susceptibility of water χ_{water} = -9.05 ppm. 10x10x10 = 10^3 isochromats were simulated per voxel for an image with 1x1-mm^2 in-plane voxels and a slice thickness of 1 mm. The relaxation times for the prostate at 3T were used for the simulations of the signal arising from the background tissue, with T$_1$ = 1400 ms, T$_2$ = 80 ms (33).

All simulations and calculations were performed in MATLAB R2015a (The MathWorks Inc, Natick, United States).

5.2.3 Experiments

5.2.3.1 Experiments in phantoms

First, to validate the simulations, we compared the artifact patterns obtained in a phantom experimentally with those predicted by simulations. The experiment was performed using a clinical 3T MR scanner (Philips Ingenia, Best, The Netherlands) on an agar gel phantom with one gold FM (GM1054) implanted. A 15-channel head receive coil was used. Complex 3D phase-cycled bSSFP data were acquired using the following protocol parameter settings: TR 6.7 ms, TE 3.3 ms, FA 25°, FOV 200x200x60 mm^3, acquisition voxel size 1x1x1 mm^3, reconstruction voxel size 0.89x0.89x1 mm^3, 6 dynamics acquisitions with RF phase increment $\Delta\theta = [0, \frac{\pi}{3}, \frac{2\pi}{3}, \pi, \frac{4\pi}{3}, \frac{5\pi}{3}]$, scan time 03:59 min.

In spoiled gradient echo (SPGR) imaging the echo time TE is the most important parameter related to the susceptibility artifact's size. In bSSFP imaging the echo time TE is always equal to TR/2. To investigate, how the choice of TR influences the FM's visualization in bSSFP images, complex 3D phase-cycled bSSFP data were additionally acquired for two different TR settings: TR = 4.9 ms and TR = 10 ms. The results were compared with the case of TR = 6.7 ms, FA = 25°. Note that TE = TR/2 for each case.

Next, to assess the accuracy of the FMs localization, the experiment was performed on an agar gel phantom with four gold FMs (GM1054) implanted using the same MR scanner with the same coil. Complex 3D phase-cycled bSSFP data were acquired using the following protocol parameter settings: TR 6.7 ms, TE 3.3 ms, FA 25°, FOV 320x320x60 mm^3, acquisition voxel size 1.5x1.5x2 mm^3, reconstruction voxel size 1x1x1 mm^3, 6

dynamics acquisitions with $\Delta\theta = [0, \frac{\pi}{3}, \frac{2\pi}{3}, \pi, \frac{4\pi}{3}, \frac{5\pi}{3}]$, scan time 02:07 min. A CT scan of the same phantom was acquired using a Philips Brilliance CT Big Bore (Philips, Best, The Netherlands) with the following parameter settings: 120 kVp, exposure 450 mAs, FOV 369x369x200 mm^3, voxel size 0.72x0.72x1 mm^3.

The coordinates of the top and the bottom of each FM were measured both on MR and CT images by a single observer using an in-house developed tool called Volumetool (34). Using the measured coordinates, the coordinates of the centers on FMs were calculated. Next, the coordinates of the center of mass (average coordinates) were calculated, and the distances from FM's centers to the center of mass were calculated. The accuracy of detecting FMs was assessed by comparing the calculated distances using MR and CT images.

5.2.3.2 Experiments *in vivo*

10 patients participated in this study: 5 patients were scanned according to our institution's standard clinical EBRT protocol which includes MRI and CT exams. The other 5 patients were scanned according to the clinical MRI-only protocol. Patient data was acquired in accordance with regulations set out by the local institutional review board. For all 10 patients, in addition to clinical MRI EBRT protocol, complex 3D phase-cycled bSSFP data were acquired on a clinical 3T MR scanner using a 16-channel anterior receive coil combined with the posterior receive coil integrated in the MR table. The protocol parameter settings were used: TR 6.7 ms, TE 3.3 ms, FA 25°, FOV 320x320x60 mm^3, acquisition voxel size 1.5x1.5x2 mm^3, reconstruction voxel size 1x1x1 mm^3. Water-selective binomial excitation (ProSet type 1-3-3-1) was used for fat suppression. The acquisition time was 02:07 min. For all 10 patients the coordinates of the top and the bottom of each FM were identified on the acquired phase-cycled bSSFP MR images by a single observer using Volumetool. Next, the coordinates of the centers of FMs and the center of mass were calculated, as well as the distances from FM's centers to the center of mass (as was done for the phantom).

CT scans of 5 out of 10 patients were acquired according to our clinical CT EBRT protocol on a Philips Brilliance CT Big Bore scanner, with the following parameter settings: 120 kVp, exposure range for 5 patients was (83-186) mAs, FOV 446x446x279 mm^3, voxel size 0.87x0.87x3 mm^3. For these 5 patients the coordinates of the top and the bottom of each FM were identified on CT images by a single observer using Volumetool. Next, the coordinates of the centers of FMs and the center of mass were calculated as well as the

distances from FM's centers to the center of mass. The accuracy of localization of FMs was assessed by comparing the calculated distances using MR and CT images.

For the other 5 patients, which were scanned under clinical MRI-only protocol and thus no CT images were available, the coordinates of top and bottom of FMs were identified using MR images acquired with a clinically used high resolution bSSFP SPAIR (Spectral Attenuated Inversion Recovery) sequence in our radiotherapy department's MRI-only protocol (FOV 250x250x90 mm^3, acquisition voxel size 1x1x2 mm^3, reconstruction voxel size 0.49x0.49x1 mm^3). The acquisition time was 02:07 min. The coordinates of the centers of FMs, and the distances from the FM's centers to the center of mass were calculated. The accuracy of detecting FMs was assessed by comparing the calculated distances using both types of MR images.

Next, we visually compared the acquired dynamic images for all 10 patients and investigated, which dynamic, i.e. which RF phase increment, allows for the best visualization of FMs. As a result, a certain dynamic was selected, and the coordinates of the centers of FMs were identified using the selected scan. Again, the distances from FM's centers to the center of mass of the FM's system were calculated. The accuracy of detecting FMs in this case was assessed by comparing the calculated distances using MR images acquired with the proposed phase-cycled bSSFP method with the reference measurements (CT or MR SPAIR bSSFP for MRI-only), and the corresponding Bland-Altman plots were made.

5.3 Results

5.3.1 Simulation results

Simulation results for one gold FM are shown in Figure 5.1. Magnitude, real and imaginary images are shown for coronal and axial planes for 6 dynamic acquisitions corresponding to different RF phase increments for two different spatially constant $\gamma \Delta B_{0\ background}$ values: 0 Hz and -15 Hz. A distinct artifact pattern can be seen over all simulated dynamic images for both values of $\gamma \Delta B_{0\ background}$. A shift of about one dynamic in the artifact pattern can be observed between these cases, which is caused by the difference in $\gamma \Delta B_{0\ background}$. Figure 5.2 shows the zoomed-in images of the FM in the coronal plane, with the actual contours of the FM overlaid (case $\gamma \Delta B_{0\ background}$ = 0). The artifacts exceed the actual size of the FM as expected, since the field disturbances extend beyond the FM.

Both ends (top and bottom) of the FM are especially well visible on the images of dynamics number 1 (RF phase increment $\Delta\theta = 0$) and number 2 (RF phase increment $\Delta\theta = {}^{\pi}/_{3}$). Interestingly, on the imaginary image of dynamics number 5 (RF phase

increment $\Delta\theta = {}^{4\pi}/_3$) and number 6 (RF phase increment $\Delta\theta = {}^{5\pi}/_3$), the center of the bright spot on a dark background corresponds to the center of the FM, as can be seen in Figure 5.2.

The simulations show that signal localization corresponds with the physical locations of the FM.

5.3.2 Experimental results in phantoms

MR images acquired in the phantom with one FM are shown in Figure 5.3. Magnitude, real, and imaginary images are shown for 6 dynamic acquisitions for coronal and axial planes. The experimental $\gamma\Delta B_{0\ background}$ was found to be approximately -15 Hz in the center of the FM (by interpolating the background field not disturbed by FMs). The results match the simulation results shown in Figure 1(b). The images show a distinct MR contrast between the FM and the background for each dynamic. Unlike in the simulated MR images, where the background tissue signal is homogeneous, dark bands can be observed in MR images acquired in the phantom. These bands are known as banding artifacts and they are caused by the abrupt loss of the bSSFP signal at particular off-resonances. The spatially varying background B_0 field in the phantom was not included in the simulations, where it was assumed spatially constant. In all the images in axial plane a line can be observed in the middle of the phantom. This effect is related to the way the phantom was built: the second layer of agar was placed on the first layer containing the FM.

A comparison of the images acquired with different TR settings is presented in Figure 5.4. The magnitude, real, and imaginary images are shown in coronal and axial planes for three dynamics number 1, number 2, and number 5. Only very small differences can be observed in the FM's artifacts. The contrast differences are caused by different signal intensities acquired at different TR settings. The banding artifacts appear differently as the off-resonance frequencies at which they appear depend on TR as well. The echo time TE (which is equal to TR/2) almost does not change the appearance of the artifacts.

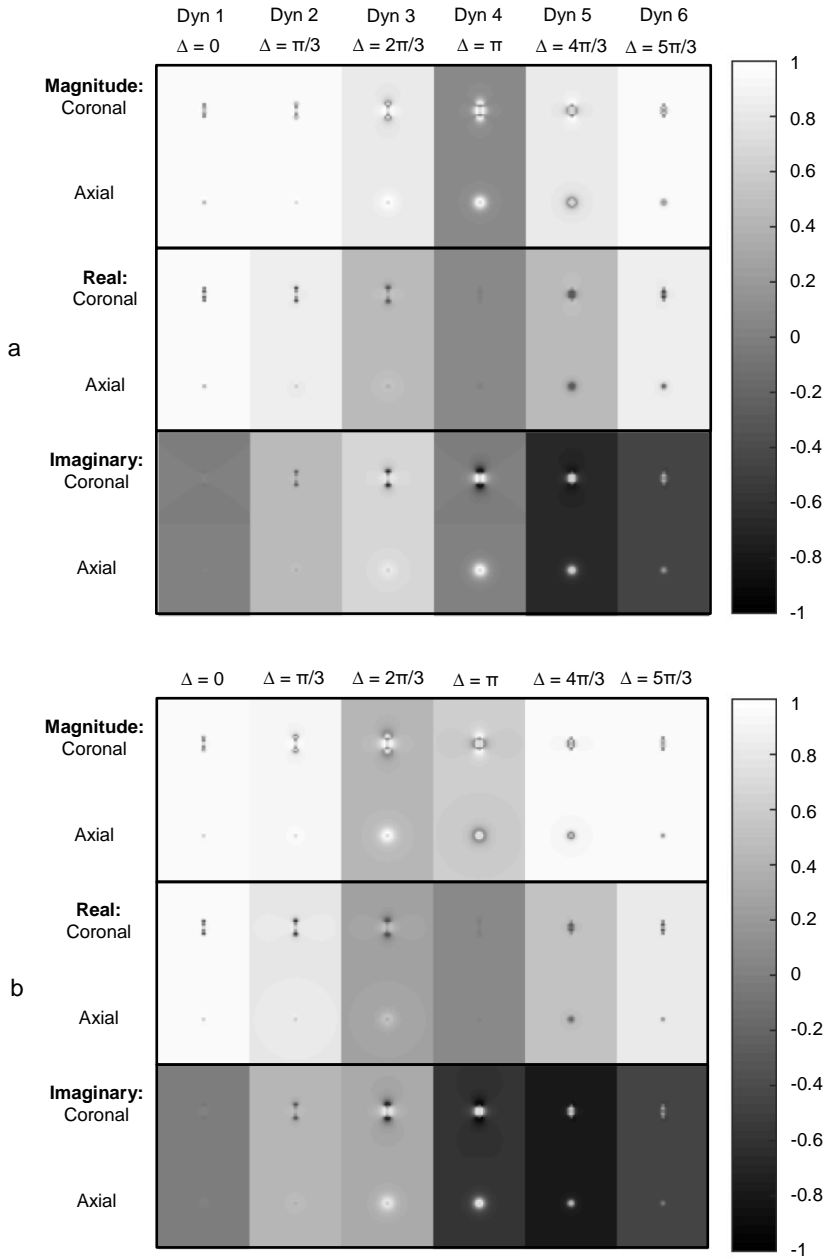FIGURE 5.1. Simulation results of a single FM embedded in a homogeneous background tissue: the magnitude, real, and imaginary images simulated for coronal and axial planes for 6 dynamic acquisitions corresponding to different RF phase increment settings $\Delta\theta$. a) The background term $\gamma\Delta B_{0\,background}$ = 0; b) The background term $\gamma\Delta B_{0\,background}$ = - 15 Hz.

The experimental results of scanning the phantom with four FMs are shown in Figure 5.5. Magnitude, real, and imaginary images are shown for 6 dynamic acquisitions for coronal and axial planes through the 3D volume. The same distinct artifact pattern, which was predicted in simulations and which was seen in the experimental results in the phantom with one FM, can be observed here as well. The only difference here is that there are four FMs placed close to each other causing the artifact pattern to be slightly different. A photograph of the coronal plane and corresponding CT images for coronal and axial planes are shown for comparison. The distances between FM's centers and the center of mass measured using MR and CT images are provided in Table 5.1.

5.3.3 Experimental results *in vivo*

The acquired data for 10 patients were processed. An example of MR images of the prostate of a patient with four implanted FMs is shown in Figure 5.6. A similar varying contrast pattern (dependent on the RF phase increment used) as induced by FM in the phantom, can be seen in this patient. FMs can be clearly seen on the acquired images and they show distinct artifact pattern. FMs appear very bright on the imaginary images of dynamics number 5 (RF phase increment $\Delta\theta = {}^{4\pi}/_{3}$) and number 6 (RF phase increment $\Delta\theta = {}^{5\pi}/_{3}$). This positive contrast facilitates a relatively straight forward direct visual localization of the FMs by an observer. Similar results were obtained in the other 9 patients: bright appearance of the FMs was observed on dynamics number 5 and 6 of real or imaginary images dependent on the actual RF phase offset $\varphi_{RF\,\text{offset}}$ (which was assumed to be zero in simulations). The results for four patients are shown in Figure 5.7. Since the center of the FM is the center of the bright spot, as shown in Figure 5.2, imaginary/real images of dynamics number 5 and number 6 can be used directly for localization of the FM's centers.

An example of a patient with calcification in the prostate is shown in Figure 5.8. FMs show distinct behavior over all dynamic acquisitions as expected. Calcification was observed at CT images as a bright spot without streaking artifacts. At MR images the same calcification was observed as a dark spot on the magnitude images and a slightly bright spot on a dark prostate background on the imaginary images. We did not observe any significant changes in the appearance of this calcification in MR images for different RF phase increments.
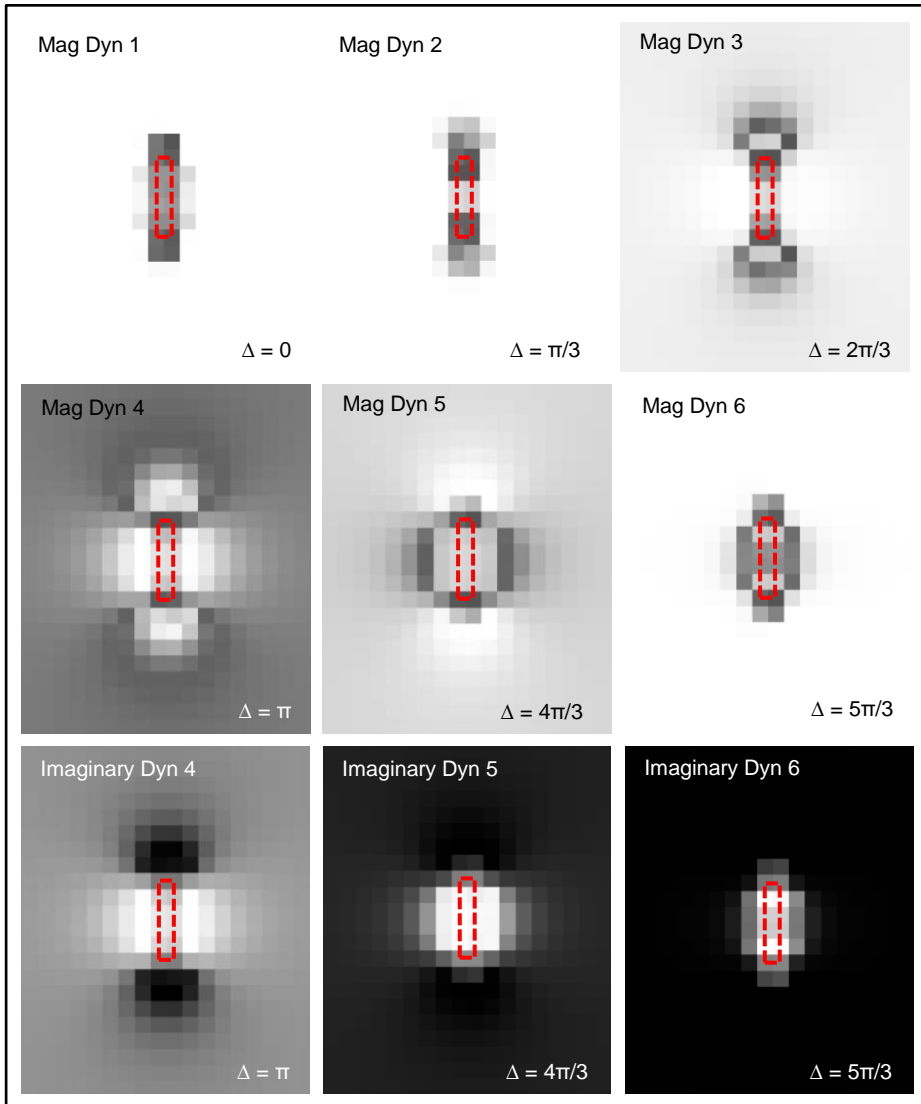
FIGURE 5.2. The zoomed-in simulated images of the artifacts around one FM in the coronal plane, for different dynamics, with the actual contour of the FM overlaid (red dashed rectangle). The simulation was done for $\gamma \Delta B_{0\ background} = 0$.

FIGURE 5.3. Experimental results of the phantom with one gold FM implanted: the magnitude, real, and imaginary images for coronal and axial planes for six dynamic acquisitions corresponding to different RF phase increment settings. The data was acquired in 3D and shown only for two middle orthogonal slices.
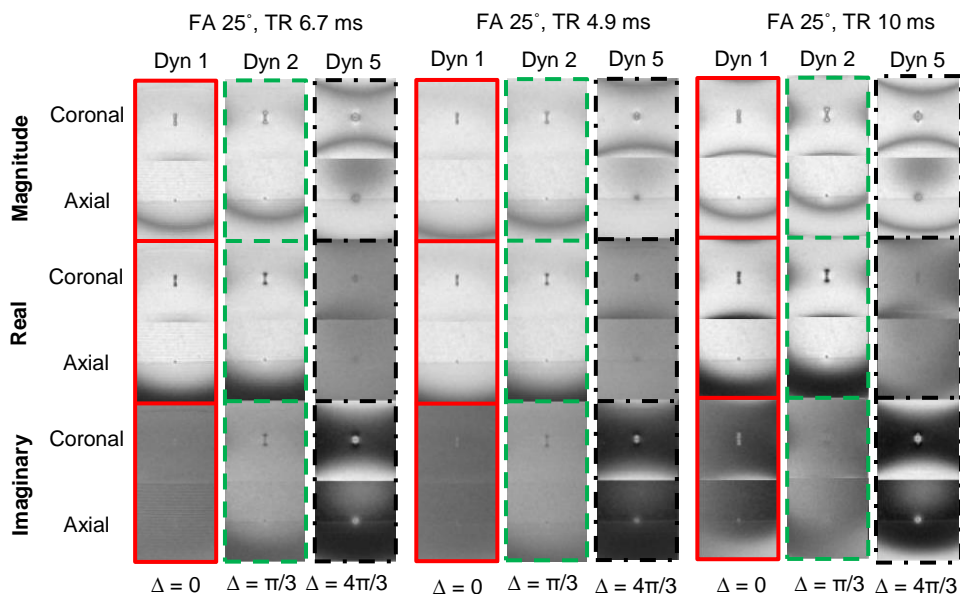
FIGURE 5.4 Comparison of the images acquired with different TR settings: the magnitude, real, and imaginary images for coronal and axial planes for dynamics number 1 (red solid frame), number 2 (green dashed frame), and nuber 5 (black dash dotted frame). Corresponding RF phase increment settings are ∆ = 0, π/3, 4π/3. Three cases are shown: TR = 6,7 ms, TR = 4.9 ms, TR = 10 ms. FA = 25˚ and TE = TR/2 for each case.
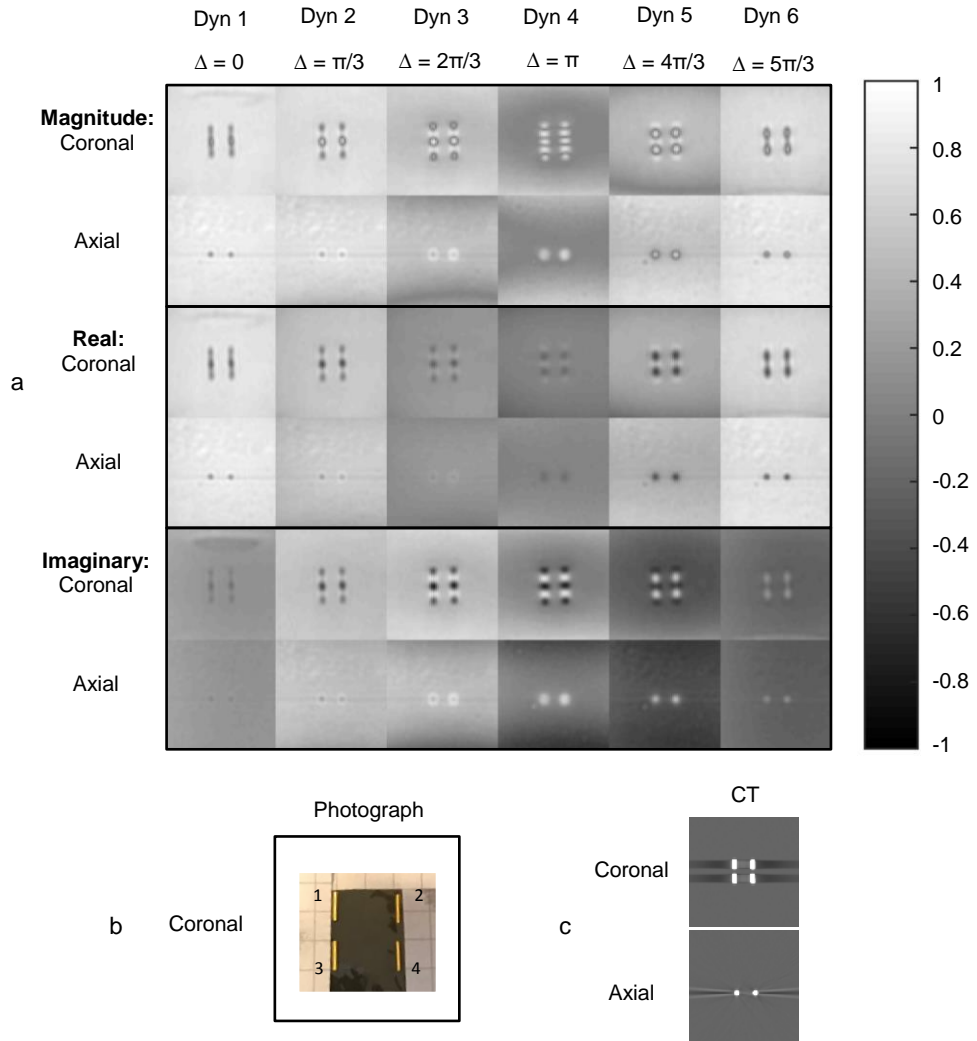
FIGURE 5.5. Experimental results of the phantom with four gold FM implanted: a) The magnitude, real, and imaginary images for coronal a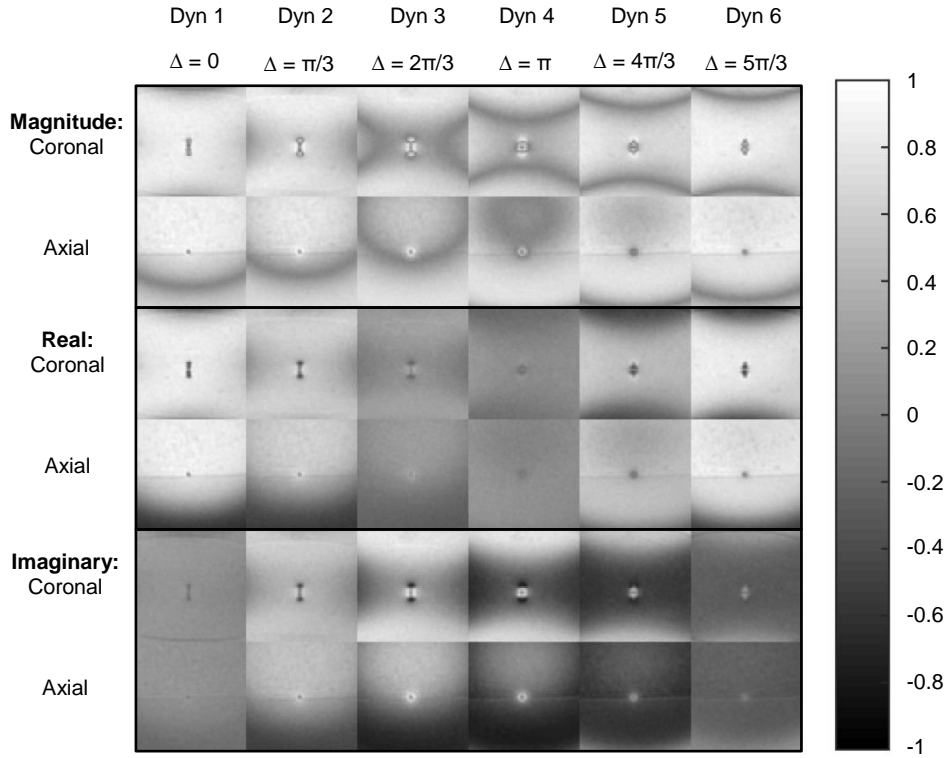nd axial planes for 6 dynamic acquisitions corresponding to different RF phase increment settings; b) A photograph of the FMs in coronal plane; c) The CT image of the phantom in coronal and axial planes.
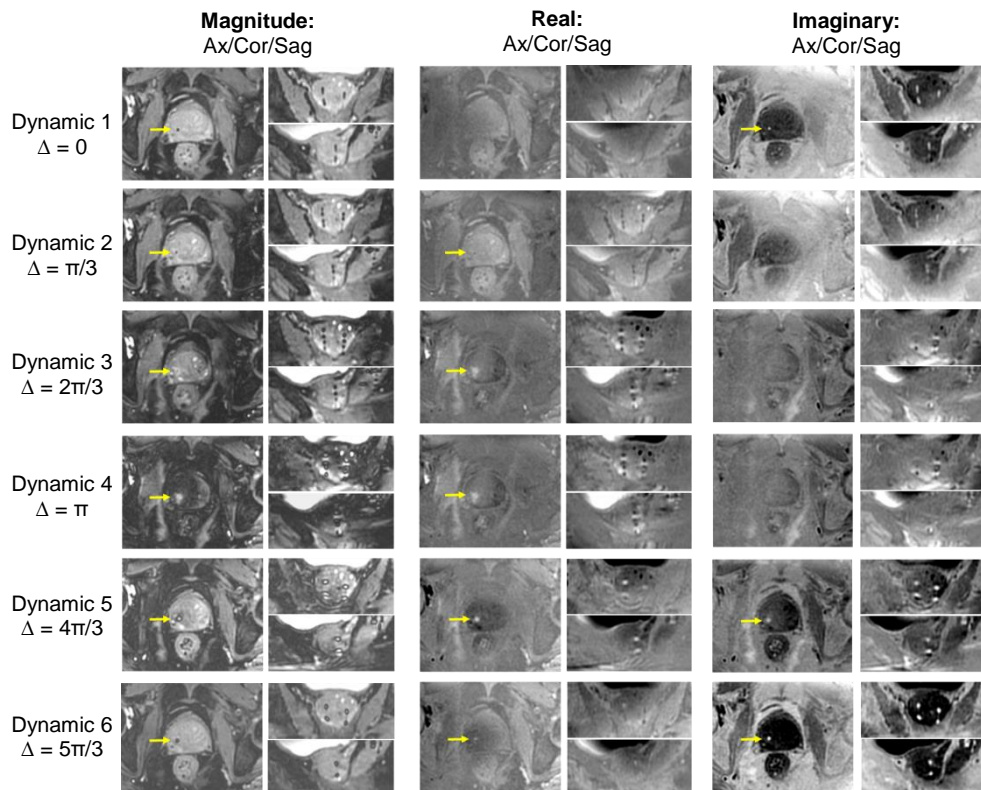
FIGURE 5.6. Example of images acquired in a patient: the magnitude, real and imaginary images for axial, coronal, and sagittal and planes for 6 dynamic acquisitions. The small yellow arrows indicate the locations of the FMs in the axial images (where visible).
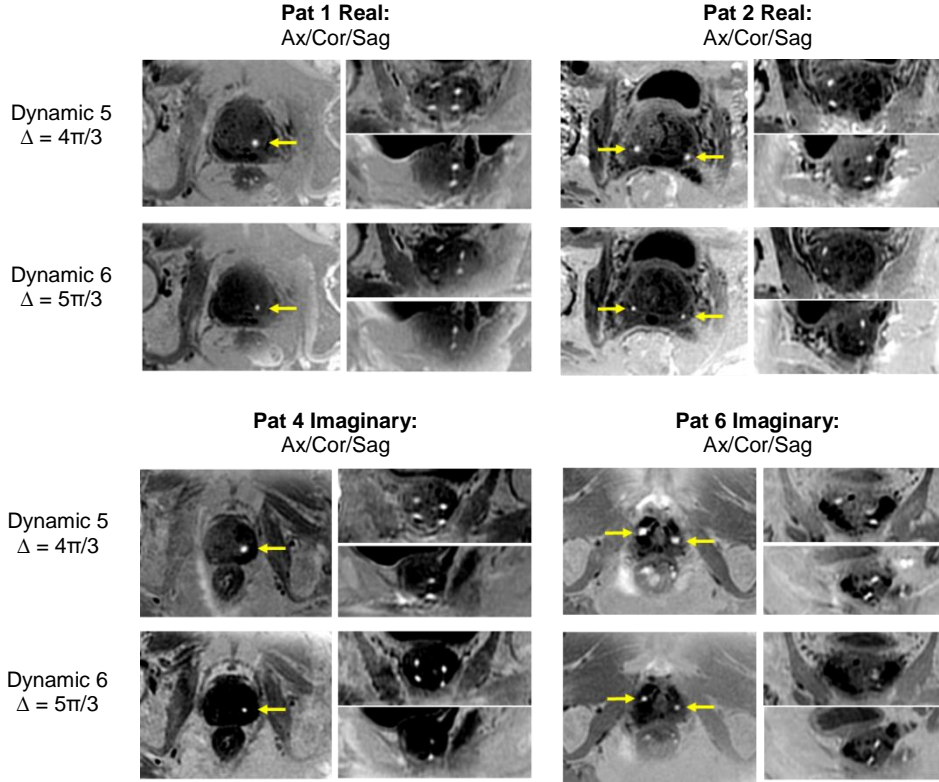
FIGURE 5.7. Comparison of images acquired in four patients: the real images for axial, coronal, and sagittal planes for dynamics number 5 and 6 for patients number 1 and 2; the imaginary images for axial, coronal, and sagittal planes for dynamics number 5 and 6 for patients number 3 and 4. The small yellow arrows indicate the locations of the FMs in the axial images.
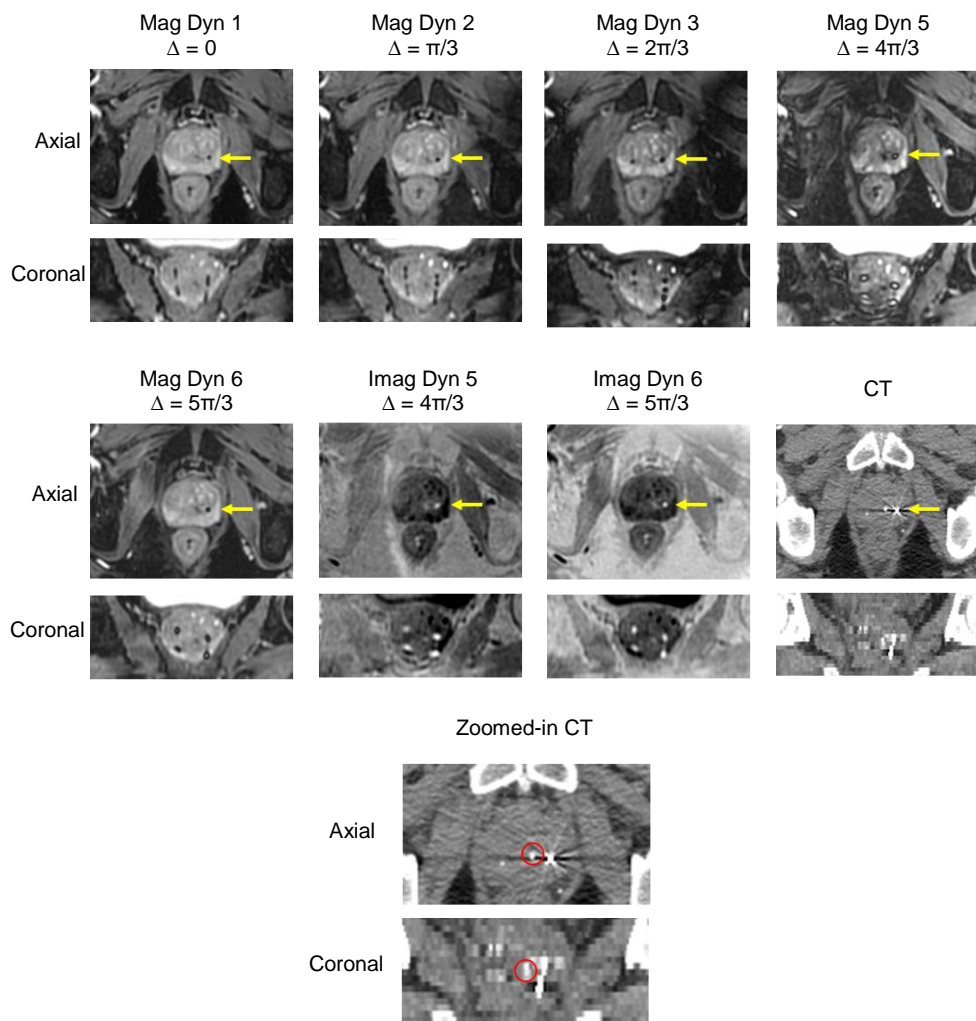
FIGURE 5.8. Example of images acquired in a patient with calcification in the prostate (identified with CT): the magnitude, real, and imaginary images for axial and coronal planes for few different dynamics; the CT images for axial and coronal planes. The small yellow arrows indicate the locations of the one of the FMs in the axial images. The calcification is marked with red circle on zoomed-in CT images.

An example of the performance of the method in a patient with rectal gas is shown in Figure 5.9. The banding artifacts, which can be seen on the prostate area, are caused by rectal gas, and their position depends on the RF phase increment. However, the FMs can still be clearly visualized over all dynamics, and the artifact pattern remains similar to the one predicted by simulations and obtained experimentally in other patients. The use of phase-cycling actually shifts the spatial location of the banding artifacts. Thus, there will always a phase-cycled image, where the bands do not coincide with the FMs.
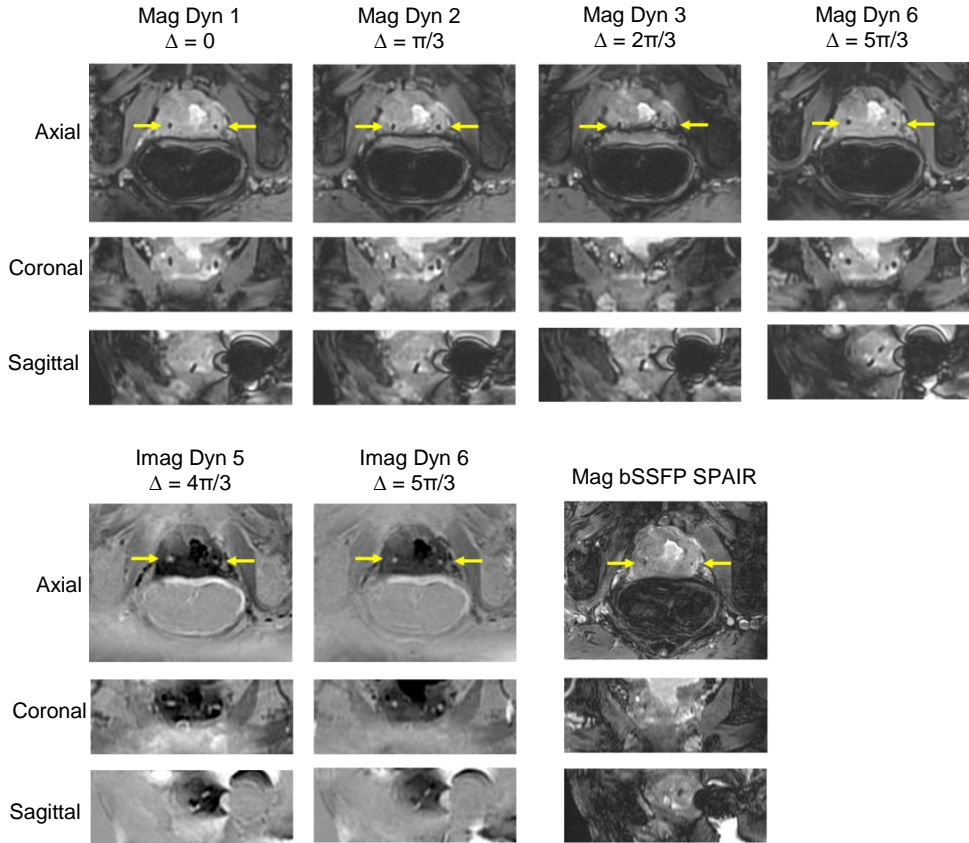
FIGURE 5.9. Example of images acquired in a patient with gas in the rectum: the magnitude, real, and imaginary images for axial, coronal, and sagittal planes for few different dynamics. Magnitude image of bSSFP SPAIR used in a standard MRI-only protocol is shown for comparison. Images are shown for 3 orthogonal slices of 3D volumes. Note that the banding artifact close to the rectal wall shifts as results of using phase-cycling. The small yellow arrows indicate the locations of the FMs in the axial images.

5.3.4 Accuracy of the FMs localization

In the phantom, the differences in distances measured between the centers of the FMs and the center of mass on MR and CT images using Volumetool are shown in Table 5.1. The errors are within 0.2 mm.

In vivo results are presented in Figure 5.10: Bland-Altman plots comparing two measurement methods are shown: a) the measurements done using the phase-cycled bSSFP MR images (top and bottom of FMs identified on the magnitude images of dynamics number 1, 2, and 3) are compared with the measurements done using the reference images (CT or SPAIR bSSFP for MRI-only); b) the measurements done using the phase-cycled bSSFP MR images (the centers of "bright spot" artifacts, identified using the real/imaginary images of dynamics number 5, 6) are compared with the measurements done using the reference images (CT or SPAIR bSSFP for MRI-only).

In these plots the differences between the two methods are plotted against the averages of these two methods. Horizontal lines are drawn at the mean difference, and at the limits of agreement, which were defined as the mean difference plus and minus 1.96 times the standard deviation of the differences. The mean values for both cases are close to zero. Standard deviations were around 0.5 mm.

Table 5.1. The measurements in the phantom with four FMs implanted

Type of imaging	Distance (D_n) between the center of the nth FM and the center of mass of FMs system (mm)			
	D_1	D_2	D_3	D_4
CT	7.0	7.0	6.9	7.0
MRI	7.0	7.1	7.0	7.1
Deviation (MRI-CT)	0	0.1	0.1	0.1

Bland-Altman plot: MRI vs Ref CT/MRI-only

a

Bland-Altman plot: MRI (center of the bright spots) vs Ref CT/MRI-only

b
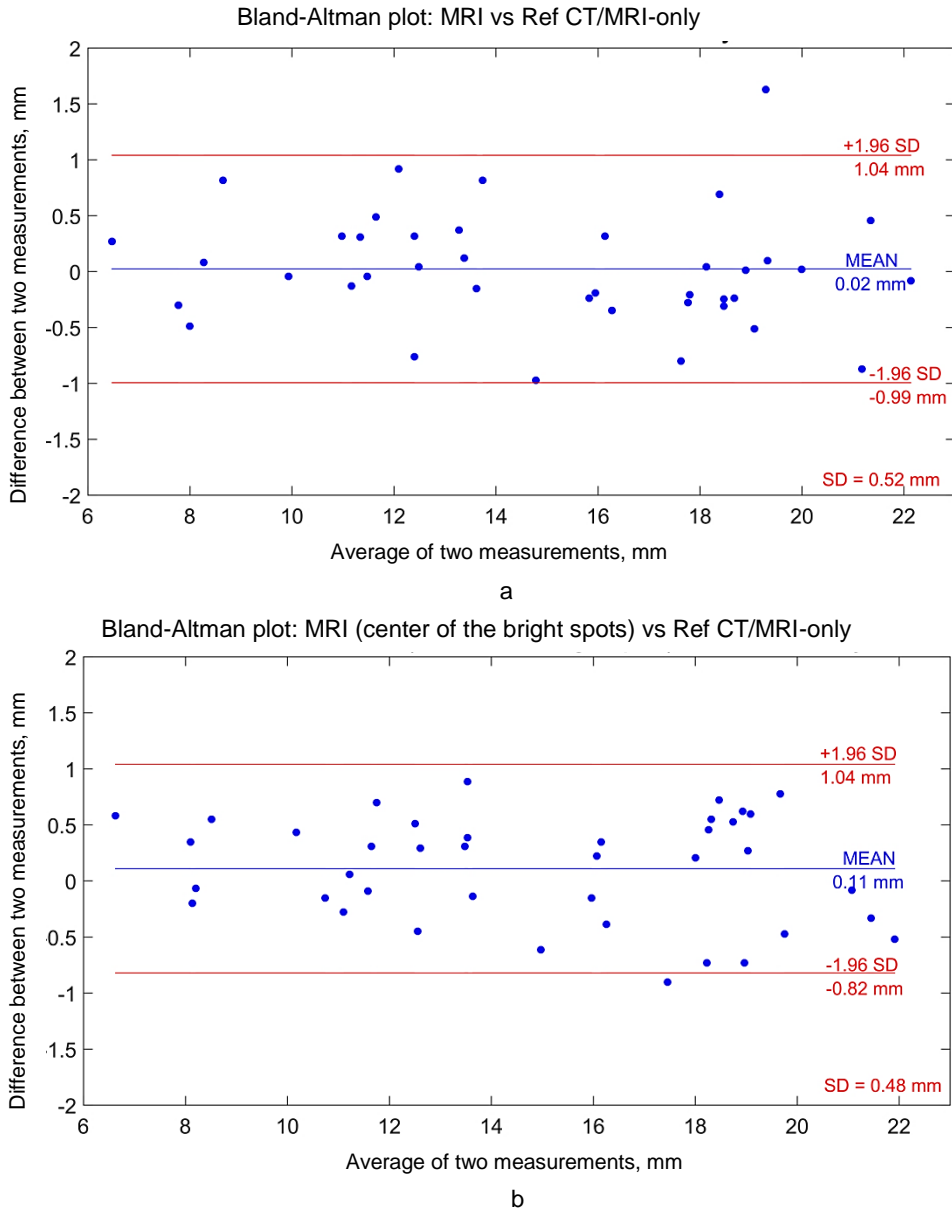
FIGURE 5.10. Bland-Altman plots: a) The measurements done using MR images (top and bottom of the FMs identified on the magnitude images of dynamics number 1, 2, and 3) acquired using phase-cycled bSSFP sequence are compared with the measurements done using the reference images (CT or SPAIR bSSFP for MRI-only); b) The measurements done using MR images (the centers of "bright spot" artifacts, identified using the real/imaginary images of dynamics number 5, 6) acquired using phase-cycled bSSFP sequence are compared with the measurements done using the reference images (CT or SPAIR bSSFP for MRI-only).

5.4 Discussion

In this work, we introduced a new method for FMs visualization in the prostate for MRI-only radiotherapy. There are other techniques for visualization of markers with positive contrast (35–38), however, they rely on non-standard acquisition modifications or dedicated post-processing software. We opted for the use of bSSFP sequence for this purpose, since it is available on most clinical scanners, works without the need for dedicated processing software, provides the highest SNR efficiency with respect to other existing MR sequences, and allows for good visualization of the prostate. The bSSFP sequence employs a relatively short TR, leading to acceptable acquisition time and high bandwidth, ensuring geometric fidelity.

The presented method is based on acquiring complex phase-cycled bSSFP data with different RF phase increment settings such that the manifestation of the artifacts around FMs in the acquired complex images is different for each dynamic acquisition and depends on the RF phase increment used.

By inspecting the acquired dynamic complex images, a certain dynamic can be chosen and used by RT technicians for FMs localization. We found that the imaginary/real images of dynamics number 5 and number 6 provide optimal positive contrast for direct localization of the FM's centers (applicable at 3T, TR 6.7 ms, TE 3.3 ms, 6 dynamics with RF phase increment $\Delta\theta = [0, \frac{\pi}{3}, \frac{2\pi}{3}, \pi, \frac{4\pi}{3}, \frac{5\pi}{3}]$). The simulations and phantom results indicate that the centers of bright spots within a dark prostate background coincide with the FM's centers. Hence, the proposed method facilitates FMs visualization with a positive contrast directly at the MR console, allowing RT technicians to localize FMs during the scan session.

However, a bright appearance of the FMs on real or imaginary images of dynamics number 5 and number 6 depends on the actual background B_0 field. Spatial variations of the B_0 field induce differences in the artifacts around FMs in MR images. As we showed in the simulations, different background B_0 field causes a shift in the artifact pattern. In the prostate, the B_0 field is usually quite homogeneous with the differences in $\gamma\Delta B_{0\,background}$ in the range [-10 Hz; 10 Hz] or maximum absolute differences in $\gamma\Delta B_{0\,background}$ within the prostate of around 20 Hz. Due to imperfect shimming or B_0 drift, the off-resonance $\gamma\Delta B_{0\,background}$ can vary even more, in such a case the bright appearance of the FMs can be observed on different dynamics, shifted relative to the original one, for example, number 4 and number 5, or number 6 and number 1.

In general, for a similar experimental setup (field strength 3T, TR 6.7 ms, TE 3.3 ms, 6 dynamics with RF phase increment $\Delta\theta = [0, \frac{\pi}{3}, \frac{2\pi}{3}, \pi, \frac{4\pi}{3}, \frac{5\pi}{3}]$, we believe that for most patients with the same gold FMs, the positive contrast will be visible in dynamics number 5

($\Delta\theta = \frac{4\pi}{3}$) and number 6 ($\Delta\theta = \frac{5\pi}{3}$). At different magnetic field strengths and/or different MR acquisition parameter settings, the appearance of FMs might be different, and the RF phase increment for which positive contrast is seen may vary. Nevertheless, FMs will always show positive contrast with the background at certain specific RF phase increment.

The simulations were performed for a single FM. In reality four FMs will be implanted in the prostate, however, we do not expect them to influence each other's appearance. The changes in the local magnetic field due to the presence of a neighboring FM are very small compared to the local magnetic field. Therefore, the magnetic moment of a FM will not be affected by the magnetic moment of others FMs.

The simulations were only performed when a FM was parallel to the main magnetic field. We observed similar artifact patterns in cases with slight angulations of FMs, which occurred in some patients. We did not see any significant artifact deviations in all 10 patients included in this study.

In 1 out of 10 patients we observed calcification. FMs, in this case, showed a distinct behavior in all acquired dynamic images, whereas calcification remained almost the same in all acquired images. We expect that calcification cannot replicate the FM's artifact pattern and therefore they can be distinguished from one another.

The main drawback of using bSSFP imaging is the presence of banding artifacts on the acquired magnitude images due to B_0 inhomogeneity. The use of shorter TR might help to shift the banding artifacts towards outer FOV. B_0 distortions are often caused by the rectal gas, which leads to banding artifacts located very close to the rectal wall or inside the prostate. Based on an example of one patient with rectal gas, we expect FMs to be distinctly visualized in all acquired images with artifact pattern similar to the one predicted by simulations. An additional advantage of the use of phase-cycling is that the banding artifacts spatially shift for different RF phase increments allowing always an observation where the banding artifacts do not coincide with the FMs.

For this pulse sequence, TE is always chosen equal to TR/2. As we showed, the choice of TR has a very minor effect on the appearance of the artifacts, which allows for adjustment of TR (and correspondingly TE) for any specific purpose, such as to save scanning time by decreasing TR or to acquire fat-water in-phase or out-of-phase images by adjusting TE.

The acquisition time is proportional to the number of dynamics used. In our experiments, we used the RF phase-cycling scheme with 6 RF phase increment settings, which resulted in the acquisition time of about 2 min. However, the number of RF phase increment settings can be further reduced to 4 or even less to save scanning time.

The manifestations of the artifacts around FMs in phase-cycled bSSFP images depend on the RF phase increment and are different for each dynamic acquisition, which creates a specific pattern of artifacts. This knowledge can be further used for template matching algorithms, which may increase the accuracy of automatic FMs localization methods, at the cost of needing post-processing software.

The results show accurate (within 1 mm) matching of FMs localization between CT and MR images on 5 patients, proving the feasibility of *in vivo* FMs detection on MR images only.

Our results show that in the real/imaginary images of the dynamics number 5 and number 6, the prostate manifests itself as a strongly hypo-intense structure with very good contrast with neighboring tissues. In the future, we will investigate whether this technique could be used for prostate contouring as well. A multi-purpose sequence for contouring and FMs localization is desirable as for separate scans there is always the risk of inter-scan motion that will propagate as a systematic error in the position of the prostate. Additionally, the use of a multi-purpose sequence would reduce the overall examination time, which is clinically beneficial.

5.5 Conclusion

We have presented a new method for direct visualization of fiducial markers in the prostate for MRI-only radiotherapy. The method is based on phase-cycled bSSFP imaging, providing different contrast of FMs with background dependent on RF phase increment used. The method does not require any additional post-processing or software. Thereby, detection of FMs can be easily done directly at the MR console, allowing RT technicians to obtain immediate feedback on the anticipated feasibility of accurate FM localization while the patient is being scanned.

5.6 References

1. Crook JM, Raymond Y, Salhani D, Yang H, Esche B. Prostate motion during standard radiotherapy as assessed by fiducial markers. Radiother. Oncol. 1995;37:35–42. doi: 10.1016/0167-8140(95)01613-L.

2. Dehnad H, Nederveen AJ, Van Der Heide UA, Van Moorselaar RJA, Hofman P, Lagendijk JJW. Clinical feasibility study for the use of implanted gold seeds in the prostate as reliable positioning markers during megavoltage irradiation. Radiother. Oncol. 2003;67:295–302. doi: 10.1016/S0167-8140(03)00078-1.

3. Parker CC, Damyanovich A, Haycocks T, Haider M, Bayley A, Catton CN. Magnetic resonance imaging in the radiation treatment planning of localized prostate cancer using intra-prostatic fiducial markers for computed tomography co-registration. Radiother. Oncol. 2003;66:217–224. doi: 10.1016/S0167-8140(02)00407-3.

4. Herman MG, Pisansky TM, Kruse JJ, Prisciandaro JI, Davis BJ, King BF. Technical aspects of daily online positioning of the prostate for three-dimensional conformal radiotherapy using an electronic portal imaging device. Int. J. Radiat. Oncol. Biol. Phys. 2003;57:1131–1140. doi: 10.1016/S0360-3016(03)00766-1.

5. Nederveen A, Lagendijk J, Hofman P. Detection of fiducial gold markers for automatic on-line megavoltage position verification using a marker extraction kernel (MEK). Int. J. Radiat. Oncol. Biol. Phys. 2000;47:1435–1442. doi: 10.1016/S0360-3016(00)00523-X.

6. Habermehl D, Henkner K, Ecker S, Jäkel O, Debus J, Combs SE. Evaluation of different fiducial markers for image-guided radiotherapy and particle therapy. J. Radiat. Res. 2013;54:i61–i68. doi: 10.1093/jrr/rrt071.

7. Chan MF, Cohen GN, Deasy JO. Qualitative Evaluation of Fiducial Markers for Radiotherapy Imaging. Technol. Cancer Res. Treat. 2015;14:298–304. doi: 10.1177/1533034614547447.

8. Roberson PL, McLaughlin PW, Narayana V, Troyer S, Hixson G V, Kessler ML. Use and uncertainties of mutual information for computed tomography/magnetic resonance (CT/MR) registration post permanent implant of the prostate. Med. Phys. 2005;32:473–482. doi: 10.1118/1.1851920.

9. Nyholm T, Nyberg M, Karlsson MG, Karlsson M. Systematisation of spatial uncertainties for comparison between a MR and a CT-based radiotherapy workflow for prostate treatments. Radiat. Oncol. 2009;4:54–62. doi: 10.1186/1748-717X-4-54.

10. Khoo VS, Dearnaley DP, Finnigan DJ, Padhani A, Tanner SF, Leach MO. Magnetic resonance imaging (MRI): Considerations and applications in radiotherapy treatment planning. Radiother. Oncol. 1997;42:1–15. doi: 10.1016/S0167-8140(96)01866-X.

11. Lee YK, Bollet M, Charles-Edwards G, Flower MA, Leach MO, McNair H, Moore E, Rowbottom C, Webb S. Radiotherapy treatment planning of prostate cancer using magnetic resonance imaging alone. Radiother. Oncol. 2003;66:203–216. doi: 10.1016/S0167-8140(02)00440-1.

12. Korhonen J, Kapanen M, Keyriläinen J, Seppälä T, Tenhunen M. A dual model HU conversion from MRI intensity values within and outside of bone segment for MRI-based radiotherapy treatment planning of prostate cancer. Med. Phys. 2014;41:11704-1-11704–12. doi: 10.1118/1.4842575.

13. Kim J, Glide-Hurst C, Doemer A, Wen N, Movsas B, Chetty IJ. Implementation of a novel algorithm for generating synthetic CT images from magnetic resonance imaging data sets for prostate cancer radiation therapy. Int. J. Radiat. Oncol. Biol. Phys. 2015;91:39–47. doi: 10.1016/j.ijrobp.2014.09.015.

14. Tyagi N, Fontenla S, Zhang J, Cloutier M, Kadbi M, Mechalakos J, Zelefsky M, Deasy J, Hunt M. Dosimetric and workflow evaluation of first commercial synthetic CT software for clinical use in pelvis. Phys. Med. Biol. 2017;62:2961–2975. doi: 10.1088/1361-6560/aa5452.

15. Maspero M, Seevinck PR, Schubert G, Hoesl MAU, Van Asselen B, Viergever MA, Lagendijk JJW, Meijer GJ, Van Den Berg CAT. Quantification of confounding factors in MRI-based dose calculations as applied to prostate IMRT. Phys. Med. Biol. 2017;62:948–965. doi: 10.1088/1361-6560/aa4fe7.

16. Maspero M. Magnetic Resonance-only Radiotherapy for prostate cancer. PhD Thesis, Utrecht University, The Netherlands. 2018.

17. Koch KM, Hargreaves BA, Pauly KB, Chen W, Gold GE, King KF. Magnetic resonance imaging near metal implants. J. Magn. Reson. Imaging 2010;32:773–787. doi: 10.1002/jmri.22313.

18. Hargreaves BA, Worters PW, Pauly KB, Pauly JM, Koch KM, Gold GE. Metal-induced artifacts in MRI. Am. J. Roentgenol. 2011;197:547–555. doi: 10.2214/AJR.11.7364.

19. Maspero M, Seevinck PR, Willems NJW, Sikkes GG, de Kogel GJ, de Boer HCJ, van der Voort van Zyp JRN, van den Berg CAT. Evaluation of gold fiducial marker manual localisation for magnetic resonance-only prostate radiotherapy. Radiat. Oncol. 2018;13:105. doi: 10.1186/s13014-018-1029-7.

20. Jonsson JH, Garpebring A, Karlsson MG, Nyholm T. Internal fiducial markers and susceptibility effects in MRI - Simulation and measurement of spatial accuracy. Int. J. Radiat. Oncol. Biol. Phys. 2012;82:1612–1618. doi: 10.1016/j.ijrobp.2011.01.046.

21. Hong CG, Yoon BI, Choe HS, Ha US, Sohn DW, Cho YH. The prevalence and characteristic differences in prostatic calcification between health promotion center and urology department outpatients. Korean J. Urol. 2012;53:330–334. doi: 10.4111/kju.2012.53.5.330.

22. Ng M, Brown E, Williams A, Chao M, Lawrentschuk N, Chee R. Fiducial markers and spacers in prostate radiotherapy: Current applications. BJU Int. 2014;113:13–20. doi: 10.1111/bju.12624.

23. Maspero M, Van Den Berg CAT, Zijlstra F, Sikkes GG, De Boer HCJ, Meijer GJ, Kerkmeijer LGW, Viergever MA, Lagendijk JJW, Seevinck PR. Evaluation of an automatic MR-based gold fiducial marker localisation method for MR-only prostate radiotherapy. Phys. Med. Biol. 2017;62:7981–8002. doi: 10.1088/1361-6560/aa875f.

24. Zijlstra F, Bouwman JG, Braškutė I, Viergever MA, Seevinck PR. Fast Fourier-based simulation of off-resonance artifacts in steady-state gradient echo MRI applied to metal object localization. Magn. Reson. Med. 2017;78:2035–2041. doi: 10.1002/mrm.26556.

25. Zur Y, Wood ML, Neuringer LJ. Motion-insensitive, steady-state free precession imaging. Magn. Reson. Med. 1990;16:444–459. doi: 10.1002/mrm.1910160311.

26. Bangerter NK, Hargreaves BA, Vasanawala SS, Pauly JM, Gold GE, Nishimura DG. Analysis of Multiple-Acquisition SSFP. Magn. Reson. Med. 2004;51:1038–1047. doi: 10.1002/mrm.20052.

27. Lauzon M. Louis, Frayne R. Analytical Characterization of RF Phase-Cycled Balanced Steady-State Free Precession. Concepts Magn. Reson. Part A 2009;34A:133–143. doi: 10.1002/cmr.a.20138.

28. Brown RW, Cheng YCN, Haacke EM, Thompson MR, Venkatesan R. Magnetic Resonance Imaging: Physical Principles and Sequence Design: Second Edition. 2014. doi: 10.1002/9781118633953.

29. Xiang QS, Hoff MN. Banding artifact removal for bSSFP imaging with an elliptical signal model. Magn. Reson. Med. 2014;71:927–933. doi: 10.1002/mrm.25098.

30. Shcherbakova Y, van den Berg CAT, Moonen CTW, Bartels LW. PLANET: An ellipse fitting approach for simultaneous T1 and T2 mapping using phase-cycled balanced steady-state free precession. Magn. Reson. Med. 2018;79:711–722. doi: 10.1002/mrm.26717.

31. Shcherbakova Y, van den Berg CAT, Moonen CTW, Bartels LW. On the accuracy and precision of PLANET for multiparametric MRI using phase-cycled bSSFP imaging. Magn. Reson. Med. 2019;81:1534–1552. doi: 10.1002/mrm.27491.

32. Beld E, Moerland MA, van der Voort van Zyp JRN, Viergever MA, Lagendijk JJW, Seevinck PR. MRI artifact simulation for clinically relevant MRI sequences for guidance of prostate HDR brachytherapy. Phys. Med. Biol. 2019;64:95006. doi: 10.1088/1361-6560/ab15ed.

33. Bojorquez JZ, Bricq S, Acquitter C, Brunotte F, Walker PM, Lalande A. What are normal relaxation times of tissues at 3 T? Magn. Reson. Imaging 2017;35:69–80. doi: 10.1016/j.mri.2016.08.021.

34. Bol GH, Kotte ANTJ, van der Heide UA, Lagendijk JJW. Simultaneous multi-modality ROI delineation in clinical practice. Comput. Methods Programs Biomed. 2009;96:133–140. doi: 10.1016/j.cmpb.2009.04.008.

35. Seppenwoolde JH, Viergever MA, Bakker CJG. Passive tracking exploiting local signal conservation: The white marker phenomenon. Magn. Reson. Med. 2003;50:784–790. doi: 10.1002/mrm.10574.

36. Mani V, Briley-Saebo KC, Itskovich V V., Samber DD, Fayad ZA. GRadient echo Acquisition for Superparamagnetic particles with Positive contrast (GRASP): Sequence characterization in membrane and glass superparamagnetic iron oxide phantoms at 1.5T and 3T. Magn. Reson. Med. 2006;55:126–135. doi: 10.1002/mrm.20739.

37. Seevinck PR, de Leeuw H, Bos C, Bakker CJG. Highly localized positive contrast of small paramagnetic objects using 3D center-out radial sampling with off-resonance reception. Magn. Reson. Med. 2011;65:146–156. doi: 10.1002/mrm.22594.

38. Dong Y, Chang Z, Xie G, Whitehead G, Ji JX. Susceptibility-based positive contrast MRI of brachytherapy seeds. Magn. Reson. Med. 2015;74:716–726. doi: 10.1002/mrm.25453.

Chapter 6

General Discussion

In recent years, there has been considerable interest in quantitative MRI, and particularly in quantitative relaxometry, which refers to the measurement of the magnetic relaxation times of tissues (T_1, T_2, T_2^*). The contrasts in conventional MRI are often based on the relaxation times. Different tissues have different values for the relaxation times, and in case of disease, these values often change. For example, brain pathology is often associated with prolonged values of the relaxation times T_1, T_2, and T_2^* [1–3]. For this reason, quantitative relaxometry could be a useful tool for detecting the changes in tissues associated with diseases or other biological processes and based on this, for improvement of tissue characterization and differentiation [3–5].

Quantitative relaxometry has been widely used in research studies and clinical applications in the brain and in the body [3,6,7]. Relaxometry analysis has been applied in the brain in the context of the assessment of multiple sclerosis, demyelination, stroke, epilepsy, edema, tumors, etc [6,8–14]. Furthermore, 3D maps of the relaxation times can be used for automatic brain tissue segmentation and volume measurements for many neuroradiological applications [15–17]. In the body, quantitative relaxometry has been applied for the assessment of disorders of different organs, e.g. prostate, kidneys, pancreas, liver, heart [18–22].

Many different techniques and approaches have been developed to measure relaxation times. However, obtaining precise and accurate maps of the relaxation times in a reproducible manner within an acceptable time frame remains challenging. In addition to the fact that the relaxation times depend on temperature and on the magnetic field strength, considerable variations can be observed in literature. This can be caused by biological variations of the relaxation times over population [4,23–26], but may be also related to the fact that different scanners were used or different implementations of the methods were used to obtain the maps of the relaxation times. [27–33].

In this thesis, research with respect to a new method for quantitative MRI was presented. A method named PLANET was developed, which is capable of volumetric reconstruction of five parameter maps, such as the relaxation times T_1 and T_2, the local off-resonance, the RF phase (related to the combination of RF transmit and receive phases), and the banding free bSSFP signal magnitude.

As was described in Chapter 2, the method is based on the phase-cycled bSSFP sequence, which is available on most clinical scanners and allows for rapid imaging with the highest SNR efficiency among all known sequences [34]. The complex-valued bSSFP signal acquired over different RF phase increments produces an elliptical trajectory in the transverse signal plane. Prior knowledge of this elliptical trajectory was used to reformulate the fitting problem into a convex one, which was solved directly using a linear least-squares

method under an ellipse-specific constraint, resulting in the unique solution of the fitting problem. Next, analytical solutions to extract the relaxation parameters T_1, T_2, and the banding-free signal magnitude from the fitting results were derived, and the off-resonance and the RF phase were calculated from the same dataset.

The PLANET approach is simple, robust and fast. The typical PLANET acquisition consists of 8-10 phase-cycled acquisitions and takes around 10-12 min for full brain coverage with FOV 220x220x100 mm^3 and voxel size 1x1x4 mm^3 (without using any acceleration technique). The reconstruction time is very short due to the use of non-iterative linear least-squares fitting and takes approximately 6-7 seconds per slice of matrix size 224x224. The feasibility of using the PLANET method for QMRI at realistic SNR levels was demonstrated in Chapter 2. Note, that throughout this chapter, a single-component relaxation model assuming a single-peak (Lorentzian) frequency distribution for signal in each image voxel was used in the PLANET reconstruction.

A detailed study of the precision and accuracy of the method in relation to the SNR was described in Chapter 3. When applied to a phantom (a single-peak frequency distribution with mono-exponential relaxation model), the method allowed for accurate and precise parameter mapping at realistic SNR levels when the sequence parameter settings for the repetition time (TR), and the flip angle (FA) were properly chosen. In our simulations, made for a single-component signal model, a broad "sweet spot" of TR and FA combinations was found, for which high accuracy and precision in the parameter estimates can be achieved over a wide range of relaxation times at realistic SNR levels. This is a clear advantage of the PLANET method compared to conventional methods, where fine tuning of parameter settings is required for each specific range of T_1 and T_2 values. The combination of FA of 20°- 30° and TR of 10 ms was chosen for a single-component signal model to estimate T_1 in the range of 200 ms to 3000 ms, and T_2 in the range of 50 ms to 500 ms, with high accuracy and precision at realistic SNRs within acceptable scan time.

However, when the PLANET method was applied *in vivo* in a tissue where multiple components with different relaxation times and frequency distributions were present in a voxel, systematic errors in the estimated quantitative parameters were observed. The currently implemented PLANET model is based on a single-component relaxation model, which results in a symmetric bSSFP magnitude profile. However, in some biological tissues like white matter in the human brain, fat tissue, or bone marrow, multiple relaxation components with different frequency distributions are present, which has an impact on the performance of the PLANET method. For example, white matter tissue is often modeled to be a two-component system consisting of a dominant component with long T_1 and T_2, and a smaller component with short T_1 and T_2, related to the presence of myelin (35–38). The

frequency shift between the components in combination with their relative abundance and individual relaxation behavior causes asymmetries in the bSSFP profile (39,40). Then the signal coming from such tissue is a complex weighted sum of signals from the individual components. As was shown in Chapter 3, the ellipse of the dominant component is disturbed by the presence of the second component. Their weighted complex sum generally does not form a perfect ellipse. However, the myelin component has shorter relaxation times and a smaller volume fraction than the main component has, and their complex weighted sum can still be fitted reasonably well as an ellipse, but with "observed" T_1 and T_2 values shorter than the corresponding values for the dominant WM component. This fact explains the observed underestimation of the relaxation times in white matter tissue compared with the reference values. Numerical simulations showed that the underestimation in T_1 and T_2 depends on the choice of FA and TR, as well as on the individual relaxation times of the components, on the frequency shift between them, and on their volume fractions. Furthermore, as was shown in Chapters 2 and 3, the underestimation in T_1 and T_2 depends on the main magnetic field strength. By adjusting the protocol parameter settings, the effects of the presence of multiple components can be minimized or on the contrary exaggerated. This suggests that the PLANET method has a sensitivity for detecting the presence of multiple components, which, for example, might be used to detect demyelination in the human brain and deserves to be further investigated and optimized.

The center of an ellipse that is fitted to the acquired multiple-peaks data and rotated to its conic vertical form, is shifted from the imaginary axis ($Y_c = 0$), and the absolute value of the shift increases with increasing fraction of the second component, as can be seen in the simulation results shown in Figure 6.1. This feature allows to identify the presence of multiple peaks. Based on our preliminary results (41), the PLANET method can potentially be used to map the spatial distribution of voxels in which multiple spectral peaks are present, like fat, and to create a fat-only map. A new method for fat-water separation based on PLANET reconstruction can be possibly developed.

For all these reasons, the multiple-component issue requires more attention, and the possibility to develop an advanced multiple-component model-based PLANET method should be further investigated.

The PLANET method is sensitive to B_0 drift, as was shown in Chapter 4. Drift-induced errors in the estimated parameters were found to depend on the T_1 and T_2 values, as well as on the sequence parameter settings for TR and FA. For example, in the phantom ($T_1 = 430$ ms, $T_2 = 50$ ms), the B_0 drift of 10 Hz over the 11-minute duration of the PLANET acquisition was measured, and it caused errors of about 4% and 8% in the estimated T_1 and T_2 values. However, in the brain, where multiple components are present, the same amount

of drift only had a minor effect, as the presence of multiple components is the main reason for the "non-elliptical" distribution of the data points. The observed difference in the results in the phantom and in the brain is not very intuitively understood and deserves further attention.

The severity of drift depends on the field strength, history of gradient activity and heating of metallic components of the scanner, PLANET acquisition time, the used gradient mode, shimming, and other factors, which vary among different systems and over time. Even though the errors in estimated quantitative parameters caused by drift in the human brain were small (1% – 5%) compared with the errors caused by the presence of multiple components (about 30% underestimation), they cannot be predicted and can potentially affect reproducibility of the results, as drift effects are generally not reproducible. As was shown in Chapter 4, drift-induced errors can be successfully corrected by applying a linear drift correction algorithm. Acquiring two fast low-resolution reference B_0 mapping scans before and after the PLANET acquisition is generally a simple direct way to correct for drift. However, the method would benefit from a rapid drift self-correction algorithm, which could be based on estimating the B_0 drift from acquired phase-cycled bSSFP data itself without performing additional scans. The linear model for the temporal evolution of the drift over the typical duration of a PLANET acquisition (10-12 min) has been shown to be a fair approximation of the exponential drift observed in the experiments reported in this chapter. If the drift is not linear, a more sophisticated drift correction algorithm might be necessary.

As was shown in Chapter 5, the complex-valued phase-cycled bSSFP images can be used for accurate visualization of gold fiducial markers in the prostate with a positive contrast for MRI-only radiotherapy. As was shown, the manifestations of the susceptibility artifacts around FMs in the acquired complex images depend on the RF phase increment used. By inspecting the acquired complex images, a certain dynamic can be chosen and routinely used by RT technicians for FMs localization during the scan session. In the reported experimental setup (3T, TR 6.7 ms, TE 3.3 ms, 6 dynamics with RF phase increment $\Delta\theta = [0, \frac{\pi}{3}, \frac{2\pi}{3}, \pi, \frac{4\pi}{3}, \frac{5\pi}{3}]$), the imaginary/real images of dynamics number 5 and number 6 provided optimal positive contrast for direct localization of the FM's centers. However, at different magnetic field strengths and/or different MR acquisition parameter settings, or under high offsets of the background B_0 field, the appearance of FMs might be different, and the RF phase increment for which positive contrast is seen may vary. Nevertheless, FMs will always show positive contrast with the background at a certain specific RF phase increment.
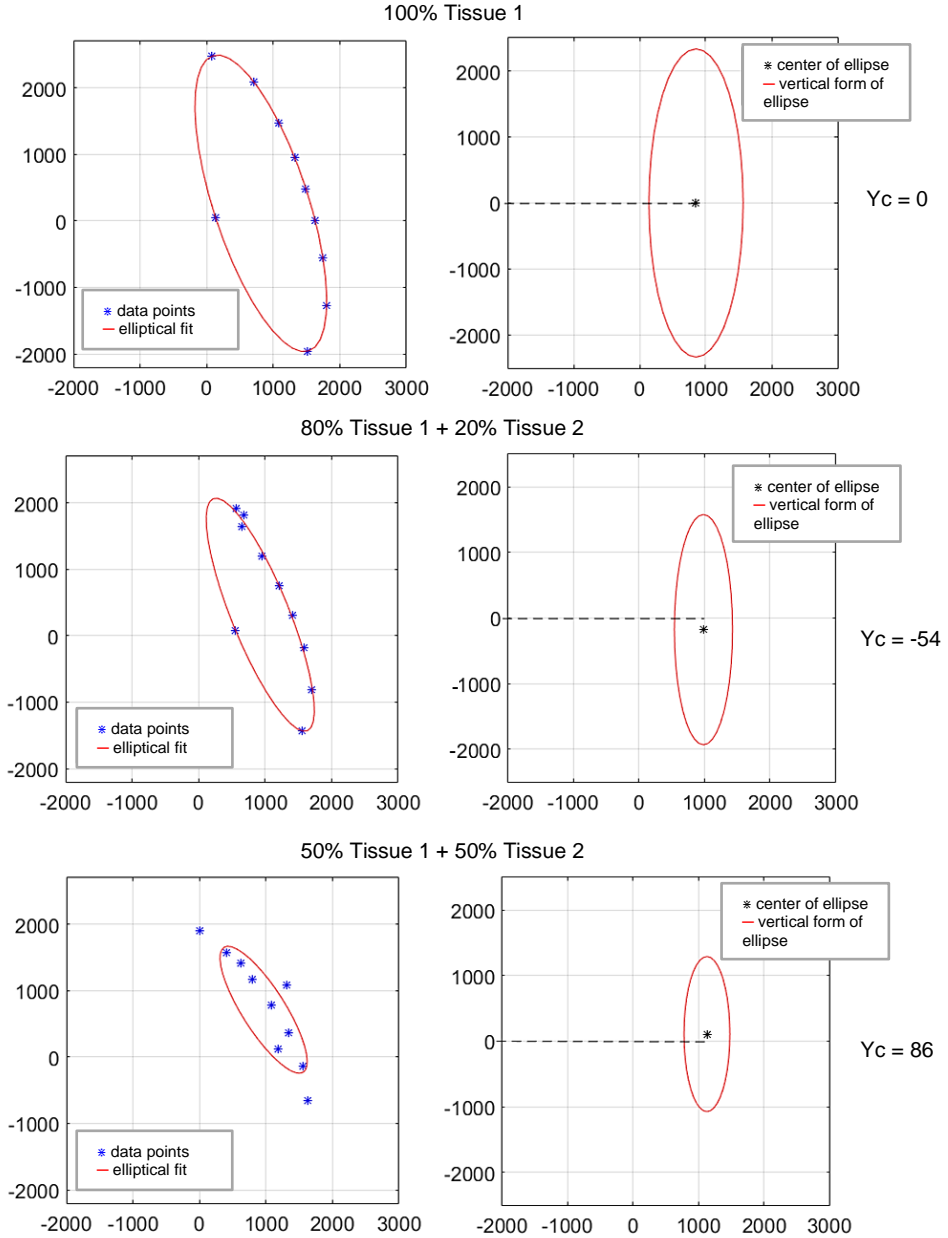
FIGURE 6.1. Simulation results for a two-component tissue depending on the fraction of the second component: 0%, 20%, 50%. Frequency shift between the components (first component: $T_{1,1}$ = 2000 ms, $T_{2,1}$ = 500 ms; second component $T_{1,2}$ = 300 ms, $T_{2,2}$ = 80 ms) for all cases Δf = 220 Hz. The simulated data points are shown with corresponding elliptical fits. The vertical conic form of the ellipse is shown for each case, as well as the value of parameter Y_c.

In the experiments reported in this chapter, the RF phase-cycling scheme with 6 RF phase increment settings was used and resulted in an acquisition time of around 2 min. However, the number of RF phase increment settings can be further reduced to 4 or even less to save scanning time. The advantage of this method is that it does not require any additional post-processing or software. Thereby, detection of FMs can be easily done directly at the MR console, allowing RT technicians to obtain immediate feedback on the anticipated feasibility of accurate FM localization while the patient is being scanned.

The method is now included in the clinical MRI-only prostate protocol in the Radiotherapy department of the UMC Utrecht. In general, the method allows to visualize any object which gives B_0 distortions, like low dose rate (LDR) brachytherapy seeds, or needles for high dose rate (HDR) brachytherapy.

7.1 Future perspectives

The PLANET method is based on the bSSFP sequence, an important advantage of which is that it offers rapid imaging with very high SNR per unit time.

The feasibility of using PLANET for QMRI *in vivo* was shown in the human brain, which is more or less a static object. As mentioned above, the typical PLANET acquisition takes around 10-12 min for full brain coverage using a common 3D cartesian sampling of *k*-space without using any acceleration technique. By applying a certain acceleration method, such as parallel imaging (42) or compressed sensing (43), the duration of a PLANET acquisition can be considerably reduced. Evaluation of the impact of acceleration in terms of SNR, accuracy, and precision is subject of further research.

The PLANET method has the potential to become a robust method for QMRI in the brain. Applications of the method in the body, where respiratory motion is present, pose additional challenges. First, the effect of motion-induced signal artifacts upon elliptical signal trajectories has to be investigated. Based on the this, the implementation of the PLANET method should be adapted. The most obvious ways to minimize the impact of motion in the abdomen are to reduce the duration of a single phase-cycled PLANET acquisition to one breath hold, or to use a respiratory-gated acquisition. Switching to more advanced motion-correction algorithms, such as using radial readouts sequences (dynamically phase-cycled radial bSSFP (44)), offers an opportunity for self-navigation, which is of interest for the specific purpose of abdominal imaging (45,46).

When volumetric coverage is not required, switching to the multiple 2D acquisition mode would considerably decrease the acquisition time, and motion would have less impact,

which would be of interest for abdominal imaging. However, based on our preliminary results (47), the non-ideal FA profile over the slice, associated with 2D slice selection, compromises the required elliptical behavior of the complex transverse magnetization, as can be seen in the simulation results presented in Figure 6.2. The optimization of the RF excitation pulse should be performed for a better slice profile. Further investigation and optimization of the 2D method is the subject of future research.

Although T_1 and T_2 probably are the most interesting parameters for clinical applications, the fact that PLANET can also reconstruct other parameters deserves further attention. The banding free bSSFP signal magnitude imaging has diagnostic value for clinical applications in cardiac imaging, angiography, abdominal and pelvic imaging, fetal imaging (48–53). PLANET method may be applied for investigating the susceptibility effects and the electrical tissue properties: the off-resonance maps can be used for quantitative susceptibility mapping (QSM) (54). RF phase maps could potentially be used for electric properties tomography (55) and conductivity mapping in the brain (56).

In conclusion, PLANET is a competitive method for QMRI in terms of acquisition time, number of estimated quantitative parameters, adaptation of the MR protocol parameters to the range of relaxation times expected, and easy implementation on a standard clinical scanner, that deserves further attention.

Next steps should be performed to investigate and validate the reproducibility, portability, and independence of the measurements of the institution, the MR scanner used, and MR protocol parameter settings.
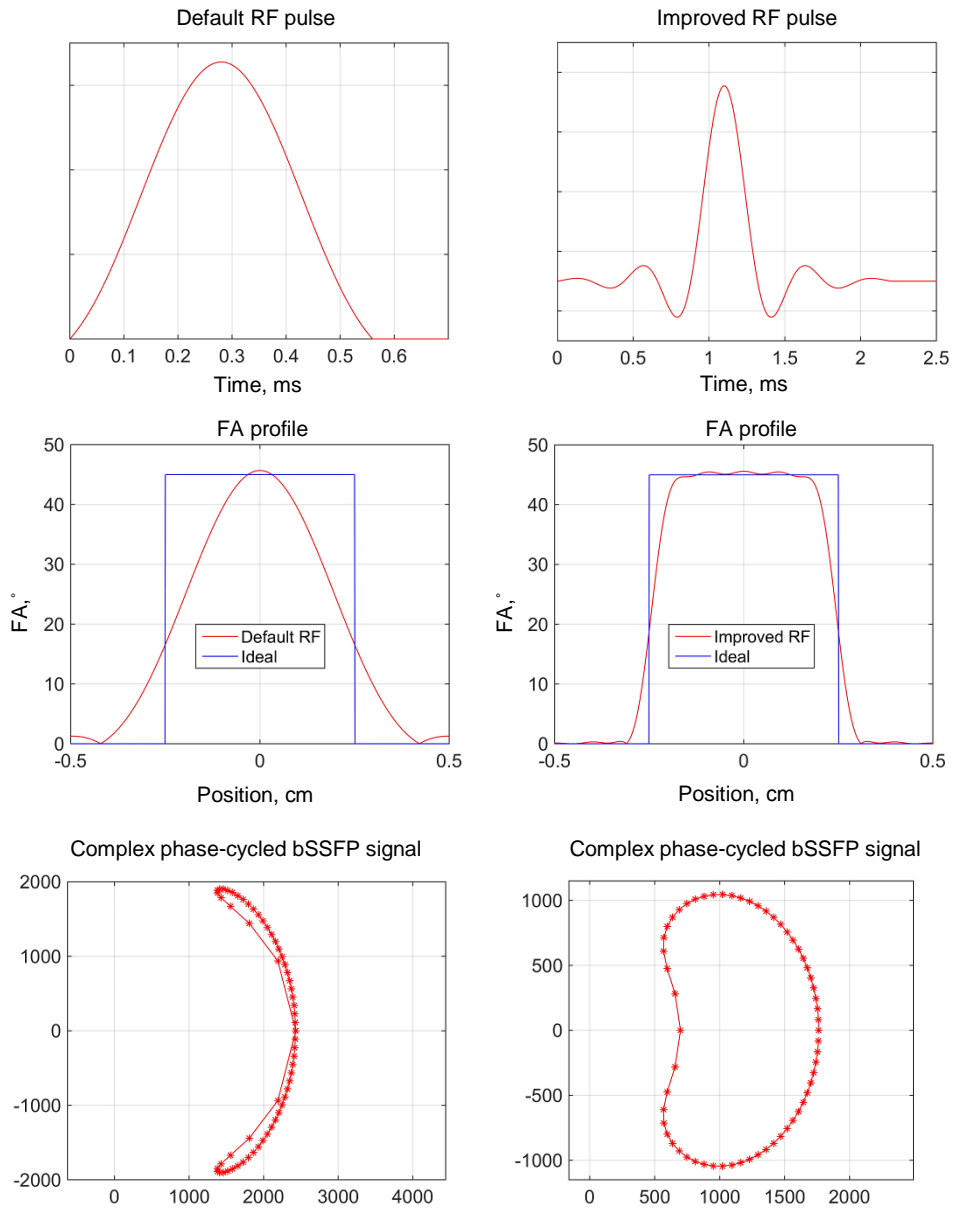
FIGURE 6.2. The results of Bloch simulation for the default and for the improved RF excitation pulses: the RF excitation pulse, the flip angle profile in comparison with ideal profile, the complex steady-state signal distributions for the default and for the improved RF pulses, slice profiles and an example of the ellipses fitted to data points.

7.2 References

1. Mills CM, Crooks LE, Kaufman L, Brant Zawadzki M. Cerebral abnormalities: Use of calculated T1 and T2 magnetic resonance images for diagnosis. Radiology 1984;150:87–94. doi: 10.1148/radiology.150.1.6689792.

2. Vymazal J, Righini A, Brooks RA, Canesi M, Mariani C, Leonardi M, Pezzoli G. T1 and T2 in the brain of healthy subjects, patients with Parkinson disease, and patients with multiple system atrophy: Relation to iron content. Radiology 1999;211:489–495. doi: 10.1148/radiology.211.2.r99ma53489.

3. Cheng HL, Stikov N, Ghugre NR, Wright GA. Practical medical applications of quantitative MR relaxometry. J. Magn. Reson. Imaging 2012;36:805–824. doi: 10.1002/jmri.23718.

4. Deoni SCL. Magnetic resonance relaxation and quantitative measurement in the brain. Methods Mol. Biol. 2010;711:65–108. doi: 10.1007/978-1-61737-992-5_4.

5. Mariappan SVS, Subramanian S, Chandrakumar N, Rajalakshmi KR, Sukumaran SS. Proton relaxation times in cancer diagnosis. Magn. Reson. Med. 1988;8:119–128. doi: 10.1002/mrm.1910080202.

6. Larsson HBW, Frederiksen J, Petersen J, Nordenbo A, Zeeberg I, Henriksen O, Olesen J. Assessment of demyelination, edema, and gliosis by in vivo determination of T1 and T2 in the brain of patients with acute attack of multiple sclerosis. Magn. Reson. Med. 1989;11:337–348. doi: 10.1002/mrm.1910110308.

7. Jackson A. Quantitative MRI of the brain: measuring changes caused by disease. Br. J. Radiol. 2014;78:87–87. doi: 10.1259/bjr.78.925.780087a.

8. Vrenken H, Geurts JJG, Knol DL, et al. Whole-Brain T1 Mapping in Multiple Sclerosis: Global Changes of Normal-appearing Gray and White Matter. Radiology 2006;240:811–820. doi: 10.1148/radiol.2403050569.

9. Englund E, Brun A, Györffy-Wagner Z, Larsson EM, Persson B. Relaxation times in relation to grade of malignancy and tissue necrosis in astrocytic gliomas. Magn. Reson. Imaging 1986;4:425–429. doi: 10.1016/0730-725X(86)90051-2.

10. Manfredonia F, Ciccarelli O, Khaleeli Z, Tozer DJ, Sastre-Garriga J, Miller DH, Thompson AJ. Normal-appearing brain T1 relaxation time predicts disability in early primary progressive multiple sclerosis. Arch. Neurol. 2007;64:411–415. doi: 10.1001/archneur.64.3.411.

11. Rugg-Gunn FJ, Boulby PA, Symms MR, Barker GJ, Duncan JS. Whole-brain T2 mapping demonstrates occult abnormalities in focal epilepsy. Neurology 2005;64:318–325. doi: 10.1212/01.WNL.0000149642.93493.F4.

12. Townsend TN, Bernasconi N, Pike GB, Bernasconi A. Quantitative analysis of temporal

lobe white matter T2 relaxation time in temporal lobe epilepsy. Neuroimage 2004;23:318–324. doi: 10.1016/j.neuroimage.2004.06.009.

13. Dewitt LD, Kistler JP, Miller DC, Richardson EP, Buonanno FS. Nmr-neuropathologic correlation in stroke. Stroke 1987;18:342–351. doi: 10.1161/01.STR.18.2.342.

14. Mackay A, Whittall K, Adler J, Li D, Paty D, Graeb D. In vivo visualization of myelin water in brain by magnetic resonance. Magn. Reson. Med. 1994;31:673–677. doi: 10.1002/mrm.1910310614.

15. Schmidt-Wilcke T. Variations in brain volume and regional morphology associated with chronic pain. Curr. Rheumatol. Rep. 2008;10:467–474. doi: 10.1007/s11926-008-0077-7.

16. Bozzali M, Cercignani M, Caltagirone C. Brain volumetrics to investigate aging and the principal forms of degenerative cognitive decline: a brief review. Magn. Reson. Imaging 2008;26:1065–1070. doi: 10.1016/j.mri.2008.01.044.

17. West J, I. B, M. E, J.B.M. W, P. L. Application of Quantitative MRI for Brain Tissue Segmentation at 1.5 T and 3.0 T Field Strengths. PLoS One 2013;8.

18. Bazelaire CMJ de, Duhamel GD, Rofsky NM, Alsop DC. Radiology of Abdominal and Pelvic Tissues Measured in Vivo at 3.0 T : Preliminary Results. Radiology 2004;230:652–659.

19. Yamauchi FI, Penzkofer T, Fedorov A, Fennessy FM, Chu R, Maier SE, Tempany CMC, Mulkern R V., Panych LP. Prostate cancer discrimination in the peripheral zone with a reduced field-of-view T2-mapping MRI sequence. Magn. Reson. Imaging 2015;33:525–530. doi: 10.1016/j.mri.2015.02.006.

20. Papakonstantinou O, Alexopoulou E, Economopoulos N, Benekos O, Kattamis A, Kostaridou S, Ladis V, Efstathopoulos E, Gouliamos A, Kelekis NL. Assessment of iron distribution between liver, spleen, pancreas, bone marrow, and myocardium by means of r2 relaxometry with mri in patients with β-thalassemia major. J. Magn. Reson. Imaging 2009;29:853–859. doi: 10.1002/jmri.21707.

21. Schein A, Enriquez C, Coates TD, Wood JC. Magnetic resonance detection of kidney iron deposition in sickle cell disease: A marker of chronic hemolysis. J. Magn. Reson. Imaging 2008;28:698–704. doi: 10.1002/jmri.21490.

22. Dass S, Suttie JJ, Piechnik SK, et al. Myocardial tissue characterization using magnetic resonance noncontrast T1 mapping in hypertrophic and dilated cardiomyopathy. Circ. Cardiovasc. Imaging 2012;5:726–733. doi: 10.1161/CIRCIMAGING.112.976738.

23. Bottomley PA, Foster TH, Argersinger RE, Pfeifer LM. A review of normal tissue hydrogen NMR relaxation times and relaxation mechanisms from 1-100 MHz: Dependence on tissue type, NMR frequency, temperature, species, excision, and age. Med. Phys. 1984;11:425–448. doi: 10.1118/1.595535.

24. Lim Y, Cha JG, Yi J, Kang SJ, Lee YK, Lee SJ, Kim HJ, Lee BR. Topographical and sex variations in the T2 relaxation times of articular cartilage in the ankle joints of healthy young adults using 3.0T MRI. J. Magn. Reson. Imaging 2016;43:455–462. doi: 10.1002/jmri.25004.

25. Georgiades CS, Itoh R, Golay X, Van Zijl PCM, Melhem ER. MR imaging of the human brain at 1.5 T: Regional variations in transverse relaxation rates in the cerebral cortex. Am. J. Neuroradiol. 2001;22:1732–1737.

26. Träber F, Block W, Lamerichs R, Gieseke J, Schild HH. 1H Metabolite Relaxation Times at 3.0 Tesla: Measurements of T1 and T2 Values in Normal Brain and Determination of Regional Differences in Transverse Relaxation. J. Magn. Reson. Imaging 2004;19:537–545. doi: 10.1002/jmri.20053.

27. Bauer CM, Jara H, Killiany R. Whole brain quantitative T2 MRI across multiple scanners with dual echo FSE: Applications to AD, MCI, and normal aging. Neuroimage 2010;52:508–514. doi: 10.1016/j.neuroimage.2010.04.255.

28. Keenan KE, Stupic KF, Boss MA, et al. Multi-site, multi-vendor comparison of T1 measurement using ISMRM/NIST system phantom. In: Proceedings of the 24th Annual Meeting of ISMRM, Singapore, Singapore, 2016. Abstract 3290.

29. Panda A, Jokerst CE, Cummings KW, Panse PM. Inter-Scanner T1 and T2 Measurement Variability Evaluation on Two 3T Scanners with Identical Hardware and Software Configuration. In: Proceedings of the 24th Annual Meeting of ISMRM, Honolulu, HI, USA, 2017. Abstract 2766.

30. Bojorquez JZ, Bricq S, Acquitter C, Brunotte F, Walker PM, Lalande A. What are normal relaxation times of tissues at 3 T? Magn. Reson. Imaging 2017;35:69–80. doi: 10.1016/j.mri.2016.08.021.

31. Lee Y, Callaghan MF, Acosta-Cabronero J, Lutti A, Nagy Z. Establishing intra- and inter-vendor reproducibility of T 1 relaxation time measurements with 3T MRI. Magn. Reson. Med. 2019;81:454–465. doi: 10.1002/mrm.27421.

32. Deoni SCL, Williams SCR, Jezzard P, Suckling J, Murphy DGM, Jones DK. Standardized structural magnetic resonance imaging in multicentre studies using quantitative T1 and T2 imaging at 1.5 T. Neuroimage 2008;40:662–671. doi: 10.1016/j.neuroimage.2007.11.052.

33. Fenrich FRE, Beaulieu C, Allen PS. Relaxation times and microstructures. NMR Biomed. 2001;14:133–139. doi: 10.1002/nbm.685.

34. Bieri O, Scheffler K. Fundamentals of balanced steady state free precession MRI. J. Magn. Reson. Imaging 2013;38:2–11. doi: 10.1002/jmri.24163.

35. Does MD, Beaulieu C, Allen PS, Snyder RE. Multi-component T1 relaxation and magnetisation transfer in peripheral nerve. Magn. Reson. Imaging 1998;16:1033–1041. doi:

10.1016/S0730-725X(98)00139-8.

36. Deoni SCL, Rutt BK, Arun T, Pierpaoli C, Jones DK. Gleaning multicomponent T1 and T2 information from steady-state imaging data. Magn. Reson. Med. 2008;60:1372–1387. doi: 10.1002/mrm.21704.

37. Whittall KP, Mackay AL, Graeb DA, Nugent RA, Li DKB, Paty DW. In vivo measurement of T2 distributions and water contents in normal human brain. Magn. Reson. Med. 1997;37:34–43. doi: 10.1002/mrm.1910370107.

38. Stanisz GJ, Kecojevic A, Bronskill MJ, Henkelman RM. Characterizing white matter with magnetization transfer and T2. Magn. Reson. Med. 1999;42:1128–1136. doi: 10.1002/(SICI)1522-2594(199912)42:6<1128::AID-MRM18>3.0.CO;2-9.

39. Miller KL. Asymmetries of the balanced SSFP profile. Part I: Theory and Observation. Magn. Reson. Med. 2010;63:385–395. doi: 10.1002/mrm.22212.

40. Miller KL, Smith SM, Jezzard P. Asymmetries of the balanced SSFP profile. Part II: White matter. Magn. Reson. Med. 2010;63:396–406. doi: 10.1002/mrm.22249.

41. Shcherbakova Y, van den Berg C, Gavazzi S, Moonen C, Bartels L. Detecting the presence of fat using PLANET-based parameter mapping. In: Proceedings of the 27th Annual Meeting of ISMRM, Montreal, QC, Canada, 2019. Abstract 4015.

42. Pruessmann KP, Weiger M, Scheidegger MB, Boesiger P. SENSE: Sensitivity encoding for fast MRI. Magn. Reson. Med. 1999;42:952–962. doi: 10.1002/(SICI)1522-2594(199911)42:5<952::AID-MRM16>3.0.CO;2-S.

43. Cukur T. Accelerated phase-cycled SSFP imaging with compressed sensing. IEEE Trans. Med. Imaging 2015;34:107–115. doi: 10.1109/TMI.2014.2346814.

44. Benkert T, Ehses P, Blaimer M, Jakob PM, Breuer FA. Dynamically phase-cycled radial balanced SSFP imaging for efficient banding removal. Magn. Reson. Med. 2015;73:182–194. doi: 10.1002/mrm.25113.

45. Buerger C, Clough RE, King AP, Schaeffter T, Prieto C. Nonrigid motion modeling of the liver from 3-D undersampled self-gated golden-radial phase encoded MRI. IEEE Trans. Med. Imaging 2012;31:805–815. doi: 10.1109/TMI.2011.2181997.

46. Han F, Zhou Z, Cao M, Yang Y, Sheng K, Hu P. Respiratory motion-resolved, self-gated 4D-MRI using rotating cartesian k-space (ROCK): Med. Phys. 2017;44:1359–1368. doi: 10.1002/mp.12139.

47. Shcherbakova Y, van den Berg CAT, Borman PT, Moonen CT, Bartels LW. 2D Acquisition Mode for T1 and T2 Estimation Using an Ellipse-Fitting Approach on Phase Cycled BSSFP Data. In: Proceedings of the 25th Annual Meeting of ISMRM, Honolulu, HI, USA, 2017. Abstract 5057.

48. Scheffler K, Lehnhardt S. Principles and applications of balanced SSFP techniques. Eur. Radiol. 2003;13:2409–2418. doi: 10.1007/s00330-003-1957-x.

49. Fuchs F, Laub G, Othomo K. TrueFISP - Technical considerations and cardiovascular applications. Eur. J. Radiol. 2003;46:28–32. doi: 10.1016/S0720-048X(02)00330-3.

50. Keogan MT, Edelman RR. Technologic Advances in Abdominal MR Imaging. Radiology 2013;220:310–320. doi: 10.1148/radiology.220.2.r01au22310.

51. Chung HW, Chen CY, Zimmerman RA, Lee KW, Lee CC, Chin SC. T2-weighted fast MR imaging with true FISP versus HASTE: Comparative efficacy in the evaluation of normal fetal brain maturation. Am. J. Roentgenol. 2000;175:1375–1380. doi: 10.2214/ajr.175.5.1751375.

52. Deshpande VS, Shea SM, Laub G, Simonetti OP, Finn JP, Li D. 3D magnetization-prepared true-FISP: A new technique for imaging coronary arteries. Magn. Reson. Med. 2001;46:494–502. doi: 10.1002/mrm.1219.

53. Wagner S, Buser P, Auffermann W, Holt WW, Wolfe CL, Higgins CB. Cine Magnetic Resonance Imaging: Tomographic Analysis of Left Ventricular Function. Cardiol. Clin. 2018;7:651–659. doi: 10.1016/s0733-8651(18)30423-5.

54. Wang Y, Liu T. Quantitative susceptibility mapping (QSM): Decoding MRI data for a tissue magnetic biomarker. Magn. Reson. Med. 2015;73:82–101. doi: 10.1002/mrm.25358.

55. Katscher U, van den Berg CAT. Electric properties tomography: Biochemical, physical and technical background, evaluation and clinical applications. NMR Biomed. 2017;30. doi: 10.1002/nbm.3729.

56. Gavazzi S, Shcherbakova Y, Bartels LW, Stalpers LJ, Lagendijk JJ, Crezee H, van den Berg CA, van Lier AL. Transceive phase mapping using the PLANET method and its application for conductivity mapping in the brain. Magn. Reson. Med. 2019. doi: 10.1002/mrm.27958.

Chapter 7

Summary

Recent years have witnessed a considerable interest in quantitative MRI (QMRI), which aims to map quantitative imaging biomarkers (QIBs) representing underlying biological and physiological tissue characteristics or processes.

The relaxation times (T_1, T_2, T_2*) are intrinsic tissue parameters, on which the contrasts in conventional MR images are often based, as was described in details in **Chapter 1**. Different tissues have different values for the relaxation times, and in case of disease, the values often change. This makes the relaxation times relevant QIBs. Measuring relaxation times has been a goal of research for a long time and many techniques and approaches have been developed to measure these parameters. However, reproducibly obtaining precise and accurate maps of relaxation times within an acceptable time frame remains challenging. Measurement results are known to depend on the methods used for quantification, on the implementation of the pulse sequences used, on MR protocol parameter settings, and even on the type and brand of the MR scanner on which the patient was scanned.

This thesis is about a new method for quantitative MRI. First, the methodology of the method was described. Next, its performance was further investigated, and the method was optimized for different applications.

In **Chapter 2,** the PLANET method: an elli**P**se fitting approach for simu**L**taneous T_1 and T_2 m**A**pping using phase-cycled bala**N**ced st**E**ady-s**T**ate free precession was introduced. The fitting of the elliptical model to the acquired complex phased-cycled bSSFP data is performed under an "ellipse-specific" constraint, directly by a linear least-squares method, which resulted in simple and fast post-processing. Following this approach, the maps of relaxation times T_1 and T_2, the banding free magnitude image, the off-resonance map, and the RF phase map are simultaneously reconstructed from the fitting results.

The feasibility of the method was demonstrated in a dedicated phantom and in the brain of healthy volunteers on a standard clinical MR scanner with a regular coil setup. The results for T_1 and T_2 values in the phantom were in good agreement with the reference values. However, in the brain, an underestimation in both T_1 and T_2 values was observed compared with both the reference values and the values published in the literature. Unlike T_2 estimates, T_1 estimates showed sensitivity to the actual Flip Angle (FA) errors, and a correction for B_1 field inhomogeneity was required as part of PLANET post-processing. Magnetization Transfer (MT) effects were shown to influence T_1 quantification as well, particularly in WM, and a partial mitigation strategy to minimize the impact of MT effects was employed. Still, an underestimation in T_1 values of about 15-20% and in T_2 values of about 10% was observed in the brain at 1.5T.

In **Chapter 3,** the influence of sequence parameter settings for the repetition time TR, the flip angle FA, and the number of RF phase increments N, on the accuracy and precision of quantitative parameter maps reconstructed using the PLANET method was investigated. First, numerical simulations and experiments were performed to assess the errors in quantitative parameter maps reconstructed using the PLANET method for a single-component signal, i.e. a single resonance MR signal resulting from one tissue component exhibiting mono-exponential longitudinal and transverse relaxation). Next, it was investigated which SNR is required for accurate and precise parameter estimation, and the results showed, that for a single-component signal model there is a broad "sweet spot" of sequence parameter value combinations for which high accuracy and precision in the parameter estimates are achieved over a wide range of relaxation times at realistic SNR levels.

However, in practice voxels at boundaries of different tissue types will contain mixed signals, with multiple relaxation times. In addition, in many biological tissues, like white matter in the human brain, adipose tissue, and bone marrow, multiple components with different relaxation times and different resonance frequencies are present. In such cases, a single-component model-based PLANET reconstruction might fail. For this reason, the performance of the PLANET method for a two-component signal model was investigated. For this, white matter tissue containing a second myelin-related component was used as a model for numerical simulations and volunteer experiments. The results showed that the presence of a second component does influence the performance of the method. An underestimation in T_1 and T_2 values of about 30% was observed in the brain at 3T and was confirmed by numerical simulations for a similar experimental setup. Furthermore, the simulation results showed that the errors in the estimated parameters caused by the presence of the second component depend on the choice of FA and TR, on the relaxation times of the components, on the frequency shift between them and on their volume fractions.

The effects of Gibbs ringing were also investigated, because the RF phase-cycling spatially shifts the banding artifacts, causing the Gibbs ringing to be different for each phase-cycled image. The results showed that using a high resolution in combination with a suitable method for removal of Gibbs ringing artifacts improves the precision and accuracy of the parameter estimates when PLANET is applied to an object with sharp signal intensity edges. For *in vivo* use, using a relatively high resolution (in-plane voxel size of 0.98x0.98 mm^2) was enough to minimize Gibbs ringing artifacts.

An important prerequisite for the PLANET model is a static main magnetic field (B_0) throughout the phase-cycled bSSFP acquisition, which can take up to 10-15 min depending

on the resolution and the required field-of-view (FOV). Due to intensive gradient activity, B_0 drift can occur, which might result in errors in the PLANET-estimated quantitative parameters. In **Chapter 4,** the results of the investigation of the influence of B_0 drift on the performance of the PLANET method for single-component and two-component signal models are presented. The influence of B_0 drift on the quantitative parameter estimates was assessed experimentally in a phantom and in the brain of healthy volunteers. The results were consequently verified by numerical simulations. A simple drift correction algorithm was proposed by acquiring two fast low-resolution reference B_0 mapping scans before and after the PLANET acquisition. The results showed that B_0 drift over the duration of PLANET acquisition causes errors in the estimated quantitative parameters. For both single-component and two-component signal models, drift-induced errors were successfully corrected by applying the proposed drift correction algorithm.

While applying the PLANET method in patients undergoing prostate radiotherapy, it was observed that the acquired phase-cycled bSSFP images are useful for qualitative assessment of fiducial markers (FMs) in the prostate, which are implanted there as landmarks for localization of the prostate during radiotherapy. **Chapter 5** describes a clinical application of the phase-cycled bSSFP imaging in the prostate. A new method for visualization of FMs in the prostate with positive contrast for MRI-only radiotherapy was presented.

First, numerical simulations were performed to investigate the complex-valued phase-cycled bSSFP signal in the presence of a gold FM, and the relation of the true physical location of the FM with the geometrical manifestation of the artifacts was investigated. Next, phantoms and *in vivo* studies were performed to validate the simulations. The experimentally obtained artifacts were compared with those predicted in simulations, and the accuracy of the localization of FMs was assessed in both a phantom and *in vivo*. The experiments showed that the FMs have a positive contrast with respect to the prostate background on real/imaginary phase-cycled bSSFP images in all ten patients. The same positive contrast of FMs with respect to the prostate background on real/imaginary phase-cycled bSSFP images was observed in the phantoms and was confirmed by simulations. For all ten patients, the results showed accurate (within 1 mm) matching of FMs localization done using MR images acquired with phase-cycled bSSFP sequence compared with FMs localization done using the reference images (CT or SPAIR bSSFP for MRI-only), which proves the feasibility of *in vivo* FMs detection on MR images only. Thereby, detection of FMs can be easily done directly at the MR console, allowing RT technicians to obtain immediate feedback on the anticipated feasibility of accurate FM localization while the patient is being examined.

Chapter *8*

Nederlandse Samenvatting

In de afgelopen jaren is er veel aandacht geweest voor kwantitatieve MRI (QMRI). Hieronder wordt verstaan het met behulp van MRI afbeelden van kwantitatieve imaging biomarkers (QIB's), die de kwantitatieve parameters vertegenwoordigen die verband houden met biologische en fysiologische eigenschappen van weefsels.

De relaxatietijden (T_1, T_2, T_2*) zijn intrinsieke weefselparameters, die de contrasten in conventionele MR-beelden, zoals die gebruikt worden in de radiologische praktijk, bepalen. Tevens zijn deze parameters relevante QIB's, zoals in detail wordt beschreven in **Hoofdstuk 1**. Verschillende weefsels hebben verschillende waarden voor de relaxatietijden, en het meten daarvan (relaxometrie) is reeds lang een onderzoeksfocus. Er zijn veel verschillende QMRI-technieken voor relaxometrie voorgesteld. Het reproduceerbaar verkrijgen van precieze en nauwkeurige *maps* van relaxatietijden binnen een acceptabel tijdsbestek blijft echter een uitdaging. Het is bekend dat meetresultaten afhangen van de methoden die worden gebruikt voor kwantificering, van de implementatie van de gebruikte pulssequenties, van parameterinstellingen van het MR-protocol en zelfs van het type en merk van de MR-scanner waarop de patiënt werd gescand.

Dit proefschrift gaat over een nieuwe methode voor kwantitatieve MRI. Eerst werd de methodologie van de methode beschreven. Vervolgens werden de prestaties ervan verder onderzocht en werd de methode geoptimaliseerd voor verschillende toepassingen.

In **Hoofdstuk 2** wordt de PLANET-methode geïntroduceerd: *an elli**P**se fitting approach for simu**L**taneous T_1 and T_2 m**A**pping using phase-cycled bala**N**ced st**E**ady-s**T**ate free precession.* De methode is gebaseerd op de lineaire kleinste-kwadraten-aanpassing van een ellips aan meetpunten van het complexe MRI-signaal gemeten met een zogenaamde phase-cycled bSSFP sequentie. De aanpassing van het elliptische model aan de verkregen meetpunten werd geherformuleerd als een lineair convex probleem, dat rechtstreeks werd opgelost met een kleinste-kwadratenmethode specifiek voor ellipsen, die resulteerde in een eenvoudige en snelle nabewerking. De relaxatietijden T_1 en T_2, de signaalmagnitude zonder *banding* artefacten, de *off-resonance* Δf_0 en de RF-fase φ_{RF}, kunnen gelijktijdig worden gereconstrueerd.

De haalbaarheid van de methode werd aangetoond in een speciaal fantoom en in de hersenen van gezonde vrijwilligers op een klinische MR-scanner met een reguliere spoelopstelling en met reguliere scanparameterinstellingen. De resultaten voor T_1- en T_2-waarden in het fantoom kwamen goed overeen met de referentiewaarden. In de hersenen werd echter een onderschatting in zowel T_1- als T_2-waarden waargenomen in vergelijking met de referentiewaarden. In tegenstelling tot T_2-schattingen bleken T_1-schattingen gevoelig voor afwijkingen in de fliphoek, waardoor een correctie voor B_1-veldinhomogeniteit vereist was als onderdeel van de PLANET-nabewerking. *Magnetization Transfer* (MT)-effecten

bleken ook de T_1-kwantificatie te beïnvloeden, met name in witte stof, en een gedeeltelijke mitigatiestrategie om de impact van MT-effecten te minimaliseren werd toegepast. Toch werd een systematische onderschatting in T_1-waarden van ongeveer 15-20% en in T_2-waarden van ongeveer 10% waargenomen in de hersenen vergeleken met de referentiewaarden.

In **Hoofdstuk 3** werd de invloed van sequentieparameterinstellingen (de repetitietijd TR, de fliphoek FA en het aantal RF-fase-stappen N) op de nauwkeurigheid en precisie in door PLANET geschatte kwantitatieve parameters onderzocht. Door numerieke simulaties en experimenten uit te voeren, werden de fouten in kwantitatieve parameterschattingen onderzocht voor de PLANET-reconstructie van een signaal met één component (afkomstig van weefsel met mono-exponentiële T_1 en T_2 relaxatie). Verder werd de minimale SNR berekend die vereist is voor nauwkeurige en precieze parameterschatting. De resultaten toonden aan dat er voor een signaalmodel met slechts één component een brede "*sweet spot*" van sequentieparametercombinaties bestaat waarvoor een hoge nauwkeurigheid en een hoge precisie in de parameterschattingen worden bereikt over een breed bereik aan relaxatietijden bij realistische SNR's.

In de praktijk zullen voxels bij grenzen van verschillende weefseltypen echter gemengde signalen bevatten, met meerdere relaxatietijden. Bovendien zijn in veel biologische weefsels, zoals witte stof in het brein, vetweefsel en beenmerg, meerdere componenten met verschillende relaxatietijden en verschillende resonantiefrequenties aanwezig. In dergelijke gevallen kan een modelgebaseerde PLANET-reconstructie met één component mislukken. Om deze reden werd de werking van de PLANET-methode voor een tweecomponentensignaalmodel onderzocht. Hiervoor werd witte-stofweefsel met een tweede myeline-gerelateerde component gebruikt als model voor numerieke simulaties en vrijwilligersexperimenten. De resultaten toonden aan dat de aanwezigheid van een tweede component de prestaties van de methode beïnvloedt. Een onderschatting in T_1- en T_2-waarden van ongeveer 30% werd waargenomen in de hersenen bij 3T en werd bevestigd door numerieke simulaties voor een vergelijkbare experimentele opstelling. Verder toonden de simulatieresultaten aan dat de fouten in de geschatte parameters veroorzaakt door de aanwezigheid van de tweede component afhangen van de keuze van FA en TR, van de relaxatietijden van de componenten, van het frequentieverschil tussen de twee componenten en van hun volumefracties.

Er is ook onderzoek gedaan naar de effecten van *Gibbs-ringing*, gemotiveerd door het besef dat tijdens de RF-fasecyclus de bandartefacten ruimtelijk verschuiven, waardoor de *Gibbs-ringing* in principe verschilt per beeld. De resultaten toonden aan dat een hoge acquisitiematrix in combinatie met een geschikte methode voor het verwijderen van *Gibbs-*

ringing artefacten de precisie en nauwkeurigheid van de parameterschattingen verbetert, wanneer PLANET wordt toegepast op een object met scherpe signaalintensiteitsranden. Voor *in vivo* gebruik was een relatief hoge acquisitiematrix voldoende om de effecten van *Gibbs-ringing* artefacten te minimaliseren.

De belangrijkste vereiste voor het PLANET-model is een statisch hoofdmagneetveld (B_0) gedurende de fase-cyclus van de bSSFP-acquisitie, die 10-15 minuten kan duren, afhankelijk van de resolutie en het vereiste gezichtsveld (FOV). Vanwege intensieve gradiëntactiviteit en verwarming van metalen componenten van de scanner kunnen B_0-afwijkingen optreden, wat ook kan leiden tot fouten in de geschatte parameters. In **Hoofdstuk 4** worden de resultaten van het onderzoek naar de invloed van een verloop in B_0 (drift) op de prestaties van de PLANET-methode voor signaalmodellen met één component en twee componenten gepresenteerd. De invloed van B_0-drift op de kwantitatieve parameterschattingen werd experimenteel beoordeeld in een fantoom en in de hersenen van gezonde vrijwilligers en werd geverifieerd door numerieke simulaties. Een eenvoudig driftcorrectie-algoritme werd voorgesteld gebaseerd op twee snelle referentiescans om de B0 veldverdeling in kaart te brengen met lage resolutie voor en na de PLANET-acquisitie. Het algoritme werd getest op een fantoom en *in vivo*. In het fantoom (een één-component signaalmodel) veroorzaakte drift fouten van 4% en 8% in de geschatte T_1- en T_2-waarden. In de hersenen, waar meerdere componenten aanwezig zijn, had drift slechts een gering effect. Voor zowel eencomponent- als tweecomponentensignaalmodellen werden door drift veroorzaakte fouten met succes gecorrigeerd door het voorgestelde driftcorrectie-algoritme toe te passen.

Hoofdstuk 5 beschrijft een geval van "serendipiteit". Bij het toepassen van PLANET-scans in het klinische protocol bij patiënten die prostaatradiotherapie ondergaan, werd bij toeval ontdekt dat de fase-cyclische bSSFP-sequentie ook kan worden gebruikt voor kwalitatieve beoordeling van *fiducial markers* (FM's) in de prostaat. Het hoofdstuk is gewijd aan een klinische toepassing van de fase-cyclische bSSFP-beeldvorming in de prostaat. Een nieuwe methode voor visualisatie van FM's in de prostaat met positief contrast voor *MRI-only* radiotherapie werd gepresenteerd.

Eerst werden numerieke simulaties uitgevoerd om het complexe fase-cyclische bSSFP-signaal in aanwezigheid van een gouden FM te onderzoeken. De relatie tussen de werkelijke fysieke locatie van de FM en de geometrische manifestatie van de artefacten werd onderzocht. Vervolgens werden fantomen en *in vivo* studies uitgevoerd om de simulaties te valideren. De experimenteel verkregen artefacten werden vergeleken met de artefacten die in de simulaties werden voorspeld. De nauwkeurigheid van de lokalisatie van FM's werd zowel in een fantoom als *in vivo* beoordeeld. De experimenten lieten zien dat de

FM's een positief contrast hebben met de prostaat. Op reële/ imaginaire fase-cyclische bSSFP-beelden bij alle tien patiënten. Hetzelfde positieve contrast werd waargenomen in de fantomen en bevestigd door simulaties. Voor alle tien de patiënten toonden de resultaten nauwkeurige (binnen 1 mm) overeenkomst van de FM lokalisatie op basis van de fase-cyclische bSSFP-sequentie met de lokalisatie op basis van de referentiebeelden (CT of SPAIR bSSFP voor *MRI-only*). Met deze methode kan de detectie van FM's eenvoudig rechtstreeks op de MR-console worden gedaan, waardoor radiotherapeutische laboranten onmiddellijk feedback kunnen krijgen over de verwachte haalbaarheid van nauwkeurige FM-lokalisatie terwijl de patiënt wordt onderzocht.

Publications

Publications in international journals

- ❖ **PLANET: An Ellipse Fitting Approach for Simultaneous T_1 and T_2 Mapping Using Phase-Cycled Balanced Steady-State Free Precession**
  Shcherbakova Y, van den Berg CAT, Moonen CTW, Bartels LW.
  Magn. Reson. Med. 2018;79:711–722. doi: 10.1002/mrm.26717.

- ❖ **On the accuracy and precision of PLANET for multiparametric MRI using phase-cycled bSSFP imaging**
  Shcherbakova Y, van den Berg CAT, Moonen CTW, Bartels LW.
  Magn. Reson. Med. 2019;81:1534–1552. doi: 10.1002/mrm.27491.

- ❖ **Investigation of the influence of B_0 drift on the performance of the PLANET method and an algorithm for drift correction**
  Shcherbakova Y, van den Berg CAT, Moonen CTW, Bartels LW.
  Magn. Reson. Med. 2019;82:1725–1740. doi: 10.1002/mrm.27860

- ❖ **Visualization of gold fiducial markers in the prostate using phase-cycled bSSFP imaging for MRI-only radiotherapy**
  Shcherbakova Y, Bartels LW, Mandija S, Beld E, Seevinck PR, van der Voort van Zyp JRN, Kerkmeier LGW, Moonen CTW, Lagendijk JJW, van den Berg CAT.
  Phys. Med. Biol. 2019; 64:185001. doi: 10.1088/1361-6560/ab35c3

- ❖ **Transceive phase mapping using the PLANET method and its application for conductivity mapping in the brain**
  Gavazzi S, Shcherbakova Y, Bartels LW, Stalpers LJA, Lagendijk JJW, Creeze H, van den Berg CAT, van Lier ALHMW.
  Magn. Reson. Med. 2019;00:1–18. doi: 10.1002/mrm.27958

Conference proceedings

❖ **Impact of B_1 Field Inhomogeneity on DESPOT-Based T_1 and T_2 Mapping at 1.5T**
Shcherbakova Y, van den Berg CAT, Lagendijk JJW, Moonen CTW, Bartels LW.

In: Proc. of the 23rd Annual Meeting of ISMRM, Toronto, Canada, 2015, p. 4155
[Electronic Poster]

❖ **Accurate T_1 and T_2 Mapping by Direct Least-Squares Ellipse Fitting to Phase-Cycled BSSFP Data**
Shcherbakova Y, van den Berg CAT, Lagendijk JJW, Moonen CTW, Bartels LW.

In: Proc. of the 8th Annual Meeting of ISMRM Benelux Chapter, Eindhoven, The Netherlands, 2016, [Oral]
In: Proc. of the 24th Annual Meeting of ISMRM, Singapore, Singapore, 2016, p. 0695 [Oral]

❖ **SNR Analysis and Sequence Parameter Optimization for T_1 and T_2 Mapping Using an Ellipse Fitting Approach of Phase Cycled BSSFP Data**
Shcherbakova Y, van den Berg CAT, Moonen CTW, Bartels LW.

In: Proc. of the 9th Annual Meeting of ISMRM Benelux Chapter, Tilburg, The Netherlands, 2017, [Poster]
In: Proc. of the 25th Annual Meeting of ISMRM, Honolulu, HI, USA, 2017, p. 3590 [Electronic Poster]

❖ **2D Acquisition Mode for T_1 and T_2 Estimation Using an Ellipse-Fitting Approach on Phase Cycled BSSFP Data**
Shcherbakova Y, van den Berg CAT, Borman PTS, Moonen CTW, Bartels LW.

In: Proc. of the 25th Annual Meeting of ISMRM, Honolulu, HI, USA, 2017, p. 5057 [Electronic Poster]

❖ **Sequences for transceive phase mapping: a comparison study and application to conductivity imaging**

Gavazzi S, Mandija S, van den Berg CAT, Shcherbakova Y, Bennis M, Lagendijk JJW, Stalpers LJA, Creeze H, van Lier ALHMW.

In: Proc. of the 26th Annual Meeting of ISMRM, Paris, France, 2018, p. 5084
[Electronic Poster]
In: Proc. of the ESTRO 37, Barcelona, Spain, 2018, [Electronic Poster]

❖ **Fast clinically feasible MR sequences to map electrical tissue conductivity for improved accuracy in hyperthermia treatment planning (HTP)**
Gavazzi, S., Mandija, S., van den Berg, C. A.T., Shcherbakova, Y., Bennis, M., Lagendijk, J. J.W., Stalpers, L.J.A., Crezee, H., van Lier, A.L.H.M.W.

In: Proc. Strahlentherapie und Onkologie 194 (5), 2018, p. 491-492

❖ **The influence of B$_0$ drift on the performance of the PLANET method and an algorithm for correction**
Shcherbakova Y, van den Berg CAT, Moonen CTW, Bartels LW.

In: Proc. of the 10th Annual Meeting of ISMRM Benelux Chapter, Antwerp, Belgium, 2018
[Poster]
In: Proc. of the 27th Annual Meeting of ISMRM, Montreal, QC, Canada, 2019, p. 4608
[Electronic Poster]

❖ **Detecting the presence of fat using PLANET-based parameter mapping**
Shcherbakova Y, van den Berg CAT, Gavazzi S, Moonen CTW, Bartels LW.

In: Proc. of the 27th Annual Meeting of ISMRM, Montreal, QC, Canada, 2019, p. 4015
[Electronic Poster]

❖ **Visualization of gold fiducial markers in the prostate using phase-cycled bSSFP MRI for MR-only radiotherapy**
Shcherbakova Y, Mandija S, Bartels LW, Moonen CTW, van den Berg CAT

In: Proc. of the 27th Annual Meeting of ISMRM, Montreal, QC, Canada, 2019, p. 1829
[Electronic Poster]
In: Proc. of the ESTRO 38, Milan, Italy, 2019, [Electronic Poster]

Awards

❖ ISMRM - Summa cum Laude Award

Accurate T_1 and T_2 Mapping by Direct Least-Squares Ellipse Fitting to Phase-Cycled bSSFP Data
Shcherbakova Y, van den Berg CAT, Lagendijk JJW, Moonen CTW, Bartels LW.
In: Proc. of the 24th Annual Meeting of ISMRM, Singapore, Singapore, 2016, p. 0695
[Oral]

❖ TOP DOWNLOADED ARTICLE in Magnetic Resonance in Medicine 2017-2018

PLANET: An Ellipse Fitting Approach for Simultaneous T_1 and T_2 Mapping Using Phase-Cycled Balanced Steady-State Free Precession
Shcherbakova Y, van den Berg CAT, Moonen CTW, Bartels LW. Magn. Reson. Med. 2018;79:711–722. doi: 10.1002/mrm.26717.

Acknowledgements

2014 is a year I made the most difficult decision in my life and career. Moving from Russia to the Netherlands and living there for more than five years was both rewarding and challenging. Now, at the end of my PhD program, I am glad to say I have taken the right path. My research experiences have helped me identify and develop specific technical and social skills. I have learned a lot professionally and I have evolved as a person.

I would like to thank everyone who was involved in my PhD journey and have helped me to get the motivation to complete this research.

First, I would like to thank my promoter, Prof. Chrit Moonen, for the opportunity to be a part of his research group and to work in the Imaging Division of the UMC Utrecht. It was a great pleasure working with you. I appreciate your support and help in achieving my research goals.

Second, I'm deeply thankful to my supervisors, Dr. Ir. Wilbert Bartels and Dr. Ir. Nico van den Berg, for their help and support to bring this thesis to a successful end. It was a great pleasure working with both of you. Thank you for the weekly discussions, for reading and reviewing all my papers, for checking my abstracts, posters, and presentations. Thank you for teaching me and guiding me towards the right direction. It was always valuable to have a "double opinion", which always helped to find relevant and smart solutions to all issues and problems we confronted. Thank you for all your advice and valuable feedback.

Next, I would like to thank all my colleagues for a good time together (in random order): Soraya (paranymph), Cornel (paranymph), Pim, Cyril, Stefano, Ellis, Oscar, Beatrice, Robin, Anita, Isabell, Suzanne, Alex, Alberto, Tom, Jeroen S., Janot, Tim, Tijl, Arjan, Matteo, Alessandro, Bjorn, Niek, Stefan, Charis, Roel, Pascal, Marijn, Helen, Anneloes, Clemens, Mario, Peter S., Hugo, Bas, Ivana, Jaco, Lennart, Jolanda, Anna K., Filipa, Maureen, Hans, Freddy, Mike, Frank, Marjolein, Josanne, Szabolcs, Hamed, Nadieh, Nikki, Flavio, Federico, Ayodeji, Catalina, Alexander R., Ieva, Ivan, Ilya, Xiaoxu, Charles, Markus, Samuel, Aidin, Fenghua, Mariëlle, Ingmar, Marc, Baudouin, Yuana, Kim, Tuan, Teun. Thank you all for the great atmosphere during group meetings, conferences and IMAGOs. Thank you for the discussions, meetings, presentations, lunches, and a nice time together!

Dear Anna V. and Viviana, my housemates, it was a pleasure to share the house with you in Utrecht in 2014-2015 (Laura, Joana, Maria as well ☺). Thank you all for a great time together.

Хочу поблагодарить мою семью и всех моих родственников за поддержку в течение этих 5 лет. Это, однозначно, было непростое решение уехать из России. Конечно, были сложные моменты, когда хотелось всё бросить и вернуться домой, но благодаря вам я дошла до конца. И сейчас перед вами результат моей научной работы.

Женя, папа, Серёжа, тетя Люда, бабушка, большое спасибо, что вы всегда были "рядом". Я вас всех очень люблю! Наташа, тетя Лена, дядя Костя, все мои троюродные братья и сестры, всем спасибо за поддержку.

Любимая мама, ты ушла так рано, но я знаю, ты бы гордилась мной. Эта диссертация посвящена тебе. Покойся с миром. Ты всегда в моем сердце.

Спасибо всем-всем моим друзьям, кто поддерживал меня и был на связи. Я бы очень хотела иметь возможность со всеми вами встречаться чаще. Катя П., Света К., Женя Г., Варя, Ульяна, Наташа Г., Лена Б., вам всем спасибо за поддержку ☺

Леночка, дорогая моя, тебе отдельное спасибо. Ты сама всё знаешь... Я тебя люблю и очень ценю то, что у меня есть такой лучший друг.

Derk, thank you so much for being by my side during all these years. I could not have done it without your support and understanding. I am very happy to have you in my life, and I wish all our dreams will come true soon. ☺

Curriculum Vitae

Yulia Shcherbakova was born on August 21st, 1985 in Russia in a small town called Bogoroditsk (Tula region). She grew up there and in 2002 she received her high-school "cum laude" diploma. Next, she moved to Moscow and entered the Moscow Engineering Physics Institute MEPhI (now National Research Nuclear University), the faculty of experimental and theoretical physics. In 2008, she graduated from the University with a "cum laude" M.Sc. diploma in Medical Physics.

From 2010 to 2014 she worked in General Electric Healthcare (covering Russia and CIS) as an Application Specialist in MRI. She delivered many on-site MRI trainings in different hospitals and institutions on MR scanners, as well as many classroom sessions on dedicated GE workstations.

In April 2014 she started as a PhD candidate at the University Medical Center Utrecht under the supervision of Prof. C.T.W. Moonen, Dr. Ir. L.W. Bartels, and Dr. Ir. C.A.T. van den Berg in the project "Image Guided Cancer Therapy: Real-Time Target Tracking in MRI-guided HIFU and MRI-guided RadioTherapy". She has been working on MRI acquisition methods for accurate 3D tumor visualization, and on the optimization of methods for quantitative MRI. The results of her research are presented in this thesis.